Mathematical Analysis of Novel Magnetic Recording Heads

by

Hazel Anne Shute

A thesis submitted to the University of Plymouth in partial
fulfilment for the degree of

Doctor of Philosophy

School of Mathematics and Statistics

October 1995

To my family

Abstract

Mathematical Analysis of Novel Magnetic Recording Heads

Hazel A. Shute

As a contribution to increasing the areal density of digital data stored on a magnetic recording medium, this thesis provides mathematical analyses of various magnetic recording heads. Each of the heads considered here is for use in a perpendicular recording system, writing to or reading from a multi-layer medium which includes a high magnetic permeability layer between the data storage layer and the substrate. The exact two-dimensional analysis is performed in each case by one of two methods: either Fourier analysis or conformal mapping. The types of heads analysed include conventional styles but particular emphasis is placed on the effects of the novel idea of potential grading across the pole pieces.

Exact head fields are derived for thin film heads with both constant and linearly varying pole potentials, single pole heads with linearly and arbitrarily varying pole potentials and shielded magnetoresistive heads, all in the presence of a magnetic underlayer. These and other published solutions are used to derive output characteristics for perpendicular replay heads, which are compared with published theoretical and experimental results where possible.

The Fourier solutions obtained are in the form of infinite series dependent on at least one set of coefficients which are determined by infinite systems of linear equations. Approximations to the potentials in the head face planes, independent of these coefficients, are derived from the exact Fourier solutions. The accuracy of these approximations is demonstrated when they are used to estimate the vertical field components and the spectral response functions.

Heads with graded pole potentials are found to have more localised vertical field components than the corresponding constant potential heads. They are also better suited for use with thin media for 'in contact' recording.

Acknowledgements

I would like to express my sincere gratitude to my supervisors, Dr. David T. Wilton and Prof. Desmond J. Mapps for their enthusiasm and support throughout this study. The constructive comment and the encouragement of Prof. Barry K. Middleton are also much appreciated.

I would like to thank the University of Plymouth for providing my studentship and the funding to attend conferences, via the Centre for Research in Information Storage Technology and the School of Mathematics and Statistics. I am grateful for the assistance of the staff of Computing Services, both at the Plymouth campus and at the Seale-Hayne campus. Thank also go to my fellow researchers in the School of Mathematics and Statistics, particularly Ms. Jenny Sharp, who have provided technical and moral support.

Finally, I must mention my family, without whose cooperation and support this work could not have been completed.

Author's Declaration

At no time during the registration for the degree of Doctor of Philosophy has the author been registered for any other University award.

This study, with the Centre for Research in Information Storage Technology, was financed with the aid of a studentship from the University of Plymouth.

Regular discussions were held with Prof. B.K. Middleton, Head of the School of Electrical Engineering, at the Victoria University of Manchester.

Publications:

D.T. Wilton, D.J. Mapps and H.A. Shute
    Exact field calculations for conventional and graded magnetisation thin film recording heads.
    IEEE Trans. Magn., vol.30, no.2, pp. 253-263, Mar. 1994.
D.T. Wilton, D.J. Mapps and H.A. Shute
    Improved replay performance of a single pole head with graded magnetisation for perpendicular recording.
    J. Mag. Soc. Japan, vol.18, no.S1, pp.157-160, 1994.
D.T. Wilton, D.J. Mapps and H.A. Shute
    A graded magnetisation single pole head for perpendicular recording.
    IEEE Trans. Magn., vol.31, no.3, pp. 2339-2350, May 1995.
H.A. Shute, D.T. Wilton and D.J. Mapps
    Exact spectral response functions for perpendicular recording heads.
    Submitted to *IEEE Trans. Magn.*, Jan. 1995.
H.A. Shute, D.T. Wilton and D.J. Mapps
    Approximate spectral response functions for single pole heads.
    Accepted by *JMMM.*, Sep. 1995.
H.A. Shute, D.T. Wilton and D.J. Mapps
    A theoretical analysis of shielded magnetoresistive heads by conformal mapping.
    Submitted to *IEEE Trans. Magn.*, Jul. 1995.

Conferences attended:

International Magnetics Conference, April, 1993, in Stockholm.

6th European Magnetic Materials and Applications Conference, September, 1995, in Vienna, to present the poster 'Approximate Spectral Response Functions for Single Pole Heads'.

Signed...H...A...Shute.......

Date..........6-10-95..................

Contents

List of Figures

List of Tables

Chapter 1

Introduction to Magnetic Recording

1.1 Historical Background

Magnetic materials have been known for well over 2000 years but it was not until the nineteenth century that the major scientific discoveries were made. In 1820, Oersted made the initial discovery that an electric current produces a magnetic field, which stimulated other research in electromagnetism. Ampère found that two currents have a mutual magnetic effect, and in 1831 Faraday discovered electromagnetic induction [1].

The first magnetic sound recording was made by Oberlin Smith in 1888 and the first commercial magnetic recording machine, the telegraphone, was invented in 1898 by Valdemar Poulsen. This was a dictating machine which recorded onto steel wire. By the 1920's the steel wire had been replaced by steel tape, then by paper tape coated with iron particles. Plastic tape coated with gamma ferric oxide was first used as a recording medium in 1935. Floppy disks and tapes are still made with a plastic substrate although alloys are commonly used as the magnetic media. Computer hard disk technology has become very sophisticated. For many years aluminium has been used as the substrate for these large disks but with the demand for portable computers, smaller hard disks based on glass are in production [2]. Glass provides a rigid substrate which can be polished to give a very smooth surface onto which the magnetic medium is deposited.

At first, Poulsen's telegraphone used a single electromagnetic pole to record onto the wire but later he found that better results were obtained using two offset poles. In the 1930's recording with 'ring-shaped' heads was established. Apart from miniaturisation and improved materials this type of head is still in use in production machines.

The early machines used analog recording. Today, both analog and digital recording techniques are used in different applications. This thesis considers magnetic recording and replay heads for computers which, today, store information digitally.

1.2 Longitudinal and Perpendicular Modes of Recording

Digital information is stored on a magnetic medium by the direction in which the magnetic material is magnetised. Two ideal extremes are possible, which are depicted in Fig. 1.1. The arrows represent the magnetic vector and the magnetic poles of the individual magnetised regions are indicated as + or −. If the direction of the magnetic vector is parallel to the plane of the medium, the recording is said to be longitudinal, but if the magnetic vector is normal to the plane of the medium, the recording is perpendicular. By careful choice of particles and methods used in its production, a medium can be given a particular anisotropy, *ie.* a preferred axis of magnetic orientation. The

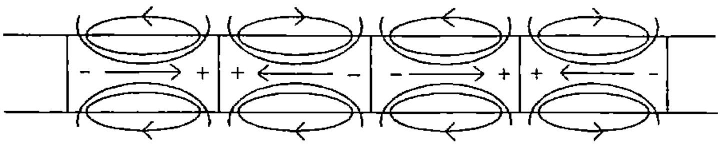

a) Longitudinal

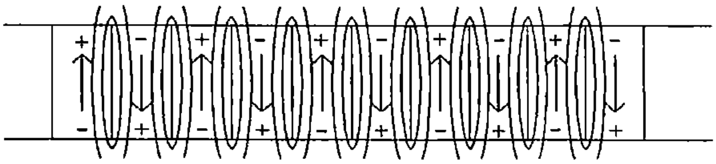

b) Perpendicular

Figure 1.1: Diagram of ideal longitudinal and perpendicular magnetic recordings.

laws of magnetism state that 'like poles repel', therefore in a longitudinal recording the magnetic fields due to adjacent magnetic regions of opposite polarity cause a demagnetising field, represented by the ellipses in the diagram. These fields due to the individual magnetic regions have been observed in practice [3]. The demagnetising field prevents sharp transitions between bits of opposite polarity. A mathematically convenient, arctangent form is generally accepted as a good approximation to the shape of a longitudinal transition.

In a perpendicular recording on the sort of medium used for longitudinal recording, adjacent oppositely magnetised regions attract each other so that they form a stable low potential energy magnetic system, therefore the amount of flux detectable outside the medium is much less than for a longitudinal recording. This was the reason for Poulsen's improved replay signal when he used the two offset poles. The initial single pole recordings were predominantly perpendicular, but the two pole system created mainly longitudinal recordings on the unstructured media of the time. Therefore research into perpendicular recording systems was very limited until Iwasaki, Nakamura and Ouchi [4] used a medium with an in-built perpendicular anisotropy and placed a layer of highly permeable material such as nickel-iron (NiFe) behind the recording layer. This 'flux sink' increased the magnitude of the field, of each individual magnetised region detectable outside the medium. Using an magnetic underlayer, replay from a perpendicular recording is of similar quality to that from a longitudinal recording. The perpendicular medium and underlayer, commonly described as a double-layer medium, actually consists of several layers of material deposited on the substrate. Typically, first there is the underlayer of NiFe onto which is placed a layer of a non-magnetic material such as gold or titanium. This gives a good surface for the promotion of a perpendicularly oriented magnetic film. Cobalt-chromium alloy (CoCr) forms columnar grains about 200Å in diameter and was first used as a perpendicular recording medium in 1975 [5]. The orientation of the alloy grains can be controlled so that their longest axis is normal to the underlayer, thereby maximising the number of grains adjoining the surface of the medium. Experiments with this type of medium have resulted in the detection of up to 680,000 flux reversals per inch [6] which indicates that the magnetised regions are composed of individual CoCr grains. This far exceeds the capabilities of magneto-optic recording which is limited by the wavelength of light [7]. Clearly, higher bit densities can be stored on a perpendicular medium than a longitudinal one of this type.

The transitions between bits of opposite polarity are stable in a perpendicular recording *ie.* there is virtually no demagnetising field at the transitions. Therefore the transitions are much sharper than in the longitudinal case and at high densities a perfect step function is considered a good model of the true transition shape [8, 9, 10].

1.3 Recording Heads

High density recording requires recording heads with high intensity, sharply focused magnetic fields. The strong magnetic field is needed to ensure that the medium is saturated when a bit is written and hence retains the magnetisation. Steep magnetic field gradients are required to prevent adjacent bits being overwritten in error.

The conventional longitudinal recording head is the ring head which consists of two relatively long poles of opposite polarity separated by a narrow gap. With miniaturisation of all recording systems, the poles of this type of head are becoming shorter. Heads with very thin poles, made by vacuum deposition and photo-fabrication, are termed thin film heads. Ring heads can also be used in perpendicular recording but in 1977 Iwasaki and Nakamura [3] proposed a single pole type head for use in perpendicular recording which consisted of a read/write pole on the medium side of the underlayer and a larger auxilliary pole on the other side. The double-sided nature of this head makes it difficult to use in hard disk drives [11]. Ohtsubo [11] proposed a novel trapezoidal perpendicular recording head. The design was refined into a laminated rectangular head presented in [12]. The constituents of the laminations were varied to produce a non-uniform permeability across the head. A single-sided W-shaped head [13] has also been proposed.

Each of the heads mentioned above, when used for reading, is inductive *ie.* the changing magnetic flux as the medium passes close to the head causes an electric current to flow through the coils which are wound around the head, obeying Faraday's Law. These heads are usually made of alloys of which the most commonly used are Molybdenum Permalloy, Alfenol and Sendust [14], which have been chosen for their high permeability and low coercivity. Therefore they are easily strongly magnetised. In 1971 the magnetoresistive replay head was introduced by Hunt. This is a very thin rectangular-shaped film made from alloys such as nickel-iron, nickel-cobalt or cobalt-iron [14]. The resistivity of these materials varies with the magnetic field applied to them. To prevent the field due to adjacent bits on the medium influencing the sensor, shields have been added which also increase the sensitivity of the head [15].

1.4 Motivation

The demand for smaller, faster machines with high storage capacities drives research on information storage systems. Areal data densities have increased steadily from the 2000 bits per square inch of the first random access hard disk, the IBM 305 of 1955 [16, 5]. Several major manufacturers are experimenting with disk drives capable of storing 1 gigabit per square inch and it is hoped that a tenfold increase will be achieved within the next five years by employing magnetoresistive replay heads [2].

All present production machines employ longitudinal recording on single layer media. Although some manufacturers are experimenting with vertical recording, the industry as a whole is unlikely to consider changing to this technology until a significant advantage over longitudinal systems has been demonstrated. Perpendicular particulate media can support very high bit densities but systems are limited by the capabilities of the recording heads. Interference between the output voltages due to adjacent bits and head-dependent ouput nulls restrict the range of usable bit densities. Sophisticated decoding techniques, such as the partial-response maximum-likelihood concept, are being developed to cope with a certain degree of adjacent bit interference but any system can only operate over a limited range of output voltages. Therefore, if the areal data density is to increase to its ultimate limit, improved recording heads are needed.

In order to evaluate the performance of any combination of head and medium in a system for high density magnetic recording, it is important to know the shape of the head field. The most common approaches for such field calculations are approximate numerical techniques such as finite difference, finite element and boundary element methods, Fourier analysis and conformal mapping techniques based on the Schwarz-Christoffel transformation. Each has its merits and limitations. The numerical techniques may most easily handle complicated geometries but can be computationally expensive, requiring artificial boundaries at distances far from the region of interest and large numbers of nodes or elements near pole corners, and are restricted to producing numerical output. Fourier analysis is the only approach to provide an exact explicit analytic solution, although this is in the form of an infinite series and it is necessary to calculate certain coefficients and evaluate field integrals, numerically in some cases. The expressions provided by Fourier analysis can lead to approximate solutions, useful in practice within their ranges of validity, which may show directly the dependence of the field upon the parameters of the problem, and can be valuable for further calculations such as system outputs. The conformal mapping method can be applied to more complicated geometries than Fourier analysis. It can be fast but normally requires a numerical iterative technique to find the inverse mapping, for which convergence may be a problem. Both of the analytic methods are used in this thesis.

Conventional heads are designed to provide a constant pole potential. Two such heads, each in the presence of an underlayer, are analysed here for the first time: namely the thin film head and the shielded magnetoresistive sensor. Heads with varying pole potentials are also considered. Exact solutions for thin film heads and single pole heads with linearly graded pole potentials and for single pole heads with arbitrary pole potential are derived. These and other published solutions are used to derive output characteristics and accurate approximations, for perpendicular replay heads. Further details are given in Section 2.2.

Much of this work has either already been published or has been submitted for publication. There have also been three conference presentations of the work. Fourier analyses of thin film heads and single pole-type heads all in the presence of underlayers have been published in [17, 18] and [19]. Comparison of the replay characteristics of all the perpendicular recording heads for which analytic head fields have been obtained to date, are made in [20]. Simple approximations to replay characteristics for single pole-type heads are given in [21]. The conformal mapping technique has been used in the analysis of a shielded magnetoresistive head for perpendicular replay [22].

1.5 Summary

This introducory chapter has covered:

- The discovery of the magnetic recording technology.
- The development of double-layer media for perpendicular recording.
- Improved bit densities on particulate media.
- Recording head designs.
- Evaluation of the merits of various numerical and anaytic mathematical methods.
- A brief description of the new knowledge gained from this work.

Chapter 2

Introduction to the Theoretical Methods

2.1 Mathematical Methods

2.1.1 Introduction

Here the theory behind the relationships used in the analysis of magnetic recording heads and their replay characteristics is developed from the laws of physics. The mathematical methods which are employed in the new analyses, namely the Fourier and the conformal mapping methods, are described with specific reference to the classic cases of a single pole head and a ring head, respectively. The Fourier method can only be applied to simple geometries but it provides analytic solutions which give causal insight into the phenomena observed in practical systems. The conformal mapping method, although in principle analytic, usually requires numerical inversion of the mapping, but it can be applied to more complicated geometries than the Fourier method. This chapter concludes with a detailed statement of the new work contained in this thesis.

2.1.2 Laplace's Equation

In simple terms, magnetic fields are caused by the movement of charge either as an electric current flowing through a circuit or within the atoms of magnetic materials due to an inbalance in the spins of the electrons. Magnetic poles are considered to be the point sources or sinks of a magnetic field. Flux is emitted from a positive pole and the magnetic field strength $\underline{H}$ at any point $\underline{r}$ in the field, is the force exerted at that point, due to the magnetic flux density $\underline{B}$ at $\underline{r}$, which acts in the same direction as the flux. Therefore

$$\underline{H} = \mu_0 \mu \underline{B}\,, \tag{2.1}$$

where μ_0 = the permeability of a vacuum

and μ = the permeability of the material at $\underline{r}$, relative to μ_0.

Maxwell's equations summarise the laws of electricity and magnetism:

$$\underline{\nabla} \cdot \underline{E} = \frac{\rho}{\varepsilon_0} \qquad \underline{\nabla} \times \underline{E} = -\frac{\partial \underline{B}}{\partial t} \tag{2.2}$$

$$\underline{\nabla} \cdot \underline{B} = 0 \qquad \underline{\nabla} \times \underline{B} = \mu_0 \varepsilon_0 \frac{\partial \underline{E}}{\partial t} + \mu_0 \underline{j} \tag{2.3}$$

where $\underline{E}$ is the electric field vector,

ρ is the charge density,

ε_0 is the permittivity of a vacuum,

and $\underline{j}$ is the current density.

Taking equations (2.3) only, the first is the continuity equation for magnetism. In static models, the second equation reduces to $\underline{\nabla} \times \underline{B} = \mu_0 \underline{j}$. In a region where there are no current sources $\underline{\nabla} \times \underline{B} = \underline{0}$. Therefore $\underline{\nabla} \times \underline{H} = \underline{0}$ also. Hence, there is a scalar potential function, $\varphi(x, y, z)$, such that $\underline{H} = -\underline{\nabla}\varphi$. From (2.1) and the continuity equation

$$\nabla^2\varphi \equiv \frac{\partial^2\varphi}{\partial x^2} + \frac{\partial^2\varphi}{\partial y^2} + \frac{\partial^2\varphi}{\partial z^2} = 0 \tag{2.4}$$

which is Laplace's equation. Therefore the magnetic field $\underline{H}$, exterior to a recording head, can be computed from the solution of Laplace's equation for the magnetic potential φ.

2.1.3 The Fourier Method

2.1.3.1 Introduction

The Fourier method was first used in the context of magnetic recording heads by Fan [23], who analysed the field of a single pole head in the presence of an underlayer. Except for the new models to be presented in Chapter 3, the Fourier method has been applied to:

- A single pole head with an underlayer [23].
- A ring head without an underlayer [24, 25, 26, 27].
- A ring head with an underlayer [28].
- A symmetrically shielded pole head with an underlayer [29].
- A symmetrically shielded MR head without an underlayer [30].

In each case, the following modelling assumptions have been made:

1. The head is infinitely deep, so that a two-dimensional model is applicable.
2. The pole pieces have perfectly rectangular corners.
3. The pole pieces are infinitely high.

4. The pole pieces are infinitely permeable and therefore each has a constant magnetic potential distribution.

5. The effect on the field exterior to the pole pieces due to the recording medium, other than the possible presence of an underlayer, is negligible.

6. Where an underlayer is present, it is infinitely permeable and infinitely long.

Assumption 1 is valid because typically the track width of a pole or ring head is at least 10 times the other significant dimensions. However as the areal density of the bits of digital information recorded onto disks increases, this assumption is becoming less realistic. Assumption 2 results in singularities in the solutions at the corners of the pole pieces, although in reality the magnetic material in these regions saturates [31]. In general, the pole pieces are much higher than the length of either the gap, in the case of a ring head, or the head – underlayer separation for a single pole, hence assumption 3. The pole pieces are constructed from very high permeability materials, hence assumption 4. Assumption 5 depends on the fact that the permeability of the recording medium is very low compared with that of the pole and the underlayer. Recording media are designed in this way so that a strong magnetic field is needed to affect their intrinsic magnetic domains. Hence also, they retain the information recorded on them for long periods of time unless they are further exposed to sufficiently strong magnetic fields. Therefore, relative to the pole and the underlayer, the permeability of the medium is only slightly greater than that of air, which is also only slightly greater than the permeability of a vacuum. The underlayer, which is usually a part of the recording medium, is very long compared to the recording head and is made of a very high permeability material such as nickel-iron (assumption 6).

The Fourier method relies upon dividing the area exterior to the recording head and the underlayer, if one is present, into rectangular regions. In a region between two parallel boundaries on each of which the potential is known, Laplace's equation can be solved by the technique of separation of variables [32], which results in an infinite series solution dependent on at least one set of coefficients. The Fourier transform method [32] is applicable in a semi-infinite region producing an integral solution which depends on an unknown function, say $C(k)$. The sets of coefficients and the unknown function are found by matching the solutions and the appropriate derivative at the common boundary between the regions, so ensuring that the complete solution is both continuous and smooth. $C(k)$ is found in terms of the coefficients which themselves are defined by infinite systems of linear algebraic equations.

The Fourier method is demonstrated here by Fan's solution for a single pole head [23] and the models and some of the results for each of the other head configurations listed above are given, in coordinate systems and notation consistent with that used in this thesis.

2.1.3.2 The single pole head

Fig. 2.1 shows Fan's idealised two-dimensional model of the single pole head with an underlayer [23]. A semi-infinite pole of width $2L$ is perpendicular to and at a distance t from an infinitely long, highly permeable underlayer at zero potential. The pole is assumed to have a constant potential V and the negative potential pole is effectively the reflection of the positive pole, in the underlayer. Due to symmetry it is only necessary to solve Laplace's equation for $x \geq 0$ and the area is further subdivided into two regions, B and C as shown. The general solutions to Laplace's equation which satisfy the boundary conditions in these two regions are, with the subscript denoting

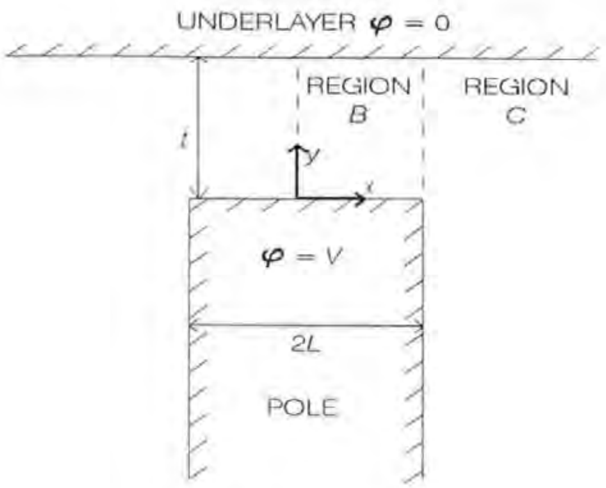

Figure 2.1: The single pole head.

the region and the superscript P denoting a conventional single pole head,

$$\varphi_B^P(x,y) = V\frac{t-y}{t} + \sum_{n=1}^{\infty} B_n^P \sin\left(\frac{n\pi(t-y)}{t}\right)\cosh\left(\frac{n\pi x}{t}\right) \qquad 0 \le x \le L \tag{2.5}$$

and

$$\varphi_C^P(x,y) = \int_0^{\infty} C(k)\sin\left(\frac{k(t-y)}{t}\right) e^{-kx/t}\, dk\,. \tag{2.6}$$

Matching the solutions at $x = L$ gives:

$$C(k) = \frac{2V}{\pi} e^{kL/t}\frac{\sin(k)}{k^2} + e^{kL/t}\sum_{n=1}^{\infty} B_n^P 2n(-1)^n \cosh\left(\frac{n\pi L}{t}\right)\frac{\sin(k)}{k^2-(n\pi)^2}\,. \tag{2.7}$$

So that in region C

$$\varphi_C^P(x,y) = \frac{2V}{\pi} I_0^P + \sum_{n=1}^{\infty} B_n^P 2n(-1)^n \cosh\left(\frac{n\pi L}{t}\right) I_n^P \tag{2.8}$$

where

$$I_n^P = \int_0^{\infty} \frac{\sin(k)\sin\left(k(t-y)/t\right)}{k^2-(n\pi)^2} e^{-k(x-L)/t}\, dk\,. \tag{2.9}$$

Now matching the x derivatives of both solutions at $x = L$ gives

$$\frac{\pi}{4} B_m^P \sinh\left(\frac{m\pi L}{t}\right) + \sum_{n=1}^{\infty} B_n^P n\pi(-1)^{m+n} \cosh\left(\frac{n\pi L}{t}\right) I_{mn} = V(-1)^{m+1} I_{m0}\,, \tag{2.10}$$

for $m = 1, 2, 3, \cdots$ where

$$I_{mn} = \int_0^{\infty} \frac{k \sin^2(k)}{[k^2 - (m\pi)^2][k^2 - (n\pi)^2]}\, dk \tag{2.11}$$

which is an infinite set of linear algebraic equations for the coefficients B_m^P depending on the ratio L/t only. Normalised coefficients, $B_m^{P'} = B_m^P \cosh(m\pi L/t)/V$, are computed by truncating the system of equations to some finite size $N \times N$. Fan gives no further information on how he evaluated the constants, in [26] $N = 6$ was used and in [27] systems up to 640×640 were solved and extrapolation using library routines [33] was used to obtain coefficients correct to 6dp.

The normalised horizontal $H_x^P = -\partial\varphi^P/\partial x$ and vertical $H_y^P = -\partial\varphi^P/\partial y$ field components follow by partial differentiation,

$$\frac{H_x^P}{V} = \begin{cases} -\sum_{n=1}^{\infty} B_n^{P'} \frac{n\pi}{t} \sin\left(\frac{n\pi(t-y)}{t}\right) \sinh\left(\frac{n\pi x}{t}\right) \Big/ \cosh\left(\frac{n\pi L}{t}\right) & 0 \le x \le L \\ \frac{2}{\pi t} J_0^P + \sum_{n=1}^{\infty} B_n^{P'} \frac{2n}{t} (-1)^n J_n^P & L \le x < \infty \end{cases} \tag{2.12}$$

$$\frac{H_y^P}{V} = \begin{cases} \frac{1}{t} + \sum_{n=1}^{\infty} B_n^{P'} \frac{n\pi}{t} \cos\left(\frac{n\pi(t-y)}{t}\right) \cosh\left(\frac{n\pi x}{t}\right) \Big/ \cosh\left(\frac{n\pi L}{t}\right) & 0 \le x \le L \\ \frac{2}{\pi t} K_0^P + \sum_{n=1}^{\infty} B_n^{P'} \frac{2n}{t} (-1)^n K_n^P & L \le x < \infty \end{cases} \tag{2.13}$$

where

$$J_n^P = \int_0^{\infty} \frac{k \sin(k) \sin\left(k(t-y)/t\right)}{k^2 - (n\pi)^2} e^{-k(x-L)/t}\, dk \tag{2.14}$$

$$K_n^P = \int_0^{\infty} \frac{k \sin(k) \cos\left(k(t-y)/t\right)}{k^2 - (n\pi)^2} e^{-k(x-L)/t}\, dk\,. \tag{2.15}$$

The integrals I_{m0} and I_{mn} are given in closed form by Fan [23], and appear in Appendix A, Section A.2.1. Analytic expressions for integrals of the same form as I_n^P, J_n^P and K_n^P are given in [25] and are given in Sections A.3.1, A.3.2 and A.3.3, respectively.

2.1.3.3 The ring head without an underlayer

The ring head without an underlayer has also been analysed by Fan [24] under the first five assumptions of Section 2.1.3.1. The idealised two-dimensional model is shown in Fig. 2.2, in the more generalised form adopted here.

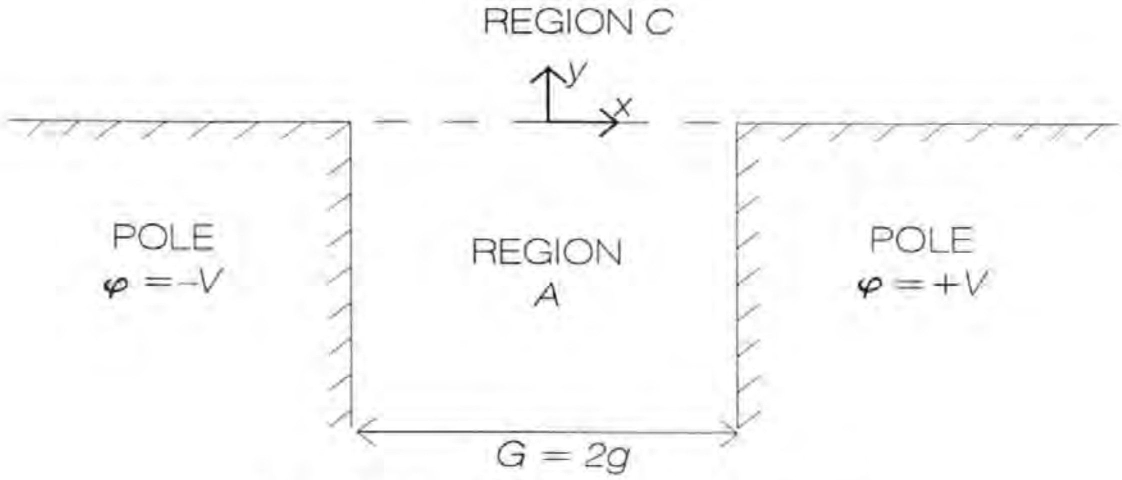

Figure 2.2: Ring head without an underlayer.

The semi-infinitely long and high pole pieces at constant potentials $+V$ and $-V$ are separated by a gap of width $G = 2g$. The area exterior to the head is divided into two regions A and C as shown, and due to the symmetry of the model about the centre of the gap, Laplace's equation is solved for $x \geq 0$ only.

In a practical system, the recording medium would pass through region C only, where, with the superscript R denoting a ring head without an underlayer,

$$\varphi^R(x,y) = \frac{2V}{\pi} I_0^R + \sum_{n=1}^{\infty} A_n^R 2n(-1)^n I_n^R \qquad y \geq 0 \qquad (2.16)$$

and

$$I_n^R = \int_0^\infty \frac{\sin(k)\sin(kx/g)}{k^2-(n\pi)^2} e^{-ky/g}\,dk\,. \tag{2.17}$$

The normalised coefficients $A_m^{R'} = A_m^R/V$ satisfy the infinite set of linear algebraic equations

$$\frac{\pi}{4}A_m^{R'} + \sum_{n=1}^{\infty} A_n^{R'} n\pi(-1)^{m+n} I_{mn} = (-1)^{m+1} I_{m0} \tag{2.18}$$

for $m = 1, 2, 3, \cdots$ with I_{mn} and I_{m0} defined by (2.11). Coefficients correct to 6dp. have been obtained by Wilton [27] which are consistent with those evaluated in [26] but which exceed the values given in [25] and [24].

The normalised horizontal and vertical field components in region C follow by the partial differentiation of (2.16) so that

$$\begin{aligned}
\frac{H_x^R}{V} &= -\frac{1}{\pi g}\left(\arctan\left(\frac{g+x}{y}\right) + \arctan\left(\frac{g-x}{y}\right)\right) - \sum_{n=1}^{\infty} A_n^{R'}\frac{2n}{g}(-1)^n K_n^R && (2.19)\\
\frac{H_y^R}{V} &= \frac{1}{2\pi g}\ln\left(\frac{(g+x)^2+y^2}{(g-x)^2+y^2}\right) + \sum_{n=1}^{\infty} A_n^{R'}\frac{2n}{g}(-1)^n J_n^R && (2.20)
\end{aligned}$$

where

$$\begin{aligned}
J_n^R &= \int_0^\infty \frac{k\sin(k)\sin(kx/g)}{k^2-(n\pi)^2} e^{-ky/g}\,dk && (2.21)\\
K_n^R &= \int_0^\infty \frac{k\sin(k)\cos(kx/g)}{k^2-(n\pi)^2} e^{-ky/g}\,dk\,, && (2.22)
\end{aligned}$$

and the first terms of (2.19) and (2.20) are $-2K_0^R/\pi g$ and $2J_0^R/\pi g$ respectively. I_n^R, J_n^R and K_n^R are of the same form as I_n^P (2.9), J_n^P (2.14) and K_n^P (2.15) respectively, with $(t-y)/t$ replaced by x/g and $(x-L)/t$ replaced by y/g, closed form expressions are listed in Sections A.3.1, A.3.2 and A.3.3 respectively. The similarities between the fields of a single pole with an underlayer and a ring head without an underlayer have been discussed in [27].

2.1.3.4 The ring head with an underlayer

The ring head with an underlayer has been analysed in [28], under the assumptions of Section 2.1.3.1. The idealised two-dimensional model is shown in Fig. 2.3. The pole pieces at constant potentials $+V$ and $-V$ are separated by a semi-infinite gap of width $G = 2g$ and are at a distance t from the underlayer at zero potential. The area exterior to the pole pieces and the underlayer is divided into two regions A and C as shown. In a practical system, the recording medium would pass through region C only where, with the superscript RU denoting a ring head with an underlayer,

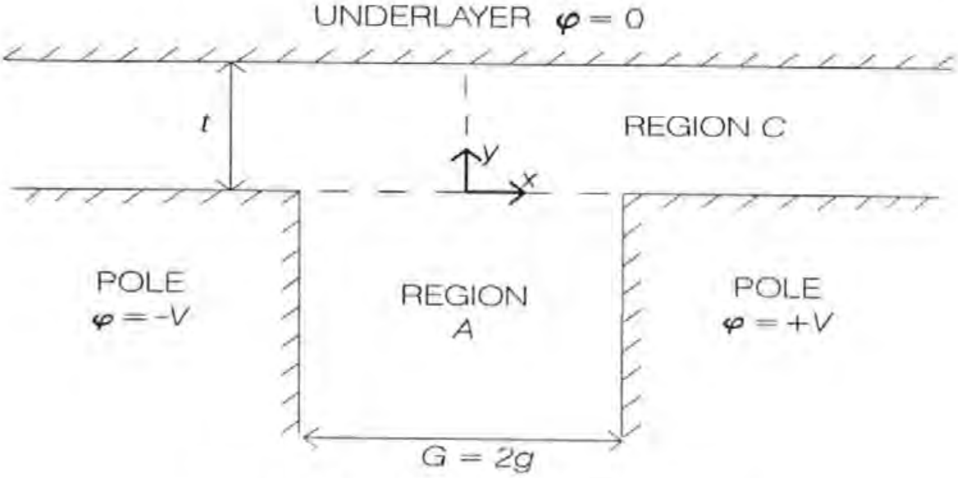

Figure 2.3: Ring head with an underlayer.

$$\varphi^{RU}(x,y) = \frac{2V}{\pi} I_0^{RU} + \sum_{n=1}^{\infty} A_n^{RU} 2n(-1)^n I_n^{RU} \tag{2.23}$$

and

$$I_n^{RU} = \int_0^{\infty} \frac{\sin(k)\sin(kx/g)}{k^2 - (n\pi)^2} \frac{\sinh(k(t-y)/g)}{\sinh(kt/g)}\, dk \tag{2.24}$$

The normalised coefficients $A_m^{RU'} = A_m^{RU}/V$, which depend on g/t, satisfy the infinite set of linear algebraic equations:

$$\frac{\pi}{4}A_m^{RU'} + \sum_{n=1}^{\infty} A_n^{RU'} n\pi(-1)^{m+n} I_{mn}^{RU} = (-1)^{m+1} I_{m0}^{RU} \qquad m = 1, 2, 3, \cdots \tag{2.25}$$

where

$$I_{mn}^{RU} = \int_0^{\infty} \frac{k\sin^2(k)}{[k^2-(m\pi)^2][k^2-(n\pi)^2]} \coth\left(\frac{kt}{g}\right) dk. \tag{2.26}$$

Hence, the normalised horizontal and vertical field components for $0 \le y \le t$ are given by

$$\frac{H_x^{RU}}{V} = -\frac{2}{\pi g}K_0^{RU} - \sum_{n=1}^{\infty} A_n^{RU'} \frac{2n}{g}(-1)^n K_n^{RU} \tag{2.27}$$

and

$$\frac{H_y^{RU}}{V} = \frac{2}{\pi g}J_0^{RU} + \sum_{n=1}^{\infty} A_n^{RU'} \frac{2n}{g}(-1)^n J_n^{RU} \tag{2.28}$$

where

$$K_n^{RU} = \int_0^{\infty} \frac{k\sin(k)\cos(kx/g)}{k^2-(n\pi)^2} \frac{\sinh(k(t-y)/g)}{\sinh(kt/g)} dk \tag{2.29}$$

and

$$J_n^{RU} = \int_0^{\infty} \frac{k\sin(k)\sin(kx/g)}{k^2-(n\pi)^2} \frac{\cosh(k(t-y)/g)}{\sinh(kt/g)} dk. \tag{2.30}$$

Closed form expressions have not been obtained for the integrals I_{mn}^{RU}, I_n^{RU}, J_n^{RU} and K_n^{RU}. As $t \longrightarrow \infty$, each of these integrals approaches the corresponding integral for the ring head without an underlayer, *eg.* $\lim_{t\to\infty} I_n^{RU} = I_n^R$ (2.17). Numerical integration of I_{mn}^{RU} [33] in the evaluation of the coefficients *via* equn. (2.25) limits the size of the system which can be used. Coefficients believed correct to 4dp. have been obtained using a system of 40 linear equations [28].

2.1.3.5 The symmetrically shielded pole head

Wilton and Mapps [29] have analysed the symmetrically shielded pole head in the presence of an underlayer, under the assumptions listed in Section 2.1.3.1. Each shield is assumed to be both semi-infinitely high and long and to be infinitely deep. The potential across each shield is assumed to be constant at αV. In later work, for Chapter 4, it has been found that for semi-infinitely long shields $\alpha \equiv 0$. For this head geometry, it is possible to divide the area exterior to the pole, shields and the underlayer in two ways, so that two equivalent solutions can be obtained. However, both of these solutions require two sets of Fourier coefficients unlike each of the solutions given in the previous three subsections, where only one set of coefficients is needed.

The idealised two-dimensional model for the first solution is shown in Fig. 2.4. The semi-infinite pole of width $2L$, at constant potential V, is separated from each shield at constant potential αV by a gap of width $G = 2g$. The faces of the pole and both shields lie in the same plane, which is parallel to, and at a distance t from, the underlayer at zero potential. For Solution I, the non-conducting area is divided into two regions A

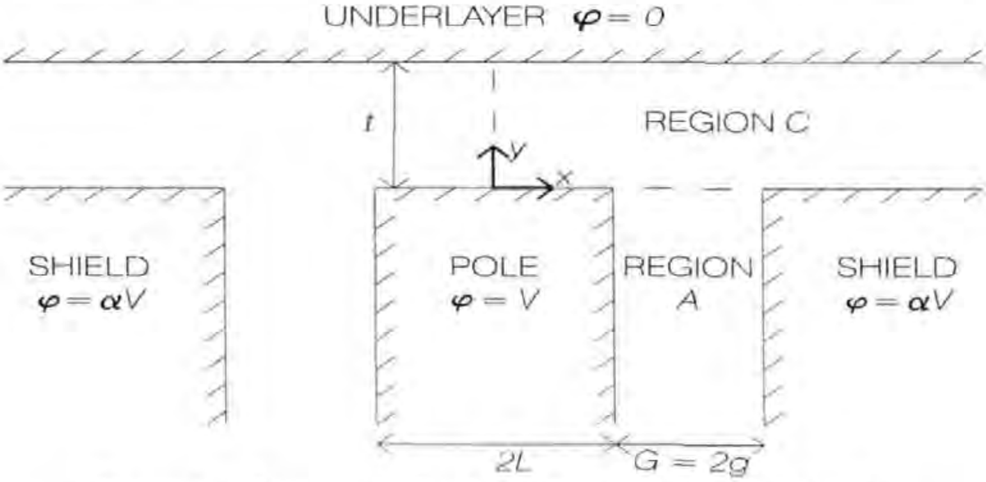

Figure 2.4: Symmetrically shielded pole head – Solution I.

and C, as shown where, with the superscript I denoting Solution I,

$$\varphi^{\mathrm{I}}(x,y)=\begin{cases} \frac{V(G+(\alpha-1)(x-L))}{G}+\sum_{n=1}^{\infty}A_n^{\mathrm{I}}\sin\left(\frac{n\pi(x-L-g)}{g}\right)e^{n\pi y/g} & \\ \quad+\sum_{n=1}^{\infty}B_n^{\mathrm{I}}\cos\left(\frac{(n-\frac{1}{2})\pi(x-L-g)}{g}\right)e^{(n-\frac{1}{2})\pi y/g} & L\le x\le L+G,\ y\le 0 \\ (1-\alpha)\frac{2V}{\pi}L_0+\alpha V\left(\frac{t-y}{t}\right) & \\ \quad+\sum_{n=1}^{\infty}A_n^{\mathrm{I}}4n(-1)^{n+1}L_n+\sum_{n=1}^{\infty}B_n^{\mathrm{I}}4\left(n-\frac{1}{2}\right)(-1)^nM_n & \\ & 0\le x<\infty,\ 0\le y\le t \end{cases} \tag{2.31}$$

where

$$L_n = \int_0^{\infty}\frac{\sin(k)\cos(kx/g)\sin(k(L+g)/g)}{k^2-(n\pi)^2}\frac{\sinh(k(t-y)/g)}{\sinh(kt/g)}\,dk \tag{2.32}$$

$$M_n = \int_0^{\infty}\frac{\cos(k)\cos(kx/g)\cos(k(L+g)/g)}{k^2-((n-\frac{1}{2})\pi)^2}\frac{\sinh(k(t-y)/g)}{\sinh(kt/g)}\,dk\,. \tag{2.33}$$

The normalised coefficients, $A_m^{\mathrm{I}'}=A_m^{\mathrm{I}}/V$ and $B_m^{\mathrm{I}'}=B_m^{\mathrm{I}}/V$, which depend on the ratios L/g and g/t, satisfy the two coupled infinite systems of linear algebraic equations

$$\begin{aligned} \frac{\pi}{4}A_m^{\mathrm{I}'}+\sum_{n=1}^{\infty}A_n^{\mathrm{I}'}2n\pi(-1)^{m+n}J_{mn} &+ \sum_{n=1}^{\infty}B_n^{\mathrm{I}'}2\left(n-\frac{1}{2}\right)\pi(-1)^{m+n+1}K_{mn} \\ &= (-1)^{m+1}(\alpha-1)J_{m0} \end{aligned} \tag{2.34}$$

$$\begin{aligned} \sum_{n=1}^{\infty}A_n^{\mathrm{I}'}2n\pi(-1)^{m+n+1}K_{nm}+\frac{\pi}{4}B_m^{\mathrm{I}'} &+ \sum_{n=1}^{\infty}B_n^{\mathrm{I}'}2\left(n-\frac{1}{2}\right)\pi(-1)^{m+n}L_{mn} \\ &= (-1)^m(\alpha-1)K_{0m}+\frac{\alpha g(-1)^m}{2\pi t\left(m-\frac{1}{2}\right)^2} \end{aligned} \tag{2.35}$$

both for $m=1,2,3,\cdots$ where,

$$J_{mn} = \int_0^{\infty}\frac{k\sin^2(k)\sin^2(k(L+g)/g)}{[k^2-(m\pi)^2][k^2-(n\pi)^2]}\coth\left(\frac{kt}{g}\right)dk \tag{2.36}$$

$$K_{mn} = \int_0^{\infty}\frac{k\sin(k)\cos(k)\sin(k(L+g)/g)\cos(k(L+g)/g)}{[k^2-(m\pi)^2][k^2-((n-\frac{1}{2})\pi)^2]}\coth\left(\frac{kt}{g}\right)dk \tag{2.37}$$

and

$$L_{mn} = \int_0^\infty \frac{k\cos^2(k)\cos^2(k(L+g)/g)}{\left[k^2 - \left((m-\frac{1}{2})\pi\right)^2\right]\left[k^2 - \left((n-\frac{1}{2})\pi\right)^2\right]} \coth\left(\frac{kt}{g}\right) dk\,. \tag{2.38}$$

The normalised field components are obtained from (2.31) by partial differentiation so that the vertical field component in region *C* is given by

$$\begin{aligned} \frac{H_y^{\mathrm{I}}}{V} &= (1-\alpha)\frac{2}{g\pi}N_0 + \frac{\alpha}{t} + \sum_{n=1}^{\infty} A_n^{\mathrm{I}'}\frac{4n}{g}(-1)^{n+1}N_n \\ &\quad + \sum_{n=1}^{\infty} B_n^{\mathrm{I}'}\frac{4(n-\frac{1}{2})}{g}(-1)^n P_n \end{aligned} \tag{2.39}$$

where

$$N_n = \int_0^\infty \frac{k\sin(k)\cos(kx/g)\sin(k(L+g)/g)}{k^2-(n\pi)^2}\frac{\cosh(k(t-y)/g)}{\sinh(kt/g)}\,dk \tag{2.40}$$

and

$$P_n = \int_0^\infty \frac{k\cos(k)\cos(kx/g)\cos(k(L+g)/g)}{k^2 - \left((n-\frac{1}{2})\pi\right)^2}\frac{\cosh(k(t-y)/g)}{\sinh(kt/g)}\,dk\,. \tag{2.41}$$

The division of the non-conducting area into three regions *A*, *B* and *C*, for the second solution, is shown in Fig. 2.5. For this model, the recording medium passes through all three regions so that, with the superscript II denoting Solution II,

$$\varphi^{\mathrm{II}}(x,y) = \begin{cases} \frac{V(t-y)}{t} + \sum_{n=1}^{\infty} C_n^{\mathrm{II}} \sin\left(\frac{n\pi(t-y)}{t}\right)\cosh\left(\frac{n\pi x}{t}\right) & 0 \le x \le L,\ 0 \le y \le t \\ \frac{2V}{\pi}(I_0^{\mathrm{II}} + \alpha Q_0^{\mathrm{II}}) + \sum_{n=1}^{\infty} C_n^{\mathrm{II}} 2n(-1)^n \cosh\left(\frac{n\pi L}{t}\right) I_n^{\mathrm{II}} & \\ \qquad + \sum_{n=1}^{\infty} D_n^{\mathrm{II}} 2n(-1)^n e^{-n\pi(L+G)/t} Q_n^{\mathrm{II}} & L \le x \le L+G,\ y \le t \\ \frac{\alpha V(t-y)}{t} + \sum_{n=1}^{\infty} D_n^{\mathrm{II}} \sin\left(\frac{n\pi(t-y)}{t}\right) e^{-n\pi x/t} & x \ge L+G,\ 0 \le y \le t \end{cases} \tag{2.42}$$

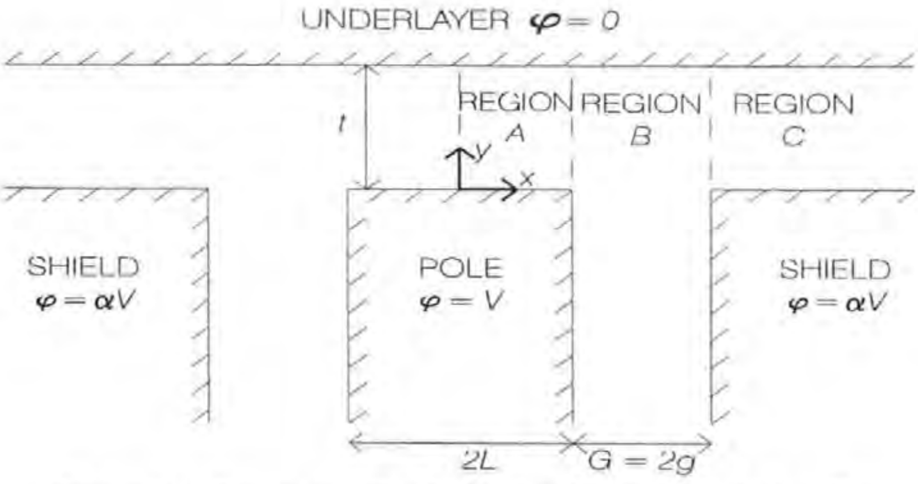

Figure 2.5: Symmetrically shielded pole head – Solution II.

where

$$I_n^{\mathrm{II}} = \int_0^\infty \frac{\sin(k)\sin(k(t-y)/t)}{k^2-(n\pi)^2}\frac{\sinh(k(L+G-x)/t)}{\sinh(kG/t)}\,dk \tag{2.43}$$

$$Q_n^{\mathrm{II}} = \int_0^\infty \frac{\sin(k)\sin(k(t-y)/t)}{k^2-(n\pi)^2}\frac{\sinh(k(x-L)/t)}{\sinh(kG/t)}\,dk\,. \tag{2.44}$$

The normalised coefficients, $C_m^{\mathrm{II}'} = C_m^{\mathrm{II}}\cosh(m\pi L/t)/V$ and $D_m^{\mathrm{II}'} = D_m^{\mathrm{II}}e^{-m\pi(L+G)/t}/V$, which depend on the ratios L/t and G/t, satisfy the two coupled infinite systems of linear equations

$$\begin{aligned}\frac{\pi}{4}C_m^{\mathrm{II}'}\tanh\left(\frac{m\pi L}{t}\right) &+ \sum_{n=1}^{\infty} C_n^{\mathrm{II}'} n\pi(-1)^{m+n} I_{mn}^{\mathrm{II}} + \sum_{n=1}^{\infty} D_n^{\mathrm{II}'} n\pi(-1)^{m+n+1} M_{mn} \\ &= (-1)^{m+1}(I_{m0}^{\mathrm{II}} - \alpha M_{m0}) \end{aligned} \tag{2.45}$$

$$\begin{aligned}\sum_{n=1}^{\infty} C_n^{\mathrm{II}'} n\pi(-1)^{m+n+1} M_{mn} &+ \frac{\pi}{4}D_m^{\mathrm{II}'} + \sum_{n=1}^{\infty} D_n^{\mathrm{II}'} n\pi(-1)^{m+n} I_{mn}^{\mathrm{II}} \\ &= (-1)^m(M_{m0} - \alpha I_{m0}^{\mathrm{II}}) \end{aligned} \tag{2.46}$$

both for $m = 1, 2, 3, \cdots$, where

$$I_{mn}^{\mathrm{II}} = \int_0^\infty \frac{k\sin^2(k)}{[k^2-(m\pi)^2][k^2-(n\pi)^2]}\coth\left(\frac{kG}{t}\right)\,dk \tag{2.47}$$

$$M_{mn} = \int_0^\infty \frac{k\sin^2(k)}{[k^2-(m\pi)^2][k^2-(n\pi)^2]} \operatorname{cosech}\left(\frac{kG}{t}\right) dk\,. \tag{2.48}$$

The normalised vertical field component, obtained by partial differentiation of (2.42), for Solution II is:

$$\frac{H_y^{\,\mathrm{II}}(x,y)}{V} = \begin{cases} \frac{1}{t} + \sum_{n=1}^{\infty} C_n^{\,\mathrm{II}'} \frac{n\pi}{t} \cos\left(\frac{n\pi(t-y)}{t}\right) \cosh\left(\frac{n\pi x}{t}\right) \Big/ \cosh\left(\frac{n\pi L}{t}\right) & 0 \le x \le L, \\ & 0 \le y \le t \\ \frac{2}{\pi t}(K_0^{\,\mathrm{II}} + \alpha R_0^{\,\mathrm{II}}) + \sum_1^\infty C_n^{\,\mathrm{II}'} \frac{2n}{t}(-1)^n K_n^{\,\mathrm{II}} & \\ \qquad + \sum_1^\infty D_n^{\,\mathrm{II}'} \frac{2n}{t}(-1)^n R_n^{\,\mathrm{II}} & L \le x \le L+G, \\ & y \le t \\ \frac{\alpha}{t} + \sum_{n=1}^{\infty} D_n^{\,\mathrm{II}'} \frac{n\pi}{t} \cos\left(\frac{n\pi(t-y)}{t}\right) e^{-n\pi(x-L-G)/t} & x \ge L+G, \\ & 0 \le y \le t \end{cases} \tag{2.49}$$

where

$$K_n^{\,\mathrm{II}} = \int_0^\infty \frac{k\sin(k)\cos(k(t-y)/t)}{k^2-(n\pi)^2} \frac{\sinh(k(L+G-x)/t)}{\sinh(kG/t)}\, dk \tag{2.50}$$

and

$$R_n^{\,\mathrm{II}} = \int_0^\infty \frac{k\sin(k)\cos(k(t-y)/t)}{k^2-(n\pi)^2} \frac{\sinh(k(x-L)/t)}{\sinh(kG/t)}\, dk\,. \tag{2.51}$$

Closed form expressions for the integrals which occur in both of the solutions for the symmetrically shielded pole head have not yet been derived. When the area exterior to the pole, shields and the underlayer is divided as shown in Fig. 2.5 (Solution II), as the gap length increases the geometry approaches that of a single pole head. Hence, $\lim_{g\to\infty} I_{mn}^{\,\mathrm{II}} = I_{mn}$ where I_{mn} is given for a single pole head by (2.11) and $\lim_{g\to\infty} M_{mn} = 0$. Similarly for the potential and the vertical field component, $\lim_{g\to\infty} I_n^{\mathrm{II}} = I_n^P$ (2.9) and $\lim_{g\to\infty} Q_n = 0$, $\lim_{g\to\infty} K_n^{\mathrm{II}} = K_n^P$ (2.15) and $\lim_{g\to\infty} R_n = 0$. Numerical integration [33] of J_{mn}, K_{mn}, and L_{mn} (equns. (2.36) – (2.38)) for Solution I, and of I_{mn}^{II} and M_{mn} (equns. (2.47) and (2.48)) for Solution II, limit the size of the systems of equations it is possible to solve for the coefficients. In [29] a system of total size 40 × 40 for Solution I and of size 80 × 80 for Solution II was used. For Solution II, the recording medium passes through all three regions but for Solution I it lies in region C only. Close to the boundaries between the regions, relatively large numbers of terms in the series are necessary for convergence. Therefore, computationally, Solution I is preferable to Solution II. Solution II is useful for comparison with other models which are divided in the same way, and for deriving approximations, as will be discussed in Chapter 3.

2.1.4 The Conformal Mapping Method

Conformal mapping methods have been used to obtain the exact head fields of idealised two-dimensional models of magnetic recording heads including:

- Gapped planes [34, 35, 36].
- Symmetric ring heads without underlayers [34, 35, 37, 38, 36].
- Symmetric ring heads with underlayers [37, 39].
- Symmetric thin film heads without underlayers [40, 41, 36].
- Single pole heads with underlayers [42, 43]
- Symmetrically shielded, infinitely thin magnetoresistive sensors [44].
- Infinitely thin single pole heads with underlayers [45].

- Asymmetric thin film heads without underlayers [41].

- Finite height, symmetric thin film heads without underlayers [46].

- Asymmetric ring heads without underlayers [47, 48].

- Asymmetric ring heads with underlayers [49].

- Symmetric and asymmetric polygonal thin film heads [50].

The modelling assumptions made in most cases are the same as those given in Section 2.1.3.1 except for assumption 2 which is not applicable to the analyses of the asymmetric ring and thin film heads. Assumption 3 does not apply to [46] or [50].

This method of analysis makes use of the fact that the real and imaginary parts of a complex analytic function satisfy Laplace's equation [32]. Under a conformal mapping, harmonic functions remain harmonic and constant potential boundary conditions transform 'directly'. Therefore, by conformally transforming the problem onto a simple region of the complex plane where all the boundary conditions are defined, the solution in the complex w-plane is readily deduced. For all the examples quoted above, the area exterior to either the full or the semi-head and the underlayer, if one is present, is mapped to the entire upper half of the complex plane, by means of the Schwarz-Christoffel transformation [51, 32]. This maps any polygon in the complex z-plane onto the complex w-plane, so that the boundary of the polygon lies along the real axis of w-plane. For a polygon with internal angles α, β, γ, $\cdots$ at vertices A, B, C, $\cdots$ respectively, mapping to the points a, b, c, $\cdots$ on the real axis in the w-plane, the transformation is given by

$$\frac{dz}{dw} = S(w-a)^{\alpha/\pi-1}(w-b)^{\beta/\pi-1}(w-c)^{\gamma/\pi-1}\cdots \tag{2.52}$$

where S is a scaling and rotating constant. On integration, a further constant of translation z_0 is obtained. Any convenient vertex may be mapped to $\pm\infty$, and does not appear in the transformation. A further two points on the w-plane may be fixed at convenient values according to the problem. The coordinates of the other points on the w-plane real axis corresponding to the remaining vertices of the polygon in the z-plane are found by either comparing the solutions in the two planes or by residue methods [32]. This may result in a system of non-linear equations which must be solved numerically [33].

When the area in the z-plane exterior to the head and underlayer, if one is present, maps to the entire upper half of the complex w-plane so that the potential along $v = 0$ is completely defined, the solution to Laplace's equation may either be deduced by observation or it can be derived using the complex Poisson integral [32],

$$F(w) = \frac{i}{\pi}\int_{-\infty}^{\infty} \frac{1 + pw}{(1 + p^2)(w - p)}\bar{\varphi}(p)\, dp \tag{2.53}$$

where $F(w)$ is the complex potential function, whose real and imaginary parts define the potential and the flux respectively, and $\bar{\varphi}(p)$ is the known potential along the real axis, in the w-plane. From the Cauchy-Riemann equations, it can be shown that [32]

$$H_x - iH_y = -\frac{dF(w)}{dw} \bigg/ \frac{dz}{dw} \tag{2.54}$$

Therefore the transformation must be inverted in order to evaluate the field components. Except in very simple cases, the inversion requires numerical treatment.

The study by Westmijze [35] includes a solution for the ring head without an underlayer which is used here to demonstrate the method. The dimensions are scaled and the order of the poles is reversed from that used by Westmijze to be consistent with the Fourier solution of Section 2.1.3.3.

2.1.4.1 The ring head without an underlayer

Fig. 2.6 shows the idealised model, as described in Section 2.1.2.3, in the z-plane. Using the Schwarz-Christoffel transformation, the points A, B, C, D and E in the z-plane are mapped to A', B', C', D' and E', respectively, in the complex w-plane, as shown in Fig. 2.7. C and D are treated as a single vertex with interior angle of 0°, occuring at $z = (-g/2, -\infty)$.

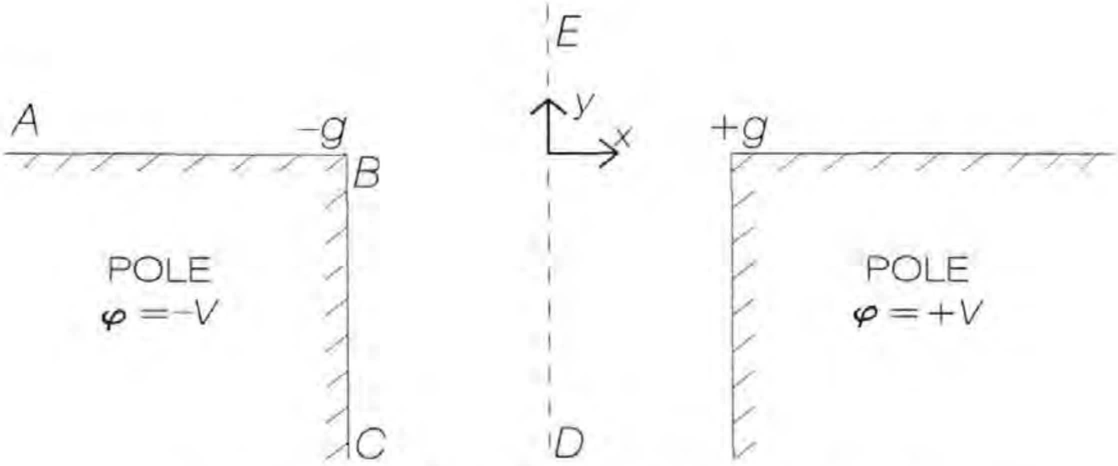

Figure 2.6: Ring head without an underlayer in the z-plane.

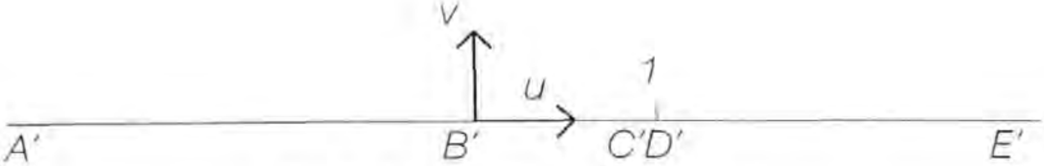

Figure 2.7: The complex w-plane.

Under the conditions for a Schwarz-Christoffel transformation, A and E are mapped to $w = -\infty$ and $w = +\infty$ respectively and the positions of B' and $C'D'$ are chosen as the convenient points $w = 0$ and $w = 1$, respectively. Therefore the mapping function is

$$\frac{dz}{dw} = S\frac{\sqrt{w}}{w-1}. \tag{2.55}$$

Integrating gives

$$z = S\left[2\sqrt{w} + \ln\left(\frac{\sqrt{w}-1}{\sqrt{w}+1}\right)\right] + z_0 . \tag{2.56}$$

Applying the method of residues at the open vertex CD, where there is a jump in the z-plane, gives $S = ig/\pi$, and equating the solutions at B and B' where $z = -g$ and $w = 0$, gives $z_0 = 0$.

The complex potential function, as defined above, which satisfies Laplace's equation with the boundary condition $\bar{\varphi}(u,0) = -V$ for $u \leq 1$ and $\bar{\varphi}(u,0) = 0$ for $u > 1$ is

$$F(w) = i\frac{V}{\pi}\ln(w-1) . \tag{2.57}$$

Hence,

$$\frac{dF(w)}{dw} = i\frac{V}{\pi(w-1)} , \tag{2.58}$$

so that the field components are given by

$$H_x - iH_y = -\frac{V}{g\sqrt{w}} . \tag{2.59}$$

Therefore it is necessary to solve equn. (2.56) explicitly for specific values of z. Clearly, this requires numerical treatment. Due to the limited computing facilities of the time, Westmijze investigated the solution along the boundary A–E only, where $\sqrt{w}$ is easily evaluated. More recent solutions [38] and [36] have used the Newton-Raphson method [51],

$$w_{n+1} = w_n - \frac{f(w_n)}{f'(w_n)} \tag{2.60}$$

to obtain the field components in the region of interest. For Westmijze's solution, $f(w)$ is given by rearranging equn. (2.56) so that the full expression equals zero and $f'(w) = dz/dw$ as given by equn. (2.55). Accurate initial values w_0 must be chosen in order that the Newton-Raphson method will converge. Curland and Judy [38] substituted for w in terms of $F(w)$ into both $f(w)$ and $f'(w)$ of their solution to obtain a single expression for the quotient in equn. (2.60); the Karlqvist approximations (see Section 2.1.4.2) provided suitable starting values for the inversion process. A later solution by Yang and Huang [36] mapped the entire head to the complex plane and employed a slotted plane solution, which, due to its simplicity, could be inverted analytically, to provide the initial values for the Newton-Raphson iterations.

Details of other solutions by this method are omitted here as they give no further insight into the method or into the fields of the individual heads without numerical evaluation.

2.1.4.2 The Karlqvist approximations

Exact conformal mapping solutions were used by Karlqvist [37] to assess the accuracy of his approximations. He compared the exact potential across the straight line joining the gap edge corners of symmetric ring heads of several types with a linear approximation to the potential. The configurations which he considered included:

1. Assuming the pole pieces were infinitely high with internal angles of 90° when the medium had infinite permeability. This is equivalent to later analyses for symmetric ring heads in the presence of an underlayer, as shown in Fig. 2.3;
2. As in case 1 but with internal angles of 0°, making the head infinitely thin;
3. As in case 1 but with the relative permeability of the medium assumed to be unity, as has been assumed for later analyses of ring heads without underlayers, as shown in Fig. 2.2,

and other more general specifications for the medium. His results showed that a linear approximation to the true potential across the gap was most accurate for case 3 and least appropriate for case 1. Applying the linear approximation in case 3, the potential at any point outside the head was computed using the well-known solution for the half plane [52]:

$$\varphi(x,y) = \frac{y}{\pi}\int_{-\infty}^{\infty} \frac{\varphi(u,0)}{y^2+(u-x)^2}\,du\,. \tag{2.61}$$

Hence, the following approximate horizontal and vertical field components were obtained, for the present coordinate system:

$$H_x(x,y) \approx -\frac{V}{\pi g}\left(\arctan\left(\frac{g+x}{y}\right) + \arctan\left(\frac{g-x}{y}\right)\right) \tag{2.62}$$

and

$$H_y(x,y) \approx \frac{V}{2\pi g}\ln\left(\frac{y^2+(g+x)^2}{y^2+(g-x)^2}\right). \tag{2.63}$$

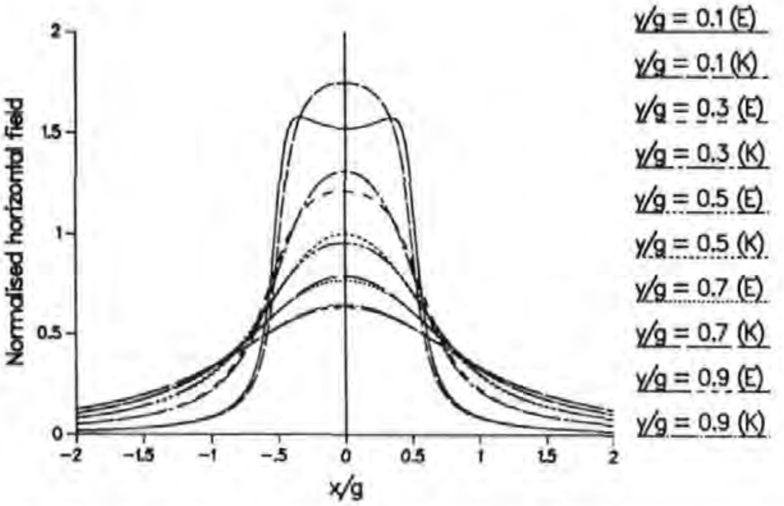

Figure 2.8: The Karlqvist approximation (K-curves) and the exact (E-curves) horizontal field component for a ring head without an underlayer, $g = 0.5$.

Karlqvist demonstrated that these approximations provided acceptable results at distances from the head of $y > 0.5g$ as shown in Figs. 2.8 and 2.9. Here the negative of the horizontal field is plotted which corresponds to a reversed polarity of the poles and follows the convention for this head. So because of their comparative simplicity, they

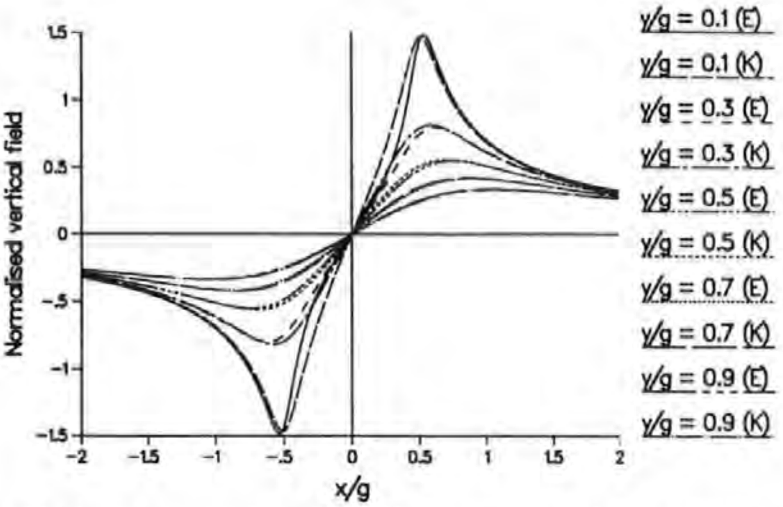

Figure 2.9: The Karlqvist approximation (K-curves) and the exact (E-curves) vertical field component for a ring head without an underlayer, $g = 0.5$.

have formed the basis of much of the later analytic work. But for present day systems, where the head – medium separation is very small, they are not sufficiently accurate.

The Karlqvist approximations are the leading terms of the exact field components equns. (2.19) and (2.20) derived by Baird [25] from Fan's Fourier solution [23].

2.1.5 The Reciprocity Theorem

The reciprocity theorem provides a method of calculating the output from a particular head, reading a known magnetisation pattern on the recording medium, if the field of the read head is also known. This is easier than directly calculating the flux due to the medium which threads the head coils and is the standard method of evaluating output. The theorem is derived from the properties of electricity and magnetism. Here the derivation is specifically tailored to perpendicular replay where the magnetisation on the medium is assumed to have a vertical component only although the theorem can be extended to apply to the general case.

If two coils, C_1 and C_2, in separate electric circuits, are placed close to each other but do not actually connect, passing a current through one coil will induce a current in the other. This is because the energised coil exhibits a magnetic field, whose flux threads through the other coil. The rôles of the two coils are interchangeable. The flux, ϕ, threading through one coil depends on the current, i, passing through the other coil so that [53]

$$\phi_1 = L_m i_2 \qquad \text{and} \qquad \phi_2 = L_m i_1 \tag{2.64}$$

where L_m is the mutual inductance, a constant for a particular pair of coils.

A recording head is wound with a coil C_1, and the magnetisation on the recording medium can be considered to be a varying solenoidal electric current i_2 in a coil C_2. For perpendicular recording, the medium has a vertical anisotropy and so is assumed to be affected by, and to affect, the vertical component of the head field only.

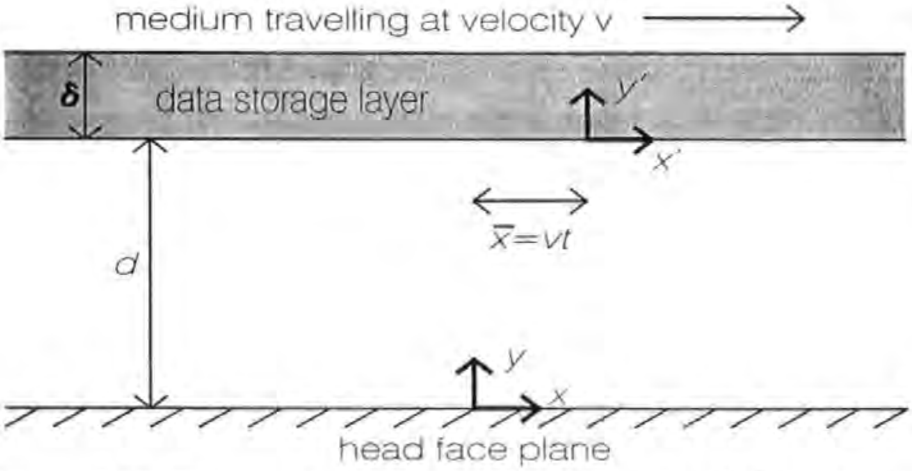

Figure 2.10: The coordinate systems for the head and the medium.

Fig. 2.10 shows the coordinate systems for the head and for the magnetic medium of thickness δ and track width w (into the page), at a distance d from the head face plane, which moves across the head at velocity v. The flux though a small cross section of the medium, $\delta y\,\delta z$, caused by the current i_1 is

$$\delta\phi_2 = \mu_0 H_y(x, y)\,\delta y\,\delta z \tag{2.65}$$

where μ_0 is the permeability of a vacuum as assumed for the medium (Section 2.1.3).

At x' on the medium, the small component of equivalent current δi_2 due to a small length of the medium $\delta x'$ associated with the y component of the magnetisation $M_y(x')$ is

$$\delta i_2 = M_y(x')\,\delta x' = M_y(x-\bar{x})\,\delta x\,. \tag{2.66}$$

But from (2.64) $\delta\phi_1 = \delta\phi_2 \delta i_2 / i_1$ giving

$$\delta\phi_1 = \mu_0 M_y(x-\bar{x}) \frac{H_y(x,y)}{i_1}\,\delta x\,\delta y\,\delta z\,. \tag{2.67}$$

The total flux threading the head coil is given by integrating over the entire volume of the medium:

$$\phi_1 = \frac{\mu_0}{i_1} \int_{z=-w/2}^{w/2} \int_{y=d}^{d+\delta} \int_{x=-\infty}^{\infty} M_y(x-\bar{x}) H_y(x,y)\,dx\,dy\,dz\,. \tag{2.68}$$

If the track width w of the medium is assumed to be large compared with its other dimensions, as in the case of two-dimensional models then, dropping the subscripts,

$$\phi = \frac{\mu_0 w}{i} \int_{y=d}^{d+\delta} \int_{x=-\infty}^{\infty} M_y(x-\bar{x}) H_y(x,y)\,dx\,dy\,. \tag{2.69}$$

The output voltage for an inductive head depends on the rate of change of flux threading through it so that

$$e^{In}(\bar{x}) = -\frac{\mu_0 v w}{i} \int_{y=d}^{d+\delta} \int_{x=-\infty}^{\infty} \frac{d}{d\bar{x}}\Big(M_y(x-\bar{x}) \Big) H_y(x,y)\,dx\,dy\,. \tag{2.70}$$

In a magnetoresistive head, the resistance of the sensor depends on the magnitude of the flux from the medium, which can be measured by passing a current across the sensor. Therefore, for a deep head, reading from a perpendicular medium, the output voltage is

$$e^{MR}(\bar{x}) \propto \frac{\mu_0 w}{i} \int_{y=d}^{d+\delta} \int_{x=-\infty}^{\infty} M_y(x-\bar{x}) H_y(x,y)\, dx\, dy\,. \tag{2.71}$$

2.2 Introduction to the New Applications

Perpendicular recording has been shown to be capable of achieving optimum bit density magnetic recording both theoretically [54] and experimentally [6]. The aim of the work presented here is to extend the knowledge of perpendicular recording systems in particular, and therefore all of the new analyses are for heads in the presence of a highly permeable underlayer.

In Chapter 3, the Fourier method is first applied to the conventional thin film head, with pole pieces at constant potentials. Previous solutions for thin film heads without underlayers have been obtained by a boundary element method [55], the finite difference method [56] and conformal mapping [41, 36]. When an underlayer is present, a finite difference solution has been given in [56] and the Fourier solution has been derived independently and published almost simultaneously in [57]. Approximations to either the magnetic potential or the field components in the head face plane at $y = 0$, from which approximate integral solutions can be obtained, have been suggested by several authors. For the case of no underlayer, approximations to the potential are given in [58] and [59], and approximations to the horizontal field component at $y = 0$ are given in [60, 61, 62]. In [60] and [61] a finite difference method has been used to obtain the horizontal field component at $y = 0$ and then a simple model has been fitted to the numerical results. The same method can be applied when an underlayer is present, but the approximation has not been published. Yeh [63] gives an explicit approximation to the potential at $y = 0$, derived from the Karlqvist approximation to the horizontal field component for a ring head which will be discussed further in Section 3.1.4.

The field components for the thin film head have peaks due to the outer edges of the pole pieces which, although they are of lesser magnitude than the peaks due to the gap edges of the pole pieces, could influence the medium during the writing process. As the whole of the vertical field component is convolved with the magnetisation on the medium when evaluating perpendicular output *via* the reciprocity theorem, the outer peaks always influence the replay characteristics, and in Chapter 4 this effect is shown to limit the upper usable frequency of the head. In order to reduce the effect of the pole edges, a linear potential distribution, rising from zero at the outer edges to maximum magnitudes at the gap edges is applied and shown to give better results. Mallinson [64] states that the true potential distribution across the poles of a thin film head is not constant and that a linear distribution is probably a better approximation.

Due to the beneficial effect of the linear potential poles on the field components of a thin film head, the Fourier method is used to analyse a single pole head with a linear potential rising from zero at one edge to a maximum at the other edge. The method is also generalised to apply to single pole heads of arbitrary pole potential and several potential distributions are investigated.

Each of the exact solutions is in the form of an infinite series dependent on at least one set of coefficients which must be computed by the solution of a truncated, infinite system of linear algebraic equations. Single term approximations to the potential in the head face plane, independent of the coefficients, are derived from the exact solutions to evaluate approximations to the head field components, for each head configuration. These approximations are shown to give good results, especially close to the head face plane, where Karlqvist-type approximations, obtained by taking the leading term only of each of the field components, are least accurate.

New conformal mapping solutions are derived for idealised 2-dimensional models of infinitely thin magnetoresistive (MR) elements both symmetrically and asymmetrically placed between shields of semi-infinite width. The pole is permitted to be recessed and an underlayer is assumed present. By allowing the shield - underlayer distance to increase, the case of no underlayer may also be modelled. Previous analyses of non-recessed shielded heads for longitudinal recording, include an approximation for the horizontal field component based on the superposition of two simple Karlqvist ring head approximations [65], generalised in [66] to the asymmetric case. Transmission line models have been considered in [67] and [68]. In [44] a conformal mapping solution was developed for an infinitely thin, non-recessed head symmetrically placed between shields of finite width with no underlayer present. Recent purely numerical finite element and boundary element analyses include [69, 70, 71, 72]. The effect of pole recession was briefly considered in [73] using an approximate Fourier/Karlqvist solution and in [74] using a large scale resistive paper model. An exact solution for the symmetric case in the presence of an underlayer, using Fourier analysis was given in [29], and whilst in principle this approach would extend to the asymmetric problem, the calulations would seem to become rather complicated.

The effects of varying the individual head parameters are investigated. Heads with graded pole potentials are shown to have locally stronger vertical field components, close to the head face.

In Chapter 4, the reciprocity theorem is invoked to provide the output characteristics for each of the heads considered in Chapter 3 and also for the ring head and the symmetrically shielded pole head both in the presence of an underlayer, for which the head fields are given in [28] and [29] respectively and have been summarised in Sections 2.1.3.4 and 2.1.3.5 respectively. The output characteristics computed are: the spectral response function and the phase thereof, linear dibit shift and roll-off. Each measure is defined and its method of evaluation is explained within the appropriate section of the chapter. Since the analysis of ring heads for longitudinal recording [24] until this work, the only exact analytic spectral response function published has been for a parallel plate head without an underlayer [75]. Other theoretical studies of the replay process have provided either purely numerical results, which give no causal insight, or approximations to the response functions which often fail to predict certain phenomena observed in practice. These approximations include:

1. The assumption of a simple form for the potential in the pole face plane [65, 76, 77, 63, 78, 62]
2. Superposition or extension of known exact or approximate results [75, 79, 66, 64].
3. The assumption of duality between a ring head for longitudinal recording and a single pole with an underlayer [8].

Here, the effects of varying the individual head parameters are investigated. Comparisons are made between the results for each of the different head configurations, and also with other published theoretical results. Where possible, the underlying modelling assumptions are justified by reference to published experimental data.

Finally, in Chapter 5, recommendations for optimising the achievable bit density, given the present state of knowledge, and for further investigation are made.

2.3 Summary

This chapter has covered:

- The derivation of Laplace's equation for the magnetic potential.
- The modelling assumptions.

- An outline of the Fourier method, applied to a single pole head with an underlayer.
- A brief list of the other previously published Fourier results.
- An outline of the conformal mapping method, applied to a ring head without an underlayer.
- A review of the previously published analyses by conformal mapping.
- The derivation of the reciprocity theorem.
- Details of the new work and its relation to previously published analyses.

Chapter 3

Head Fields

3.1 Fourier Analysis

3.1.1 The Thin Film Head

3.1.1.1 The general model

Fig. 3.1 shows the idealised model of a symmetric thin film head. Semi-infinitely high poles each of width, $2L$, at potentials $+f(x)$ and $-f(|x|)$, are separated by a gap of width, $G = 2g$, and are perpendicular to and at a distance, t, from the infinitely long underlayer, at zero potential. Laplace's equation need only be solved for $x \geq 0$ where

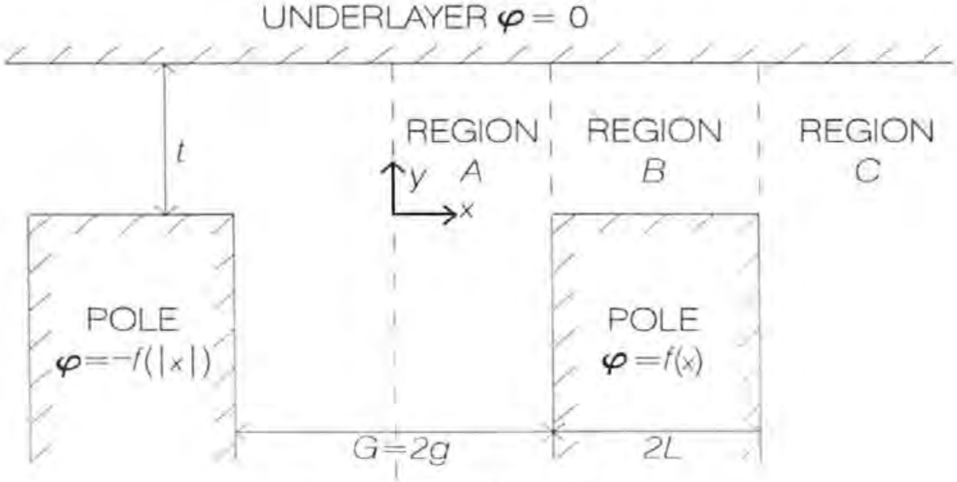

Figure 3.1: The thin film head.

the area exterior to the pole and the underlayer is divided into three regions A, B and C as shown. All of the assumptions listed in Section 2.1.3.1. apply to the constant pole potential case, but for the thin film head with linearly varying pole potentials, assumption 4 is modified to: the pole potential is known and is invariant in the vertical direction. Here results applicable to thin film heads with either constant or linearly varying pole potentials are denoted by the superscript TF while those specific to a particular case are indicated by the use of C or L, corresponding to the constant or linear cases respectively.

3.1.1.2 Constant potential poles

For the thin film head with constant potential poles, $f(x) = V$ in the general model. In region A, the general solution of Laplace's equation which satisfies the conditions:

$$\varphi_A^{TF}(x,t) = 0, \qquad \varphi_A^{TF}(x,y) = -\varphi_A^{TF}(-x,y), \quad \text{and} \quad \varphi_A^{TF} \text{ is bounded as } y \longrightarrow -\infty\,, \tag{3.1}$$

is

$$\varphi_A^{TF}(x,y) = \int_0^\infty A(k) \sinh\left(\frac{kx}{t}\right) \sin\left(\frac{k(t-y)}{t}\right) dk\,. \tag{3.2}$$

In region B the harmonic series $\sum_{n=1}^{\infty} \sin\left(n\pi(t-y)/t\right)\left[B_n^C e^{n\pi x/t} + D_n^C e^{-n\pi x/t}\right]$ satisfies $\varphi^C(x,0) = \varphi^C(x,t) = 0$ so that by adding the particular solution which takes the correct values at $y = 0$ and at $y = t$, the full solution

$$\varphi_B^C(x,y) = V\frac{(t-y)}{t} + \sum_{n=1}^{\infty} \sin\left(\frac{n\pi(t-y)}{t}\right)\left[B_n^C e^{n\pi x/t} + D_n^C e^{-n\pi x/t}\right] \tag{3.3}$$

is obtained. In region C the integral

$$\varphi_C^{TF}(x,y) = \int_0^\infty C(k) \sin\left(\frac{k(t-y)}{t}\right) e^{-kx/t}\, dk \tag{3.4}$$

satisfies the conditions:

$$\varphi_C^{TF}(x,t) = 0, \qquad \lim_{x\to\infty} \varphi_C^{TF}(x,y) = 0 \quad \text{and} \quad \varphi_C^{TF} \text{ is bounded as } y \longrightarrow -\infty\,. \tag{3.5}$$

The coefficients B_n^C and D_n^C and the functions $A(k)$ and $C(k)$ are to be determined.

Matching the potential functions at $x = g$ where

$$\varphi_A^C(g,y) = \begin{cases} V & -\infty < y \leq 0 \\ \varphi_B^C(g,y) & 0 \leq y \leq t \end{cases} \tag{3.6}$$

and taking a sine transform

$$\mathcal{F}_s[f(y)] = \int_{-\infty}^{t} \sin(k(t-y)/t) f(y)\, dy \tag{3.7}$$

enables $A(k)$ to be expressed in terms of the coefficients B_n^C and D_n^C so that (3.2) becomes

$$\varphi_A^C(x,y) = \frac{2V}{\pi} Q_0^{TF} + \sum_{n=1}^{\infty} 2n(-1)^n \left[B_n^C e^{n\pi g/t} + D_n^C e^{-n\pi g/t}\right] Q_n^{TF} \tag{3.8}$$

where

$$Q_n^{TF} = \int_0^\infty \frac{\sin(k)\sin(k(t-y)/t)}{k^2 - (n\pi)^2} \frac{\sinh(kx/t)}{\sinh(kg/t)}\, dk\,. \tag{3.9}$$

Similarly matching the potentials at $x = g + 2L$,

$$\varphi_C^C(g+2L, y) = \begin{cases} V & -\infty < y \le 0 \\ \varphi_B^C(g+2L, y) & 0 \le y \le t \end{cases} \tag{3.10}$$

and taking a sine transform (3.7) leads to

$$\varphi_C^C(x, y) = \frac{2V}{\pi} I_0^{TF} + \sum_{n=1}^{\infty} 2n(-1)^n \left[B_n^C e^{n\pi(g+2L)/t} + D_n^C e^{-n\pi(g+2L)/t} \right] I_n^{TF} \tag{3.11}$$

where

$$I_n^{TF} = \int_0^{\infty} \frac{\sin(k)\sin(k(t-y)/t)}{k^2 - (n\pi)^2} e^{-k(x-g-2L)/t}\, dk \tag{3.12}$$

and is given in closed form in Section A.3.1.

The coefficients are determined by matching the x-derivatives of the appropriate potentials over the common boundaries at $x = g$ and at $x = g + 2L$, and employing the orthogonality properties of the functions $\sin(m\pi(t-y)/t)$, where m is an integer, over the range $0 \le y \le t$. At $x = g$ this gives

$$\begin{aligned} &\int_{y=0}^{t} \int_{k=0}^{\infty} A(k) k \sin\left(k \frac{(t-y)}{t}\right) \cosh\left(\frac{kg}{t}\right) \sin\left(m\pi \frac{(t-y)}{t}\right) dk\, dy \\ &\qquad = \int_0^t \sum_{n=1}^{\infty} n\pi \sin\left(n\pi \frac{(t-y)}{t}\right) \left[B_n^C e^{n\pi g/t} - D_n^C e^{-n\pi g/t} \right] dy\,. \end{aligned} \tag{3.13}$$

Similarly at $x = g + 2L$,

$$\begin{aligned} &\int_{y=0}^{t} \int_{k=0}^{\infty} -C(k) k \sin\left(k \frac{(t-y)}{t}\right) e^{-k(g+2L)/t} \sin\left(m\pi \frac{(t-y)}{t}\right) dk\, dy \\ &= \int_0^t \sum_{n=1}^{\infty} n\pi \sin\left(n\pi \frac{(t-y)}{t}\right) \left[B_n^C e^{n\pi(g+2L)/t} - D_n^C e^{-n\pi(g+2L)/t} \right] dy\,. \end{aligned} \tag{3.14}$$

This leads to the two coupled infinite systems of linear simultaneous equations

$$\frac{\pi}{4}[B_m^C e^{m\pi g/t} - D_m^C e^{-m\pi g/t}]$$
$$+\sum_{n=1}^{\infty}(-1)^{m+n+1} n\pi [B_n^C e^{n\pi g/t} + D_n^C e^{-n\pi g/t}] I_{mn}^{TF}$$
$$= V(-1)^m I_{m0}^{TF} \tag{3.15}$$

$$\frac{\pi}{4}[B_m^C e^{m\pi(g+2L)/t} - D_m^C e^{-m\pi(g+2L)/t}]$$
$$+\sum_{n=1}^{\infty}(-1)^{m+n} n\pi [B_n^C e^{n\pi(g+2L)/t} + D_n^C e^{-n\pi(g+2L)/t}] I_{mn}$$
$$= V(-1)^{m+1} I_{m0} \tag{3.16}$$

for $m = 1, 2, 3, \cdots$ in each case, where

$$I_{mn}^{TF} = \int_0^{\infty} \frac{k \sin^2(k)}{[k^2 - (m\pi)^2][k^2 - (n\pi)^2]} \coth(kg/t)\, dk \tag{3.17}$$

and I_{mn} is given in Section A.2.1. The normalised coefficients B_n^C/V and D_n^C/V depend on the ratios g/t and L/t only. It is neccessary to restrict each system of equations (3.15) and (3.16) to some finite size N to obtain a solution and it is computationally convenient to define scaled normalised coefficients $B_n^{C'} = B_n^C e^{n\pi(g+2L)/t}/V$ and $D_n^{C'} = D_n^C e^{-n\pi g/t}/V$ which satisfy the $2N \times 2N$ system of the general form:

$$[A^{TF}]\underline{x}^C = \underline{b}^C\,. \tag{3.18}$$

Here

$$\begin{aligned}
A^{TF}_{m,n} &= (-1)^{m+n+1} n\pi I^{TF}_{mn} - \begin{cases} \pi/4 & m=n \\ 0 & m \neq n \end{cases} \\
A^{TF}_{m,n+N} &= (-1)^{m+n+1} n\pi e^{-2n\pi L/t} I^{TF}_{mn} + \begin{cases} \pi e^{-2m\pi L/t}/4 & m=n \\ 0 & m \neq n \end{cases} \\
A^{TF}_{m+N,n} &= (-1)^{m+n} n\pi e^{-2n\pi L/t} I_{mn} - \begin{cases} \pi e^{-2m\pi L/t}/4 & m=n \\ 0 & m \neq n \end{cases} \\
A^{TF}_{m+N,n+N} &= (-1)^{m+n} n\pi I_{mn} + \begin{cases} \pi/4 & m=n \\ 0 & m \neq n \end{cases}
\end{aligned} \tag{3.19}$$

for $m, n = 1, 2, \cdots, N$

$$x^C_m = D^{C'}_m, \qquad x^C_{m+N} = B^{C'}_m, \tag{3.20}$$

$$b^C_m = (-1)^m I^{TF}_{m0} \qquad \text{and} \qquad b^C_{m+N} = (-1)^{m+1} I_{m0} \tag{3.21}$$

for $m = 1, 2, \cdots, N$ and I^{TF}_{mn} and I_{mn} are given by (3.17) and (A.6) respectively. No analytic expression for I^{TF}_{mn} has yet been derived, therefore numerical integration [33] is necessary.

Various known solutions are special limiting cases of the solution derived here and may be used to verify the correctness of this solution. These limiting cases are consistent with the observation that the integral I_{mn} which occurs in the equations (3.16) for the coefficients here, also occurs in the equations for the coefficients for the single pole head (2.10) and for the ring head without an underlayer (2.18). Q^{TF}_n (3.9) is of the same form as Q^{II}_n (2.44) which occurs in the equations defining the coefficients for Solution II of a shielded pole head, with $(x - L)$ replace by x and G replaced by

g. If the width $2L$ of the pole pieces increases, the geometry approaches that of the idealised model of a ring head with a highly permeable underlayer [28] given in Section 2.1.3.4. The integral I^{TF}_{mn} (3.17) is the same as the integral I^{RU}_{mn} (2.26) which occurs in the equations defining the coefficients for a ring head with an underlayer except that the rôles of g and t are reversed. If the coordinate origin is moved to $(g + L, 0)$, at the centre of the pole at potential $+V$, as the gap length g increases, the geometry becomes that of the single pole [23] as given in Section 2.1.3.2. The integral I^{TF}_n (3.12) is the same as I^P_n (2.9) except that here $x - L$ is replaced by $x - 2L - g$ which is consistent with the change in origin described. Also $\lim_{g\to\infty} I^{TF}_{mn} = I_{mn}$ so that equns. (3.15) and (3.16) yield the same single set of coefficients as (2.10) does for the conventional single pole head. Finally, if the origin is moved to $(g + 2L, t)$, above the outer edge

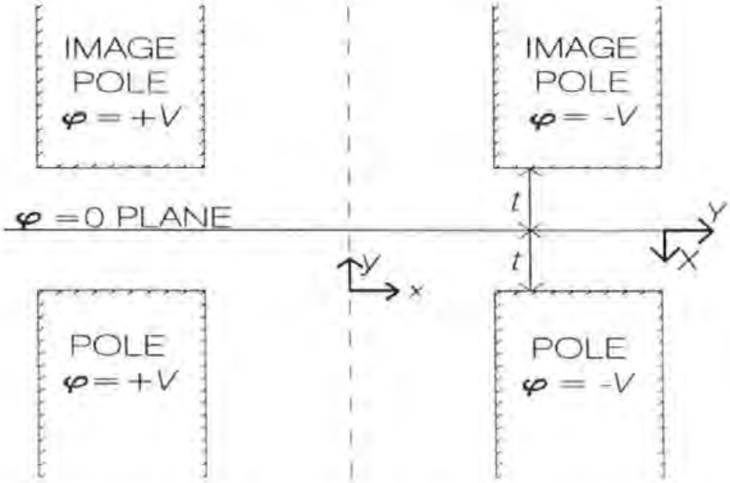

Figure 3.2: Equivalence of a thin film head having constant potential poles with a ring head without an underlayer.

of the pole at potential $+V$, and the axes are rotated through 90° clockwise the new coordinate system (X, Y) where $X = t - y$ and $Y = x - 2L - g$ shown in Fig. 3.2 is obtained. Image poles are shown reflected in the $y = t$ ($\varphi = 0$) plane. As the width $2L$ of the pole pieces increases, the geometry in regions B and C becomes that of a ring head without an underlayer [24] for which the solution is given in Section 2.1.3.3, but here the gap width is $2t$. For each of these three cases, the present solution and the equations satisfied by the Fourier coefficients do reduce to the established solutions quoted.

The first six coefficients for the solutions for thin film heads of various dimensions are tabulated in Appendix B. Table B.1 shows the first six coefficients, $B_n^{C'}$ and $D_n^{C'}$ computed for $N = 40$ with a fixed ratio $L/t = 0.5$ for a range of g/t values. As g/t increases the correspondence with a single pole head requires that both $B_n^{C'}$ and $D_n^{C'}$, scaled by the factor $(1 + e^{-2n\pi L/t})$ should approach the equivalent coefficients $B_n^{P'}$ for a single pole head. For comparison, the scaled coefficients for $g/t = 16$ and the pole head coefficients for $L/t = 0.5$ computed from an $N = 40$ system *via* equn. (2.10) are also shown in Table B.1, verifying the expected correspondence. This equivalence may also be used to assess the accuracy of the coefficients computed for the thin film head with constant potential poles. For a single pole head, the integrals appearing in the equations for the coefficients may be evaluated analytically (Section 2.3.1) which permits larger values of N to be considered. Computation with values of N up to 640 together with an extrapolation technique gives the pole head coefficients shown in the last column of Table B.1 which are believed to be correct to the accuracy shown. The $N = 40$ single pole head values are seen to be correct to within one figure in the fourth decimal place and hence this is the expected accuracy of all of the coefficients shown in Table B.1 and of the coefficients in the other tables in Section B.1.

Table B.2 gives the coefficients for a fixed gap, $g/t = 0.5$, and a range of pole widths. As the pole width increases the correspondence with a ring head without an underlayer discussed previously requires that the $B_n^{C'}$ coefficients approach those for a ring head, which are independent of the ring gap [27], and that the $D_n^{C'}$ coefficients remain finite. The ring head coefficients computed from an $N = 40$ system and extrapolated values which are claimed [27] to be correct to six decimal places are also shown in Table B.2.

This confirms both the stated correspondence and the estimated accuracy of the new coefficients computed with $N = 40$. The final correspondence is with a ring head with an underlayer as L/t increases. This requires that the $B_n^{C'}$ coefficients remain finite and that the $D_n^{C'}$ coefficients approach those given in [28] with the rôles of g and t reversed. The appropriate coefficients for a ring head with an underlayer for $g/t = 2.0$ are given in Table B.2, also computed from an $N = 40$ system, and are seen to be the same as those for $L/t = 2.0$, confirming the equivalence.

As the head - underlayer separation t increases the Fourier coefficients get larger and consequently the resulting series for the field components will converge more slowly. Typical coefficients for $g/L = 1.0$ as t increases are given in Table B.3.

The horizontal and vertical field components are given by $-\partial\varphi^C/\partial x(x, y)$ and $-\partial\varphi^C/\partial y(x, y)$ respectively, so that normalised by V/t and in terms of the scaled coefficients,

$$\frac{t}{V}H_x^C(x,y) = \begin{cases} -\frac{2}{\pi}R_0 \; - \; \sum_{n=1}^{\infty} 2n(-1)^n \left[B_n^{C'} e^{-2n\pi L/t} + D_n^{C'}\right] R_n & 0 \le x \le g \\ & y \le t \\ \sum_{n=1}^{\infty} n\pi \sin(n\pi(t-y)/t) & \\ \quad \cdot \left[D_n^{C'} e^{-n\pi(x-g)/t} - B_n^{C'} e^{n\pi(x-g-2L)/t}\right] & g \le x \le g+2L \\ & 0 \le y \le t \\ \frac{2}{\pi}J_0^{TF} \; + \; \sum_{n=1}^{\infty} 2n(-1)^n \left[B_n^{C'} + D_n^{C'} e^{-2n\pi L/t}\right] J_n^{TF} & g+2L \le x < \infty \\ & y \le t \end{cases} \tag{3.22}$$

and

$$\frac{t}{V}H_y^C(x,y) = \begin{cases} \frac{2}{\pi}S_0^{TF} + \sum_{n=1}^{\infty} 2n(-1)^n \left[B_n^{C'} e^{-2n\pi L/t} + D_n^{C'}\right] S_n^{TF} & 0 \leq x \leq g \\ & y \leq t \\ 1 + \sum_{n=1}^{\infty} n\pi \cos(n\pi(t-y)/t) & \\ \quad \cdot \left[B_n^{C'} e^{n\pi(x-g-2L)/t} + D_n^{C'} e^{-n\pi(x-g)/t}\right] & g \leq x \leq g+2L \\ & 0 \leq y \leq t \\ \frac{2}{\pi}K_0^{TF} + \sum_{n=1}^{\infty} 2n(-1)^n \left[B_n^{C'} + D_n^{C'} e^{-2n\pi L/t}\right] K_n^{TF} & g+2L \leq x < \infty \\ & y \leq t \end{cases} \tag{3.23}$$

where

$$R_n = \int_0^{\infty} \frac{k\sin(k)\sin(k(t-y)/t)}{k^2-(n\pi)^2} \frac{\cosh(kx/t)}{\sinh(kg/t)}\, dk \tag{3.24}$$

$$J_n^{TF} = \int_0^{\infty} \frac{k\sin(k)\sin(k(t-y)/t)}{k^2-(n\pi)^2} e^{-k(x-g-2L)/t}\, dk\,, \tag{3.25}$$

$$S_n^{TF} = \int_0^{\infty} \frac{k\sin(k)\cos(k(t-y)/t)}{k^2-(n\pi)^2} \frac{\sinh(kx/t)}{\sinh(kg/t)}\, dk \tag{3.26}$$

and

$$K_n^{TF} = \int_0^{\infty} \frac{k\sin(k)\cos(k(t-y)/t)}{k^2-(n\pi)^2} e^{-k(x-g-2L)/t}\, dk\,. \tag{3.27}$$

Closed forms for J_n^{TF} and K_n^{TF} are given in Sections A.3.2 and A.3.3 respectively. Analytic expressions have not yet been obtained for R_n and S_n^{TF}. The integrals occurring in the field components correspond to integrals appearing in other solutions as is the case for the potential function. Figs. 3.3 and 3.4 show the horizontal and vertical field components respectively, normalised by V/t, at various heights between the head face plane at $y = 0$ and the underlayer at $y/t = 1.0$. The negative of the horizontal field has been plotted to conform to convention as in the case of the ring head in Section

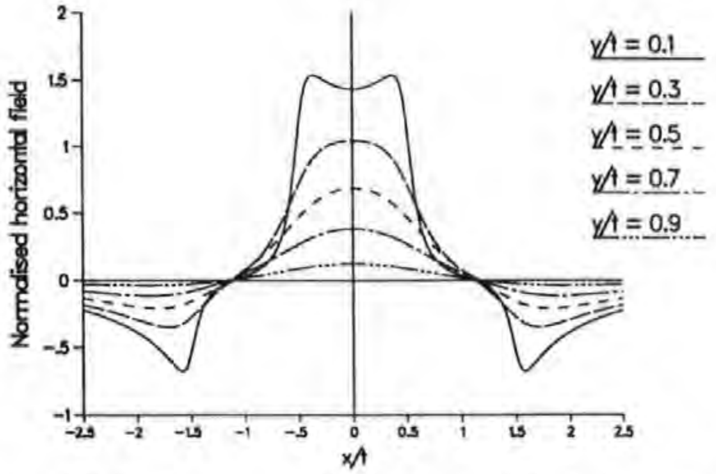

Figure 3.3: Horizontal field component for a thin film head with constant potential poles, $g/t = L/t = 0.5$.

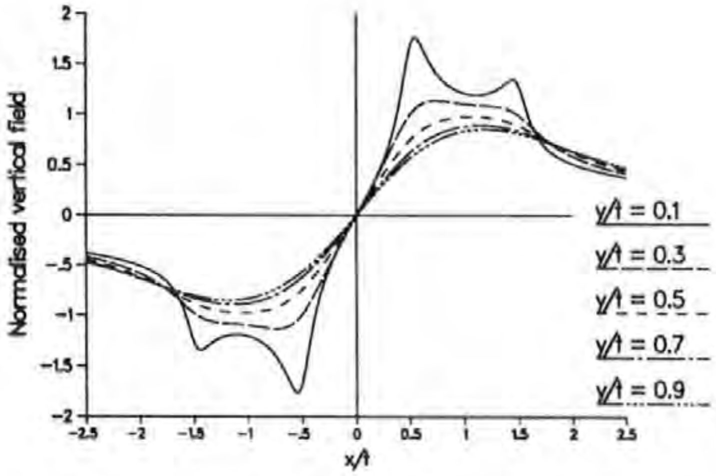

Figure 3.4: Vertical field component for a thin film head with constant potential poles, $g/t = L/t = 0.5$.

2.1.4.2.

Both field components have peaks which increase in magnitude and decrease in width towards the head face plane. Close to the head the peaks become bimodal. The horizontal component has a peak and undershoots corresponding to the gap and the outer edges of the pole pieces respectively. The vertical field component, which is of greater interest for perpendicular recording, has two peaks of opposite sign corresponding to the two pole pieces.

3.1.1.3 Linearly varying potential poles

For the thin film head with linearly varying pole potentials, $f(x) = V(2L + g - x)/2L$ in the general model shown in Fig. 3.1. The boundary conditions given for the constant potential case in regions A and C (equns. (3.1) and (3.5) respectively) apply here also, so that the general solutions to Laplace's equation in these two regions are also the same as for the constant pole potential thin film head, and are given by equns. (3.2) and (3.4). In region B the particular solution which satisfies the true boundary conditions at $y = 0$ and $y = t$ and complements the general solution when $\varphi(x, 0) = \varphi(x, t) = 0$ is linear in both x and y. Therefore, with the subscript denoting the region,

$$\varphi_B^L(x, y) = V\frac{(t-y)}{2tL}(g+2L-x)+\sum_{n=1}^{\infty} \sin\left(n\pi\frac{(t-y)}{t}\right)\left[B_n^L e^{n\pi x/t} + D_n^L e^{-n\pi x/t}\right] . \quad (3.28)$$

Matching the appropriate potentials at $x = g$, where the pole has potential V, as in the constant potential case, and taking the sine transform (equn. (3.7)), provides the same relationship between the functions $A(k)$ and the coefficients B_n^L and D_n^L here, as found for the thin film head with constant pole potentials. Hence the potential in region A for the case of linearly varying pole potentials is given by equn. (3.8). Matching the correct potentials at $x = g + 2L$, where the pole potential is zero,

$$\varphi_C^L(g + 2L, y) = \begin{cases} 0 & -\infty < y \leq 0 \\ \varphi_B^L(g + 2L, y) & 0 \leq y \leq t \end{cases} \quad (3.29)$$

and taking the sine transform (3.7) leads to

$$\varphi_C^L(x, y) = \sum_{n=1}^{\infty} 2n(-1)^n \left[B_n^L e^{n\pi(g+2L)/t} + D_n^L e^{-n\pi(g+2L)/t}\right] I_n^{TF} \quad (3.30)$$

where I_n^{TF} is given by equn. (3.12).

Matching the x-derivatives of the appropriate potentials over their common boundaries and employing the properties of orthogonal functions as described for the constant potential case leads to the two coupled infinite systems of linear equations for the coefficients:

$$\begin{aligned}
&\frac{\pi}{4}\left[B_m^L e^{m\pi g/t} - D_m^L e^{-m\pi g/t}\right] \\
&\qquad + \sum_{n=1}^{\infty}(-1)^{m+n+1} n\pi \left[B_n^L e^{n\pi g/t} + D_n^L e^{-n\pi g/t}\right] I_{mn}^{TF} \\
&\qquad\qquad = V(-1)^m \left[I_{m0}^{TF} - \frac{t}{4m^2\pi L}\right] \qquad (3.31)
\end{aligned}$$

$$\begin{aligned}
&\frac{\pi}{4}\left[B_m^L e^{m\pi(g+2L)/t} - D_m^L e^{-m\pi(g+2L)/t}\right] \\
&\qquad + \sum_{n=1}^{\infty}(-1)^{m+n} n\pi \left[B_n^L e^{n\pi(g+2L)/t} + D_n^L e^{-n\pi(g+2L)/t}\right] I_{mn} \\
&\qquad\qquad = V(-1)^{m+1} \left[\frac{t}{4m^2\pi L}\right] \qquad (3.32)
\end{aligned}$$

where I_{mn}^{TF} and I_{mn} are given by equns. (3.17) and (2.11) respectively.

As for the constant pole potential thin film head, it is convenient to define scaled coefficients $B_n^{L'} = B_n^L e^{n\pi(g+2L)/t}/V$ and $D_n^{L'} = D_n^L e^{-n\pi g/t}/V$. Restricting each system of equations to some finite size N, and writing the equations in the matrix form, $[A^{TF}]\underline{x}^L = \underline{b}^L$ the $2N \times 2N$ matrix $[A^{TF}]$ is the same as in the constant pole potential case, equn. (3.19) but here $\underline{x}^L$ and the right-hand side vector, $\underline{b}^L$, are given by

$$x_m^L = D_m^{L'}, \qquad\qquad x_{m+N}^L = B_m^{L'}, \qquad (3.33)$$

$$b_m^L = (-1)^m \left(I_{m0}^{TF} - \frac{t}{4m^2\pi L}\right) \quad \text{and} \quad b_{m+N}^L = (-1)^{m+1}\frac{t}{4m^2\pi L} \qquad (3.34)$$

for $m = 1, 2, \cdots, N$, where I_{m0}^{TF} is defined by equn. (3.17).

Here, no comparisons with other solutions in limiting cases are appropriate. The first six coefficients for thin film heads with linearly varying pole potentials which correspond to those given for the constant pole potential case, are given in Tables B.4 – B.6.

The horizontal and vertical field components, normalised by V/t, which follow by the partial differentiation of the potential function, in terms of the scaled coefficients are,

$$\frac{t}{V}H_x^L(x,y) = \begin{cases} -\frac{2}{\pi}R_0 - \sum_{n=1}^{\infty} 2n(-1)^n \left[B_n^{L'}e^{-2n\pi L/t} + D_n^{L'}\right] R_n & 0 \le x \le g \\ & y \le t \\ \frac{t-y}{2L} - \sum_{n=1}^{\infty} n\pi \sin\left(n\pi\frac{(t-y)}{t}\right)\left[B_n^{L'}e^{n\pi(x-g-2L)/t} - D_n^{L'}e^{-n\pi(x-g)/t}\right] & \\ & g \le x \le g+2L \\ & 0 \le y \le t \\ \sum_{n=1}^{\infty} 2n(-1)^n \left[B_n^{L'} + D_n^{L'}e^{-2n\pi L/t}\right] J_n^{TF} & g+2L \le x < \infty \\ & y \le t\,, \end{cases} \tag{3.35}$$

and

$$\frac{t}{V}H_y^L(x,y) = \begin{cases} \frac{2}{\pi}S_0^{TF} + \sum_{n=1}^{\infty} 2n(-1)^n \left[B_n^{L'}e^{-2n\pi L/t} + D_n^{L'}\right] S_n^{TF} & 0 \le x \le g \\ & y \le t \\ \frac{g+2L-x}{2L} + \sum_{n=1}^{\infty} n\pi \cos\left(n\pi\frac{(t-y)}{t}\right)\left[B_n^{L'}e^{n\pi(x-g-2L)/t} + D_n^{L'}e^{-n\pi(x-g)/t}\right] & \\ & g \le x \le g+2L \\ & 0 \le y \le t \\ \sum_{n=1}^{\infty} 2n(-1)^n \left[B_n^{L'} + D_n^{L'}e^{-2n\pi L/t}\right] K_n^{TF} & g+2L \le x < \infty \\ & y \le t \end{cases} \tag{3.36}$$

where R_n, J_n^{TF}, S_n^{TF} and K_n^{TF} are the same integrals that occur in the solution for the thin film head with constant potential poles and are given by equns. (3.24) –

(3.27), respectively. Figs. 3.5 and 3.6 show the normalised, horizontal and vertical

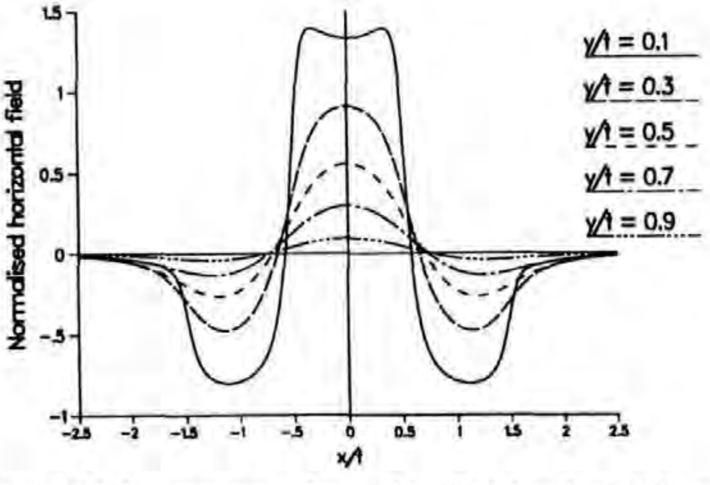

Figure 3.5: Horizontal field component for a thin film head with linearly varying potential poles, $g/t = L/t = 0.5$.

field components respectively, at various heights between the head face plane at $y = 0$ and the underlayer at $y/t = 1.0$. The horizontal field exhibits three peaks of which the one corresponding to the gap between the pole pieces is of greater magnitude than each of the pair of peaks corresponding to the pole pieces. Close to the head the central peak becomes bimodal. The vertical component has a pair of equal magnitude peaks of opposite sign corresponding to the gap edges and close to the head undershoots occur due to the outer edges of the poles.

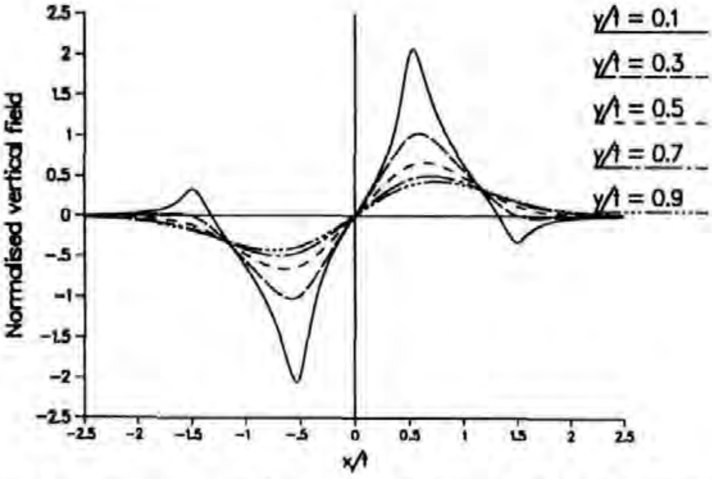

Figure 3.6: Vertical field component for a thin film head with linearly varying potential poles, $g/t = L/t = 0.5$.

3.1.2 The Single Pole with Linearly Varying Pole Potential

The idealised 2-dimensional, general model of a single pole recording head is shown in Fig. 3.7. All of the assumptions of Section 2.1.3.1 apply here except for the fourth which is modified to accommodate the non-constant pole potential, as described in Section 3.1.1.1. A semi-infinite pole of width $2L$ is perpendicular to and at a distance t from an infinite plane at zero potential. Here, the pole potential is assumed to vary linearly from zero at the left-hand edge to $+V$ at the right-hand edge, giving $f(x) = V(x+L)/2L$, with $\alpha = 0$ and $\beta = 1$ in Fig. 3.7. For this pole potential there is no line of symmetry in the system therefore, in order to solve Laplace's equation for the magnetic potential exterior to the pole and the underlayer, it is necessary to subdivide this area into the three regions A, B and C shown in Fig. 3.7.

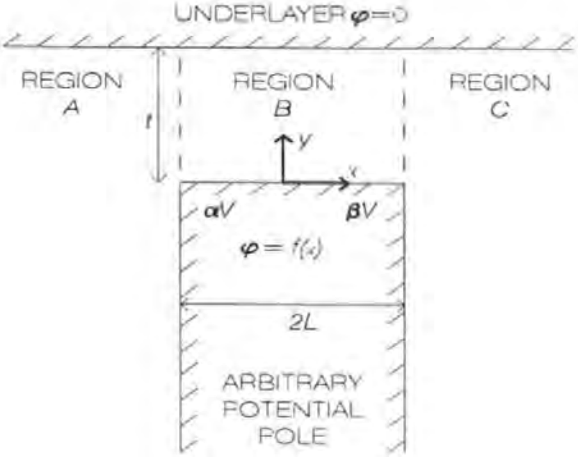

Figure 3.7: The general model for a single pole head.

The general solution of Laplace's equation in region A which is zero at $y = t$ and which has the correct behaviour as $x \longrightarrow -\infty$ may be expressed as the Fourier integral

$$\varphi_A^{LP}(x,y) = \int_0^\infty A(k) \sin\left(k\frac{(t-y)}{t}\right) e^{kx/t}\, dk \tag{3.37}$$

where the superscript LP denotes a single pole head with linearly varying pole potential. In region B the series

$$\varphi_B^{LP}(x,y) = V\frac{(t-y)}{t}\frac{(x+L)}{2L}+\sum_{n=1}^{\infty}\sin\left(n\pi\frac{(t-y)}{t}\right)\left[B_n^{LP}\cosh\left(\frac{n\pi x}{t}\right)+D_n^{LP}\sinh\left(\frac{n\pi x}{t}\right)\right] \tag{3.38}$$

takes the correct values at $y=0$ and $y=t$. The solution for the single pole head with linearly varying pole potential depends on two sets of coefficients, unlike the solution for the conventional single pole for which there is only one set of coefficients. In region C the integral

$$\varphi_C^{LP}(x,y) = \int_0^{\infty} C(k)\sin\left(k\frac{(t-y)}{t}\right)e^{-kx/t}\,dk \tag{3.39}$$

is appropriate. The coefficients B_n^{LP} and D_n^{LP} and the functions $A(k)$ and $C(k)$ need to be determined.

Matching the potential at $x=-L$

$$\varphi_A^{LP}(-L,y) = \begin{cases} 0 & -\infty < y \leq 0 \\ \varphi_B^{LP}(-L,y) & 0 \leq y \leq t \end{cases} \tag{3.40}$$

and taking a Fourier sine transform in y (equn. (3.7)) enables $A(k)$ to be expressed in terms of B_n^{LP} and D_n^{LP} to give

$$\varphi_A^{LP}(x,y) = \sum_{n=1}^{\infty} 2n(-1)^n\left[B_n^{LP}\cosh\left(\frac{n\pi L}{t}\right) - D_n^{LP}\sinh\left(\frac{n\pi L}{t}\right)\right]I_n^P \tag{3.41}$$

where

$$I_n^P = \int_0^{\infty}\frac{\sin(k)\sin(k(t-y)/t)}{k^2-(n\pi)^2}e^{-k(|x|-L)/t}\,dk \tag{3.42}$$

which is the same integral as that which occurs in the solution for the conventional constant potential single pole (2.9), although here it is defined for $x<0$ also. I_n^P

appears in closed form in Section A.3.1. Similarly, matching the potential at $x = L$

$$\varphi_C^{LP}(L,y) = \begin{cases} V & -\infty < y \leq 0 \\ \varphi_B^{LP}(L,y) & 0 \leq y \leq t \end{cases} \tag{3.43}$$

and taking a Fourier sine transform in y leads to

$$\varphi_C^{LP}(x,y) = \frac{2V}{\pi} I_0^P + \sum_{n=1}^{\infty} 2n(-1)^n \left[B_n^{LP} \cosh\left(\frac{n\pi L}{t}\right) + D_n^{LP} \sinh\left(\frac{n\pi L}{t}\right) \right] I_n^P . \tag{3.44}$$

The coefficients B_n^{LP} and D_n^{LP} are found by matching the x-derivatives of the appropriate potential representations at the two boundaries $0 \leq y \leq t$ for $x = \pm L$ and using the orthogonality property of the functions $\sin(m\pi(t-y)/t)$ over $0 \leq y \leq t$, where m is an integer. This initially results in the two coupled infinite systems of linear simultaneous equations:

$$\begin{aligned} &\frac{\pi}{4}\left[B_m^{LP} \sinh\left(\frac{m\pi L}{t}\right) + D_m^{LP} \cosh\left(\frac{m\pi L}{t}\right) \right] \\ &\quad + \sum_{n=1}^{\infty} (-1)^{m+n} n\pi \left[B_n^{LP} \cosh\left(\frac{n\pi L}{t}\right) + D_n^{LP} \sinh\left(\frac{n\pi L}{t}\right) \right] I_{mn} \\ &\qquad = V(-1)^m \left[\frac{t}{4m^2\pi L} - I_{m0} \right] \end{aligned} \tag{3.45}$$

$$\begin{aligned} &\frac{\pi}{4}\left[B_m^{LP} \sinh\left(\frac{m\pi L}{t}\right) - D_m^{LP} \cosh\left(\frac{m\pi L}{t}\right) \right] \\ &\quad + \sum_{n=1}^{\infty} (-1)^{m+n} n\pi \left[B_n^{LP} \cosh\left(\frac{n\pi L}{t}\right) - D_n^{LP} \sinh\left(\frac{n\pi L}{t}\right) \right] I_{mn} \\ &\qquad = V(-1)^{m+1} \frac{t}{4m^2\pi L} \end{aligned} \tag{3.46}$$

for $m = 1, 2, 3, \cdots$ in each case, where I_{mn} is as given for the conventional single pole head in equn. (2.9). However it is clear that either by adding or by subtracting these systems, they uncouple to give equations for the B_m^{LP} or D_m^{LP} alone. The Fourier coefficients may be evaluated by restricting each of the uncoupled infinite systems to some finite size N. Computationally it is convenient to solve for the scaled normalised coefficients $B_m^{LP'} = B_m^{LP}\cosh(n\pi L/t)/V$ and $D_m^{LP'} = D_m^{LP}\sinh(n\pi L/t)/V$ which depend on the ratio L/t only. Each set of coefficients satisfies an $N \times N$ system of equations, $[A^{LP}]\underline{x}^{LP} = \underline{b}^{LP}$ where for the $B_m^{LP'}$,

$$A_{mn}^{LP_B} = (-1)^{m+n} n\pi I_{mn} + \begin{cases} \pi\tanh(m\pi L/t)/4 & m = n \\ 0 & m \neq n \end{cases}$$

for $m, n = 1, 2, \cdots, N$, and

$$b_m^{LP_B} = (-1)^{m+1}\frac{I_{m0}}{2}, \qquad x_m^{LP_B} = B_m^{LP'} \tag{3.47}$$

for $m = 1, 2, \cdots, N$. For the $D_m^{LP'}$,

$$A_{mn}^{LP_D} = (-1)^{m+n} n\pi I_{mn} + \begin{cases} \pi\coth(m\pi L/t)/4 & m = n \\ 0 & m \neq n \end{cases}$$

for $m, n = 1, 2, \cdots, N$, and

$$b_m^{LP_D} = (-1)^m\left[\frac{t}{4m^2\pi L} - \frac{I_{m0}}{2}\right], \qquad x_m^{LP_D} = D_m^{LP'} \tag{3.48}$$

for $m = 1, 2, \cdots, N$.

Table B.7 in Appendix B shows the first six coefficients $B_n^{LP'}$ and $D_n^{LP'}$ for a range of L/t values. These coefficients are based on solving systems of N up to 640 together with an extrapolation technique [33] and are believed to be correct to the number of figures given. The coefficients get larger as L/t decreases, showing that as the pole – underlayer distance increases the resulting series for the magnetic field will converge more slowly. The scaled normalised coefficients for the single pole with constant potential satisfy equn. (2.10) which is the same as equn. (3.47) with a factor of 2 omitted from the right-hand side and hence the constant potential pole coefficients are twice the $B_n^{LP'}$ for the single pole with linearly varying pole potential. As L/t increases there is a correspondence in region C between the conventional pole solution given in Section 2.1.3.2 and the one given here which requires that the $D_n^{LP'}$ coefficients approach half of those for the constant potential pole. Computation with very large values of L/t confirms this; results when $L/t = 50$ for both the constant $(f(x) = V)$ and the linearly varying potential cases are included in Table B.7.

The field components, found by the partial differentiation of the potential, normalised by V/t and in terms of the scaled coefficients are:

$$\frac{t}{V}H_x^{LP}(x,y) = \left\{ \begin{array}{lll} & \sum_{n=1}^{\infty} 2n(-1)^n \left[B_n^{LP'} - D_n^{LP'}\right] J_n^P & -\infty < x \leq -L \\ & & y \leq t \\ \frac{y-t}{2L} & - \sum_{n=1}^{\infty} n\pi \sin\left(\frac{n\pi(t-y)}{t}\right) \left[B_n^{LP'} \sinh\left(\frac{n\pi x}{t}\right) / \cosh\left(\frac{n\pi L}{t}\right)\right. & \\ & \qquad \left. + D_n^{LP'} \cosh\left(\frac{n\pi x}{t}\right) / \sinh\left(\frac{n\pi L}{t}\right)\right] & -L \leq x \leq L \\ & & 0 \leq y \leq t \\ \frac{2}{\pi} J_0^P & + \sum_{n=1}^{\infty} 2n(-1)^n \left[B_n^{LP'} + D_n^{LP'}\right] J_n^P & L \leq x < \infty \\ & & y \leq t \end{array} \right. \tag{3.49}$$

and

$$\frac{t}{V}H_y^{LP}(x,y) = \begin{cases} \sum_{n=1}^{\infty} 2n(-1)^n \left[B_n^{LP'} - D_n^{LP'}\right] K_n^P & -\infty < x \leq -L \\ & y \leq t \\ \frac{x+L}{2L} + \sum_{n=1}^{\infty} n\pi \cos\left(\frac{n\pi(t-y)}{t}\right) \left[B_n^{LP'} \cosh\left(\frac{n\pi x}{t}\right) / \cosh\left(\frac{n\pi L}{t}\right)\right. & \\ \qquad \left. + D_n^{LP'} \sinh\left(\frac{n\pi x}{t}\right) / \sinh\left(\frac{n\pi L}{t}\right)\right] & -L \leq x \leq L \\ & 0 \leq y \leq t \\ \frac{2}{\pi}K_0^P + \sum_{n=1}^{\infty} 2n(-1)^n \left[B_n^{LP'} + D_n^{LP'}\right] K_n^P & L \leq x < \infty \\ & y \leq t \end{cases} \tag{3.50}$$

where J_n^P and K_n^P are the same integrals that occur in the solution for the conventional single pole head except that here they are defined in terms of $|x|$ to apply for $x < 0$ also. They are given in closed form in Sections A.3.2 and A.3.3 respectively. Figs. 3.8 and 3.9 show the normalised, horizontal and vertical field components respectively, at various heights between the head face plane at $y = 0$ and the underlayer at $y/t = 1.0$. The horizontal component has two unequal peaks of opposite sign. The peak corresponding to the pole is broader and of greater magnitude than the peak due to the right-hand pole edge. The vertical component has a single peak corresponding to the right-hand

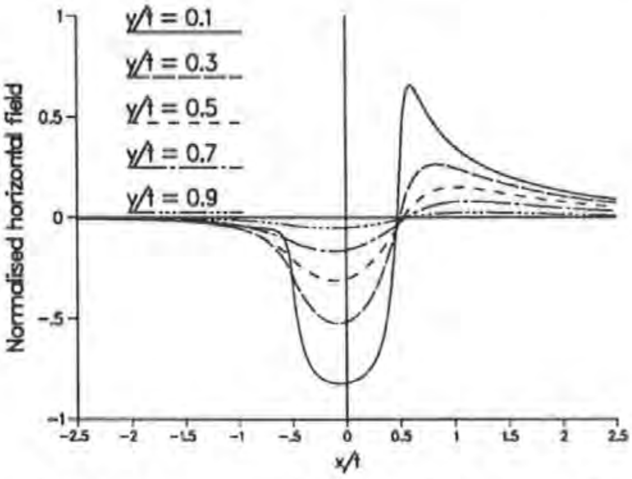

Figure 3.8: Horizontal field component for a single pole head with linearly varying potential poles, $L/t = 0.5$.

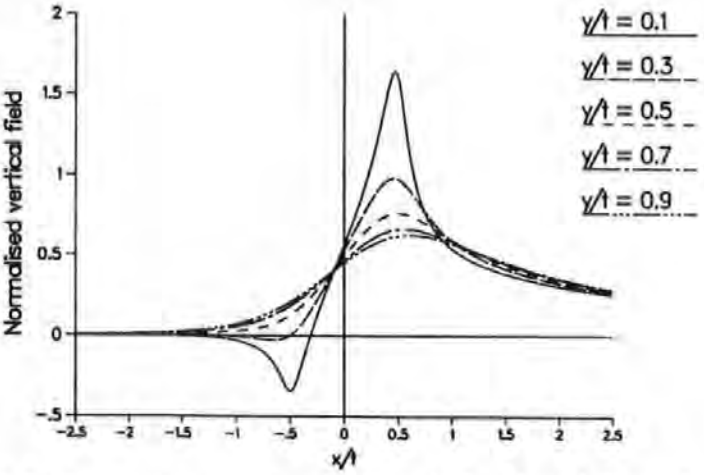

Figure 3.9: Vertical field component for a single pole head with linearly varying potential poles, $L/t = 0.5$.

pole edge and close to the head an undershoot occurs due to the zero potential pole corner.

3.1.3 The Single Pole with Arbitrary Pole Potential

The idealised 2-dimensional model is shown in Fig. 3.7, and has been desribed in Section 3.1.2. Here no assumptions are made about the potential distribution across the pole except that it is a function of x only and takes the values αV and βV, where α and β are arbitrary real numbers, at the left- and right-hand edges, respectively.

The general solutions of Laplace's equation for the magnetic potential in regions A and C are the same as those given for the single pole with linearly varying pole potential, equns. (3.37) and (3.39), respectively. In region B the general solutions of Laplace's equation for both the constant and the linearly varying pole potential cases are obtained by solving for zero boundary condtions at $y = 0$ and at $y = t$ and then adding the particular solution which satisfies the true boundary conditions, $\varphi_B(x, y) = f(x)(t - y)/t$, which is only a solution of Laplace's equation when $f(x)$ is either a constant or a linear function of x. For single pole heads with arbitrary pole potentials, $f(x)$ must be expressed in terms of either trigonometric or hyberbolic functions which satisfy Laplace's equation.

Any function of x can be expanded as a Fourier series so that the normalised magnetic potential of the pole may be written as

$$\frac{f(x)}{V} = \frac{a_0}{2} + \sum_{N=1}^{\infty} a_N \cos\left(\frac{N\pi x}{p}\right) + b_N \sin\left(\frac{N\pi x}{p}\right), \tag{3.51}$$

by extending the function to make it periodic over the interval $-p \leq x \leq p$ with $p \geq L$, while retaining its original definition over the interval of interest. The choice of period is purely arbitrary but on evaluation, the series converges to $f(x)/V$ more rapidly if the extended function is continuous. Therefore a general solution of Laplace's equation in region B, which satisfies the boundary conditions $\varphi_B^{AP}(x,0) = f(x)$ and $\varphi_B^{AP}(x,t) = 0$ can be written as

$$\begin{aligned}\varphi_B^{AP}(x,y) &= V\left(\frac{a_0}{2}\right)\frac{(t-y)}{t} \\ &+V\sum_{N=1}^{\infty}\left[a_N \cos\left(\frac{N\pi x}{p}\right) + b_N \sin\left(\frac{N\pi x}{p}\right)\right]\left[\frac{\sinh(N\pi(t-y)/p)}{\sinh(N\pi t/p)}\right] \\ &+\sum_{n=1}^{\infty}\sin\left(n\pi\frac{(t-y)}{t}\right)\left[B_n^{AP}\cosh\left(\frac{n\pi x}{t}\right) + D_n^{AP}\sinh\left(\frac{n\pi x}{t}\right)\right] \end{aligned} \tag{3.52}$$

where the superscript AP denotes a single pole with an arbitrary pole potential distribution. Here the choice $p = 2L$ is made and $f(x)$ is assumed to be symmetric about $x = L$, to ensure a continuous periodic extension of $f(x)$. Hence

$$f(x)_{\text{extended}} = \begin{cases} f(2L+x) & -2L \leq x \leq -L \\ f(x) & -L \leq x \leq L \\ f(2L-x) & L \leq x \leq 2L\,. \end{cases} \tag{3.53}$$

This choice also provides the best convergence properties of several periods tested, and it results in the simplification of the Fourier series representations of some of the functions considered. When $f(x)$ is odd $a_N = 0$ and when $f(x)$ is even $b_N = 0$, for $N \geq 1$.

The particular potential distributions which are considered here are

1. Linear:

$$\alpha = 0\,, \qquad \beta = 1\,. \tag{3.54}$$

$$\frac{f(x)}{V} = \frac{x+L}{2L} = \frac{1}{2} + \sum_{N=1}^{\infty} \frac{4}{(N\pi)^2} \sin\left(\frac{N\pi}{2}\right) \sin\left(\frac{N\pi x}{2L}\right). \tag{3.55}$$

2. Quadratic:

$$\alpha = 0\,, \qquad \beta = 1\,. \tag{3.56}$$

$$\begin{aligned} \frac{f(x)}{V} &= \left(\frac{x+L}{2L}\right)^2 \\ &= \frac{1}{3} + \sum_{N=1}^{\infty} \frac{4}{(N\pi)^2} \left[\sin\left(\frac{N\pi}{2}\right) \sin\left(\frac{N\pi x}{2L}\right)\right. \\ &\qquad \left. + \cos\left(\frac{N\pi}{2}\right) \cos\left(\frac{N\pi x}{2L}\right)\right]. \end{aligned} \tag{3.57}$$

3. Cubic:

$$\alpha = 0\,, \qquad \beta = 1\,. \tag{3.58}$$

$$\begin{aligned} \frac{f(x)}{V} &= \left(\frac{x+L}{2L}\right)^3 \\ &= \frac{1}{4} + \sum_{N=1}^{\infty} \frac{6}{(N\pi)^2} \left[\left(1 - \frac{4}{(N\pi)^2}\right) \sin\left(\frac{N\pi}{2}\right) \sin\left(\frac{N\pi x}{2L}\right)\right. \\ &\qquad \left. + \cos\left(\frac{N\pi}{2}\right) \cos\left(\frac{N\pi x}{2L}\right)\right]. \end{aligned} \tag{3.59}$$

4. Cosine-squared:

$$\alpha = \beta = 0\,. \tag{3.60}$$

$$\frac{f(x)}{V} = \cos^2\left(\frac{\pi x}{2L}\right) = \frac{1}{2}\left[1 + \cos\left(\frac{\pi x}{L}\right)\right]. \tag{3.61}$$

Determination of the functions $A(k)$ and $C(k)$ appearing in the solutions of Laplace's equation in regions A and C respectively, and of the coefficients B_n^{AP} and D_n^{AP}, is achieved in the same way as described for the thin film heads and the single pole with linearly varying pole potential. Matching the potentials at $x = -L$ and taking a Fourier sine transform (equn. (3.7)) gives $A(k)$ in terms of B_n^{AP} and D_n^{AP} so that in region A:

$$\begin{aligned} \varphi_A^{AP}(x,y) &= \frac{2V}{\pi}\left\{\frac{a_0}{2}T_0 + \left(\alpha - \frac{a_0}{2}\right)U_0 + \sum_{N=1}^{\infty}\left[a_N\cos\left(\frac{N\pi}{2}\right) - b_N\sin\left(\frac{N\pi}{2}\right)\right]\eta_N\right\} \\ &\quad + \sum_{n=1}^{\infty} 2n(-1)^n\left[B_n^{AP}\cosh\left(\frac{n\pi L}{t}\right) - D_n^{AP}\sinh\left(\frac{n\pi L}{t}\right)\right] I_n^P, \end{aligned} \tag{3.62}$$

where

$$\eta_N = N\pi s\coth(N\pi s)T_N - U_N, \quad s = t/2L, \tag{3.63}$$

$$I_n^P = \int_0^{\infty} \frac{\sin(k)\sin(k(t-y)/t)}{k^2 - (n\pi)^2} e^{-k(|x|-L)/t}\,dk \tag{3.64}$$

$$T_N = \int_0^{\infty} \frac{\sin(k)\sin(k(t-y)/t)}{k^2 + (N\pi s)^2} e^{-k(|x|-L)/t}\,dk \tag{3.65}$$

$$U_N = \int_0^{\infty} \frac{k\cos(k)\sin(k(t-y)/t)}{k^2 + (N\pi s)^2} e^{-k(|x|-L)/t}\,dk. \tag{3.66}$$

Closed forms for each of these integrals are given in Sections A.3.1, A.3.4 and A.3.5 respectively. Similarly, matching at $x = L$ gives $C(k)$ in terms of B_n and D_n so that in region C:

$$\varphi_C^{AP}(x,y) = \frac{2V}{\pi}\left\{\frac{a_0}{2}T_0 + \left(\beta - \frac{a_0}{2}\right)U_0 + \sum_{N=1}^{\infty}\left[a_N\cos\left(\frac{N\pi}{2}\right) + b_N\sin\left(\frac{N\pi}{2}\right)\right]\eta_N\right\}$$

$$+\sum_{n=1}^{\infty} 2n(-1)^n \left[B_n^{AP}\cosh\left(\frac{n\pi L}{t}\right) + D_n^{AP}\sinh\left(\frac{n\pi L}{t}\right)\right] I_n^P \tag{3.67}$$

with η_N, I_n^P, T_N and U_N given in equns. (3.63) - (3.66).

Matching expressions for $\partial\varphi^{AP}/\partial x$ at $x = -L$ and at $x = L$ and taking a sine transform (equn. (3.7)) in each case provides the two coupled, infinite systems of linear equations for the coefficients:

$$\begin{aligned}
&\sum_{n=1}^{\infty} n\pi(-1)^{m+n}\left[B_n^{AP}\cosh\left(\frac{n\pi L}{t}\right) - D_n^{AP}\sinh\left(\frac{n\pi L}{t}\right)\right] I_{mn} \\
&\qquad + \frac{\pi}{4}\left[B_m^{AP}\sinh\left(\frac{m\pi L}{t}\right) - D_m^{AP}\cosh\left(\frac{m\pi L}{t}\right)\right] \\
&= (-1)^{m+1}\left\{\frac{a_0}{2}N_{m0} + \left(\alpha - \frac{a_0}{2}\right)P_{m0} + \sum_{N=1}^{\infty}\tau_{mN}\left[a_N\sin\left(\frac{N\pi}{2}\right) + b_N\cos\left(\frac{N\pi}{2}\right)\right]\right. \\
&\qquad \left. + \left[a_N\cos\left(\frac{N\pi}{2}\right) - b_N\sin\left(\frac{N\pi}{2}\right)\right]\sigma_{mN}\right\}
\end{aligned} \tag{3.68}$$

and

$$\begin{aligned}
&\sum_{n=1}^{\infty} n\pi(-1)^{m+n}\left[B_n^{AP}\cosh\left(\frac{n\pi L}{t}\right) + D_n^{AP}\sinh\left(\frac{n\pi L}{t}\right)\right] I_{mn} \\
&\qquad + \frac{\pi}{4}\left[B_m^{AP}\sinh\left(\frac{m\pi L}{t}\right) + D_m^{AP}\cosh\left(\frac{m\pi L}{t}\right)\right] \\
&= (-1)^{m+1}\left\{\frac{a_0}{2}N_{m0} + \left(\beta - \frac{a_0}{2}\right)P_{m0} + \sum_{N=1}^{\infty}\tau_{mN}\left[a_N\sin\left(\frac{N\pi}{2}\right) - b_N\cos\left(\frac{N\pi}{2}\right)\right]\right. \\
&\qquad \left. + \left[a_N\cos\left(\frac{N\pi}{2}\right) + b_N\sin\left(\frac{N\pi}{2}\right)\right]\sigma_{mN}\right\},
\end{aligned} \tag{3.69}$$

where, with $s = t/2L$,

$$\sigma_{mN} = N\pi s\coth(N\pi s)N_{mN} - P_{mN}, \tag{3.70}$$

$$\tau_{mN} = \frac{Ns}{2\left[(Ns)^2 + m^2\right]}, \tag{3.71}$$

$$I_{mn} = \int_0^\infty \frac{k\sin^2(k)}{[k^2-(m\pi)^2]\,[k^2-(n\pi)^2]}\,dk\,, \tag{3.72}$$

$$N_{mN} = \int_0^\infty \frac{k\sin^2(k)}{[k^2-(m\pi)^2]\,[k^2+(N\pi s)^2]}\,dk \tag{3.73}$$

and

$$P_{mN} = \int_0^\infty \frac{k^2\sin(k)\cos(k)}{[k^2-(m\pi)^2]\,[k^2+(N\pi s)^2]}\,dk\,. \tag{3.74}$$

Analytic expressions for I_{mn}, N_{mN} and P_{mN} are given in Sections A.2.1, A.2.2 and A.2.3 respectively.

These two systems of equations can be uncoupled by either addition or subtraction to give two infinite systems of linear simultaneous equations. It is convenient to define scaled coefficients $B_m^{AP'} = B_m^{AP}\cosh(m\pi L/t)/V$ and $D_m^{AP'} = D_m^{AP}\sinh(m\pi L/t)/V$ which satisfy matrix equations of the form $[A^{AP}]\underline{x}^{AP} = \underline{b}^{AP}$ where for the $B_m^{AP'}$

$$\begin{aligned} A_{m,n}^{AP_B} &= (-1)^{m+n} n\pi I_{mn} + \begin{cases} \pi\tanh(m\pi L/t)/4 & m=n \\ 0 & m\neq n \end{cases} \\ x_m^{AP_B} &= B_m^{AP'} \end{aligned}$$

and

$$\begin{aligned} b_m^{AP_B} &= (-1)^{m+1}\left\{\frac{a_0}{2}N_{m0} + \frac{(\alpha+\beta-a_0)}{2}P_{m0}\right. \\ &\qquad \left. + \sum_{N=1}^{\infty} a_N\left[\sigma_{mN}\cos\left(\frac{N\pi}{2}\right) + \tau_{mN}\sin\left(\frac{N\pi}{2}\right)\right]\right\} \end{aligned} \tag{3.75}$$

for $m, n = 1, 2, 3, \cdots$ with σ_{mN}, τ_{mN} given by equns. (3.70) and (3.71) respectively, and for the $D_m^{AP'}$

$$A_{m,n}^{AP_D} = (-1)^{m+n} n\pi I_{mn} + \begin{cases} \pi \coth(m\pi L/t)/4 & m = n \\ 0 & m \neq n \end{cases}$$

$$x_m^{AP_D} = D_m^{AP'}$$

and

$$\begin{aligned} b_m^{AP_D} = (-1)^{m+1} \Bigg\{ & \frac{(\beta-\alpha)}{2} P_{m0} \\ & + \sum_{N=1}^{\infty} b_N \left[\sigma_{mN} \sin\left(\frac{N\pi}{2}\right) - \tau_{mN} \cos\left(\frac{N\pi}{2}\right)\right]\Bigg\} \end{aligned} \qquad (3.76)$$

for $m, n = 1, 2, 3, \cdots$ with σ_{mN}, τ_{mN} given by equns. (3.70) and (3.71) respectively.

Approximate coefficients $B_n^{AP'}$ and $D_n^{AP'}$ are computed by truncating each system to some finite size. Clearly, the right-hand side series in both sets of equations can be simplified to the sum of two separate series, one for N even and the other for N odd, thereby increasing the speed of computation. If $f(x)$ is an odd function each term in the right-hand series of the equations for the $B_m^{AP'}$ is indentically zero, and if $f(x)$ is even, the right-hand side series in equn. (3.76) is eliminated. The Fourier series for a constant potential $f(x) = V$ is simply the constant, V, so that $\alpha = \beta = 1$ in the general model. Hence when $a_N = b_N = 0$ for $N > 0$, equn. (3.75) simplifies to equn. (2.10) and equn. (3.76) has the solution $\underline{x}^{AP_D} = \underline{0}$, confirming the consistency of these equations. For a linear pole potential, rising from zero at the left-hand pole edge to a maximum of V at the right-hand edge, $\alpha = 0$ and $\beta = 1$ in the general model. Due to the form of the Fourier expansion chosen for $f(x)$, $a_N \equiv 0$ for $N > 0$ so that equn. (3.75) reduces to the system of equations for the $B_m^{LP'}$ derived by the earlier analysis of a single pole with linearly varying pole potential, equn. (3.47). However, the coefficients evaluated from (3.76) are not the same as the $D_m^{LP'}$ obtained using (3.48).

The first six coefficients for each of the pole potential distributions listed above are shown in Table B.8 for a pole where $L/t = 0.5$ each computed using systems of equations of size N = 320. For all except the cosine-squared potential distribution, which is expressed exactly in 2 Fourier terms, 200 terms of the Fourier expansion were used in the evaluation of the coefficients. The analytic forms of the integrals N_{mN} and P_{mN} appearing in equns. (3.75) and (3.76) are functions of the exponential integral E_1 (A.2) which is evaluated *via* the summation of a truncated infinite series. Hence the large number of these integrals involved in $b_m^{AP_B}$ and $b_m^{AP_D}$ makes computation of the coefficients expensive.

The accuracy of the coefficients provided in Table B.8 can be assessed by comparison of the $B_n^{AP'}$ computed for a linear pole potential with the $B_n^{LP'}$ computed using equn. (3.47). When the system of equations used is of size $N = 320$ in both cases, coefficients which agree to at least 6dp. are obtained. The $B_n^{LP'}$ coefficients computed using $N = 320$ and those evaluated using $N = 640$ and an extrapolation technique [33], which are believed correct to 6dp., are also shown in Table B.8. These two sets of coefficients computed *via* (3.47) agree to within 1 figure in the fifth decimal place, hence this is the expected accuracy of the $B_n^{AP'}$ and $D_n^{AP'}$ coefficients in the table.

The magnitudes of the first six coefficients do not form a non-increasing sequence in all cases. This occurs for small n only and as n increases further both the $B_n^{AP'}$ and the $D_n^{AP'}$ decrease in magnitude. In the limit, as $n \longrightarrow \infty$ $\left|B_n^{AP'}\right| \longrightarrow 0$ and $\left|D_n^{AP'}\right| \longrightarrow 0$ which is a neccessary condition for the series representation of the potential function to converge.

The generalised field components, normalised by V/t, in terms of the scaled coefficients, are given by:

$$\frac{t}{V} H_x^{AP}(x,y) = \begin{cases} \frac{2}{\pi}\left\{\frac{a_0}{2} V_0 + \left(\alpha - \frac{a_0}{2}\right) W_0 \right. \\ \quad \left. + \sum_{N=1}^{\infty} \left[a_N \cos\left(\frac{N\pi}{2}\right) - b_N \sin\left(\frac{N\pi}{2}\right)\right] \sigma_N \right\} \\ \quad + \sum_{n=1}^{\infty} 2n(-1)^n \left[B_n^{AP'} - D_n^{AP'}\right] J_n^P & -\infty < x \leq -L \\ & y \leq t \\ \sum_{N=1}^{\infty} N\pi s \left[a_N \sin\left(\frac{N\pi x}{2L}\right) - b_N \cos\left(\frac{N\pi x}{2L}\right)\right] \\ \qquad \cdot \left[\sinh\left(\frac{N\pi(t-y)}{2L}\right) / \sinh\left(N\pi s\right)\right] \\ \quad - \sum_{n=1}^{\infty} n\pi \sin\left(n\pi \frac{(t-y)}{t}\right) \left[B_n^{AP'} \sinh\left(\frac{n\pi x}{t}\right) / \cosh\left(\frac{n\pi L}{t}\right) \right. \\ \quad \left. + D_n^{AP'} \cosh\left(\frac{n\pi x}{t}\right) / \sinh\left(\frac{n\pi L}{t}\right)\right] & -L \leq x \leq L \\ & 0 \leq y \leq t \\ \frac{2}{\pi}\left\{\frac{a_0}{2} V_0 + \left(\beta - \frac{a_0}{2}\right) W_0 \right. \\ \quad \left. + \sum_{N=1}^{\infty} \left[a_N \cos\left(\frac{N\pi}{2}\right) + b_N \sin\left(\frac{N\pi}{2}\right)\right] \sigma_N \right\} \\ \quad + \sum_{n=1}^{\infty} 2n(-1)^n \left[B_n^{AP'} + D_n^{AP'}\right] J_n^P & L \leq x < \infty \\ & y \leq t \end{cases} \tag{3.77}$$

where

$$\sigma_N = N\pi s \coth(N\pi s) V_N - W_N, \quad s = t/2L, \tag{3.78}$$

$$J_n^P = \int_0^{\infty} \frac{k \sin(k) \sin(k(t-y)/t)}{k^2 - (n\pi)^2} e^{-k(|x|-L)/t}\, dk\,, \tag{3.79}$$

$$V_N = \int_0^{\infty} \frac{k \sin(k) \sin(k(t-y)/t)}{k^2 + (N\pi s)^2} e^{-k(|x|-L)/t}\, dk\,, \tag{3.80}$$

$$W_N = \int_0^{\infty} \frac{k^2 \cos(k) \sin(k(t-y)/t)}{k^2 + (N\pi s)^2} e^{-k(|x|-L)/t}\, dk\,, \tag{3.81}$$

and

$$\frac{t}{V}H_y^{AP}(x,y) = \begin{cases} \frac{2}{\pi}\left\{\frac{a_0}{2}X_0 + \left(\alpha - \frac{a_0}{2}\right)Y_0 \right. & \\ \quad \left. + \sum_{N=1}^{\infty}\left[a_N\cos\left(\frac{N\pi}{2}\right) - b_N\sin\left(\frac{N\pi}{2}\right)\right]\tau_N\right\} & \\ \quad + \sum_{n=1}^{\infty}2n(-1)^n\left[B_n^{AP'} - D_n^{AP'}\right]K_n^P & -\infty < x \leq -L \\ & y \leq t \\ \frac{a_0}{2} + \sum_{N=1}^{\infty}N\pi s\left[a_N\cos\left(\frac{N\pi x}{2L}\right) + b_N\sin\left(\frac{N\pi x}{2L}\right)\right] & \\ \qquad\qquad \cdot\left[\cosh\left(\frac{n\pi(t-y)}{2L}\right)/\sinh\left(n\pi s\right)\right] & \\ \quad + \sum_{n=1}^{\infty}n\pi\cos\left(n\pi\frac{(t-y)}{t}\right)\left[B_n^{AP'}\cosh\left(\frac{n\pi x}{t}\right)/\cosh\left(\frac{n\pi L}{t}\right)\right. & \\ \qquad\qquad \left. + D_n^{AP'}\sinh\left(\frac{n\pi x}{t}\right)/\sinh\left(\frac{n\pi L}{t}\right)\right] & -L \leq x \leq L \\ & 0 \leq y \leq t \\ \frac{2}{\pi}\left\{\frac{a_0}{2}X_0 + \left(\beta - \frac{a_0}{2}\right)Y_0 \right. & \\ \quad \left. + \sum_{N=1}^{\infty}\left[a_N\cos\left(\frac{N\pi}{2}\right) + b_N\sin\left(\frac{N\pi}{2}\right)\right]\tau_N\right\} & \\ \quad + \sum_{n=1}^{\infty}2n(-1)^n\left[B_n^{AP'} + D_n^{AP'}\right]K_n^P & L \leq x < \infty \\ & y \leq t \end{cases} \tag{3.82}$$

where

$$\tau_N = N\pi s\coth(N\pi s)X_N - Y_N, \quad s = t/2L, \tag{3.83}$$

$$K_n^P = \int_0^{\infty}\frac{k\sin(k)\cos(k(t-y)/t)}{k^2-(n\pi)^2}e^{-k(|x|-L)/t}\,dk\,, \tag{3.84}$$

$$X_N = \int_0^{\infty}\frac{k\sin(k)\cos(k(t-y)/t)}{k^2+(N\pi s)^2}e^{-k(|x|-L)/t}\,dk\,, \tag{3.85}$$

and

$$Y_N = \int_0^{\infty}\frac{k^2\cos(k)\cos(k(t-y)/t)}{k^2+(N\pi s)^2}e^{-k(|x|-L)/t}\,dk\,. \tag{3.86}$$

For $N = 0$, the integral V_0 in the expression for H_x^{AP} could also be written as J_0^P, so that V_0 and J_n^P are both given in closed form in Section A.3.2. W_0 is given analytically in Section A.3.6. Similarly in the expression for H_y^{AP}, $X_0 = K_0^P$, and K_0^P and K_n^P are both given in Section A.3.3. The closed form of Y_0 is given in Section A.3.7. The other integrals, V_N and W_N of the x-component and X_N and Y_N appearing in the y-component have not yet been expressed in closed form.

Evaluating the field components for the linear pole potential *via* (3.77) and (3.82) gives identical results to those obtained using (3.49) and (3.50), which do not depend on a Fourier representation of $f(x)$, respectively. This gives confidence in the correctness of the approach and the computations presented here.

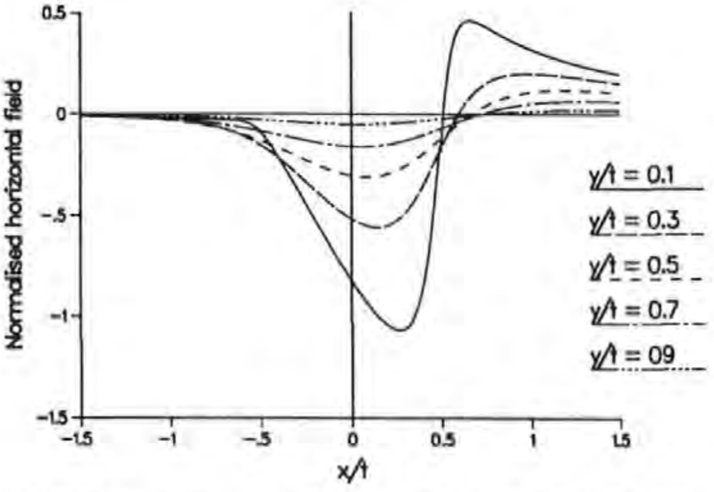

Figure 3.10: Horizontal field component for a single pole head with quadratic pole potential, $L/t = 0.5$.

The normalised, horizontal and vertical field components for single poles with quadratic, cubic and cosine-squared pole potentials, all for $L/t = 0.5$, are shown in Figs. 3.10 – 3.15 at various heights between the head and the underlayer.

For the quadratic and the cubic pole potentials, as the potential becomes less uniform the negative peak of the horizontal component becomes narrower and increases in magnitude, while the positive peak becomes broader. In the vertical component, the widths of the peaks also decrease with deviation from a constant potential, but the

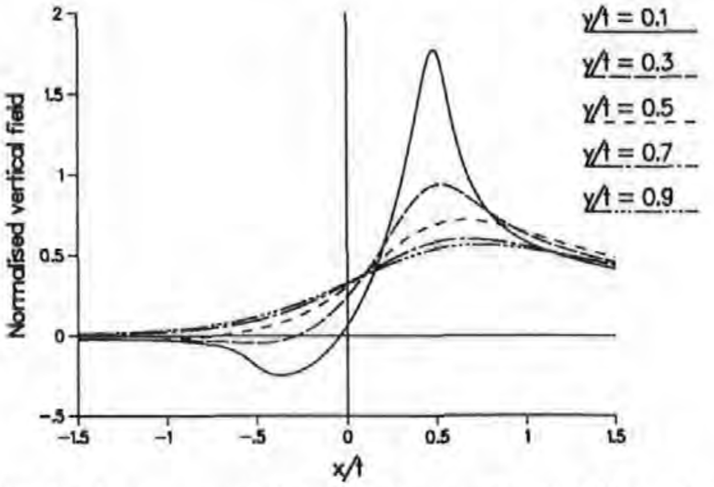

Figure 3.11: Vertical field component for a single pole head with quadratic pole potential, $L/t = 0.5$.

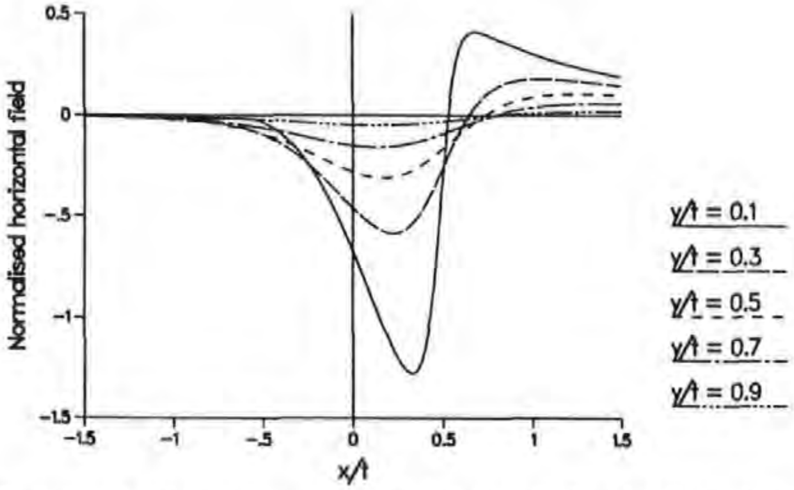

Figure 3.12: Horizontal field component for a single pole head with cubic pole potential, $L/t = 0.5$.

magnitudes of the peaks do not increase steadily. Similarly, the undershoots become broader and their depths reduce slightly with increasing non-uniformity of the pole potential.

For a cosine-squared pole potential, close to the pole, both components have narrow, high magnitude peaks. The peak in the vertical component is of greater magnitude than the peaks in the horizontal component and the presence of undershoots in the vertical component, corresponding to the outer edges of the pole, indicates that the vertical field gradient is higher than the gradient of the horizontal component.

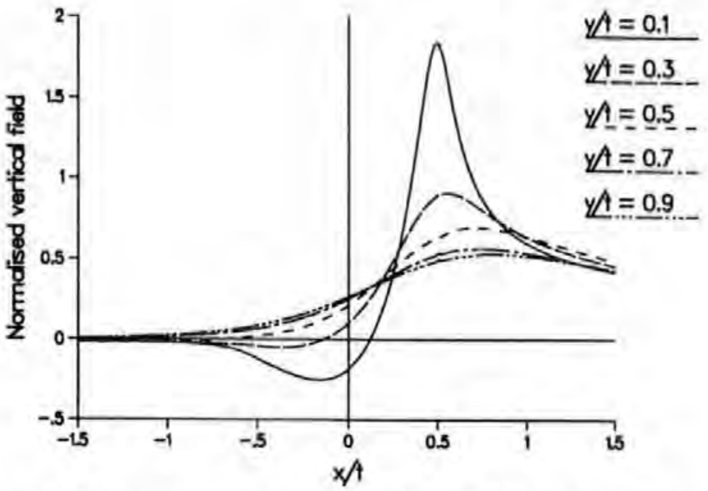

Figure 3.13: Vertical field component for a single pole head with cubic pole potential, $L/t = 0.5$.

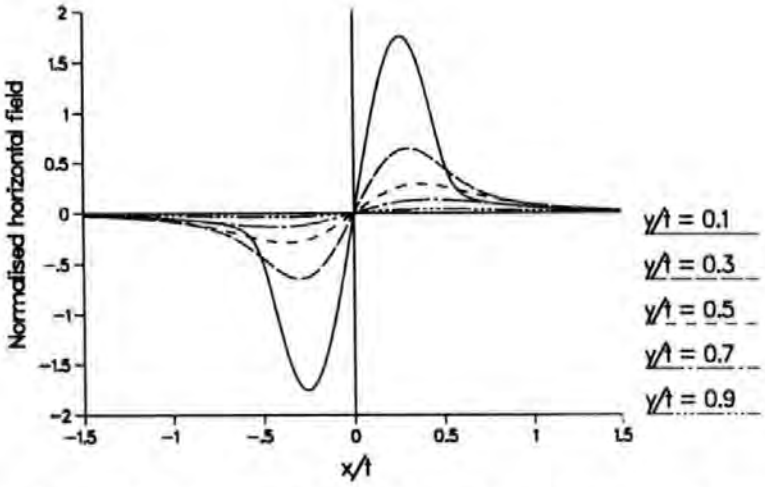

Figure 3.14: Horizontal field component for a single pole head with cosine-squared pole potential, $L/t = 0.5$.

3.1.4 Approximations

3.1.4.1 Introduction

The Karlqvist approximations (Section 2.1.4.2) were derived by assuming the potential drop across the gap of a ring head without an underlayer, in the head face plane, is linear. Across the poles the potential is constant at $\pm V$, therefore using the Poisson integral (2.61), the potential at any point in the plane $y \geq 0$ can be approximated. With such a simple approximation to the potential in the gap, the integral may be perfomed analytically to give relatively simple explicit formulae for the potential and the field components everywhere else. However, in the case of an underlayer being

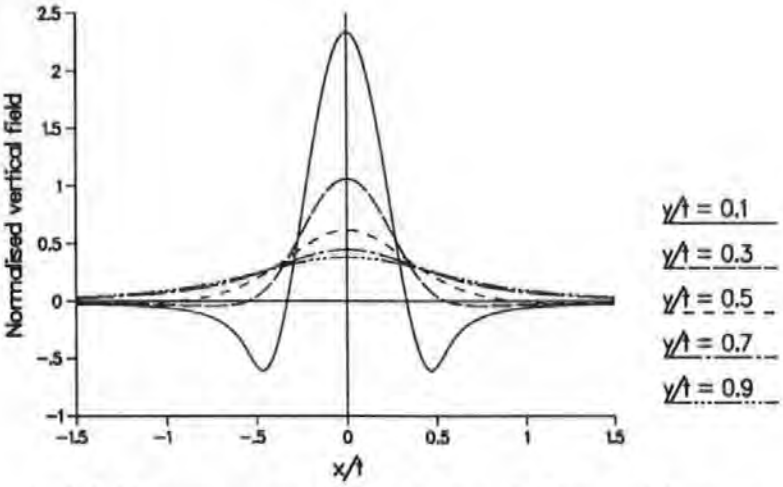

Figure 3.15: Vertical field component for a single pole head with cosine-squared pole potential, $L/t = 0.5$.

present, the Poisson integral (2.61) is not valid, and here the appropriate integral [37] is

$$\varphi(x,y) = \frac{1}{2t}\sin\left(\frac{\pi y}{t}\right)\int_{-\infty}^{\infty}\frac{\varphi(u,0)}{\cosh\left((u-x)\pi/t\right)-\cos(\pi y/t)}\,du\,, \tag{3.87}$$

for $0 < y \leq t$, which reduces to the Poisson integral as $t \longrightarrow \infty$. This integral is normally sufficiently complicated for numerical integration to be neccessary.

Only the Fourier solutions for the conventional single pole head with an underlayer (Section 2.1.3.2) and for the classic ring head without an underlayer (Section 2.1.3.3) can be evaluated without at least some numerical integration. A good analytic approximation to $\varphi(x,0)$ permits accurate estimation of $\varphi(x,y)$ using equn. (3.87), which requires only one numerical integration per field point in comparison with a large number generally needed for the full exact solution. For the field components, (3.87) may be differentiated prior to the integration.

Clearly, using the best possible approximation to the potential in the head face plane in the integral (3.87), produces the most accurate results. Here good approximations to the potential at $y = 0$ are derived from the exact Fourier solutions for: thin film heads with both constant and linearly varying pole potentials, single pole heads with various pole potentials and the symmetrically shielded pole, all in the presence of an underlayer. No Fourier coefficients need be known, which further reduces the computational difficulty.

These approximations are used to compute approximate field components for each type of head. Both the horizontal and the vertical field components are considered for the thin film heads, but for the single pole-type heads which are designed specifically for perpendicular recording, examples are provided for the vertical component only, although results of similar accuracy can be obtained for the horizontal component also.

3.1.4.2 The thin film head

The leading terms of the potential function at $y = 0$ for a thin film head with constant potential poles, from equns. (3.8), (3.3) and (3.11) provide the approximation to the normalised potential which is marked by the additional superscript a

$$\frac{\varphi^{aC}(x,0)}{V} = \begin{cases} 2Q_0^{TF}/\pi & 0 \leq x \leq g \\ 1 & g \leq x \leq g+2L \\ 2I_0^{TF}/\pi & g+2L \leq x < \infty \end{cases} \tag{3.88}$$

where, Q_0^{TF} at $y = 0$, evaluated using contour integration [80], is

$$\begin{aligned} Q_0^{TF} &= \int_0^\infty \frac{\sin^2(k)}{k^2}\frac{\sinh(kx/t)}{\sinh(kg/t)}\,dk \\ &= \frac{\pi x}{2g} + \frac{g}{2\pi t}\sum_{n=1}^{\infty}(-1)^n\frac{(1-e^{-2n\pi t/g})}{n^2}\sin\left(\frac{n\pi x}{g}\right) \end{aligned} \tag{3.89}$$

and I_0^{TF}, integrated explicitly at $y = 0$ [81], is

$$I_0^{TF} = \int_0^\infty \frac{\sin^2(k)}{k^2}e^{-kx^*}\,dk$$

$$= \arctan\left(\frac{2}{x^*}\right) - \frac{x^*}{4}\ln\left[1 + \left(\frac{2}{x^*}\right)^2\right] \tag{3.90}$$

where $x^* = (x - g - 2L)/t$.

A single term approximation to Q_0^{TF} is derived from a Padé approximation [82] of the form $a/(k^2 + b)$ to $\sinh(kx/t)/\sinh(kg/t)$. The form of the Padé approximation is chosen as the graph of the ratio of sinh terms has an approximate 'bell-shape'. Hence

$$Q_0^{TF} \approx \int_0^\infty \frac{\sin^2(k)}{k^2}\left(\frac{6xt^2}{6t^2 g + k^2 g(g^2 - x^2)}\right) dk \tag{3.91}$$

which can be integrated exactly [81] to give, with the superscript a denoting an approximation:

$$Q_0^{aTF} = \frac{x}{g}\left[1 - \frac{1}{2t}\sqrt{\frac{g^2 - x^2}{6}}\left(1 - e^{-2t\sqrt{6/(g^2-x^2)}}\right)\right]. \tag{3.92}$$

Yeh [63] has provided the only other published analytic approximation to the potential in the head face plane, for the constant potential thin film head in the presence of an underlayer. It assumes a linear potential drop across the gap and for $x > g + 2L$ it is based on the equivalence, as L increases, with a ring head without an underlayer discussed in Section 3.1.1.2 and illustrated in Fig. 3.2. For small t and $x \geq g + 2L$ a Taylor series expansion of $\varphi^R(x, 0)$ about the line $y = t$, together with the Karlqvist approximation for the H_x field of a ring head gives:

$$\frac{\varphi^{aYeh}(x,0)}{V} = \begin{cases} x/g & 0 \leq x \leq g \\ 1 & g \leq x \leq g + 2L \\ 2\arctan\left(t/(x - g - 2L)\right)/\pi & g + 2L \leq x < \infty\,. \end{cases} \tag{3.93}$$

It is not clear why the leading term in the well-known Fourier solution for the potential of a ring head (2.16) was not taken to give directly an approximation to $\varphi^C(x, 0)$ for

$x \geq g+2L$, thus avoiding the additional approximation inherent in a truncated Taylor series.

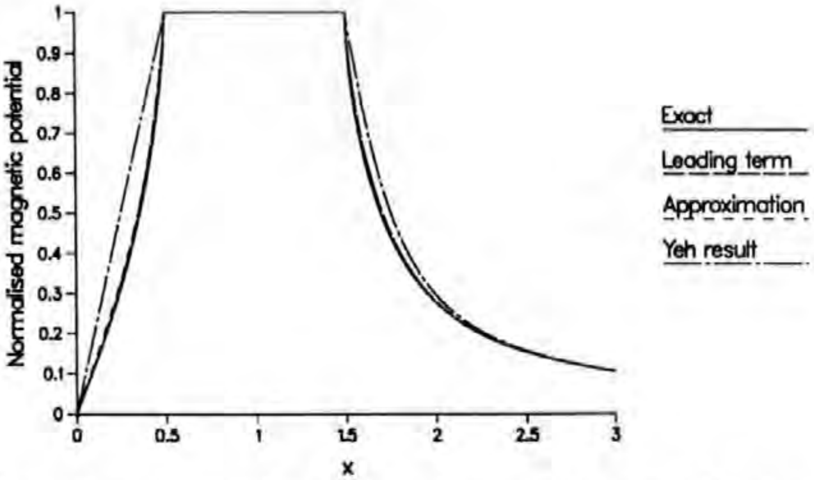

Figure 3.16: Approximations to the normalised magnetic potential at $y = 0$, for a thin film head with constant pole potential, when $g = L = 0.5$ and $t = 0.25$.

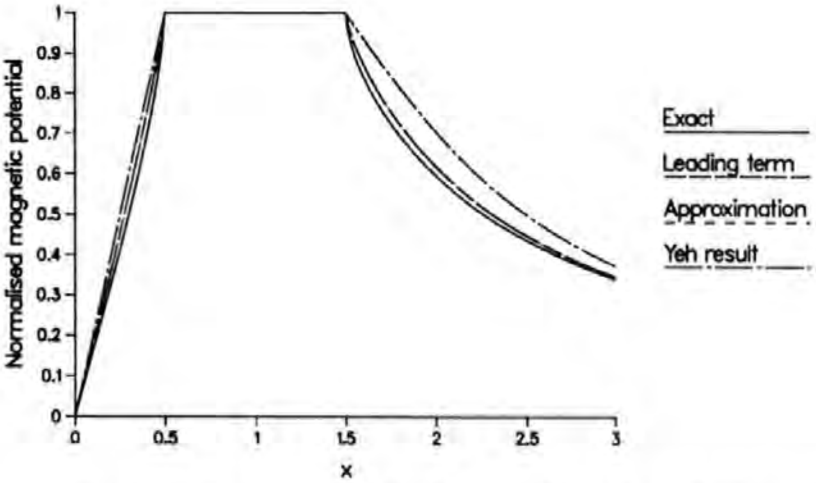

Figure 3.17: Approximations to the normalised magnetic potential at $y = 0$, for a thin film head with constant pole potential, when $g = L = 0.5$ and $t = 1.0$.

Figs. 3.16 and 3.17 show a comparison of the exact potential at $y = 0$ with Yeh's approximation (3.93) and with the approximation proposed here (3.88), for $g = L = 0.5$ and the underlayer at $t = 0.25$ and $t = 1.0$ respectively. In the gap region $0 \leq x \leq g$ both $2Q_0^{TF}/\pi$ (the exact leading term) and $2Q_0^{aTF}/\pi$ (the approximate leading term) are shown although they are almost indistinguishable. For $t = 0.25$ the leading term is seen to be a very good approximation to the full exact solution. Yeh's approximation is reasonable for $x \geq g+2L$ but the linear approximation in the gap $0 \leq x \leq g$ is seen to be poor. As the pole – underlayer separation increases, the present approximation does deterioriate, but it remains significantly better than Yeh's approximation, particularly beyond the pole edge.

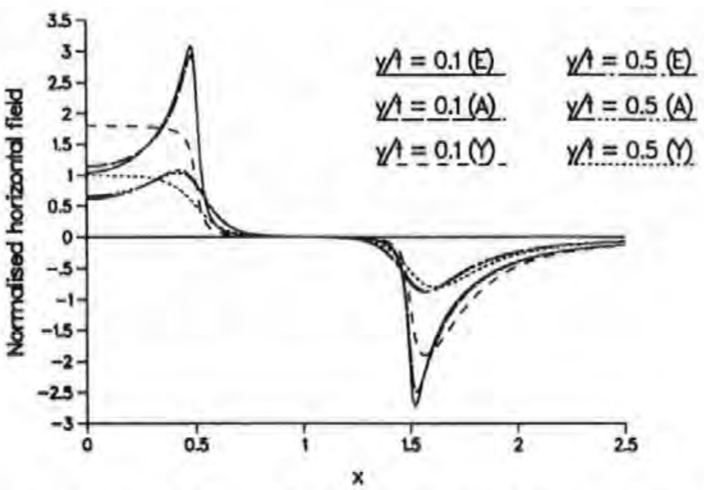

Figure 3.18: Comparison of the exact horizontal field (E-curves) for a thin film head with constant potential poles, with the leading term approximation (A-curves) and the Yeh approximation (Y-curves), $g = L = 0.5$ and $t = 0.25$.

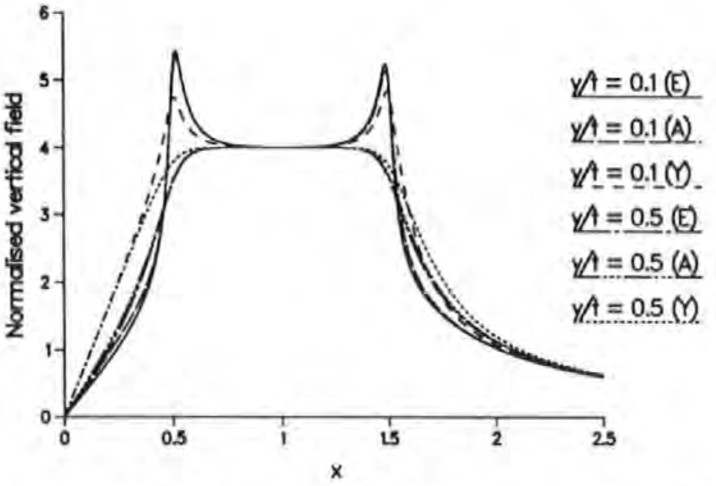

Figure 3.19: Comparison of the exact vertical field (E-curves) for a thin film head with constant potential poles, with the leading term approximation (A-curves) and the Yeh approximation (Y-curves), $g = L = 0.5$ and $t = 0.25$.

For $t = 0.25$ the corresponding field components are shown in Figs. 3.18 and 3.19. In the gap the approximate leading term $2Q_0^{aTF}/\pi$ is used. The leading term alone of the Fourier solution results in a very good approximation to the exact solution everywhere. For the horizontal field close to each pole the approximation of [63] fails to predict the peak at the inner edge of the pole and significantly underestimates the peak at the outer edge of the pole. This is similar to the problem with the Karlqvist approximation to the horizontal component in the case of a ring head without an underlayer shown in Fig. 2.8. For the vertical field, approximation φ^{aYeh} is better but underestimates the peaks and the field gradients at the pole edges. Figs. 3.20 and 3.21 show similar results for the underlayer at $t = 1.0$. At the same relative distances from the poles, approximation φ^{aYeh} performs better than when $t = 0.25$ because, as can be seen in Fig. 3.17 the correct gap potential is more nearly linear. As g/t increases the horizontal field in the gap is less well predicted close to the poles using φ^{aC}, but φ^{aC} is always an improvement over φ^{aYeh}. However, the vertical field continues to be accurately approximated using φ^{aC}.

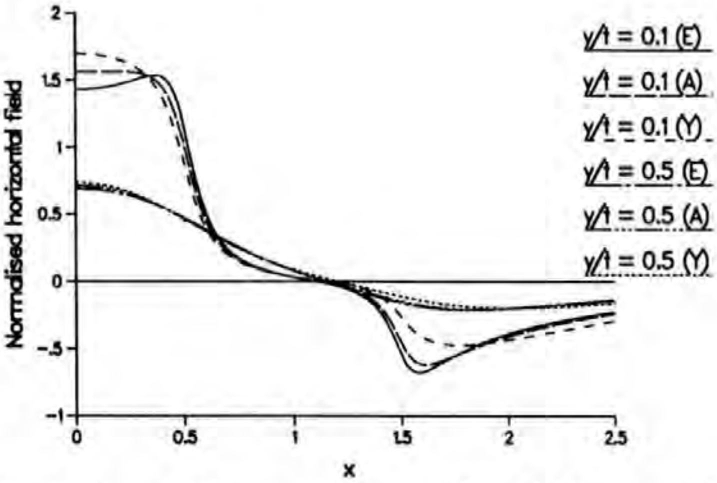

Figure 3.20: Comparison of the exact horizontal field (E-curves) for a thin film head with constant potential poles, with the leading term approximation (A-curves) and the Yeh approximation (Y-curves), $g = L = 0.5$ and $t = 1.0$.

For the case where the pole potential varies linearly, the leading term of the potential for $0 \leq x \leq g$ is the same as that for the constant pole potential case, hence the same approximate leading term in region A, $2Q_0^{TF}/\pi$, may be applied here also. For $x \geq g + 2L$ the leading term is zero. There are no other published approximations to the potential at $y = 0$ for this head geometry. Figs. 3.22 and 3.23 show comparisons of the leading term approximation with the exact magnetic potential at $y = 0$, for

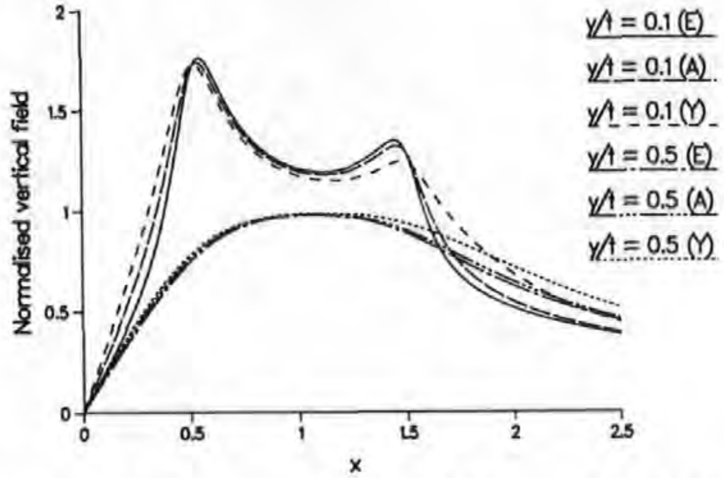

Figure 3.21: Comparison of the exact vertical field (E-curves) for a thin film head with constant potential poles, with the leading term approximation (A-curves) and the Yeh approximation (Y-curves), $g = L = 0.5$ and $t = 1.0$.

$g = L = 0.5$ and the underlayer at $t = 0.25$ and $t = 1.0$ respectively.

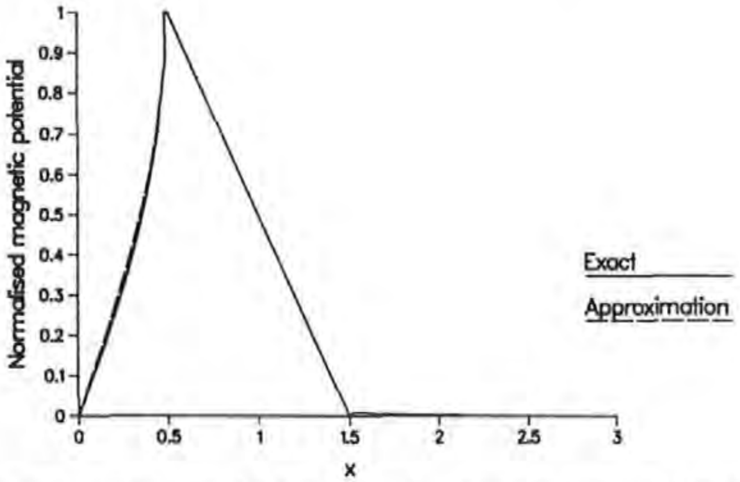

Figure 3.22: Approximations to the normalised magnetic potential at $y = 0$, for a thin film head with linearly varying pole potential, when $g = L = 0.5$ and $t = 0.25$.

Here, as in the constant pole potential case, the approximation improves as the head – underlayer separation decreases. The term $2Q_0^{TF}/\pi$ approximates the potential at $y = 0$ in region A less accurately for a linear pole potential than it does for the constant pole potential thin film head.

The corresponding horizontal and vertical field components when $t = 1.0$, are shown in Figs. 3.24 and 3.25 respectively. In each case the exact leading term $2Q_0^{TF}/\pi$ has been used. The accuracy of the approximation is very similar to that obtained in the

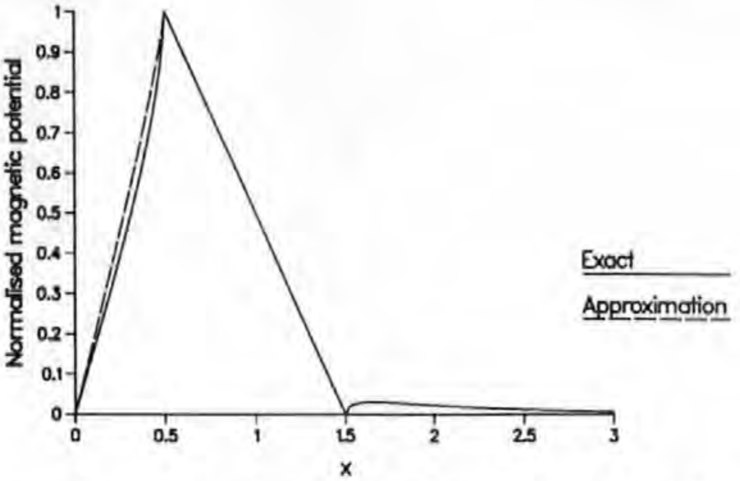

Figure 3.23: Approximations to the normalised magnetic potential at $y = 0$, for a thin film head with linearly varying pole potential, when $g = L = 0.5$ and $t = 1.0$.

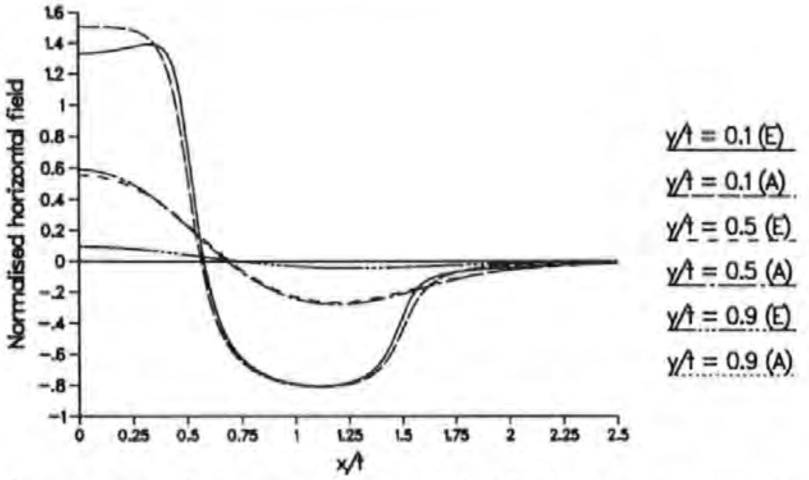

Figure 3.24: Comparison of the exact horizontal field (E-curves) with the leading term approximation (A-curves) for a thin film head with linearly varying pole potential, $g = L = 0.5$ and $t = 1.0$.

constant pole potential case.

3.1.4.3 The single pole head

No published approximations to the potential in the pole face plane for a conventional constant potential single pole head are known of in the literature. Here, the leading terms of the magnetic potential from the exact Fourier solution given in (2.5)

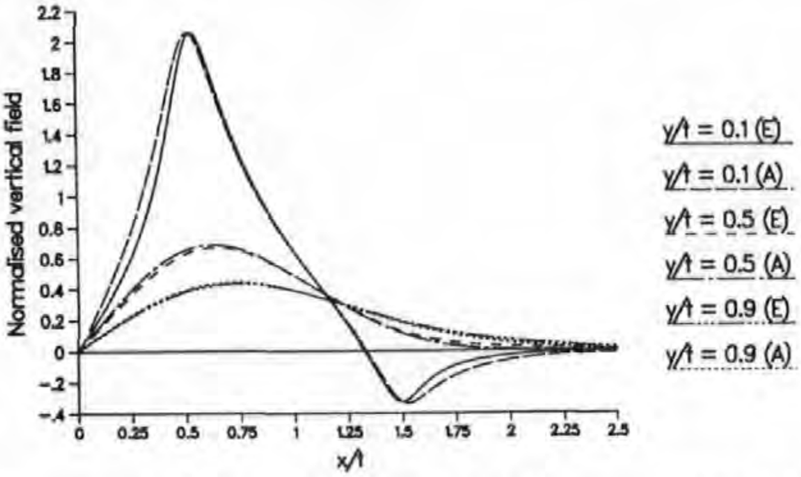

Figure 3.25: Comparison of the exact vertical field (E-curves) with the leading term approximation (A-curves) for a thin film head with linearly varying pole potential, $g = L = 0.5$ and $t = 1.0$.

and (2.8) are taken, so that

$$\frac{\varphi^{aP}(x,0)}{V} = \begin{cases} 1 & 0 \le |x| \le L \\ 2I_0^P/\pi & L \le |x| < \infty \end{cases} \tag{3.94}$$

where I_0^P is given exactly by equn. (3.90) with $x^* = (x - L)/t$.

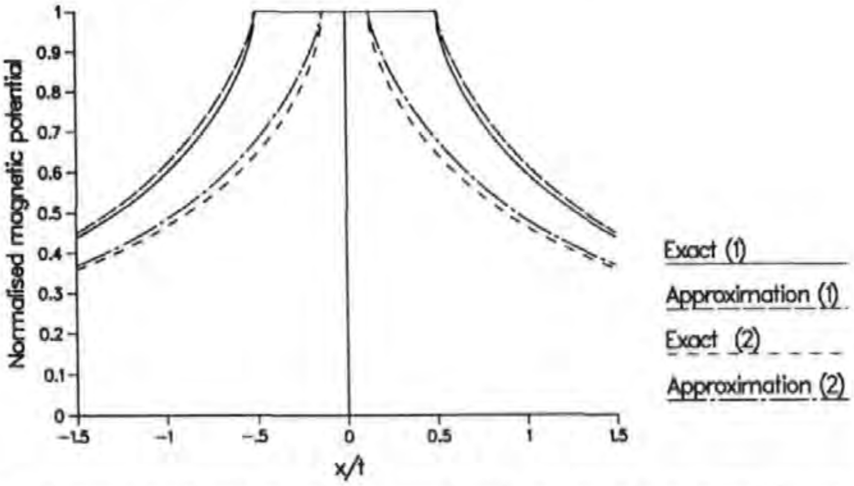

Figure 3.26: Approximations to the normalised magnetic potentials at $y = 0$, for conventional single pole heads with constant pole potential, when $L/t = 0.5$ (1-curves) and $L/t = 0.125$ (2-curves).

Fig. 3.26 shows a comparison of the approximation $\varphi^{aP}(x,0)/V$ with the exact potential for two pole dimensions, $L/t = 0.5$ and $L/t = 0.125$. For $L/t = 0.125$ the approximation is seen to be reasonable and it improves as L/t increases.

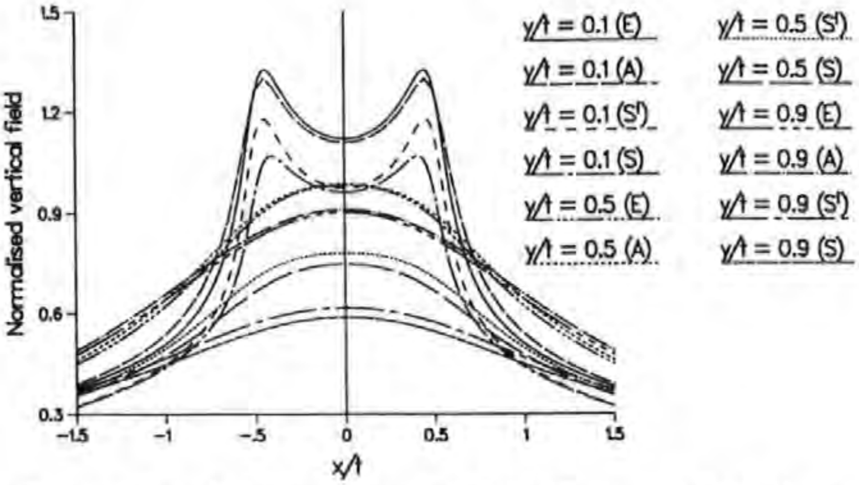

Figure 3.27: Comparison of the exact vertical field (E-curves) with the new approximation (A-curves), Szczech's approximation with adjusted pole width (S′-curves) and Szczech's approximation with the exact pole width (S-curves) for a conventional single pole head, $L/t = 0.5$.

Approximations to the field components at $y = 0$ have been given by Szczech *et al.* in [83].These approximations were derived from a conformal mapping solution and fitted to experimental results from a large scale model. A better fit to the experimental results was obtained by using a pole width 1.035% greater than the measured dimension in the approximation. This semi-empirical approximation to the vertical field component is:

$$\frac{H_y^{aS}(x,0)}{H_y(0,0)} = \begin{cases} \left(C_3 + \frac{4L^2C_2}{4L^2C_4^2 - x^2}\right) & 0 \leq |x| \leq L' \\ \left(\frac{2LC_1}{x+2LC_0}\right) & |x| \geq L' \end{cases} \tag{3.95}$$

Formulae for the coefficients C_{1-4} are given in [83]. (3.95) has been evaluated using both the exact ($L' = L$) and the adjusted pole width ($L' = 1.035L$), and is shown in Fig. 3.27 with the new approximation and the exact vertical field component, all for $L/t = 0.5$. At each height shown, the Szczech approximation significantly underestimates the theoretical vertical field although using the adjusted pole width does give slightly better results. The new approximation is very accurate.

The same strategy can be applied to a single pole with linearly varying pole potential. Taking the leading terms of the magnetic potential obtained in Section 3.1.2, at $y = 0$, the approximation

$$\frac{\varphi^{aLP}(x,0)}{V} = \begin{cases} 0 & -\infty < x \leq -L \\ (x+L)/2L & -L \leq x \leq L \\ 2I_0^P/\pi & L \leq x < \infty \end{cases} \tag{3.96}$$

where I_0^P is given by equn. (3.90) with $x^* = (x-L)/t$.

Approximations to the potential in the pole face plane can also be derived from the solution for the single pole head with arbitrary pole potential given in Section 3.1.3. Clearly it is desirable to eliminate the need to compute the dimension dependent Fourier coefficients, $B_n^{AP'}$ and $D_n^{AP'}$. Taking the leading terms only *ie.* those involving T_0 and U_0, in equns. (3.62) and (3.67) gives a less accurate approximation to the potential at $y = 0$ for a single pole with linearly varying pole potential than that defined by (3.96). When only the series involving the coefficients B_n^{AP} and D_n^{AP} is omitted from each of equns. (3.62) and (3.67) an excellent approximation is obtained. This second approximation, in the general form for an arbitrary pole potential, is

$$\frac{\varphi^{aAP}(x,0)}{V} = \begin{cases} \frac{2}{\pi}\left\{\frac{a_0}{2}T_0 + \left(\alpha - \frac{a_0}{2}\right)U_0 \right. & \\ \quad \left. + \sum_{N=1}^{\infty}\left[a_N\cos\left(\frac{N\pi}{2}\right) - b_N\sin\left(\frac{N\pi}{2}\right)\right]\eta_N\right\} & -\infty < x \leq -L \\ f(x) & -L \leq x \leq L \\ \frac{2}{\pi}\left\{\frac{a_0}{2}T_0 + \left(\beta - \frac{a_0}{2}\right)U_0 \right. & \\ \quad \left. + \sum_{N=1}^{\infty}\left[a_N\cos\left(\frac{N\pi}{2}\right) + b_N\sin\left(\frac{N\pi}{2}\right)\right]\eta_N\right\} & L \leq x < \infty \end{cases} \tag{3.97}$$

where η_N is given by (3.63) and T_N and U_N are given by (3.65) and (3.66) respectively and the closed forms are given in Sections A.3.4 and A.3.5 respectively.

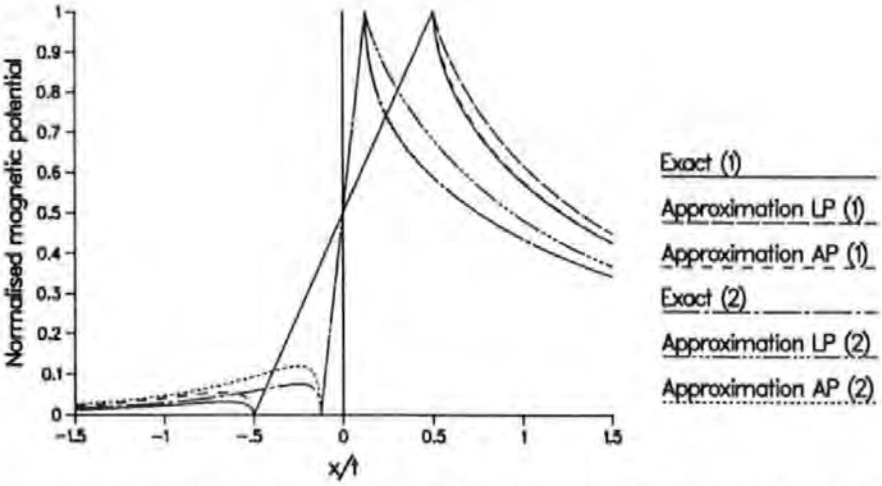

Figure 3.28: Approximations to the normalised magnetic potentials at $y = 0$, for single pole heads with linearly varying pole potential, when $L/t = 0.5$ (1-curves) and $L/t = 0.125$ (2-curves).

Fig. 3.28 compares both approximations with the exact potential at $y = 0$ for a single pole with linear pole potential distribution. Clearly φ^{aAP} is a much better approximation than φ^{aLP}, for $x > L$, but it is computationally more expensive. For $x < -L$, the approximation φ^{aAP} overestimates the potential so that, as the magnitude of the potential in region A is small, approximating the potential by zero, as in φ^{aLP}, provides a simplification, φ_0^{aAP}, with little loss of accuracy.

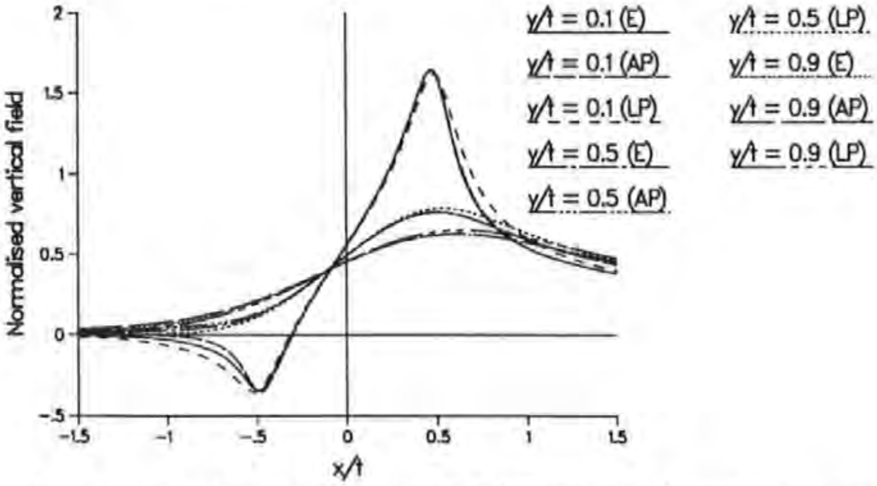

Figure 3.29: Comparison of the exact vertical field (E-curves) with the approximations (LP-curves) and (AP-curves) for a single pole head with linear pole potential, $L/t = 0.5$.

The corresponding approximate vertical field components are shown in Fig. 3.29. The accuracy of the approximation to the potential in a particular region (as defined in

Fig. 3.7) strongly influences the accuracy of the field component estimate in the same region. Hence both approximations are good in region B but using φ^{aAP} provides the better approximation in regions B and C. The approximation *via* φ^{aLP} underestimates the magnitude of the peak when $y/t = 0.1$ and overestimates the peaks farther from the pole. It also predicts that the peaks occur slightly too far from the pole edge. In region A, using φ^{aLP} gives only marginally less accurate results than using φ^{aAP} which is computationally much more expensive.

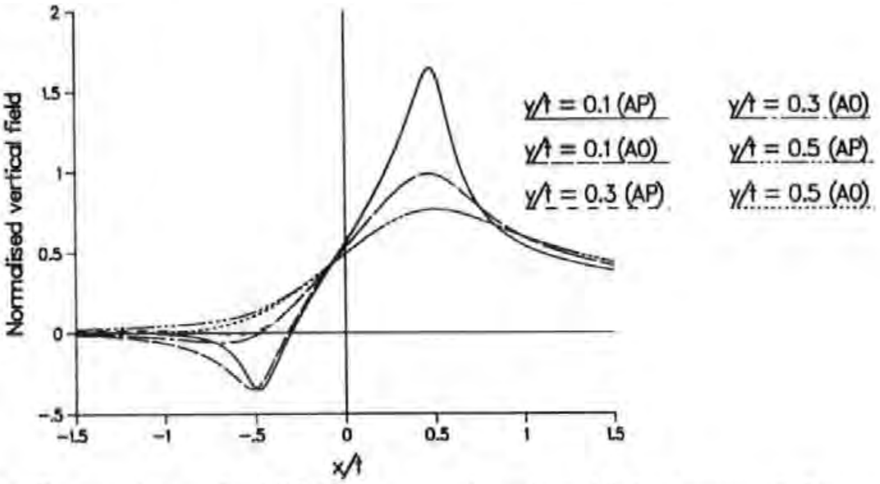

Figure 3.30: Comparison of φ^{aAP} (AP-curves) and φ_0^{aAP} (A0-curves) for a single pole head with linear pole potential, $L/t = 0.5$.

Fig. 3.30 shows the effect of simplifying φ^{aAP} by approximating the potential in region A by zero. For $x \geq 0$ the difference is negligible. For $x < 0$, the simplified approximation is marginally less accurate than φ^{aAP}, underestimating the magnitude of the vertical field component where φ^{aAP} overestimates it.

For single poles with potential distributions other than linear or constant, it is interesting to note that if it were possible to solve Laplace's equation in region B without expressing the pole potential distribution $f(x)$ as a Fourier series, the leading term of the potential in region A would be zero if $\alpha = 0$ or it would be the same as that for a constant potential pole if $\alpha = 1$. The same leading terms would occur in region C depending whether $\beta = 0$ or $\beta = 1$. Therefore the approximation given in

(3.96) can be generalised to:

$$\frac{\varphi^{aGP}(x,0)}{V} = \begin{cases} 2\alpha\left\{\arctan\left(\frac{2}{x^*}\right) - \frac{x^*}{4}\ln\left[1+\left(\frac{2}{x^*}\right)^2\right]\right\}\Big/\pi & -\infty < x \leq -L \\ f(x) & -L \leq x \leq L \\ 2\beta\left\{\arctan\left(\frac{2}{x^*}\right) - \frac{x^*}{4}\ln\left[1+\left(\frac{2}{x^*}\right)^2\right]\right\}\Big/\pi & L \leq x < \infty \end{cases} \tag{3.98}$$

where $x^* = (|x| - L)/t$.

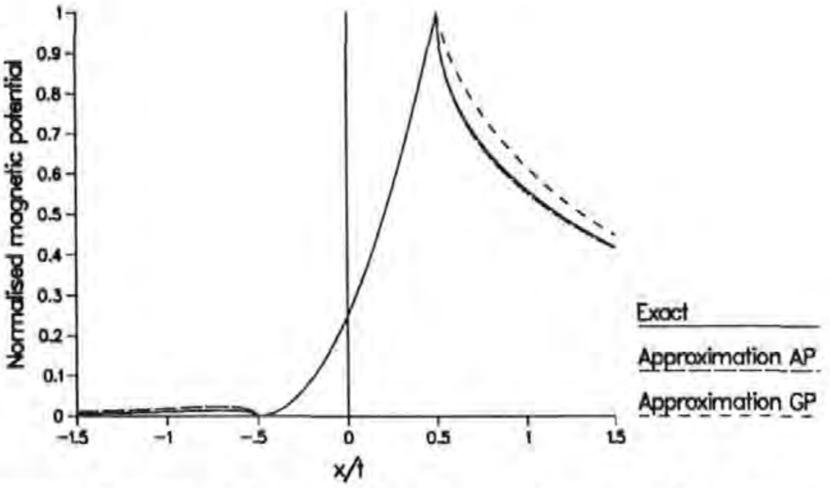

Figure 3.31: Approximations to the normalised magnetic potentials at $y = 0$, for single pole heads with quadratic pole potential, $L/t = 0.5$.

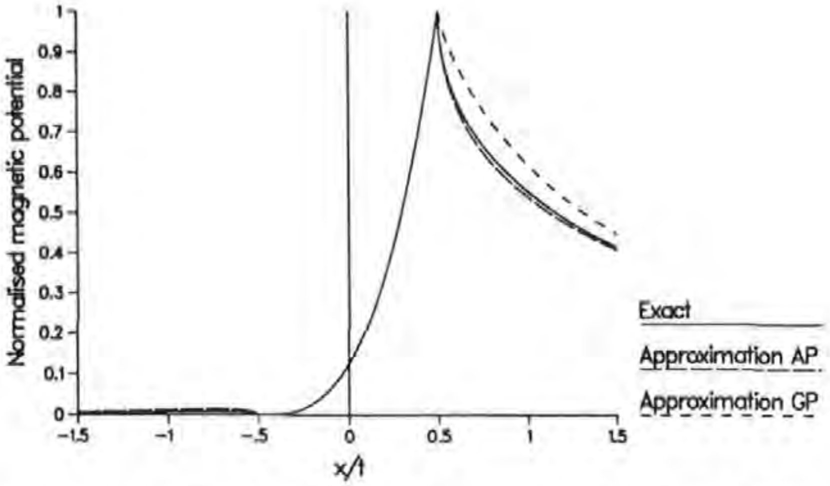

Figure 3.32: Approximations to the normalised magnetic potentials at $y = 0$, for single pole heads with cubic pole potential, $L/t = 0.5$.

Figs. 3.31 and 3.32 compare the constant potential leading term φ^{aGP} (3.98) and φ^{aAP} (3.97) with the exact potential at $y = 0$ for single pole heads with quadratic and cubic potential distributions, when $L/t = 0.5$, as defined in Section 3.1.3, respectively. For these pole potentials where $\alpha = 0$ and $\beta = 1$ the accuracy of both φ^{aAP} and φ^{aGP} decrease slightly as the potential in region B becomes less uniform but φ^{aAP} remains considerably more accurate then φ^{aGP} for $x > L$.

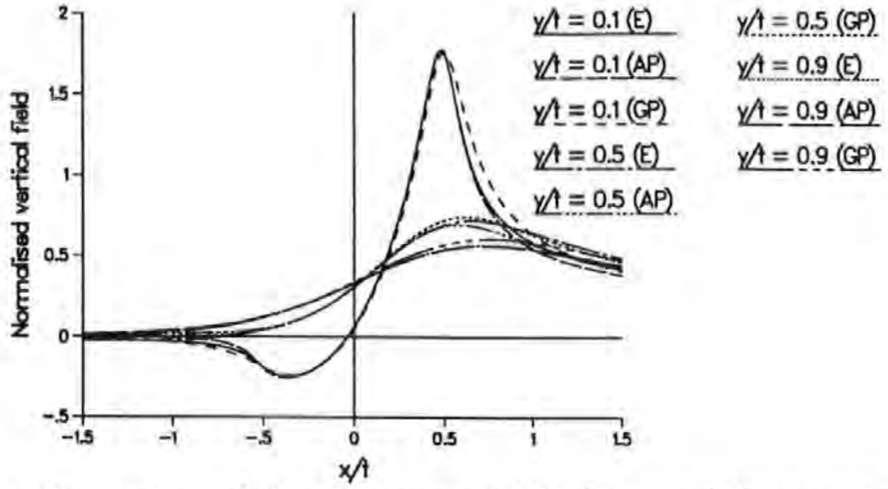

Figure 3.33: Comparison of the exact vertical field (E-curves) for a single pole with quadratic pole potential with the approximations (AP-curves) and (GP-curves), $L/t = 0.5$.

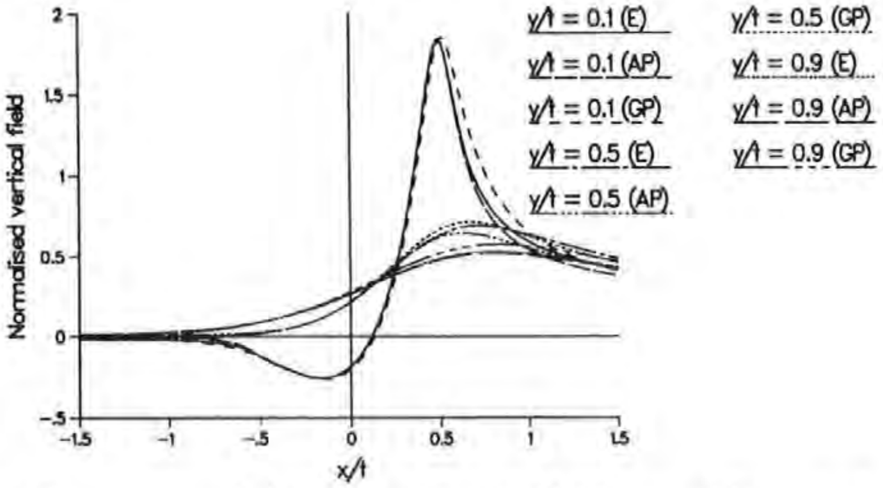

Figure 3.34: Comparison of the exact vertical field (E-curves) for a single pole with cubic pole potential with the approximations (AP-curves) and (GP-curves), $L/t = 0.5$.

The corresponding vertical field components are shown in Figs. 3.33 and 3.34. In each case, the approximation *via* φ^{aAP} is extremely accurate, showing greatest error for $y/t = 0.5$ in region C. As the average potential across the pole (given by $a_0/2$ for each case) decreases the accuracy of the approximation obtained by using φ^{aGP} increases in region A. For the cubic pole potential, the approximation from φ^{aAP} overestimates the peak at $y/t = 0.1$ but underestimates the maxima farther from the pole; the opposite is true for the linear pole potential. The simplified approximation, φ_0^{aAP} (*ie.* taking the potential as zero for $x < -L$), for each of the quadratic and the cubic pole potentials, is only marginally less accurate than φ^{aAP}, as is the case of the linear pole potential (Fig. 3.30).

For the single pole with a cosine-squared potential distribution, $\alpha = \beta = 0$ so that

$$\frac{\varphi^{aGP}(x,0)}{V} = \begin{cases} \cos^2(\pi x/2L) & -L \leq x \leq L \\ \\ 0 & \text{elsewhere.} \end{cases} \tag{3.99}$$

In this case, $\varphi^{aGP} = \varphi_0^{aAP}$.

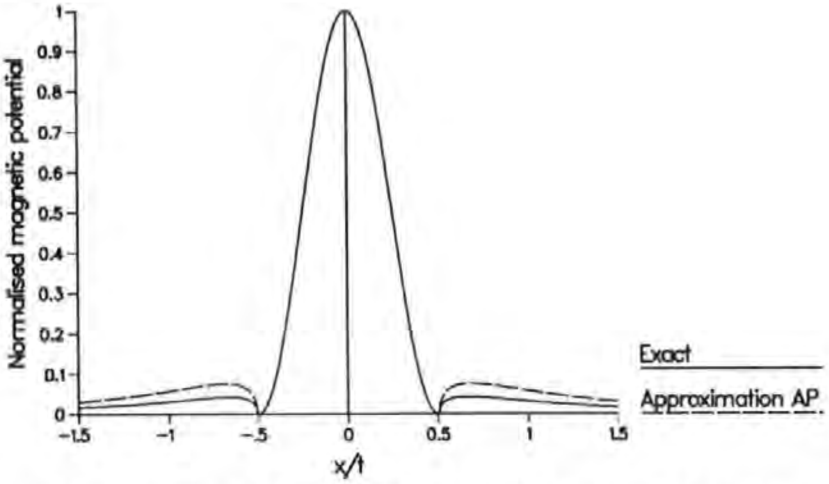

Figure 3.35: Approximations to the normalised magnetic potentials at $y = 0$, for single pole heads with cosine-squared pole potential, $L/t = 0.5$.

Fig. 3.35 compares both approximations with the exact potential at $y = 0$ for a single pole head with cosine-squared pole potential. The approximation φ^{aAP} overestimates the potential in regions A and C by about a factor of 2. Hence adopting the alternative approximation, φ^{aGP} given by (3.99), can be expected to provide results of similar accuracy to φ^{aAP} when employed in further calculations.

Both approximations have been used to estimate the vertical field component when

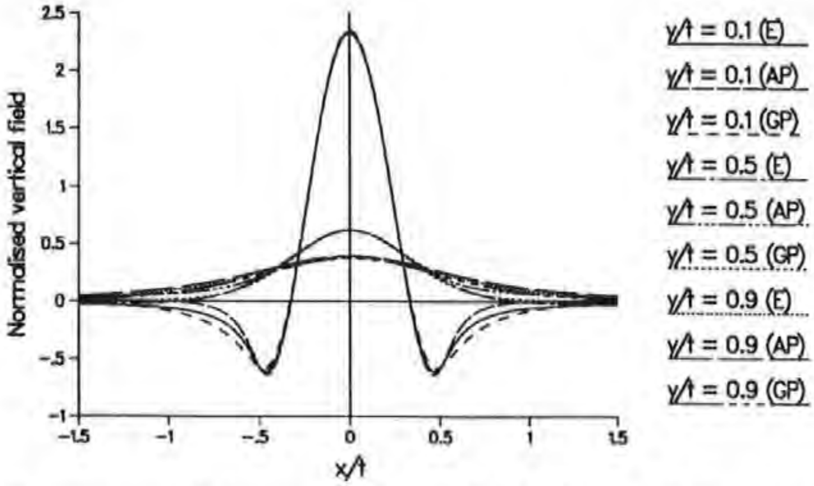

Figure 3.36: Comparison of the exact vertical field (E-curves) for a single pole with cosine-squared pole potential with the approximations (AP-curves) and (GP-curves), $L/t = 0.5$.

$L/t = 0.5$ and are shown in Fig. 3.36. As expected, there is little difference in accuracy between the two approximations. Both approximations require the numerical evaluation of one integral per field point. When φ^{aGP} is used the computation is over a finite interval but using φ^{aAP} the integral has infinite limits.

3.1.4.4 The symmetrically shielded pole head

No approximation to the potential in the head face plane was considered in [29]. From the two solutions given in Section 2.1.3.5 two different leading term approximations to the potential at $y = 0$ are possible. In each case the exact potential is taken over the pole and the shield faces so that when $\alpha = 0$

$$\frac{\varphi^{a\,\mathrm{I}\,/\,\mathrm{II}}}{V} = \frac{\varphi^{\mathrm{I}\,/\,\mathrm{II}}}{V} = \begin{cases} 1 & 0 \le x \le L \\ 0 & L + G \le x < \infty \, . \end{cases} \tag{3.100}$$

From Solution I (2.31) where $y = 0$ is the boundary between regions A and C, the leading term from either $\varphi_A^{\mathrm{I}}(x,0)$ or from $\varphi_C^{\mathrm{II}}(x,0)$ is linear so that

$$\frac{\varphi^{a\,\mathrm{I}}}{V} = \frac{L + G - x}{G} \qquad L \le x \le L + G \, . \tag{3.101}$$

From Solution II (2.42) the approximation

$$\frac{\varphi^{a\,\mathrm{II}}}{V} = \frac{2}{\pi} I_0^{\mathrm{II}} \qquad\qquad L \leq x \leq L+G \tag{3.102}$$

is obtained where

$$I_0^{\mathrm{II}} = \int_0^\infty \frac{\sin^2(k)}{k^2} \frac{\sinh(k(L+G-x)/t)}{\sinh(kG/t)}\, dk \tag{3.103}$$

which is of the same form as Q_0^{TF} (3.89) and hence can be integrated exactly or closely approximated as in (3.92). In both cases x is replaced by $(L+G-x)$ and g is replaced G.

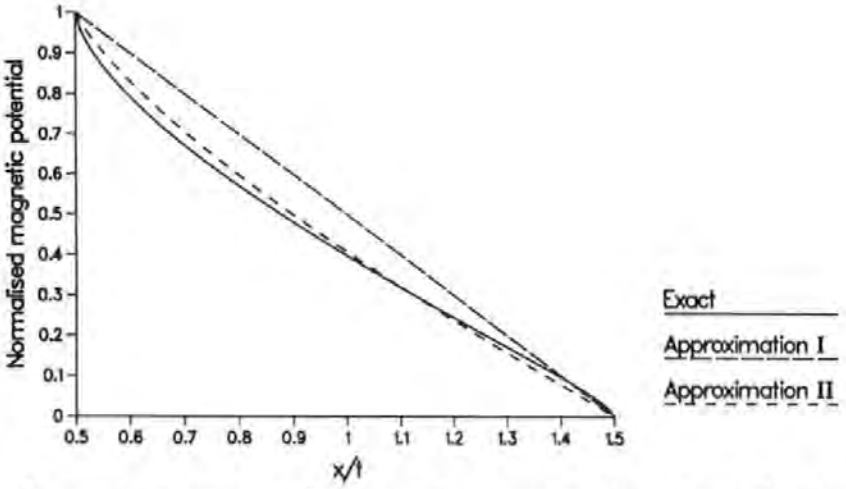

Figure 3.37: Approximations to the normalised magnetic potentials at $y = 0$, for symmetrically shielded pole heads, when $L/t = g/t = 0.5$.

Figs. 3.37 and 3.38 compare both of these approximations with the exact potential at $y = 0$, across the gap only. In Fig. 3.37 where $L/t = g/t = 0.5$ Approximation II ($\varphi^{a\,\mathrm{II}}$) is seen to be more accurate than the linear Approximation I. In Fig. 3.38 $L/t = 0.125$ and $g/t = 0.15$ so that the the head – underlayer separation has effectively increased by a factor of 4 over the case shown in Fig. 3.37 and the pole – shield gap has also increased by 20%. For these dimensions Approximation II is only slightly more accurate than the linear approximation. This is in agreement with the results given in

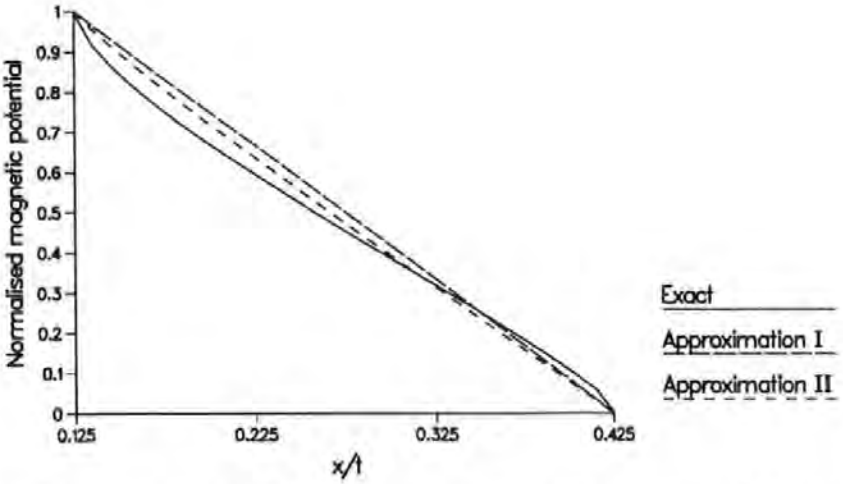

Figure 3.38: Approximations to the normalised magnetic potentials at $y = 0$, for symmetrically shielded pole heads when $L/t = 0.125$ and $g/t = 0.15$.

[29]. There the leading term of the vertical field component *via* Solution I (2.39) was taken as an approximation to the vertical field component. Substituting $\varphi^{a\,\mathrm{I}}(x,0)$ into (3.87) and differentiating with respect to y provides the same approximation to the vertical field component. The accuracy of the approximation was found to improve as g/t decreased.

3.2 Conformal Mapping

3.2.1 The Symmetrically Shielded Magnetoresistive Head

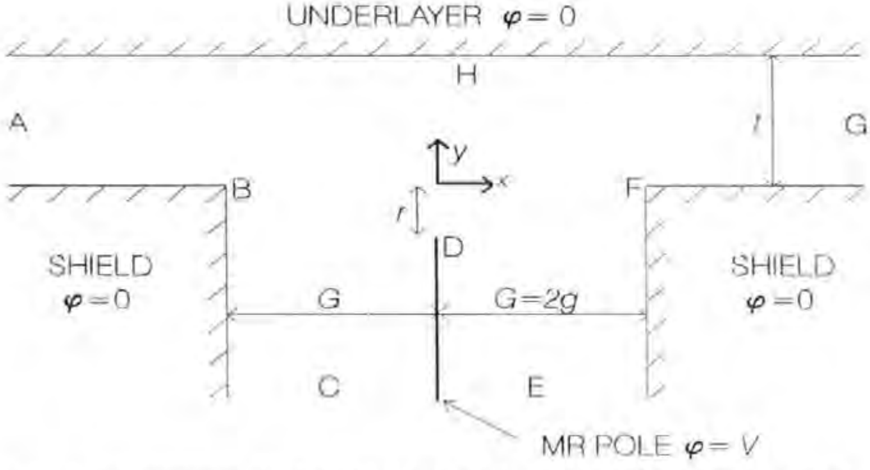

Figure 3.39: Idealised symmetrically shielded and recessed MR sensor in the z-plane.

Fig. 3.39 shows the idealised 2-dimensional model of a symmetrically shielded magnetoresistive (MR) sensor. All of the assumptions listed in Section 2.1.3.1 apply to this model. MR sensors are very thin compared with the length of their shields and therefore here they are assumed to be infinitely thin. This modelling assumption has previously been applied in [44]. An infinitely thin MR pole is placed a distance G from each of two shields and is recessed a distance r from the shield faces. The shields at zero potential, are assumed to extend to infinity in the negative y direction, be infinitely wide and semi-infinitely long and are separated from the underlayer by a distance t. The magnetic potential satisfies Laplace's equation in the region exterior to the pole, shields and the underlayer in the complex z-plane ($z = x + iy$).

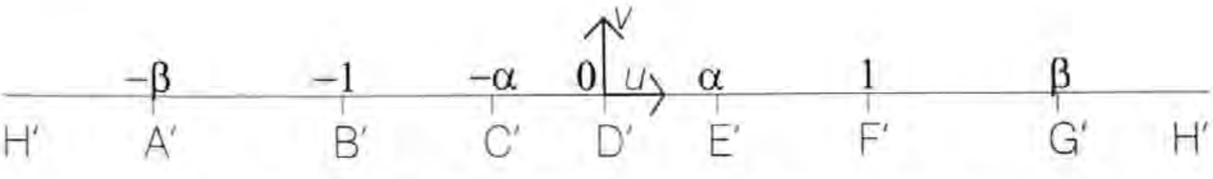

Figure 3.40: The complex w-plane in the symmetric case.

The Schwarz-Christoffel transformation which conformally maps this region to the upper half of the complex w-plane with points A–H shown in Fig. 3.39 mapping to A'–H' respectively, as shown in Fig. 3.40, is defined by

$$\frac{dz}{dw} = \frac{S^S w(w^2-1)^{\frac{1}{2}}}{(w^2-\alpha^2)(w^2-\beta^2)} \tag{3.104}$$

where the superscript S denotes the symmetric case. The pole tip D ($z = -ir$) maps to the origin $w = 0$ and due to symmetry the shield corners B and F ($z = \mp G$) map to $w = \mp 1$ respectively. The points α and β in the w-plane, and the constants S^S and z_0^S (appearing in (3.105) below) are determined by matching boundary values. The point H on the underlayer surface in the z-plane ($z = it$) which maps to the point at infinity in the w-plane does not occur in (3.104). Integrating [81] gives

$$z = \frac{S^S}{\beta^2 - \alpha^2} \left\{ \sqrt{1-\alpha^2} \arctan\left[\frac{\sqrt{w^2-1}}{\sqrt{1-\alpha^2}}\right] + \frac{\sqrt{\beta^2-1}}{2} \ln\left[\frac{\sqrt{w^2-1} - \sqrt{\beta^2-1}}{\sqrt{w^2-1} + \sqrt{\beta^2-1}}\right] \right\} + z_0^S \, . \tag{3.105}$$

The constant S^S is found by matching the geometries of the two planes. There is a jump at the point $z = (G/2, -\infty)$ which corresponds to $w = \alpha$ so that applying the method of residues [32, Section 8.2.5]

$$\int_g^0 dz = S^S i \int_0^\pi \frac{\alpha\sqrt{\alpha^2-1}}{2\alpha(\alpha^2-\beta^2)} \, d\theta \, . \tag{3.106}$$

Similarly at $w = \beta$

$$\int_{it}^0 dz = S^S i \int_0^\pi \frac{\beta\sqrt{\beta^2-1}}{2\beta(\beta^2-\alpha^2)} \, d\theta \, , \tag{3.107}$$

giving

$$S^S = \frac{-2G(\beta^2-\alpha^2)}{\pi\sqrt{1-\alpha^2}} \qquad \text{and} \qquad S^S = \frac{-2t(\beta^2-\alpha^2)}{\pi\sqrt{\beta^2-1}} \tag{3.108}$$

respectively, from which it follows that

$$\frac{\sqrt{1-\alpha^2}}{\sqrt{\beta^2-1}} = \frac{G}{t} . \tag{3.109}$$

Evaluating (3.105) at $w = 1$ and $w = 0$ where $z = -ir$ and $z = G$ respectively gives

$$z_0^S = G + it \tag{3.110}$$

and

$$G + i(t+r) = \frac{2G}{\pi} \arctan\left[\frac{it}{G\sqrt{\beta^2-1}}\right] + \frac{t}{\pi} \ln\left[\frac{i - \sqrt{\beta^2-1}}{i + \sqrt{\beta^2-1}}\right] \tag{3.111}$$

Hence

$$z = G + it - \frac{2G}{\pi}\arctan\left[\frac{t\sqrt{w^2-1}}{G\vartheta}\right] - \frac{t}{\pi}\ln\left[\frac{\sqrt{w^2-1}-\vartheta}{\sqrt{w^2-1}+\vartheta}\right] \tag{3.112}$$

where $\vartheta = \sqrt{\beta^2-1}$ satisfies

$$\ln\left[\frac{i-\vartheta}{i+\vartheta}\right] + \frac{2G}{t}\arctan\left[\frac{it}{G\vartheta}\right] - \pi r - i\pi = 0 \tag{3.113}$$

which simplifies to the real equation

$$G\ln\left[\frac{t-G\vartheta}{t+G\vartheta}\right] + 2t\arctan\left[\frac{1}{\vartheta}\right] + \pi r = 0\ . \tag{3.114}$$

Then $\beta = \sqrt{1+\vartheta^2}$, $\alpha = \sqrt{1-(G\vartheta/t)^2}$, and $S^S = -2\vartheta(G^2+t^2)/(\pi t)$. The solution of (3.114), which depends only on the ratio G/t, is easily found by, say, the Newton-Raphson method (2.60) using an initial value $w_0 < 1/r$.

For this solution with arctan evaluated as

$$\arctan(p) = \frac{1}{2i}\ln\left(\frac{1+ip}{1-ip}\right) \tag{3.115}$$

(as is required in the FORTRAN language which does not support a complex arctan function) and with $\sqrt{w^2-1}$ evaluated as $\sqrt{w-1}\sqrt{w+1}$, consideration of the branch cuts requires that π be added to the principal value given by the logarithmic evaluation of the arctan term in (3.112) for all points with $\text{Re}(w) < 0$, except those on the real axis such that $-\alpha < \text{Re}(w) < 0$. This ensures that (3.112) is valid for all w such that $\text{Im}(w) \geq 0$, *i.e.* the upper half plane and the real axis.

In the upper half of the complex w-plane the real part of the complex magnetostatic potential function

$$F^S(w) = i\frac{V}{\pi}\ln\left(\frac{w+\alpha}{w-\alpha}\right) \tag{3.116}$$

takes the value V on the real axis for $|\mathrm{Re}(w)| < \alpha$ and zero elsewhere on this axis. This gives

$$\frac{dF^S(w)}{dw} = -i\frac{2\alpha V}{\pi(w^2-\alpha^2)} \tag{3.117}$$

and the normalised field components, which follow from (2.54), are then

$$\frac{H_y^S + iH_z^S}{V} = -\frac{2\alpha(w^2-\beta^2)}{S^S\pi w\sqrt{w^2-1}}. \tag{3.118}$$

For a given point $z = x + iy$ in the z-plane, the corresponding point w required in (3.118) may be found from (3.105) in a small number of Newton-Raphson iterations, given a suitable starting value.

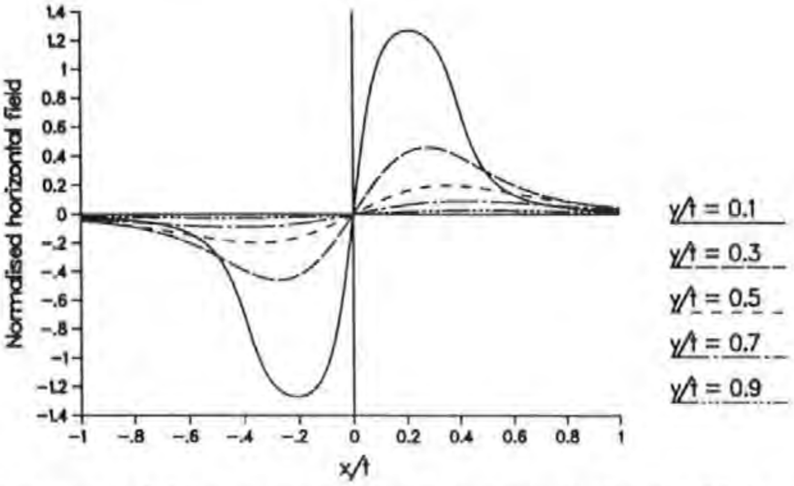

Figure 3.41: Horizontal field component for a symmetrically shielded, non-recessed, infinitely thin MR sensor, $G/t = 0.375$.

Typical horizontal and vertical field components, normalised by V/t, for a symmetrically shielded, non-recessed pole with $G/t = 0.375$, at various heights between the MR pole at $y/t = 0$ and the underlayer at $y/t = 1$, are presented in Figs. 3.41 and 3.42 respectively. These results have been confirmed by comparison with the field compo-

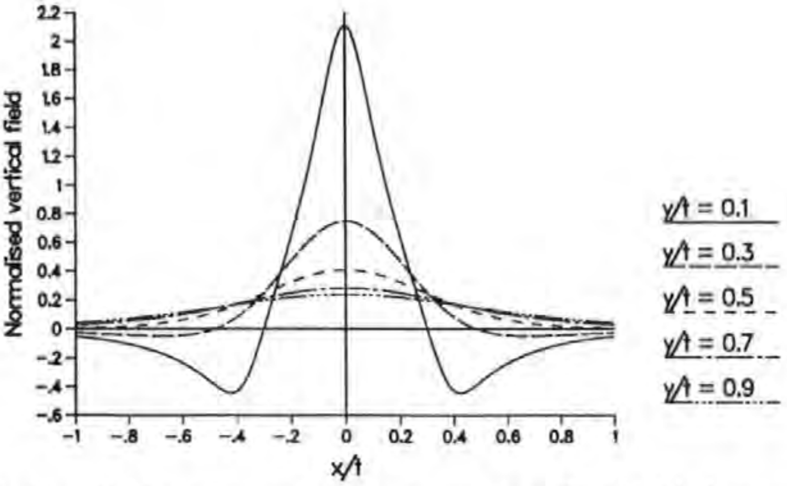

Figure 3.42: Vertical field component for a symmetrically shielded, non-recessed, infinitely thin MR sensor, $G/t = 0.375$.

nents of a very thin symmetrically shielded pole also of gap size $0.375t$, obtained by the Fourier method [29]. A pair of peaks of equal magnitude but opposite sign occurs in the horizontal component corresponding to the two gaps. In the vertical component a single peak occurs and close to the head there are undershoots which correpond to the shield corners.

3.2.2 The Asymmetrically Shielded Magnetoresistive Head

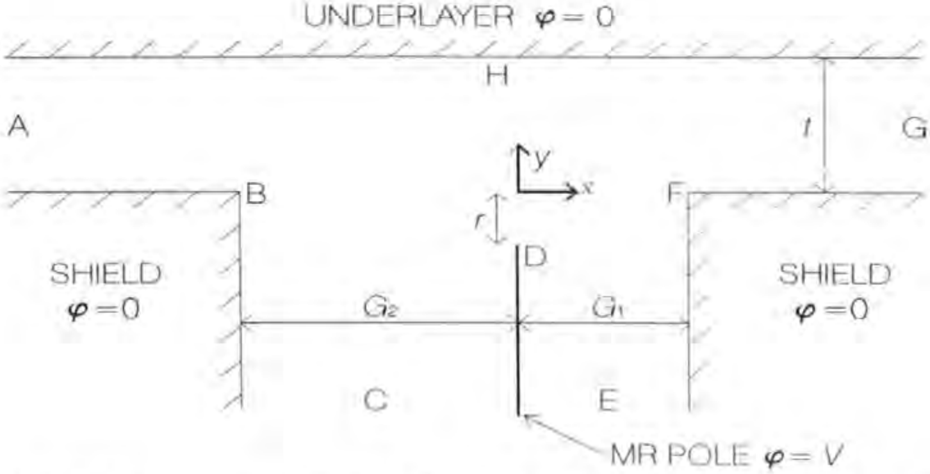

Figure 3.43: Idealised asymmetrically shielded and recessed MR sensor in the z-plane.

Here the magnetic field of an asymmetrically shielded MR sensor is analysed. Fig. 3.43 shows the idealised 2-D geometry under consideration. All of the modelling assumptions adopted in the previous section apply here also except that now the distances from the pole to the right and left-hand shields are G_1 and G_2 respectively.

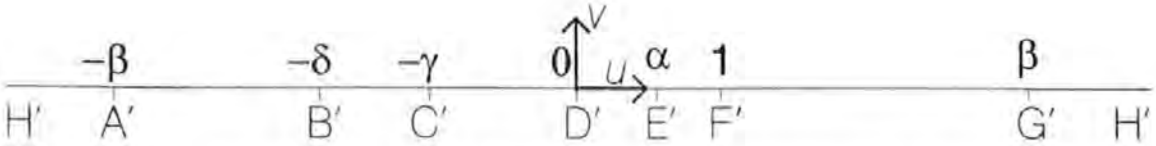

Figure 3.44: The complex w-plane in the asymmetric case.

The Schwarz-Christoffel transformation which conformally maps this region onto the upper half complex w-plane with points A–H shown in Fig. 3.43 mapping to A'–H' respectively, shown in Fig. 3.44, is defined by

$$\frac{dz}{dw} = \frac{S^A w(w-1)^{\frac{1}{2}}(w+\delta)^{\frac{1}{2}}}{(w-\alpha)(w^2-\beta^2)(w+\gamma)} \tag{3.119}$$

where the superscript A denotes the asymmetric case. As in the symmetric case, the pole tip D ($z=-ir$) maps to the origin $w=0$, the right-hand shield corner F ($z=G_1$) maps to $w=1$ and the point H on the underlayer surface in the z-plane which maps to the point at infinity in the w-plane does not occur in (3.119). Due to the lack of symmetry there are four points $\alpha, \beta, -\gamma$ and $-\delta$ in the w-plane, as well as the constants S^A and z_0^A (appearing in (3.120) below) to be determined by matching boundary values.

Integration of (3.119) [81] gives

$$\begin{aligned} z \;=\; & A \arctan\left[\frac{2(\alpha-1)(\alpha+\delta)+(2\alpha+\delta-1)(w-\alpha)}{2\sqrt{(1-\alpha)(\alpha+\delta)}\,w^{\star}}\right] \\ & +B \arctan\left[\frac{2(\gamma+1)(\gamma-\delta)+(\delta-1-2\gamma)(w+\gamma)}{2\sqrt{(1+\gamma)(\delta-\gamma)}\,w^{\star}}\right] \\ & +C \ln\left[\frac{2(\beta-1)(\beta+\delta)+(2\beta+\delta-1)(w-\beta)+2\sqrt{(\beta-1)(\beta+\delta)}\,w^{\star}}{w-\beta}\right] \end{aligned}$$

$$+D\ln\left[\frac{2(\beta+1)(\beta-\delta)+(\delta-1-2\beta)(w+\beta)+2\sqrt{(\beta+1)(\beta-\delta)}\,w^*}{w+\beta}\right]$$

$$+z_0^A \tag{3.120}$$

where

$$w^* = \sqrt{w-1}\sqrt{w+\delta}\,, \tag{3.121}$$

$$A = \frac{S^A\alpha\sqrt{(1-\alpha)(\alpha+\delta)}}{(\beta^2-\alpha^2)(\alpha+\gamma)}\,, \tag{3.122}$$

$$B = \frac{S^A\gamma\sqrt{(1+\gamma)(\delta-\gamma)}}{(\beta^2-\gamma^2)(\gamma+\alpha)}\,, \tag{3.123}$$

$$C = \frac{-S^A\sqrt{(\beta-1)(\beta+\delta)}}{2(\beta-\alpha)(\beta+\gamma)}\,, \tag{3.124}$$

$$D = \frac{-S^A\sqrt{(\beta+1)(\beta-\delta)}}{2(\beta+\alpha)(\beta-\gamma)}\,. \tag{3.125}$$

In (3.120) and the subsequent analysis it is assumed that the function arctan(p) of a complex argument p is evaluated as (3.115) in which case taking the principal values of the logarithm and the square root functions ensures (3.120) holds for $\mathrm{Im}(w) > 0$. On the real w-axis further investigation of the branch cuts of these functions is necessary.

Matching the points $w = \alpha$, $-\gamma$, β and $-\beta$ with the jumps in the boundary in the z-plane at E, C, G and A by the method of residues, as described for the symmetric case in Section 3.2.1, gives respectively,

$$A = \frac{-G_1}{\pi}, \quad B = \frac{-G_2}{\pi}, \quad C = \frac{t}{\pi}, \quad D = \frac{t}{\pi}. \tag{3.126}$$

It is now clear that S^A is a real negative constant. Evaluating (3.120) at $w = 1$ and

$w = -\delta$ and using (3.126), both give

$$z_0^A = \frac{1}{2}(G_1 - G_2) - \frac{2t}{\pi}\ln(1+\delta)\,. \tag{3.127}$$

Here care must be taken in selecting the correct values for the arctan functions, *i.e.* $-\pi/2$ in both cases for $w = 1$ and $+\pi/2$ in both cases for $w = -\delta$. Also, due to a branch cut, the value of the first ln term in (3.120) just above the real axis at $w = 1$ differs by $2\pi i$ from its value exactly at $w = 1$. The limiting value is required.

The final relation is obtained by evaluating (3.120) at the pole tip and using (3.126) and (3.127) to give

$$\begin{aligned}
&- \frac{G_1}{\pi}\arctan\left[\frac{\alpha\delta - \alpha - 2\delta}{2i\sqrt{\delta}\sqrt{(1-\alpha)(\alpha+\delta)}}\right] - \frac{G_2}{\pi}\arctan\left[\frac{\gamma - \gamma\delta - 2\delta}{2i\sqrt{\delta}\sqrt{(1+\gamma)(\delta-\gamma)}}\right] \\
&+ \frac{t}{\pi}\ln\left[\frac{\beta - \beta\delta + 2\delta - 2i\sqrt{\delta}\sqrt{(\beta-1)(\beta+\delta)}}{\beta}\right] \\
&+ \frac{t}{\pi}\ln\left[\frac{\beta - \beta\delta - 2\delta + 2i\sqrt{\delta}\sqrt{(\beta+1)(\beta-\delta)}}{\beta}\right] \\
&+ \frac{1}{2}(G_1 + G_2) - \frac{2t}{\pi}\ln(1+\delta) + ir = 0\,.
\end{aligned} \tag{3.128}$$

Due to $w = 0$ lying on a branch cut, evaluating the second arctan term *via* the principal value of the ln function requires the limiting value to be taken rather than the direct $w = 0$ value *i.e.* $\arctan[\quad] - \pi$ has been taken in deriving (3.128).

Once α, β, γ and δ have been determined, the transformation is given by (3.120), using (3.126), the constant of integration, z_0^A, is given by (3.127) and the constant S^A, required for (3.119) but not now for (3.120), is given by any of (3.122) - (3.125), using (3.126). Four suitable non-linear equations to be solved for α, β, γ and δ are (3.128) and three equations obtained from (3.122) - (3.125) and (3.126) by eliminating S^A.

These are:

$$\frac{2\alpha(\beta+\gamma)\sqrt{(1-\alpha)(\alpha+\delta)}}{(\alpha+\gamma)(\alpha+\beta)\sqrt{(\beta-1)(\beta+\delta)}} = \frac{G_1}{t}, \tag{3.129}$$

$$\frac{2\gamma(\beta-\alpha)\sqrt{(1+\gamma)(\delta-\gamma)}}{(\alpha+\gamma)(\beta-\gamma)\sqrt{(\beta-1)(\beta+\delta)}} = \frac{G_2}{t}, \tag{3.130}$$

$$\frac{(\beta-\alpha)(\beta+\gamma)\sqrt{(\beta+1)(\beta-\delta)}}{(\beta+\alpha)(\beta-\gamma)\sqrt{(\beta-1)(\beta+\delta)}} = 1. \tag{3.131}$$

Further analysis of equation (3.128) reveals it to be purely complex and that it may be written in the form

$$\frac{G_1}{2\pi}\ln\left(\frac{1+\vartheta_1}{\vartheta_1-1}\right)+\frac{G_2}{2\pi}\ln\left(\frac{1+\vartheta_2}{\vartheta_2-1}\right)-\frac{t}{\pi}(\vartheta_3-\vartheta_4)+r=0 \tag{3.132}$$

where,

$$\vartheta_1 = \frac{\alpha\delta-\alpha-2\delta}{2\sqrt{\delta}\sqrt{(1-\alpha)(\alpha+\delta)}}, \tag{3.133}$$

$$\vartheta_2 = \frac{\gamma-\gamma\delta-2\delta}{2\sqrt{\delta}\sqrt{(1+\gamma)(\delta-\gamma)}}, \tag{3.134}$$

$$\vartheta_3 = \arctan\left[\frac{2\sqrt{\delta}\sqrt{(\beta-1)(\beta+\delta)}}{\beta-\beta\delta+2\delta}\right], \tag{3.135}$$

$$\vartheta_4 = \pi-\arctan\left[\frac{2\sqrt{\delta}\sqrt{(\beta+1)(\beta-\delta)}}{\beta\delta-\beta+2\delta}\right]. \tag{3.136}$$

The four equations (3.129) – (3.132) may be conveniently solved by a suitable library routine *eg.* C05NBF in [33], the values of α, β, γ and δ only depending on the ratios G_1/t, G_2/t and r/t.

Whilst the above also holds for a pole symmetrically placed between the shields, the transformation is not the same as that given in Section 3.2.1. Substituting $\gamma = \alpha, \delta = 1$ and $G_1 = G$ in (3.122) and (3.126) provides the same relationship between S^A and the parameters α and β as given for S^S in (3.108). Taking $G_2 = G$ also in (3.127) gives $z_0^A = -2t\ln(2)$ which is independent of the gap width unlike the symmetric mapping for which $z_0^S = G + it$.

The magnetostatic potential function in the upper half w-plane which takes the value V on the real w-axis for $-\gamma < \mathrm{Re}(w) < \alpha$ and zero elsewhere on this axis is $\mathrm{Re}(F^A(w))$ where

$$F^A(w) = i\frac{V}{\pi}\ln\left[\frac{w+\gamma}{w-\alpha}\right]. \tag{3.137}$$

Therefore using the relationship (2.54) leads to

$$\frac{H_y^A + iH_x^A}{V} = \frac{-(\alpha+\gamma)(w^2-\beta^2)}{\pi S^A w\sqrt{w-1}\sqrt{w+\delta}}. \tag{3.138}$$

For a given point $z = x + iy$ in the z-plane, the corresponding point w required in (3.138) may be found from (3.120) in a small number of Newton-Raphson iterations. For most of the examples included in this thesis, setting $w = -\beta + 0.002i$ has provided a suitable starting value for the Newton-Raphson method for $x < -G_2$ and $y/t \geq 0.1$. Each successfully inverted point can be used as the starting value for the next, provided that the two points are sufficiently close together. Inverting the transformation along $y = 0$ requires very small steps between evaluations in order to provide the necessary accurate starting values. The mapping is particularly crowded near the corners of the shields and close to the pole tip. Starting the inversion with $w = b + 0.002i$ where $b = -\beta$ truncated to 2sf. at $z = (-G_2 + 0.1, 0)$ has been successful.

By the design of the mapping, $0 < \alpha < 1$, $1 < \beta < \infty$, $0 < \gamma < \delta < \beta$. As α or γ approaches zero, or as β approaches 1, crowding of the transformation makes convergence of the Newton-Raphson method more difficult, and so very accurate starting values are required. In computing the field components, the constant S^A appears in the denominator of equn. (3.138), giving greatest accuracy when S^A is large, if a fixed tolerance is applied when inverting the mapping by the Newton-Raphson method.

Tables B.9, B.10 and B.11 show some typical constants as G_1, t and r vary, respectively, while all other dimensions are held constant. Where results are given for a symmetric head, these have been obtained from the asymmetric solution with $\delta = 1$ and $\gamma = \alpha$ so that $z_0^A/t = -0.441271$, independent of G_1/t, using the definition given in equn. (3.127). As the ratio between the left and right-hand gap widths G_2/G_1 increases, the spread of γ, δ and β increases and the magnitude of S^A increases. As the head - underlayer separation increases β and $|S^A|$ increase rapidly. Recessing the pole consistently reduces the magnitudes of all the constants except β and S^A; α and γ are particularly affected. Therefore this method is more easily applied when both $G_2 \geq G_1$ and $G_1/t \leq 1$ and the pole recession is not extreme.

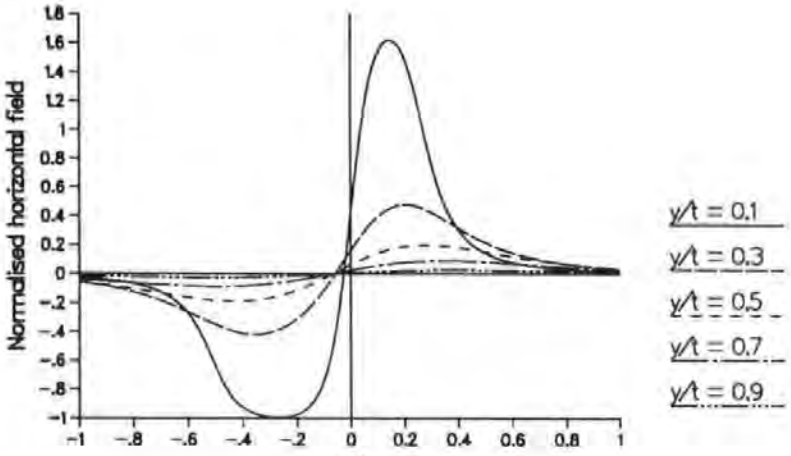

Figure 3.45: Horizontal field component for a non-recessed, infinitely thin MR sensor, $G_1/t = 0.25$ and $G_2/t = 0.5$.

Figs. 3.45 and 3.46 show typical normalised, horizontal and vertical field components for an asymmetrically shielded, non-recessed MR sensor where $G_2/G_1 = 2$. Peaks corresponding to the gaps occur in the horizontal component. The narrower peak which

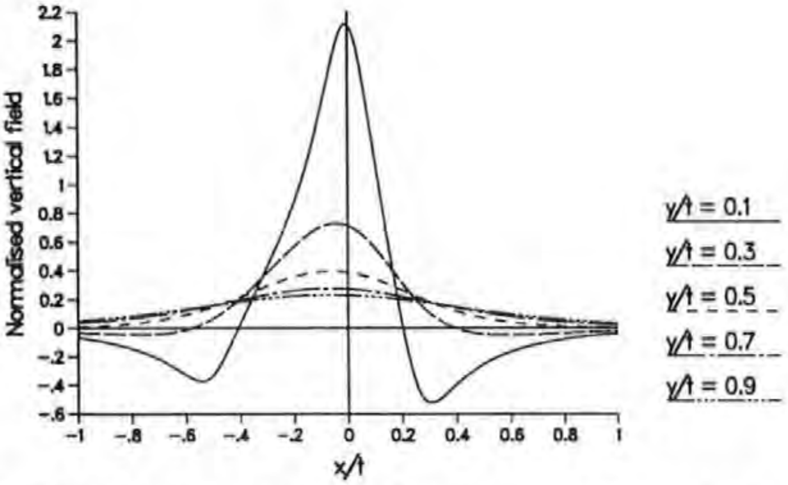

Figure 3.46: Vertical field component for an asymmetrically shielded, non-recessed, infinitely thin MR sensor, $G_1/t = 0.25$ and $G_2/t = 0.5$.

corresponds to the narrower gap has the greater maximum magnitude. Hence the zero of the horizontal component and the maximum of the vertical component occur at $x < 0$, which corresponds here to the wider gap. The gradient of the vertical field component is greater on the narrower gap side than on the wider gap side, hence the undershoot, which occurs close to and on this side of the head, is deeper and narrower than the one on the other side.

3.3 Discussion

3.3.1 Head – Underlayer Interaction

The head - underlayer interaction is such that for a head of fixed dimensions, its separation from the underlayer can have a strong influence on the head field. Figs. 3.47 - 3.49 provide examples of the effect of varying the head - underlayer separation for the constant potential thin film head, the single pole head with a linear pole potential and the asymmetrically shielded MR sensor. For each head the vertical field component for different head - underlayer separations is given at the same physical height from the head, as in practice the head - medium separation is kept as small as possible, irrespective of the medium thickness. As t decreases, the degree of head - underlayer interaction increases which improves the vertical field strength, but as the distance from the head face remains constant, the vertical field is sampled at increasing distances relative to t. In each case as t decreases the magnitude of the peaks increases, and the gradient of the field over the trailing edge of the pole becomes steeper. The rate of increase depends on the head geometry and the potential distribution across the pole.

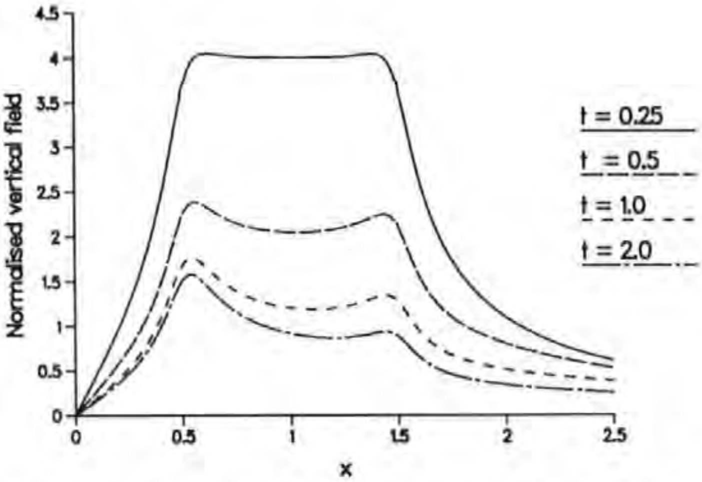

Figure 3.47: Variation in the vertical field components at $y = 0.1$ for constant potential thin film heads with head - underlayer separation, $L = g = 0.5$.

For the constant potential thin film head, the peak vertical field over the trailing edge of the head at $y = 0.1$, increases more than that at the gap edge as t decreases. The peak over the gap edge when $g/t = L/t = 2$ is 156% higher than when $g/t = L/t = 0.25$ while the corresponding increase in the peak over the trailing edge is 330%. Therefore when the head - underlayer spacing is small, recording would occur at the trailing edge of the head. Unless the head was very narrow, overwriting of adjacent bit cells by the field over the other pole could be a problem.

For the single pole head with a linear pole potential, the peak vertical field when $L/t = 2$ is 186% higher than when $L/t = 0.25$. The depth of the undershoot decreases with decreasing t so reducing the overall width of the peak. Similar results can be expected for single pole heads with other potential distributions.

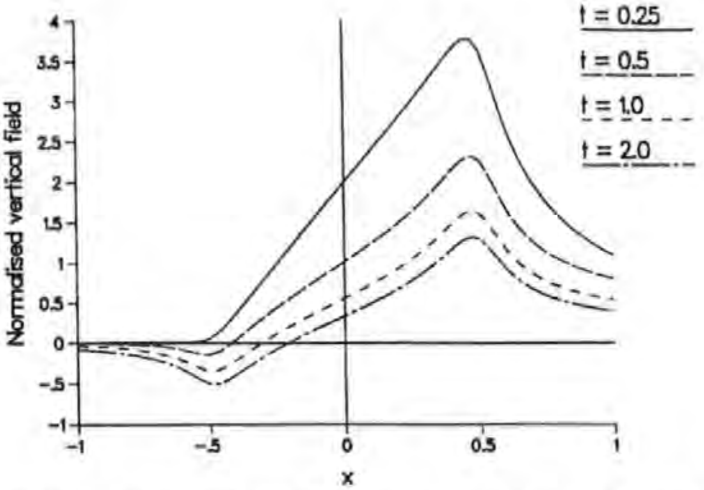

Figure 3.48: Variation in the vertical field components at $y = 0.1$ for linear potential single pole heads with head – underlayer separation, $L = 0.5$.

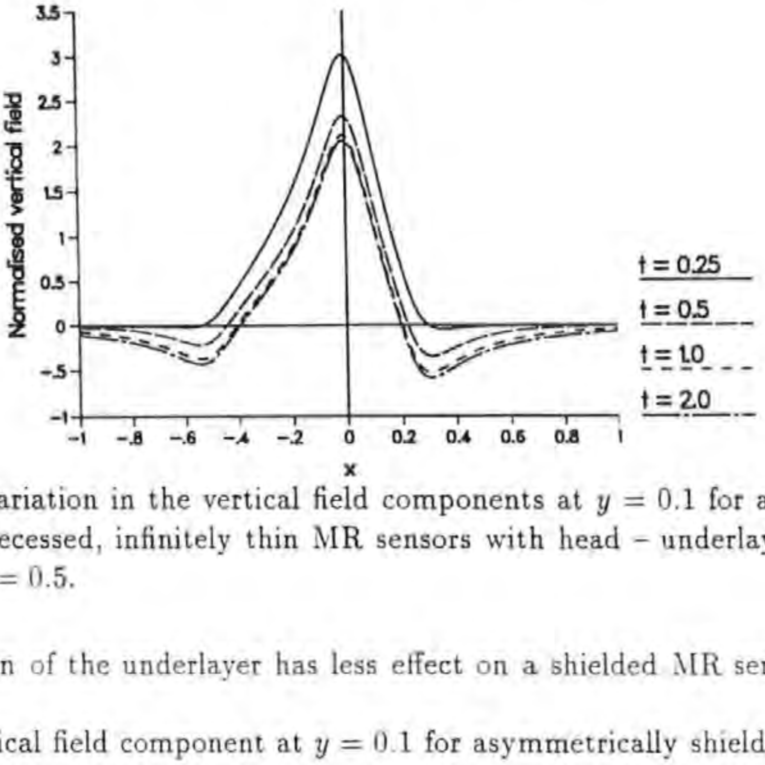

Figure 3.49: Variation in the vertical field components at $y = 0.1$ for asymmetrically shielded, non-recessed, infinitely thin MR sensors with head – underlayer separation, $G_1 = 0.25$, $G_2 = 0.5$.

The position of the underlayer has less effect on a shielded MR sensor. Fig. 3.49 shows the vertical field component at $y = 0.1$ for asymmetrically shielded MR sensors where $G_2/G_1 = 2$ for four head – underlayer separations. The peak when $G_2/t = 2$ is only 47% higher than the maximum when $G_2/t = 0.25$. The magnitude of the undershoots also decline as t decreases so that the gradient only increases slightly.

3.3.2 The Effect of Pole Potential Grading

3.3.2.1 Thin film heads

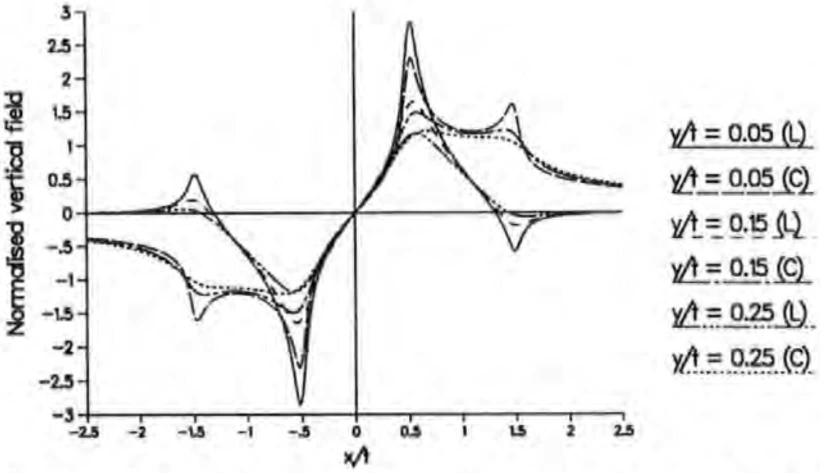

Figure 3.50: Comparison of the vertical field component for thin film heads with constant (C-curves) and linear (L-curves) potential poles, $g/t = L/t = 0.5$.

Fig. 3.50 shows the vertical field components of thin film heads with constant and linear pole potentials when $g/t = L/t = 0.5$ at three heights close to the head face plane. In both cases the magnitude of the largest peak and the maximum gradient increase as y/t decreases. The secondary peaks close to and above the outer edges of the head with constant potential poles could result in recording taking place at the trailing edge of the head instead of at the gap edge, in a sufficiently sensitive system. These secondary peaks are replaced by relatively small negative undershoots in the linear pole potential head. For $y/t < 0.25$, the magnitude of the peak over the leading edge of the right hand pole is greater with a linear pole potential than for a conventional constant pole potential. At $y/t = 0.05$, the maximum vertical field above the leading edge of the right-hand pole with a linearly varying potential increases by 24% over the equivalent maximum value for a pole with a constant potential and by 78% over the the maximum value above the trailing edge, the second peak, of a constant pole potential head. The maximum gradient as the field falls from its peak value in the linear pole potential case, increses by 28% over the maximum gradient as the field falls from the second peak for the constant pole potential head. At $y/t = 0.15$, the corresponding increases are 10%, 33% and 26%.

The resultant of the horizontal and the vertical field components in the linear pole potential case is more localised than the equivalent constant pole potential field; it is concentrated close to the gap edges, where it is both of higher magnitude and more vertically inclined. Fig. 3.51 shows the magnetic fields for constant and linearly varying pole potentials, in terms of field vectors. Each arrow represents the field at its midpoint and all magnitudes are normalised by the largest magnitude for the head with the linear pole potential. Using a linear potential grading across the poles should provide a more efficient system for 'in contact' recording.

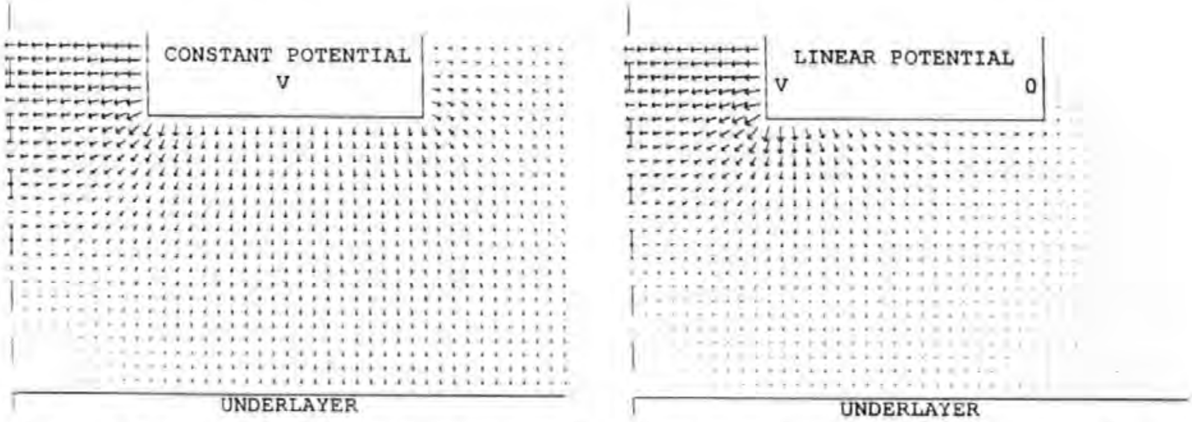

Figure 3.51: Comparison of the magnetic fields of thin film heads with constant and linearly varying pole potentials, $g/t = 0.5$, $L/t = 0.5$.

3.3.2.2 Single pole heads

Fig. 3.52 shows the normalised vertical field components at $y/t = 0.1$, for single pole heads with various pole potential distributions, all with $L/t = 0.5$. Each of the new potential distributions has the advantage that even at this relatively small distance from the pole face, their vertical field component is not bimodal, unlike that

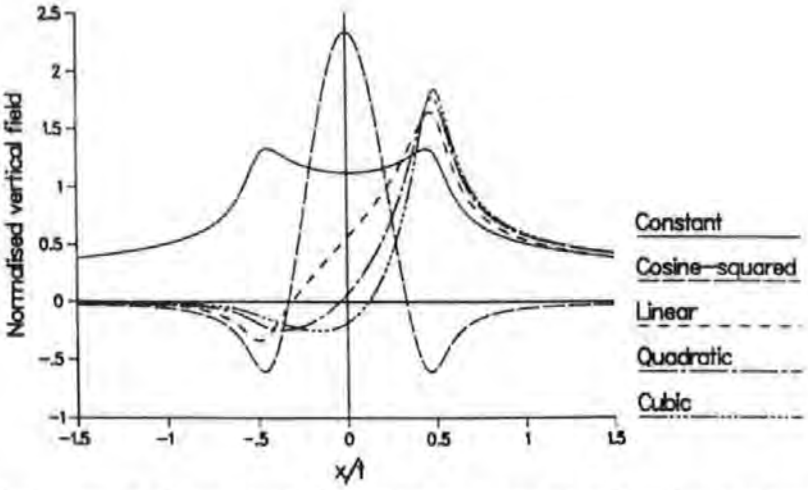

Figure 3.52: Variation in the vertical field components at $y/t = 0.1$ with pole potential grading for single pole heads, $L/t = 0.5$.

of the conventional constant potential pole. Also their peaks are higher and narrower than the peak of the constant potential pole. The peak for the cosine-squared potential distribution is 76% higher than the maximum vertical field of the constant potential single pole at $y/t = 0.1$ when $L/t = 0.5$. For the asymmetric distributions, the greater the degree of asymmetry, the narrower the peak and broader the undershoots become.

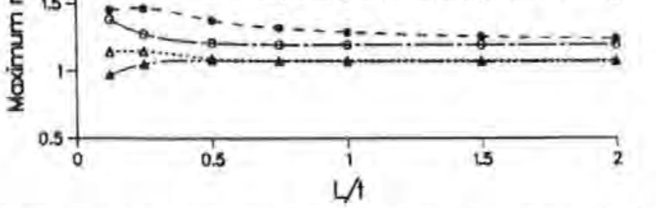

Figure 3.53: Variation of the maximum vertical field with L/t for single pole heads with linear (L-curves) and constant (C-curves) pole potentials.

The variation in the vertical field with L/t, for single pole heads with both linear and constant pole potentials, at several relative positions, y/t, is summarised in Figs. 3.53 – 3.55. Fig. 3.53 shows the variation in maximum field strength. Close to the pole at $y/t = 0.05$, the increase possible with a linear variation in pole potential varies from 10% for $L/t = 2$ to 75% for a narrow pole with $L/t = 0.125$. Fig. 3.54 shows the variation in the maximum vertical field gradient as L/t varies. This always occurs just past the trailing edge of the pole. Only for $y/t \leq 0.15$ is there an appreciable increase in gradient with a linear potential pole, but this can be as large as 108% for a narrow pole with $L/t = 0.125$ at $y/t = 0.05$. Fig. 3.55 shows the variation in pulse width, defined here as the width of the field at 50% its maximum value. The pulse widths for both the linear and constant potential poles vary approximately linearly with L/t, at least for L/t not too small, but those linear rates are different, with the constant potential pulse width decreasing faster as L/t decreases. The linear potential

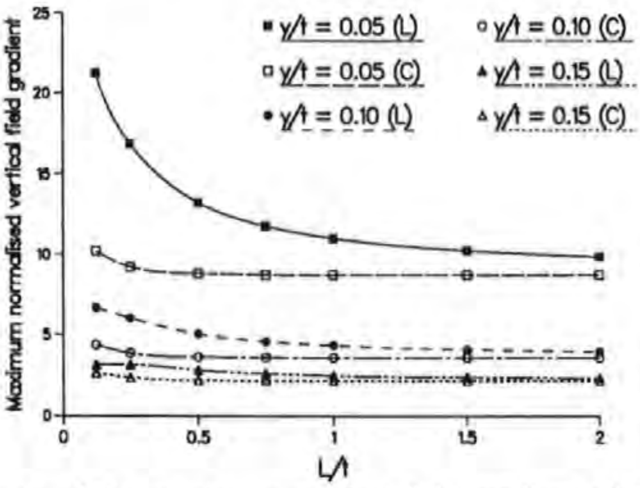

Figure 3.54: Variation of the maximum vertical field gradient with L/t for single pole heads with linear (L-curves) and constant (C-curves) pole potentials.

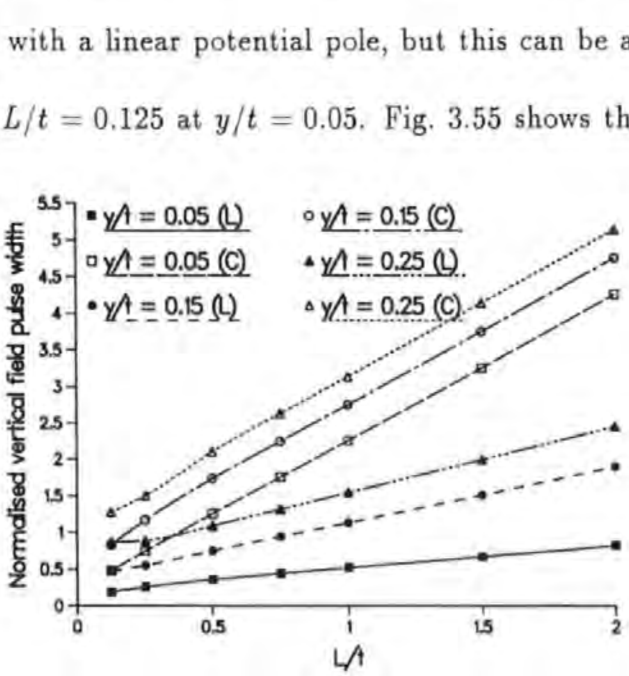

Figure 3.55: Variation of the vertical field pulse width with L/t for single pole heads with linear (L-curves) and constant (C-curves) pole potentials.

pole value is always smaller. At $y/t = 0.05$ for example, for $L/t = 2$ the linear potential pulse width is 19% of the constant potential pole value rising to 39% for $L/t = 0.125$.

As in the case of the linear thin film head, the field of the single pole head with a linear pole potential is more localised than that of the corresponding constant potential head. Here, close to the maximum potential pole edge, the field for the linear potential pole is of greater magnitude and more vertically orientated than that of the constant potential pole. This is shown in Fig. 3.56.

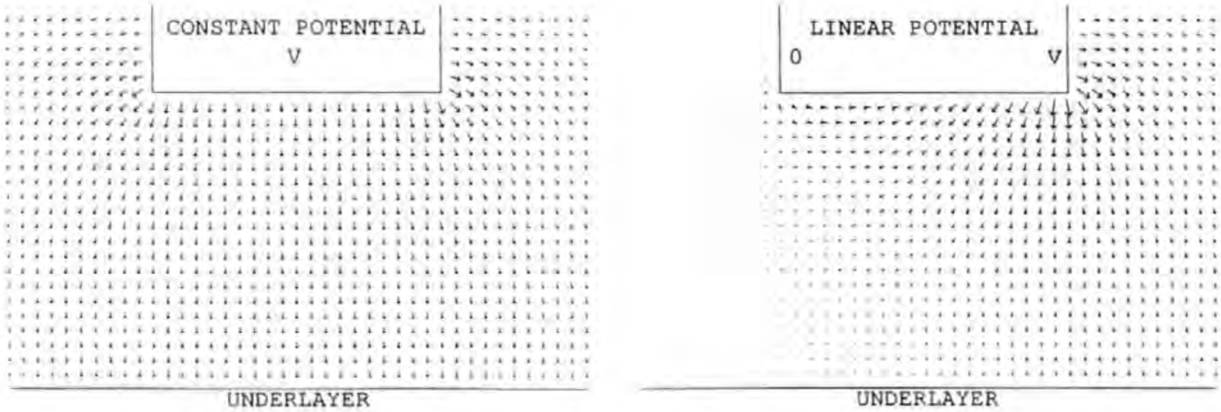

Figure 3.56: Comparison of the magnetic fields of single pole heads with constant and linearly varying pole potentials, $L/t = 0.5$.

Greater advantages are obtained by using the other asymmetric pole potentials considered here. For each of the varing potential distributions tested, the field is more localised than in the constant potential case. Consequently, further from the pole face, the peaks, although still narrower, are lower than those of the constant potential pole. The essential requirement is for the recording layer to be as close as possible to the pole.

The average potential across a pole with a cosine-squared potential distribution, reaching a maximum potential V, is half that of a pole, of the same dimensions, with constant potential V. However the improvement in the magnitude of the head field, close to the pole face, cannot be achieved by reducing the width of a conventional single pole by half. Fig. 3.57 compares the vertical field component at $y/t = 0.1$ for a single

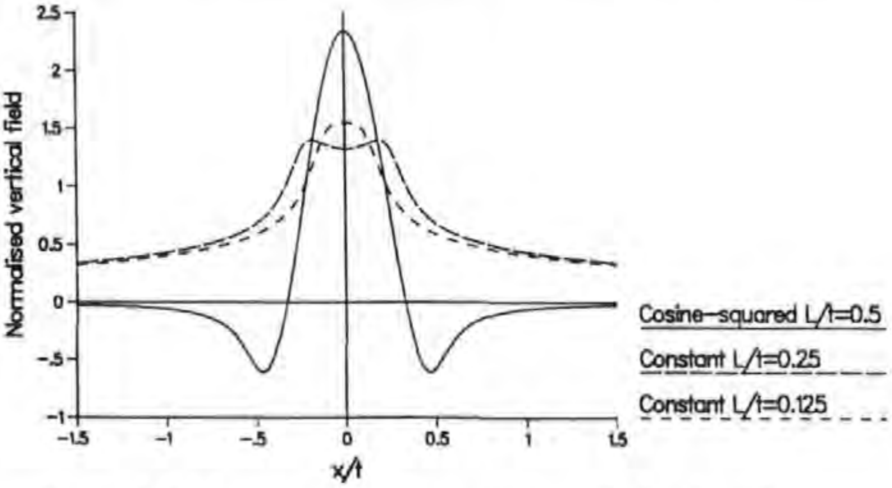

Figure 3.57: Vertical field component for a single pole head with a cosine-squared pole potential compared with those for thinner poles with constant potential, all at $y/t = 0.1$.

pole with a cosine-squared pole potential, with those for constant potential poles of half and a quarter the width. Clearly, L/t for the constant potential pole would need to be very small to raise the peak to the height of that produced by the cosine-squared potential pole with $L/t = 0.5$ especially as the constant potential vertical head field never exhibits undershoots.

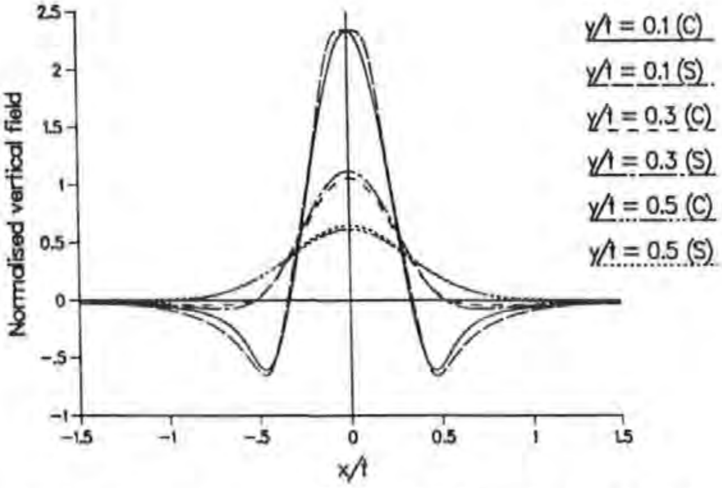

Figure 3.58: Vertical field component for a single pole head with a cosine-squared pole potential, $L/t = 0.5$, (C-curves) and a symmetrically shielded pole, $L/t = 0.125$, $g/t = 0.15$, (S-curves).

The shape of the vertical field component for a single pole with cosine-squared potential is very similar to that of a symmetrically shielded pole head [29]. Fig. 3.58

shows the vertical field component of a cosine-squared potential single pole head with $L/t = 0.5$ and of a symmetrically shielded pole head with dimensions $L/t = 0.125$ and $g/t = 0.15$, both normalised by V/t. Close to the pole face at $y/t = 0.1$, they have almost identical maxima under the pole centre, and their undershoots of similar magnitude both occur at $|x|/t = 0.47$.

These results have practical significance in two particular respects. First, the magnetic potential distribution across a practical pole is unlikely to be uniform. During manufacture, oxidation or other chemical modification to the outer surfaces of the pole may occur, or combining layers of different materials may affect the immediate microstructure of the pole. Saturation near the pole corners and other effects at high frequency such as may be caused by eddy currents, can also result in a non-uniform distribution of magnetisation across the pole. These theoretical results may help to explain the behaviour of such poles in practice. Secondly, these results suggest that it may be possible to construct a single pole head with the optimum properties for a particular system.

3.3.3 The Effects of Asymmetry and Pole Recession for a Shielded MR Sensor

Figs. 3.59 and 3.60 show the horizontal and vertical field components at $y/t = 0.1$, when G_2/t is fixed at 0.5 as G_1/t varies from 0.5 to 0.0625. As expected, the widths of the peaks of both field components reduce as the total gap width decreases. The magnitude of the positive peak for each component does not increase indefinitely with increasing asymmetry, the maximum peak magnitude occurring at a different ratio of G_2/G_1 for each component. The magnitudes of the left-hand undershoot of the vertical component and the negative peak of the horizontal component both decrease

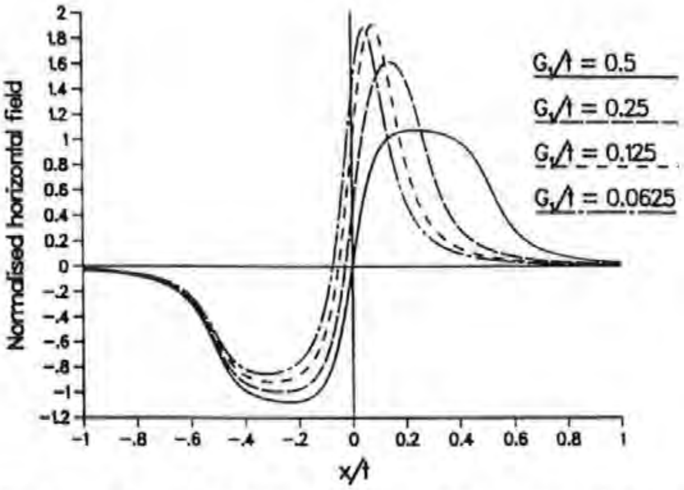

Figure 3.59: Comparison of the horizontal field components, at $y/t = 0.1$, for shielded, non-recessed, infinitely thin MR sensors, with various right-hand gap widths when $G_2/t = 0.5$.

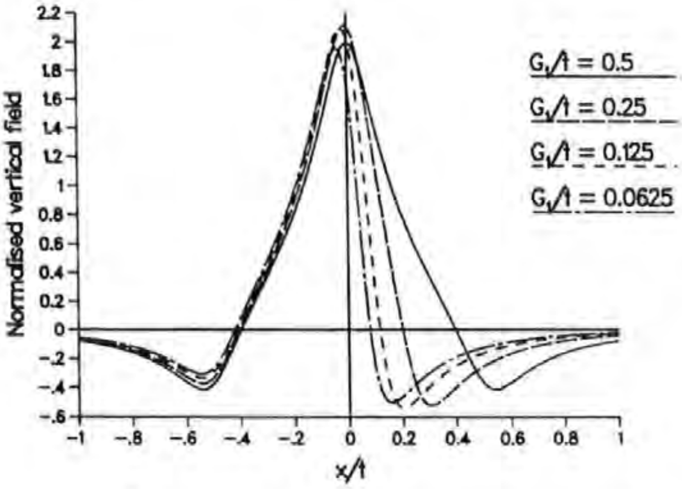

Figure 3.60: Comparison of the vertical field components, at $y/t = 0.1$, for shielded, non-recessed, infinitely thin MR sensors, with various right-hand gap widths when $G_2/t = 0.5$.

with increasing asymmetry, over the range of gap ratios tested. A maximum right-hand undershoot in the vertical field occurs for $G_2/G_1 \approx 4$.

As the head – underlayer separation increases, the magnitude of the vertical field component decreases slightly and rapidly approaches that obtained when there is no underlayer present. For the case where $g_2/g_1 = 2$, the vertical component changes by less than 4% from the no underlayer case if $t > 4g_1$. The position of the peak appears to be virtually independent of t. The horizontal component is also almost unaffected.

Recession of the pole has a detrimental effect on the magnitude of both the vertical

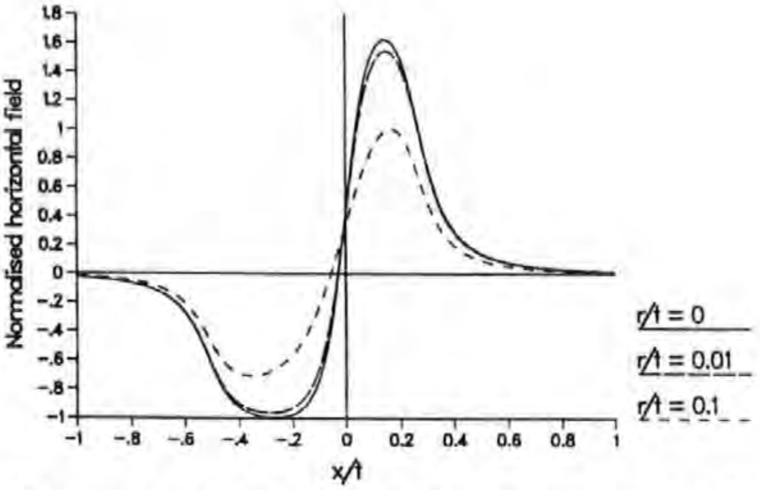

Figure 3.61: Variation in the horizontal field component with pole recession for a shielded, non-recessed, infinitely thin MR sensor, $G_1/t = 0.25$, $G_2/t = 0.5$, when $y/t = 0.1$.

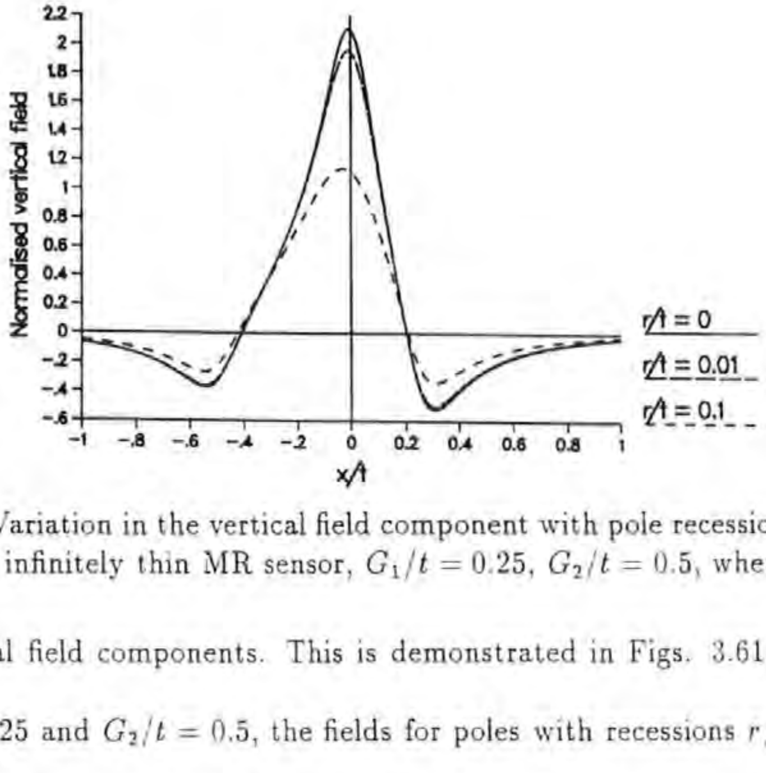

Figure 3.62: Variation in the vertical field component with pole recession for a shielded, non-recessed, infinitely thin MR sensor, $G_1/t = 0.25$, $G_2/t = 0.5$, when $y/t = 0.1$.

and horizontal field components. This is demonstrated in Figs. 3.61 and 3.62 where for $G_1/t = 0.25$ and $G_2/t = 0.5$, the fields for poles with recessions $r/t = 0.01$ and 0.1 are compared with the field of a head with a non-recessed pole. Experimental and approximate results for a longitudinal system [74], [84] are consistent with these results.

Although recessing the pole increases the distance to the recording medium, the effect is less disadvantageous than moving the medium away from the head by the same amount. Figs. 3.63 and 3.64 show the x and y field components, respectively, for a non-recessed head and a head with the pole recessed by $r/t = 0.1$. In both cases the head - underlayer separation is the same, $G_1/t = 0.25$, $G_2/t = 0.5$ and the field

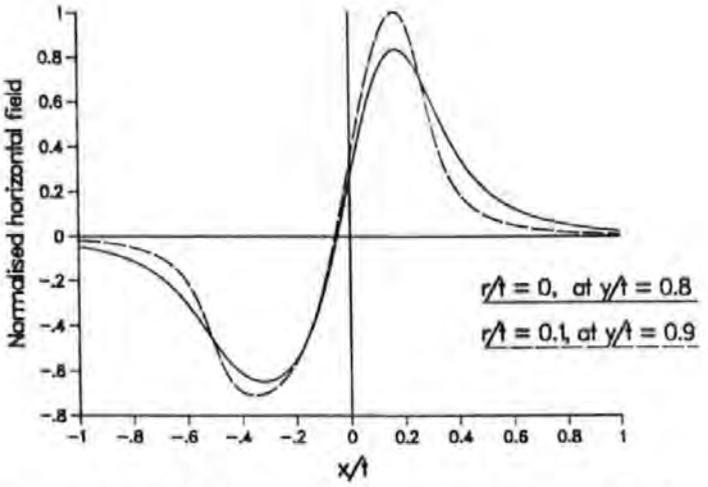

Figure 3.63: Comparison of the horizontal field components of shielded, recessed and non-recessed, infinitely thin MR sensors, both computed 0.2t from the pole tip, $G_1/t = 0.25$, $G_2/t = 0.5$.

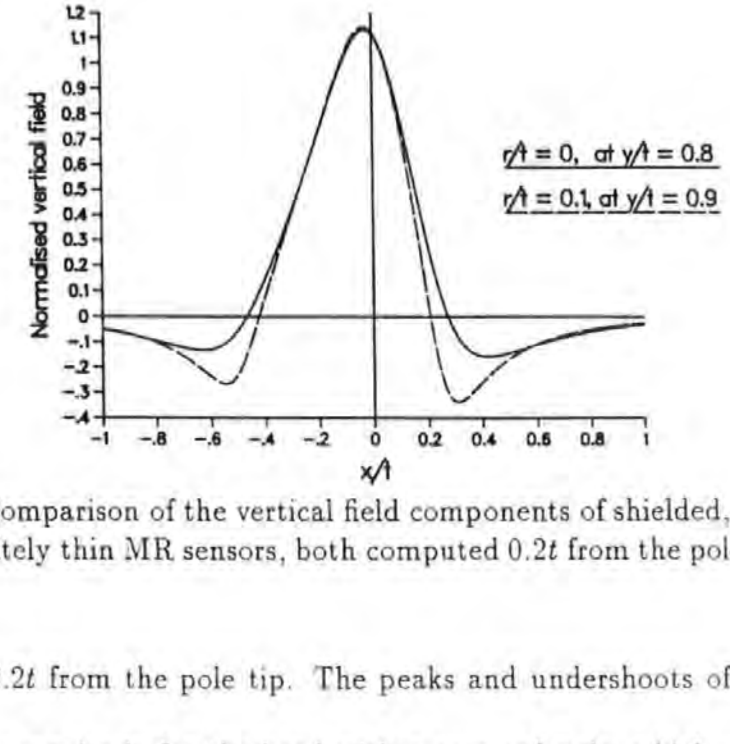

Figure 3.64: Comparison of the vertical field components of shielded, recessed and non-recessed, infinitely thin MR sensors, both computed 0.2t from the pole tip, $G_1/t = 0.25$, $G_2/t = 0.5$.

is computed 0.2t from the pole tip. The peaks and undershoots of both components are of greater magnitude for the head with a recessed pole, which also gives narrower peaks.

3.4 Summary

This chapter has discussed:

- The derivation of head field components, by Fourier analysis, for

1. Thin film heads with constant and linearly varying pole potentials.
2. Single pole heads with linear pole potential.
3. Single pole heads with arbitrary pole potential.

- Approximation to the potential at $y = 0$ for each of the heads listed above as well as for a symmetrically shielded single pole head.
- The derivation, by conformal mapping, of head field components for shielded, infinitely thin magnetoresistive sensors, both symmetrically and asymmetrically shielded, and both recessed and non-recesessed.
- Typical results in relation to the various geometric factors.

Chapter 4

Output Characteristics

4.1 Spectral Response Functions and their Approximations

4.1.1 Introduction

For an inductive head, the spectral response function is defined as the Fourier transform of the appropriate component of the head field in the head face plane *ie.*

$$\widehat{H}(\kappa, 0) = \int_{-\infty}^{\infty} H(x, 0) e^{-i\kappa x}\, dx \tag{4.1}$$

where $H(x, 0)$ is either $H_x(x, 0)$ of $H_y(x, 0)$. This function provides information about the replay limitations of a particular head.

For a head in the presence of an underlayer at $y = t$, if the potential in the head face plane at $y = 0$ is known then applying a Fourier transform to Laplace's equation for the magnetic potential in the region $0 \leq y \leq t$ leads to

$$\widehat{\varphi}(\kappa, y) = \widehat{\varphi}(\kappa, 0) \frac{\sinh(\kappa(t - y))}{\sinh(\kappa t)} \tag{4.2}$$

where

$$\widehat{\varphi}(\kappa, y) = \int_{-\infty}^{\infty} \varphi(x, y) e^{-i\kappa x} \, dx \, . \tag{4.3}$$

By differentiating (4.2) with respect to y it can be shown that

$$\widehat{H}_y(\kappa, 0) = \widehat{\varphi}(\kappa, 0) \kappa \coth(\kappa t) \, . \tag{4.4}$$

This leads to

$$\widehat{H}_y(\kappa, y) = \widehat{H}_y(\kappa, 0) \frac{\cosh(\kappa(t - y))}{\cosh(\kappa t)} \, . \tag{4.5}$$

The magnetisation on a medium with perpendicular anisotropy is assumed to have a vertical component only. The magnitude of the magnetisation is a waveform and any periodic wave can be expressed as a Fourier series. Taking the case of a single sine wave and using the notation of Section 2.1.5,

$$\frac{d}{d\bar{x}} \left(M_y(x - \bar{x}) \right) = -\kappa M_r \left[\cos(\kappa \bar{x}) \cos(\kappa x) + \sin(\kappa \bar{x}) \sin(\kappa x) \right] \tag{4.6}$$

where $\kappa = 2\pi/\lambda$ is the wavenumber of a magnetisation with wavelength λ and M_r is the remanent magnetisation of the medium. Therefore, by invoking the reciprocity theorem (2.70), the output voltage of an inductive head due to a sinusoidal magnetisation on the medium of thickness δ at a distance d from the head face plane, can be evaluated as

$$e^{In}(\bar{x}) = M_r C^{In} \kappa \left[\cos(\kappa \bar{x}) \mathrm{Re} \left[\int_d^{d+\delta} H_y(\kappa, y) \, dy \right] - \sin(\kappa \bar{x}) \mathrm{Im} \left[\int_d^{d+\delta} H_y(\kappa, y) \, dy \right] \right] \tag{4.7}$$

where C^{In} is a constant for a particular inductive head. The relationship given in equn.

(4.5) leads to

$$e^{In}(\bar{x}) = M_r C^{In} \left[\cos(\kappa\bar{x})\mathrm{Re}\left[\widehat{H}_y(\kappa,0)\right] - \sin(\kappa\bar{x})\mathrm{Im}\left[\widehat{H}_y(\kappa,0)\right]\right] \cdot \left[\frac{\sinh(\kappa(t-d)) - \sinh(\kappa(t-d-\delta))}{\cosh(\kappa t)}\right]. \qquad (4.8)$$

For the case of no underlayer

$$\lim_{t\to\infty}\left[\frac{\sinh(\kappa(t-d)) - \sinh(\kappa(t-d-\delta))}{\cosh(\kappa t)}\right] = e^{-\kappa d}(1 - e^{-\kappa\delta}). \qquad (4.9)$$

So that for an inductive head without an underlayer the instantaneous output voltage can be expressed in terms of the spectral response function $\widehat{H}_y(\kappa, 0)$, a spacing loss $e^{-\kappa d}$, and a medium thickness loss $(1 - e^{-\kappa\delta})$. However, for a head in the presence of an underlayer the terms do not completely separate. In this case the head field depends on the distance, t, to the underlayer and hence so does the spectral response function. The ratio of sinh and cosh terms in equn. (4.8) has no zeros for $\kappa, d, \delta, t > 0$ and $t \geq d + \delta$ therefore any output nulls are due to the zeros of the spectral response function.

Clearly, a replay head cannot be used over a range of frequencies which includes a null. In general asymmetric replay heads do not exhibit spectral response nulls but most symmetric ones do. Null free responses have been reported in [85] and [47] for geometries not considered here.

The spectral response function of a symmetric perpendicular replay head is either entirely real or entirely imaginary depending whether the vertical head field component is even or odd respectively. By convention, this function is plotted in decibels and therefore magnitudes only are quoted. For asymmetric heads the amplitude of the response depends on the resultant of both components and is given by

$$\left|\widehat{H}_y(\kappa,0)\right| = \sqrt{\left\{\mathrm{Re}\left[\widehat{H}_y(\kappa,0)\right]\right\}^2 + \left\{\mathrm{Im}\left[\widehat{H}_y(\kappa,0)\right]\right\}^2} \tag{4.10}$$

A similar analysis for an MR head, in the presence of an underlayer, relates the output voltage to its spectral response function by

$$\frac{e^{MR}(\bar{x})}{M_r C^{MR}} \propto \left[\sin(\kappa\bar{x})\mathrm{Re}[\widehat{\varphi}(\kappa,0)] + \cos(\kappa\bar{x})\mathrm{Im}[\widehat{\varphi}(\kappa,0)]\right] \left[\frac{\sinh[\kappa(t-d)] - \sinh[\kappa(t-d-\delta)]}{\sinh(\kappa t)}\right] \tag{4.11}$$

where C^{MR} is a constant for a particular magnetorestitive head. This relationship differs from (4.8) in the sign of the imaginary term and here the Fourier transform of the vertical head field component is replaced by $\varphi(\kappa, 0)\coth(\kappa t)$. 1 Therefore noting (4.4), it is convenient to define the MR spectral response function as $\widehat{H}_y(\kappa,0)/\kappa$ so that the magnitude of this function relates to the output voltage in an analogous manner to the inductive case.

Approximations to spectral response functions can be obtained by using the approximations to the potential in the head face plane introduced in Section 3.1.4. Some of these approximations can be expressed in closed form. An approximate spectral response function for a conventional ring head without an underlayer was derived by Lübeck [86]. This result, which can also be obtained by taking the Fourier transform of Karlqvist's approximation to $H_x(x,0)$ (2.62), is:

$$\frac{\widehat{H}_x^{aR}}{V} = \frac{\sin(\kappa g)}{\kappa g} \tag{4.12}$$

which has zeros for $\kappa = n\pi/g$ *ie.* $G/\lambda = n$ for $n = 1, 2, 3, \cdots$. The true first null for the conventional ring head occurs when $G/\lambda = 0.88$ due to the non-linearity of the potential across the gap. Armed with this scaling factor for the first null, the Lübeck approximation is still in use. The approximations derived here are not of such a simple form as (4.12), but in general they approximate the appropriate true spectral response function more accurately than (4.12) does for the ring head.

The information lost by considering only the magnitude of the spectral response function is retained by examining its phase, *ie.* the resultant direction of the real and imaginary parts of the output voltage. A phase change by π radians is equivalent to a reversal of polarity of the magnetisation replayed [87]. From (4.8) and (4.11) it is clear that the phase angle $\Phi(\kappa)$ is given by

$$\Phi^{In}(\kappa) = \arctan\left(\frac{-Im\left[\widehat{H}_y(\kappa,0)\right]}{Re\left[\widehat{H}_y(\kappa,0)\right]}\right) \tag{4.13}$$

for an inductive head and in the case of an MR head by

$$\Phi^{In}(\kappa) = \arctan\left(\frac{Im\left[\widehat{H}_y(\kappa,0)\right]}{Re\left[\widehat{H}_y(\kappa,0)\right]}\right). \tag{4.14}$$

For symmetric replay heads abrupt phase changes by π radians occur at transition frequencies corresponding to the zeros of their spectral response functions. The interaction of the real and imaginary components of the spectral response functions for asymmetric heads results in continuous changes of phase over the entire range of transition frequencies. Clearly, approximations to the phase can be obtained from the approximations to the spectral response functions whose accuracy determines the quality of the approximate phase spectra obtained.

4.1.2 The Ring Head with an Underlayer

For the ring head with an underlayer, taking the Fourier transform of (2.28) evaluated at $y = 0$ leads to

$$\frac{\widehat{H}_y^{RU}(\kappa,0)}{V} = \frac{\sin(\kappa g)}{\kappa g}\left[1 + \sum_{n=1}^{\infty} A_n^{RU'}(-1)^n \frac{n\pi(\kappa g)^2}{(\kappa g)^2 - (n\pi)^2}\right]\coth(\kappa t) \qquad (4.15)$$

where the coefficients $A_n^{RU'}$ are given by (2.25). Apart from the $\coth(\kappa t)$ term and the coefficients which depend on g/t, this function is the same as the spectral response function for a ring head without an underlayer [24]. The function $\coth(\kappa t)$ has no zeros, therefore the difference in the positions of nulls in the two heads is due entirely to the coefficients. The $\coth(\kappa t)$ term influences the magnitude of the response; for the conventional ring head $\widehat{H}_x^R(\kappa,0) \longrightarrow 1$ as $\kappa \longrightarrow 0$, but when an underlayer is present $\widehat{H}_x^{RU}(\kappa,0)$ is unbounded as $\kappa \longrightarrow 0$. These features are shown in Fig. 4.1.

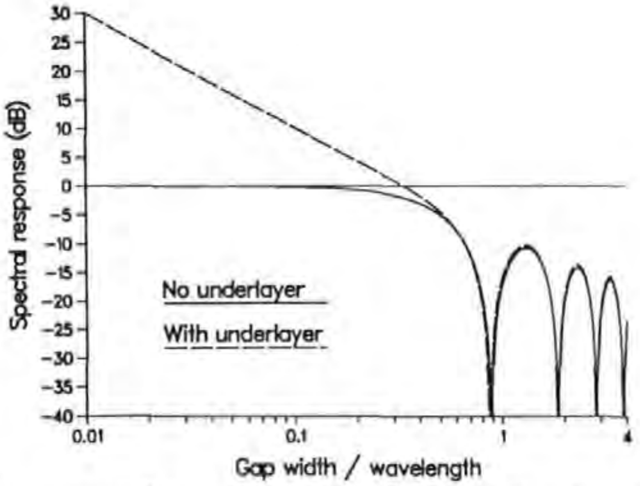

Figure 4.1: Spectral response function for a ring head with $g/t = 0.5$, and without an underlayer present.

4.1.3 The Thin Film Heads with Constant and Linearly Varying Pole Potentials

4.1.3.1 Constant potential poles

The spectral response function for the thin film head with constant potential poles has been derived using (4.4) and the potential functions given in (3.8), (3.3) and (3.11), all evaluated at $y = 0$:

$$\begin{aligned}
\frac{\widehat{H}_y^c(\kappa,0)}{V} = {} & 2\coth(\kappa t)\left\{\sin(\kappa g)\left[\frac{1}{\kappa g} + \sum_{n=1}^{\infty}\frac{\left(1-e^{-2n\pi t/g}\right)}{\left[(\kappa g)^2-(n\pi)^2\right]}\frac{\kappa g^2}{n\pi t}\right]\right. \\
& + \frac{2\kappa}{\pi} SI_0^{TF} - \cos\left(\kappa(g+2L)\right) \\
& \left. + \sum_{n=1}^{\infty} 2n\kappa(-1)^n\left[(B_n^{C'}e_n + D_n^{C'})SJ_n + (B_n^{C'} + D_n^{C'}e_n)SI_n^{TF}\right]\right\} \qquad (4.16)
\end{aligned}$$

where $e_n = e^{-2n\pi L/t}$,

$$SI_n^{TF} = \int_0^{\infty}\frac{\sin^2(k)}{\left[k^2-(n\pi)^2\right]}\frac{t}{\left[k^2+(\kappa t)^2\right]}\left[k\sin\left(\kappa(g+2L)\right) + \kappa t\cos\left(\kappa(g+2L)\right)\right] dk\,, \qquad (4.17)$$

$$SJ_n = \int_0^{\infty}\frac{\sin^2(k)}{\left[k^2-(n\pi)^2\right]}\frac{t}{\left[k^2+(\kappa t)^2\right]}\left[\frac{k\sin(\kappa g)}{\tanh(kg/t)} - \kappa t\cos(\kappa g)\right] dk\,, \qquad (4.18)$$

and $B_n^{C'}$ and $D_n^{C'}$ are the normalised constant potential Fourier coefficients calculated as in (3.19)-(3.21). Closed form expressions for SI_n^{TF} and SJ_n have not yet been obtained.

True nulls in the spectral response function occur when $\sin(\kappa g) \simeq 0$. It is clear from (4.16) that the exact null positions are influenced not only by the series which is independent of the Fourier coefficients, but also by terms dependent on the full head width, $2(g+2L)$. The series dependent on the Fourier coefficients, $B_n^{C'}$ and $D_n^{C'}$, has only a minor effect. Like the ring head without an underlayer, at long wavelength, the spectral response function of a conventional thin film head approaches unity. The variation in the position of the first null with L/g for the constant potential thin film head without an underlayer has been approximated by Lindholm [75]. When an underlayer is present a similar pattern is obtained. Fig. 4.2 shows the variation in first true null position with L/g when $g/t = 0.5$ for thin film heads with constant pole potentials. Abrupt changes in first true null position occur. This is due to the presence or absence of initial minima . Fig. 4.3 shows the spectral response functions for a

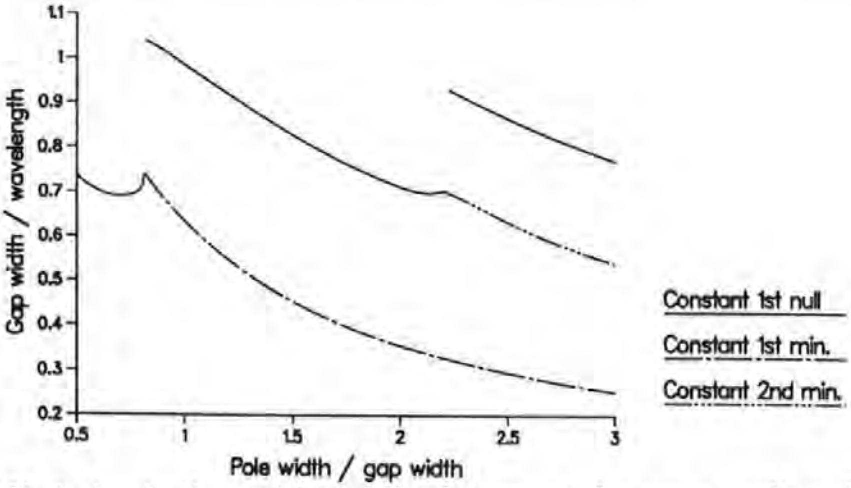

Figure 4.2: Variation in the position of the first spectral response null, and the preceding minima, with pole / gap ratio, for constant potential thin film heads, $g/t = 0.5$.

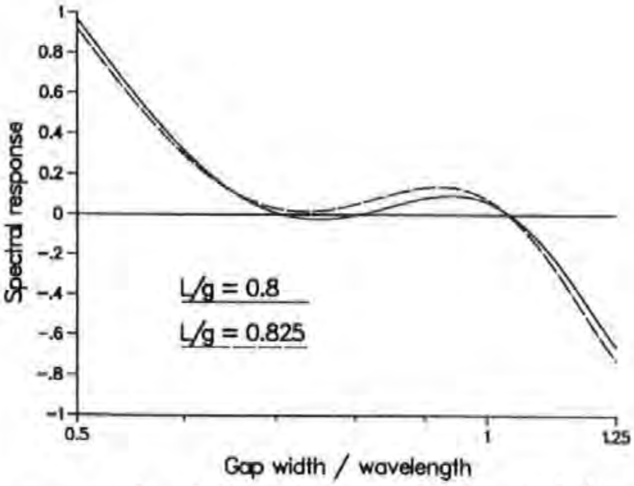

Figure 4.3: Spectral response functions for constant potential thin film heads, $L/g = 0.8$ and $L/g = 0.825$, $g/t = 0.5$.

constant potential thin film head when $L/g = 0.8$ and $L/g = 0.825$, with $g/t = 0.5$ in both cases. When $L/g = 0.8$ the first null occurs at $2g/\lambda = 0.71$ but when $L/g = 0.825$ the response does not quite drop to zero at $2g/\lambda = 0.74$ so a minimum rather than a true null occurs for this wavelength and the first null can be seen at $2g/\lambda = 1.04$. For $L/g \leq 0.82$ there is no initial minimum, but in general when the pole to gap ratio exceeds this value there will be at least one minimum at a longer wavelength than the first null, which is deep enough to limit replay.

A good approximation which requires the evaluation of only one numerical integral per wavenumber can be obtained by substituting the leading term approximation to the potential in the head face plane $\varphi^{aC}(x, 0)$ into (4.4). This results in the omission of the final series term of (4.16). The Fourier transform of the leading term of the potential function in region A can be expressed analytically but although the integral I_0^{TF} which occurs in leading term in region C can be written in closed form (3.90), its Fourier transform requires numerical evaluation.

In [63], the approximation to the potential at $y = 0$ given in (3.93) was used to derive an analytic approximate spectral response function. The approximate spectral response function for a head with relatively wide poles, $L/g = 3.32$ when $t/g = 2.4$, was compared with experimental results, corrected for spacing and thickness losses. Good agreement was found. Fig. 4.4 compares Yeh's approximate spectral response function with the approximation derived here and the exact theoretical function. A minimum occurs at a longer wavelength than does the first null for the constant potential head. As L/g increases, the number of minima preceding the first null also increases, and these have been observed in practice [63]. The interaction between the various terms in (4.16) also causes internull minima. The experimental first minimum occurred at $2g/\lambda \approx 0.208$. Yeh's approximation has its first minimum at $2g/\lambda = 0.21$, while the exact

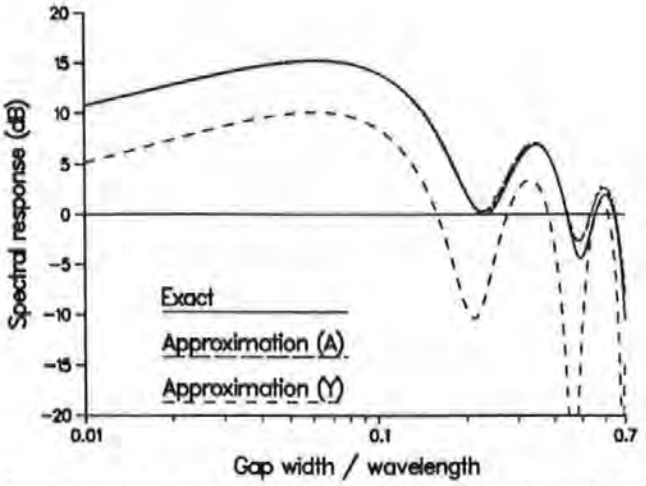

Figure 4.4: Exact and approximate spectral response functions (A-curve: the present approximation and Y-curve: the Yeh approximation) for constant potential thin film heads, $L/g = 3.32$, $g/t = 0.5$.

theoretical spectral response function and it approximation both have their first minima at $2g/\lambda = 0.23$ to 2dp. A second minimum in the experimental results is shown in [63], but although Yeh's approximation predicts the position very accurately, it has a null at this wavelength, not a minimum. Both the exact theoretical spectral response function and its approximation predict the second minimum. The experimental results which Yeh compares with his approximation have been corrected for spacing and thickness losses, but no reference is made to the constant $M_r C^{In}$ which also affects the magnitude of the output as given in (4.8). This constant might account for the difference in magnitude between Yeh's approximation which closely fits the experimental results and that of the exact theoretical spectral response.

Fig. 4.5 compares the exact and approximate spectral response functions for a constant potential thin film head where $L/g = 1.2$ and $g/t = 0.5$. The approximation proposed here and denoted A in Fig. 4.5 predicts the minima and the nulls quite accurately. Yeh's approximation predicts a much deeper initial minimum and two nulls either side of a peak at all the other minima; the gap nulls are predicted with reasonable accuracy.

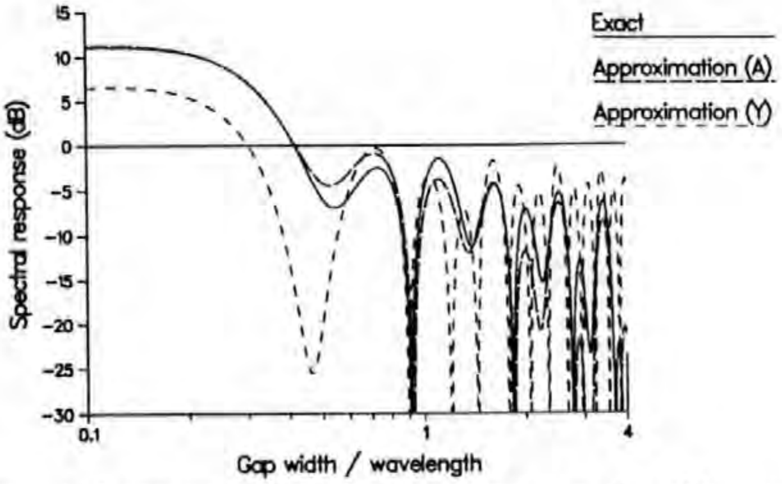

Figure 4.5: Exact and approximate spectral response functions (A-curve: the present approximation and Y-curve: the Yeh approximation) for a thin film head with constant pole potentials, $L/g = 1.2$, $g/t = 0.5$.

4.1.3.2 Linearly varying potential poles

The spectral response function for the thin film head with linearly varying pole potential is very similar to (4.16) except that the terms $(2\kappa/\pi)SI_0^{TF} - \cos(\kappa(g + 2L))$ are replaced by

$$-\frac{1}{\kappa L}\left[\cos(\kappa(g+L))\sin(\kappa L)\right] \tag{4.19}$$

and the normalised coefficients $B_n^{C'}$ and $D_n^{C'}$ are replaced by the linear potential pole coefficients $B_n^{L'}$ and $D_n^{L'}$ evaluated as in Section 3.1.1.3. Hence for a thin film head with linearly varying potential poles, where terms dependent on the full head width occur in the series involving the coefficients only, the full head width has less influence. The spectral response function for a linearly varying potential thin film head depends on the pole width, $2L$, and the gap plus one pole width, $2(g + L)$, in addition to the gap width and the full head width, on which the response of a constant potential thin film head depends. This results in a pattern of minima and peaks for a linearly varying pole potential thin film head which is more complex than for the comparable constant potential head. No minima precede the first null in the linearly varying pole potential case as can be seen in Fig. 4.7. Hence abrupt changes in the first null position do not occur when the poles have linearly varying potentials.

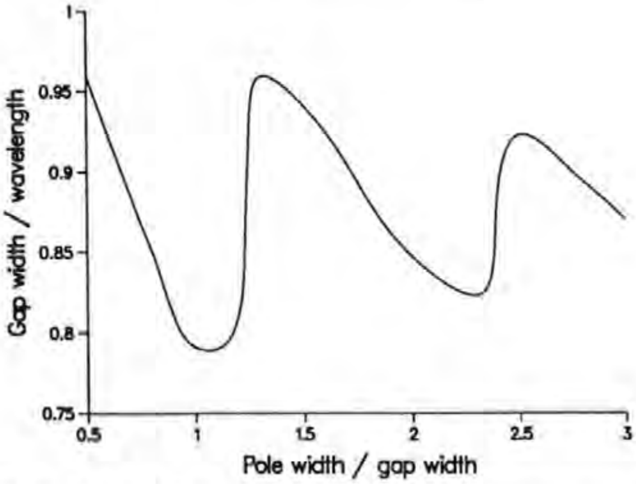

Figure 4.6: Variation in the position of the first spectral response null with pole / gap ratio, for thin film heads with linear pole potentials, $g/t = 0.5$.

Here the position of the first null, shown in Fig. 4.6 oscillates with decreasing amplitude as L/g increases to its limiting value of $2g/\lambda = 0.86$, when $g/t = 0.5$, which is the position of the first null for a ring head with an underlayer when $g/t = 0.5$. Mallinson [64] has suggested a similar behaviour when no underlayer is present, where the limiting value is that of the conventional ring head of longitudinal recording, $2g/\lambda = 0.88$. The zero potential outer edges of the poles cause severe reduction in response at long wavelengths and $\widehat{H}_y^L(\kappa, 0) \longrightarrow 0$ as $\kappa \longrightarrow 0$.

Here the approximate spectral response function obtained by using $\varphi^{aL}(x,0)$ (defined in Section 3.1.4.2) in (4.4) is fully analytic as the approximation to the potential at $y = 0$ for $x \geq g + 2L$ is zero in this case. Hence

$$\begin{aligned}\frac{\widehat{H}_y^{aL}(\kappa,0)}{V} &= 2\coth(\kappa t)\left\{\sin(\kappa g)\left[\frac{1}{\kappa g} + \frac{\kappa g^2}{\pi t}\sum_{n=1}^{\infty}\frac{1-e^{-2n\pi t/g}}{n\left((\kappa g)^2-(n\pi)^2\right)}\right]\right.\\ &\qquad\left. -\frac{1}{\kappa L}\left[\cos\left(\kappa(g+L)\right)\sin(\kappa L)\right]\right\}. \qquad (4.20)\end{aligned}$$

Fig. 4.7 compares the exact and approximate spectral response functions for a linear potential thin film head where $L/g = 1.2$ and $g/t = 0.5$. The approximation here is not

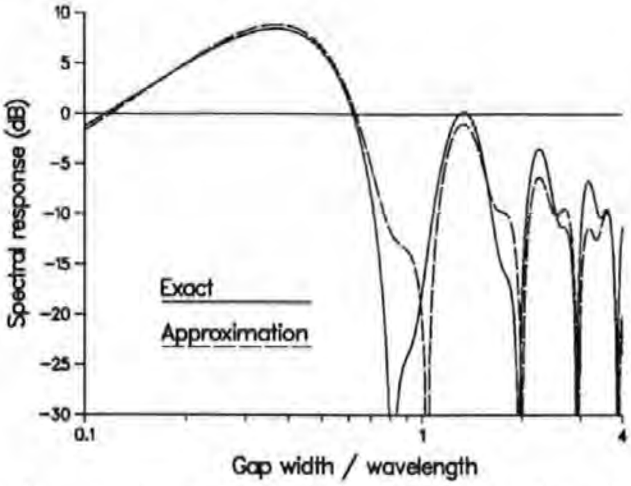

Figure 4.7: Exact and approximate spectral response functions for a thin film head with linearly varying pole potentials, $L/g = 1.2$, $g/t = 0.5$.

as accurate as the corresponding constant potential approximation. The approximation is good only up to the exact first null as it overestimates the frequencies at which nulls occur, particularly that for the first null.

4.1.3.3 Special cases

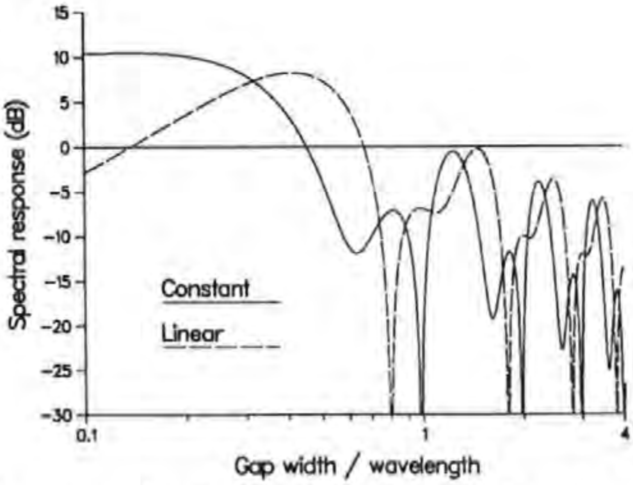

Figure 4.8: Spectral response functions for thin film heads with constant and linearly varying pole potentials, $L/g = 1.0, g/t = 0.5$.

When the head width equals the gap width some simplification of the spectral response functions occurs. Fig. 4.8 shows the spectral response functions for both thin film head types when $L = g$. For both pole potential distributions the response has two series of peaks separated by one series of nulls and one series of minima. The accuracy of each of the approximations to the constant potential thin film head for these dimensions is very similar to that shown in Fig. 4.5. For the head with linearly varying potential poles the approximation is much more accurate in this case. Here the first null position is overestimated by only 6% and the higher set of peaks are predicted quite accurately while the lower peaks at $2g/\lambda \approx n$ for $n = 1, 2, 3, \cdots$ are almost non-existent.

Another special case is when $g = 2L$; the response functions can be expressed in terms of the gap width only. Fig. 4.9 shows the response function for both pole potential distributions when $g = 2L$. Here each function has three series of peaks separated by two sets of nulls and one set of minima. No minimum occurs for the constant potential head at a longer wavelength than the first null. Neither of the approximations, for the constant potential thin film head with these dimensions, is as accurate as it is for larger L/t. Yeh's approximation can be expected to become less accurate as L/t decreases as his approximation to the potential at $y = 0$ (3.93) also deteriorates in these circumstances. The approximation to the spectral response function for the linear potential thin film head for these dimensions predicts the null positions with a maximum error of 2% but the magnitudes of all the peaks are less accurate than in the general case shown in Fig. 4.7.

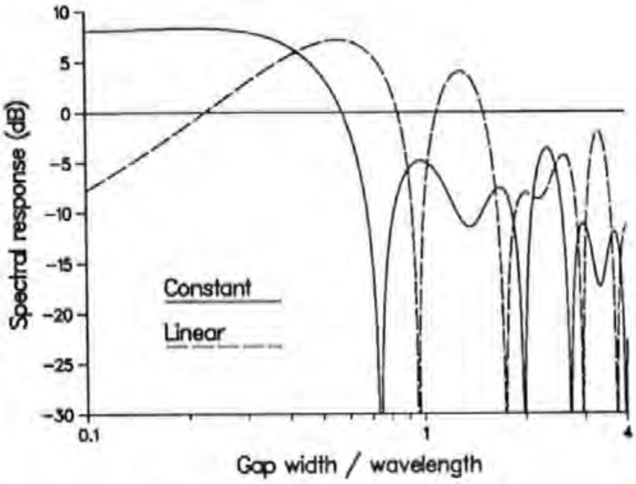

Figure 4.9: Spectral response functions for thin film head with constant and linearly varying pole potentials, $L/g = 0.5, g/t = 0.5$.

4.1.4 The Single Pole Heads with Constant and Linearly Varying Pole Potential

4.1.4.1 Constant pole potential

The spectral response function for a single pole head with constant pole potential is the Fourier transform of (2.13):

$$\begin{aligned}\frac{\widehat{H}_y^P(\kappa,0)}{V} &= \frac{2\sin(\kappa L)}{\kappa t} + \frac{1}{\pi(\kappa t)^2}\left[\cos(\kappa L)SK_0 - \sin(\kappa L)\zeta\right] \\ &+ \sum_{n=1}^{\infty}\frac{n(-1)^n B_n^{P'}}{(n\pi)^2+(\kappa t)^2}\left\{\cos(\kappa L)\left[2n\pi^2\tanh\left(\frac{n\pi L}{t}\right)+SK_n\right]+\sin(\kappa L)\left[2\kappa t\pi-\zeta\right]\right\}\end{aligned} \tag{4.21}$$

where

$$SK_n = 2n\pi\mathrm{Si}(2n\pi) + \kappa t\left[e^{-2\kappa t}\mathrm{Ei}(2\kappa t) - e^{2\kappa t}\mathrm{Ei}(-2\kappa t)\right] \tag{4.22}$$

and

$$\zeta = \kappa t\pi(1 - e^{-2\kappa t}). \tag{4.23}$$

Si and Ei are defined in Section A.1. As $\kappa \longrightarrow 0$ this function is unbounded.

Fan [23] evaluates a similar integral for the flux through a perpendicular head due to a magnetised medium adjacent to the pole by including the integration through the depth of the medium as in (2.71). However, he only appears to calculate the contribution from region B, directly underneath the pole, and there seems to be a slight error in his result ([23], equn.(11)), the factor $\cosh(n\pi)$ should be $2\cos(\pi L/\lambda)$. Computation of the null positions for a constant potential single pole confirms the accuracy of results given in [88],[89] and comparisons with practical measurements [88],[90] validate the modelling assumptions made for this head configuration.

The approximate spectral response function, derived using φ^{aP} (3.94),

$$\frac{\widehat{H}_y^{aP}(\kappa,0)}{V} = 2\coth(\kappa t)\left[\sin(\kappa L) + \frac{2\kappa}{\pi} S I_0^P\right] \tag{4.24}$$

where

$$S I_0^P = \int_L^\infty I_0^P \cos(\kappa x)\, dx \tag{4.25}$$

and I_0^P is given in closed form in (A.14), has not yet been expressed in closed form.

The semi-empirical approximate vertical field component at $y = 0$ given in [83] can also be used to estimate the spectral response function for a conventional single pole head. Hence

$$\begin{aligned} \frac{\widehat{H}_y^{aS}(\kappa,0)}{H_y(0,0)} &= 2\left\{\int_0^{L'} \left(C_3 + \frac{4L^2C_2}{4L^2C_4^2 - x^2}\right)\cos(\kappa x)\, dx \right. \\ &\quad \left. + \int_{L'}^\infty \left(\frac{2LC_1}{x + 2LC_0}\right)\cos(\kappa x)\, dx\right\}. \end{aligned} \tag{4.26}$$

Formulae for the coefficients C_{1-4} are given in [83] and to improve the approximation, the pole width is extended to $L' = 1.035L$ as suggested by Szczech.

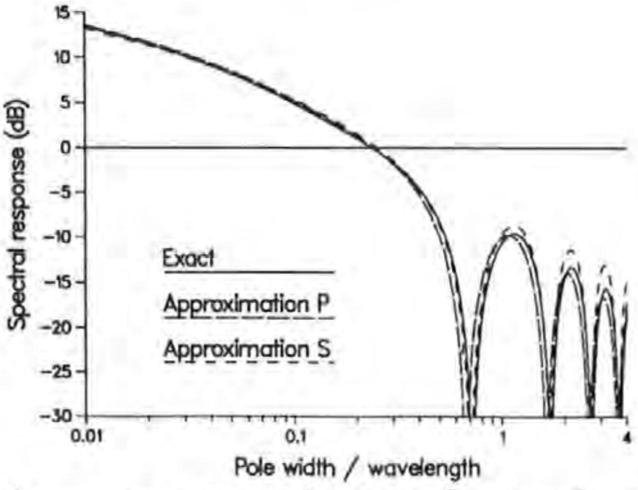

Figure 4.10: Exact and approximate spectral response functions for a constant potential single pole head, $L/t = 0.5$. $\widehat{H}_y^{aP}/V$ and $\widehat{H}_y^{aS}/V$ are denoted P and S respectively.

Fig. 4.10 shows the exact and both approximations to the spectral response of a constant potential pole when $L/t = 0.5$. $H_y(0,0)$, normalised by V, in (4.26) has been calculated using the exact vertical field component, given by (2.13). For $L/t = 0.5$, nulls in the spectral reponse function occur at $2L/\lambda = 0.71, 1.69, 2.69, 3.68 \cdots$. The approximation $\widehat{H}_y^{aP}$ has zeros at $2L/\lambda = 0.67, 1.63, 2.62, 3.61, \cdots$, while the approximation $\widehat{H}_y^{aS}$ obtained from Szczech's vertical field component is more accurate, having zeros at $2L/\lambda = 0.70, 1.68, 2.67, 3.65, \cdots$. If instead, the pole width is not adjusted in $\widehat{H}_y^{aS}$, *ie.* $L' = L$ is used, less accurate results are obtained with zeros at $2L/\lambda = 0.76, 1.80, 2.82, 3.84 \cdots$. As L/t increases, the Fourier coefficients in the exact response decrease in magnitude so that $\widehat{H}_y^{aP}$ becomes more accurate. $\widehat{H}_y^{aS}$ can be expected to give results of similar accuracy to those shown in Fig. 4.10 provided that $L/t \leq 1.25$ as recommended for the use of the Szczech field equations. Both of these approximations require some numerical integration and for $\widehat{H}_y^{aS}$ the coefficients C_{1-4} must also be computed.

4.1.4.2 Linearly varying pole potential

The spectral response of a single pole head with linearly varying pole potential has real and imaginary parts. The real component is half of $\widehat{H}_y^P(\kappa, 0)$, given in (4.21), due to the fact that $B_n^{LP'} = B_n^{P'}/2$ and

$$\mathrm{Im}\left[\frac{\widehat{H}_y^{LP}(\kappa,0)}{V}\right] = \frac{1}{\kappa t}\left[\frac{\sin(\kappa L)}{\kappa L} - \cos(\kappa L)\right] + \frac{1}{2\pi(\kappa t)^2}\left[\sin(\kappa L) SK_0 + \cos(\kappa L)\zeta\right]$$
$$+ \sum_{n=1}^{\infty} \frac{n(-1)^n D_n^{LP'}}{(n\pi)^2 + (\kappa t)^2}\left\{\sin(\kappa L)\left[2n\pi^2 \coth\left(\frac{n\pi L}{t}\right) + SK_n\right] - \cos(\kappa L)\left[2\kappa t\pi - \zeta\right]\right\} \tag{4.27}$$

with SK_n and ζ given by (4.22) and (4.23) respectively. This function is unbounded as $\kappa \longrightarrow 0$. The real and imaginary parts of the spectral response function for a single pole

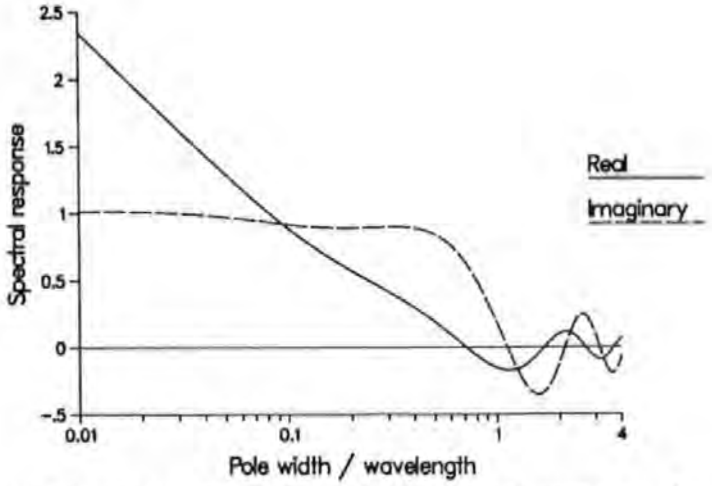

Figure 4.11: Real and imaginary parts of the spectral response function for a single pole head with linearly varying pole potential, $L/t = 0.5$.

with linearly varying pole potential are shown separately on a linear vertical scale in Fig. 4.11. At low frequency the imaginary component is unity while the real component increases without bound as $\kappa \longrightarrow 0$. At high frequency both contributions oscillate with decreasing amplitude as $\kappa \longrightarrow \infty$, the imaginary component having the larger amplitude. These spectral response function components are approximately out of phase by one quarter of their common oscillation wavelength, zeros of one corresponding to peaks of the other. Therefore the amplitude of the response has no zeros. For smaller L/t these functions have the same characteristics, with the imaginary component being even more dominant and from lower frequencies. Fig. 4.12 shows the phase spectrum for

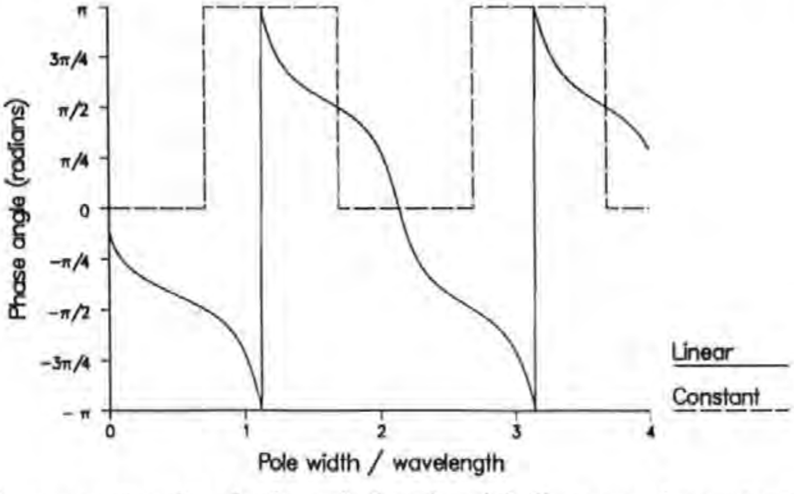

Figure 4.12: Phase spectra for single pole heads with linear and constant pole potentials, $L/t = 0.5$.

a single pole head with linear pole potential in comparison with that for a conventional constant potential pole, both when $L/t = 0.5$.

The approximate spectral response function obtained by substituting the leading terms of the potential at $y = 0$ into (4.4) is

$$\frac{\widehat{H}_y^{aLP}(\kappa,0)}{V} = \coth(\kappa t)\left\{\sin(\kappa L) + \frac{2\kappa}{\pi}SI_0^P + i\left[\frac{\sin(\kappa L)}{\kappa L} - \cos(\kappa L) + \frac{2\kappa}{\pi}SY\right]\right\} \tag{4.28}$$

where SI_0^P is given by (4.25) and

$$SY = \int_L^\infty I_0^P \sin(\kappa x)\,dx \tag{4.29}$$

with I_0^P given by (2.9). Another approximation can be derived from the solution for a single pole head with arbitrary pole potential and therefore both approximations to the spectral response function in the linear potential case are discussed in Section 4.1.5.

4.1.5 The Arbitrarily Varying Potential Single Pole Head.

4.1.5.1 Contributions from regions A and C

For the single pole heads with arbitrarily varying pole potential, the spectral response function is derived from $\varphi^{AP}(x,0)$ using (4.4). $\varphi^{AP}(x,0)$ is given by equns. (3.62) and (3.67) in regions A and C respectively, and by the exact pole potential, $f(x)$, in region B. For the analysis, the potential across the pole is assumed to be expressed as a Fourier series symmetric about $x = L$ with period $4L$, so that the contributions to the real and imaginary parts of $\widehat{\varphi}^{AP}$, normalised by V, from regions A

and C are:

$$\begin{aligned}
\mathrm{Re}\left[\frac{(\widehat{\varphi}_A^{AP}+\widehat{\varphi}_C^{AP})}{V}\right] &= \frac{2t}{\pi}\Bigg\{a_0\Big[\cos(\kappa L)SL-\sin(\kappa L)SM\Big] \\
&+(\alpha+\beta-a_0)\Big[\cos(\kappa L)SN-\sin(\kappa L)SR\Big] \\
&+\sum_{n=1}^{\infty}2n\pi(-1)^n B_n^{AP'}\Big[\cos(\kappa L)SS_n^P-\sin(\kappa L)ST_n^P\Big] \\
&+\sum_{N=1}^{\infty}2a_N\cos\left(\frac{N\pi}{2}\right)\Big[\xi_N\coth(\xi_N)\Big(\cos(\kappa L)SU_N-\sin(\kappa L)SV_N\Big) \\
&-\Big(\cos(\kappa L)SW_N-\sin(\kappa L)SX_N\Big)\Big]\Bigg\} \qquad (4.30)
\end{aligned}$$

and

$$\begin{aligned}
\mathrm{Im}\left[\frac{(\widehat{\varphi}_A^{AP}+\widehat{\varphi}_C^{AP})}{V}\right] &= \frac{2t}{\pi}\Bigg\{(\beta-\alpha)\Big[\sin(\kappa L)SN+\cos(\kappa L)SR\Big] \\
&+\sum_{n=1}^{\infty}2n\pi(-1)^n D_n^{AP'}\Big[\sin(\kappa L)SS_n^P+\cos(\kappa L)ST_n^P\Big] \\
&+\sum_{N=1}^{\infty}2b_N\sin\left(\frac{N\pi}{2}\right)\Big[\xi_N\coth(\xi_N)\Big(\sin(\kappa L)SU_N+\cos(\kappa L)SV_N\Big) \\
&-\Big(\sin(\kappa L)SW_N+\cos(\kappa L)SX_N\Big)\Big]\Bigg\} \qquad (4.31)
\end{aligned}$$

where $\xi_N = N\pi t/2L$, $B_n^{AP'}$ and $D_n^{AP'}$ are the normalised Fourier coefficients calculated as in (3.75) and (3.76), α and β are the proportions of the maximum potential at the leading and trailing edges respectively which depend on $\varphi_B^{AP}(x,0)$,

$$SL=\int_0^{\infty}\frac{\sin^2(k)}{k[k^2+(\kappa t)^2]}\,dk \qquad (4.32)$$

and

$$SS_n^P = \int_0^\infty \frac{k \sin^2(k)}{[k^2 - (n\pi)^2][k^2 + (\kappa t)^2]}\, dk \, . \tag{4.33}$$

All of the other integrals can be expressed analytically and are defined and given in closed form in Section A.4. Although SS_n^P and ST_n^P result from taking the Fourier transform of I_n^P (2.9), here the integration with respect to x has been performed first. For SI_n^P, which occurs in the spectral response functions of the single pole heads with constant and linearly varying pole potential, the integration with respect to k has been accomplished analytically, leaving the integration with respect to x to be achieved numerically.

To obtain an approximation to the spectral response function, it is only neccessary to approximate the potential at $y = 0$ for $|x| > L$ as the exact potential across the pole is known and need not be expressed as a Fourier series in deriving its Fourier transform. The two approximations considered here result from substituting φ^{aAP} (3.97) and φ^{aGP} (3.98) independently into (4.2). The approximation to the Fourier transform of $\varphi^{AP}(x,0)$ in regions A and C, when φ^{aAP} is used, omits the series including the $B_n^{AP'}$ and the $D_n^{AP'}$ in (4.30) and (4.31) respectively. When φ^{aGP} is used, the contributions from regions A and C are

$$\frac{(\hat{\varphi}_A^{aGP} + \hat{\varphi}_C^{aGP})}{V} = \frac{2}{\pi}(\alpha + \beta)\left(SI_0^P + SY\right) \tag{4.34}$$

where SI_0^P and SY, which both require partial numerical evaluation, are given by (4.25) and (4.29) respectively.

$\hat{\varphi}_B^{AP}(\kappa, 0)$ depends on the particular potential across the pole. The results for the four examples considered in Chapter 3 are given below. Single poles with at least one non-zero potential pole edge have unbounded spectral response functions as $\kappa \longrightarrow 0$.

4.1.5.2 Linear potential pole

$$\frac{\widehat{\varphi}_B^{AP}(\kappa,0)}{V} = \frac{1}{\kappa}\left\{\sin(\kappa L) - i\left[\frac{\sin(\kappa L)}{\kappa L} - \cos(\kappa L)\right]\right\}. \qquad (4.35)$$

The form of the spectral response function given here differs from that in Section 4.1.4.2 but numerical results have confirmed the equivalence and the accuracy of both expressions.

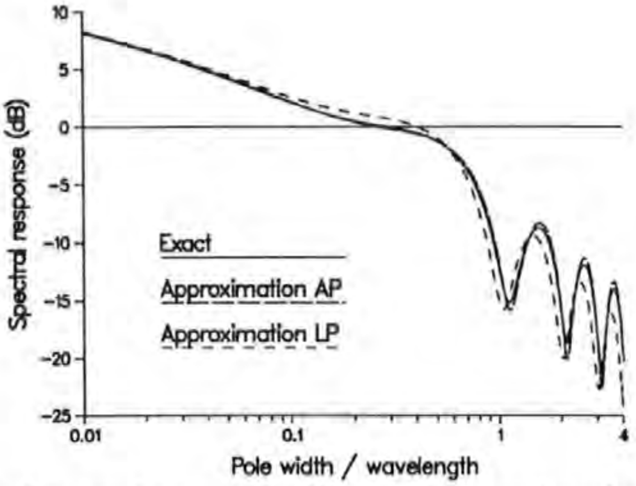

Figure 4.13: Exact and approximate spectral response functions for a linear potential single pole head, $L/t = 0.5$. $\widehat{H}_y^{aAP}/V$ and $\widehat{H}_y^{aLP}/V$ are denoted AP and LP respectively.

Fig. 4.13 shows the exact and the two approximations to the spectral response function for a single pole head with a linear pole potential when $L/t = 0.5$. Although the spectral response function has no zeros, deep minima occur at $\lambda \approx 2L$, which in practice would limit the use of the head. The approximation $\widehat{H}_y^{aAP}/V$ is more accurate and faster to compute (using library routines [33]) than $\widehat{H}_y^{aLP}/V$. $\widehat{H}_y^{aAP}$ requires the numerical evaluation of one integral over an infinite interval but $\widehat{H}_y^{aLP}$ involves two numerical integrals over a finite range. It seems that the convergence of the integrator used for $\widehat{H}_y^{aLP}$ is slower than that for $\widehat{H}_y^{aAP}$ possibly due to the oscillatory nature of the functions involved. Evaluation of $\widehat{H}_y^{aLP}$ is 2.5 times slower than the evaluation of $\widehat{H}_y^{aAP}$ using 150 terms, a relative error of 10^{-2} and an absolute error of 10^{-6}.

4.1.5.3 Quadratic potential pole

$$\begin{aligned}\frac{\widehat{\varphi}_B^{AP}(\kappa,0)}{V} &= \frac{1}{\kappa}\left\{\left[\left(1-\frac{1}{(\kappa L)^2}\right)\sin(\kappa L)+\frac{\cos(\kappa L)}{\kappa L}\right]\right.\\ &\qquad \left. -i\left[\frac{\sin(\kappa L)}{\kappa L}-\cos(\kappa L)\right]\right\}. \qquad (4.36)\end{aligned}$$

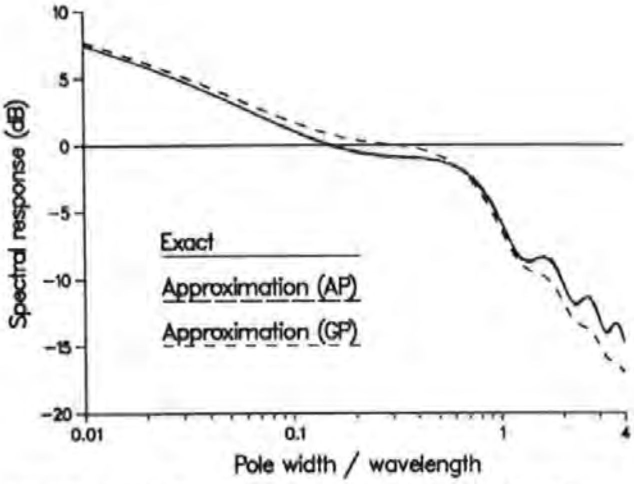

Figure 4.14: Exact and approximate spectral response functions for a quadratic potential single pole head, $L/t = 0.5$. $\widehat{H}_y^{aAP}/V$ and $\widehat{H}_y^{aGP}/V$ are denoted AP and GP respectively.

Fig. 4.14 shows the exact and the two approximations to the spectral response function for a single pole head with a quadratic pole potential when $L/t = 0.5$. The minima which occur at $\lambda \approx 2L$ are much shallower in this case than when the pole potential is linear. The approximation $\widehat{H}_y^{aAP}/V$ is very accurate but $\widehat{H}_y^{aGP}/V$ still provides a good estimate of the spectral response function and as more terms are needed for the convergence of $\widehat{H}_y^{aAP}$ here than in the linear potential case, the difference in computing time is less. Using the error bounds given in Section 4.1.5.2, the processing time has been found to increase according to

$$\text{time} = 0.0596N^{1.79}. \qquad (4.37)$$

Hence, $\widehat{H}_y^{aGP}$ is slower to compute than $\widehat{H}_y^{aAP}$, unless more than 248 terms are needed for the convergence of the latter. The phase spectrum is shown in Fig. 4.17.

4.1.5.4 Cubic potential pole

$$\begin{aligned}\frac{\widehat{\varphi}_B^{AP}(\kappa,0)}{V} &= \frac{1}{\kappa}\left\{\left(1-\frac{3}{2(\kappa L)^2}\right)\sin(\kappa L)+\frac{3\cos(\kappa L)}{2\kappa L}\right. \\ &\quad \left. - i\left[\frac{3}{2\kappa L}\left(1-\frac{1}{(\kappa L)^2}\right)\sin(\kappa L)+\left(\frac{3}{2(\kappa L)^2}-1\right)\cos(\kappa L)\right]\right\} . \qquad (4.38)\end{aligned}$$

Fig. 4.15 shows the exact and the two approximations to the spectral response function

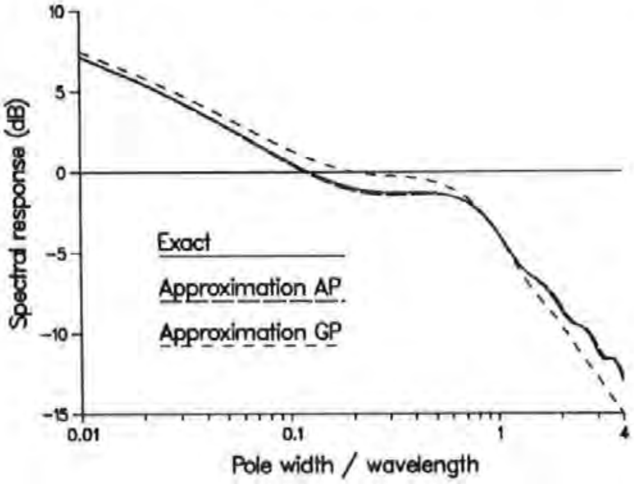

Figure 4.15: Exact and approximate spectral response functions for a cubic potential single pole head, $L/t = 0.5$. $\widehat{H}_y^{aAP}/V$ and $\widehat{H}_y^{aGP}/V$ are denoted AP and GP respectively.

for a single pole head with a cubic pole potential when $L/t = 0.5$. For this pole potential the minima in the spectral response function are almost eliminated. Here as in the linear and quadratic potential cases, $\widehat{H}_y^{aAP}/V$ is very accurate but a good estimate is given by the simpler $\widehat{H}_y^{aGP}/V$. The phase spectrum is shown in Fig. 4.17.

4.1.5.5 Cosine-squared potential pole

$$\frac{\widehat{\varphi}_B^{AP}(\kappa,0)}{V} = \frac{1}{\kappa}\left\{\sin(\kappa L)\left(\frac{\pi^2}{\pi^2-(\kappa L)^2}\right)\right\} \qquad (4.39)$$

and the spectral response function has real terms only. Here both pole edges have zero potential causing a bounded response as $\kappa \longrightarrow 0$.

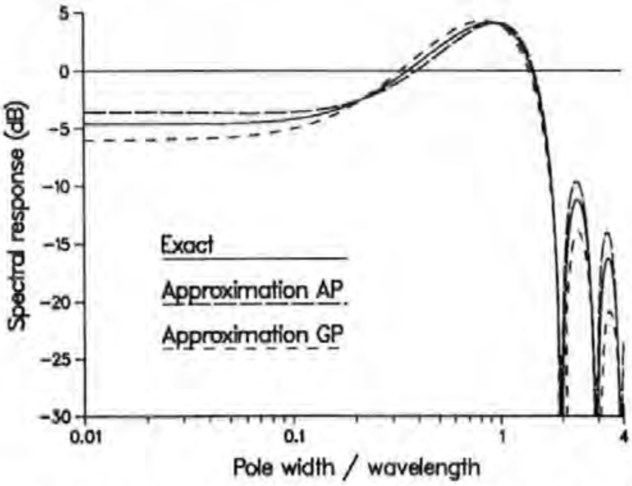

Figure 4.16: Exact and approximate spectral response functions for a cosine-squared potential single pole head, $L/t = 0.5$. $\widehat{H}_y^{aAP}/V$ and $\widehat{H}_y^{aGP}/V$ are denoted AP and GP respectively.

Fig. 4.16 shows the exact and the two approximations to the spectral response function for a single pole head with a cosine-squared pole potential when $L/t = 0.5$. The first null occurs at $2L/\lambda \approx 1.98$, a significantly higher frequency than that for a conventional constant potential pole head which occurs at $2L/\lambda \approx 0.71$ for $L/t = 0.5$.

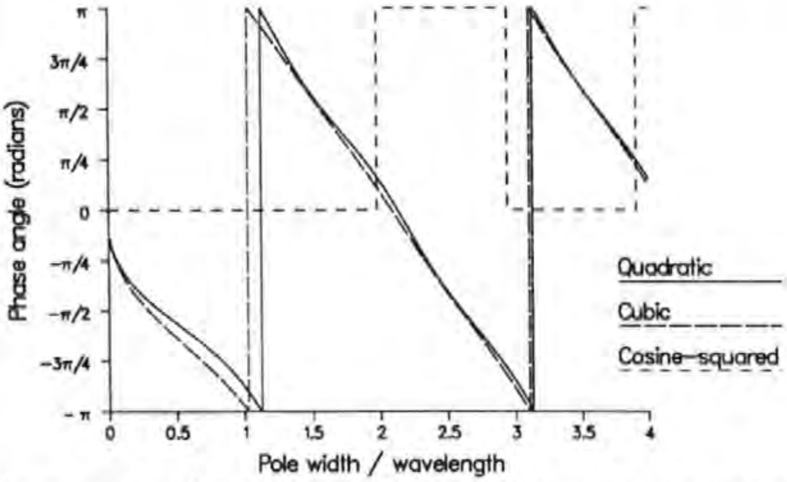

Figure 4.17: Phase spectra for single pole heads with quadratic, cubic and cosine-squared pole potentials, $L/t = 0.5$.

For this pole potential, evaluation of the exact spectral response is computationally less expensive than in the quadratic and cubic potential cases, as here the Fourier series for the potential is trivial. As $\alpha = \beta = 0$, $\widehat{H}_y^{aGP} = \kappa \coth(\kappa t)\widehat{\varphi}_B^{AP}(\kappa, 0)$, which can be evaluated on a calculator, and is only marginally less accurate than $\widehat{H}_y^{aAP}/V$.

Fig. 4.17 shows the phase spectra for single pole heads with quadratic, cubic and cosine-squared pole potentials, each when $L/t = 0.5$. In the non-symmetric cases, as the pole potential becomes less uniform, the phase variation with frequency becomes more linear and therefore more easily accommodated during the decoding of the replay signal. The phase for the cosine-squared pole potential has the typical form for a symmetric head with an even field function.

4.1.6 The Inductive Symmetrically Shielded Pole Head

The spectral response function for a symmetrically shielded pole head can be derived in two ways from the two solutions quoted in Section 2.1.3.5 but here due to its computational simplicity, the exact function is derived only from Solution I. Taking the Fourier transform of $\varphi^{\mathrm{I}}(x, 0)$ (2.31) gives:

$$\begin{aligned}
\frac{\widehat{H}_y^{\mathrm{I}}(\kappa, 0)}{V} = 2\coth(\kappa t)\Bigg\{ & \frac{\sin(\kappa g)\sin\left(\kappa(L+g)\right)}{\kappa g} \\
& + \sum_{n=1}^{\infty} A_n^{\mathrm{I}'} 2n\pi(-1)^{n+1}\left[\frac{\kappa g \sin(\kappa g)\sin\left(\kappa(L+g)\right)}{(\kappa g)^2 - (n\pi)^2}\right] \\
& + \sum_{n=1}^{\infty} B_n^{\mathrm{I}'} 2\left(n - \frac{1}{2}\right)\pi(-1)^n\left[\frac{\kappa g\cos(\kappa g)\cos\left(\kappa(L+g)\right)}{(\kappa g)^2 - \left[(n-\frac{1}{2})\pi\right]^2}\right]\Bigg\}
\end{aligned} \qquad (4.40)$$

where $A_n^{\mathrm{I}'}$ and $B_n^{\mathrm{I}'}$ are the normalised Fourier coefficients calculated as in (2.34) and (2.35) respectively.

The first null in the spectral response for a symmetrically shielded pole (4.40) occurs when $\sin(\kappa(L+g)) \approx 0$ so that $2(L+g)/\lambda \approx 1$. In general, the interference between pole- and gap-width effects causes three series of peaks and nulls, the relative size of each peak and the spacing of the nulls depending on the ratio L/g. Fig. 4.18 shows the spectral response for $L/t = 0.125$ and $g/t = 0.15$. As $\kappa \longrightarrow 0$ $\widehat{H}_y^{\mathrm{I}}(\kappa, 0) \longrightarrow 2(g+L)/t$.

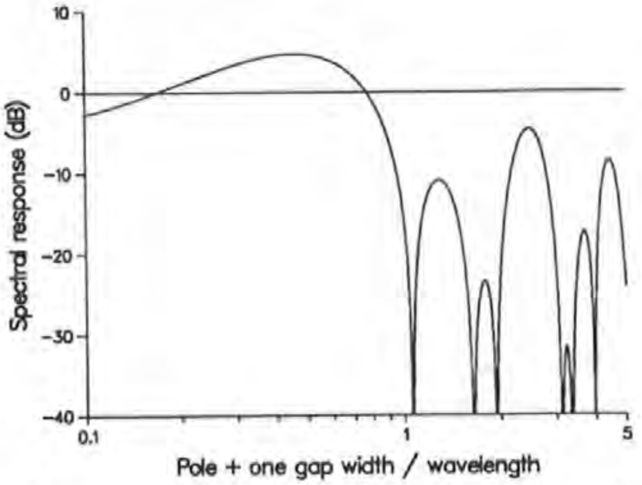

Figure 4.18: Spectral response function for a symmetrically shielded pole head, $L/g = 0.833, g/t = 0.15$.

When $L = g$ the spectral response function simplifies to:

$$\begin{aligned}\frac{\widehat{H}_y^{\mathrm{I}}(\kappa,0)}{V} &= 2\coth(\kappa t)\cos(\kappa g)\left\{2\frac{\sin^2(\kappa g)}{\kappa g}\right.\\ &\quad + \sum_{n=1}^{\infty} A_n^{\mathrm{I}'} 2n\pi(-1)^n\left[\frac{2\kappa g\sin^2(\kappa g)}{(\kappa g)^2-(n\pi)^2}\right]\\ &\quad \left.+ \sum_{n=1}^{\infty} B_n^{\mathrm{I}'} 2\left(n-\frac{1}{2}\right)\pi(-1)^n\left[\frac{\kappa g\cos(2\kappa g)}{(\kappa g)^2-[(n-\frac{1}{2})\pi]^2}\right]\right\} \qquad (4.41)\end{aligned}$$

and only two sets of peaks and one set of nulls occur.

Fig. 4.19 shows the spectral response function for a shielded pole with $L/t = 0.125$ as in Fig. 4.18 but here $g/t = 0.125$ also. True nulls occur due to the $\cos(\kappa g)$ term in (4.41) but are shifted slightly from $\kappa g = (n - \frac{1}{2})\pi$ for $n = 1, 2, 3, \cdots$ by the $B_n^{\mathrm{I}'}$ series. Minima occur because $\sin^2(\kappa g)$ is zero in the leading term and in the $A_n^{\mathrm{I}'}$ series when $\kappa g = n\pi$ for $n = 1, 2, 3, \cdots$ but the $B_n^{\mathrm{I}'}$ series is not zero for these values of κg. These minima are also shifted slightly from $\kappa g = n\pi$ by the $B_n^{\mathrm{I}'}$ series.

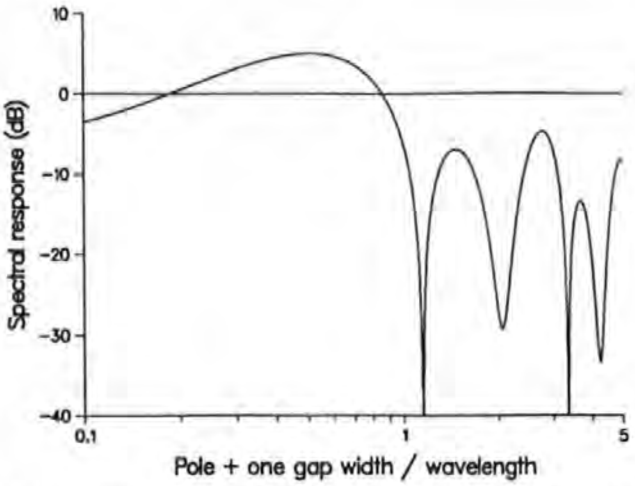

Figure 4.19: Spectral response function for a symmetrically shielded pole head, $L/g = 1.0, g/t = 0.125$.

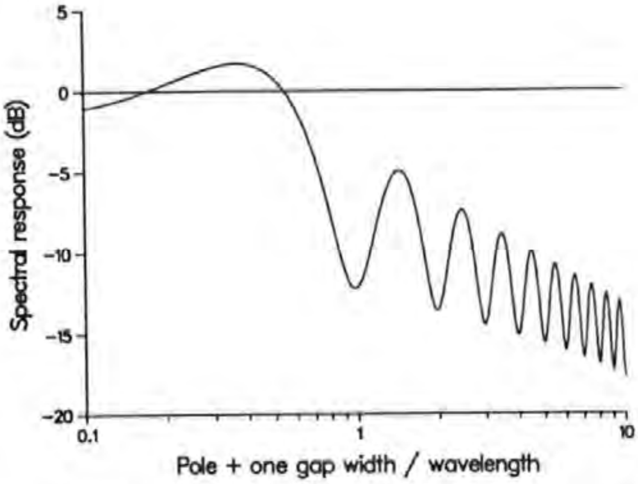

Figure 4.20: Spectral response function for a symmetrically shielded pole head, $L/g = 0.02, g/t = 0.5$.

The spectral response function of a very thin symmetrically shielded pole exhibits minima but no true nulls over usable wavebands. Fig. 4.20 shows the spectral response function for a shielded pole with an underlayer where $L/g = 0.02$ and $g/t = 0.5$. No true null occurs for $2g/\lambda < 25$, therefore no phase change occurs over the band width depicted. However, the minimum at $2g/\lambda = 0.96$ would be sufficient to limit replay. This phenomenon is discussed with particular reference to magnetoresistive heads, which are very thin, in Section 4.1.7.

Taking the leading term only of $\varphi^1(x,0)$ to compute an approximation to the spectral response function, $\widehat{H}_y^{a\,1}$, leads to the elimination of both series terms from (4.40) so that nulls are predicted to occur when $2(L+g)/\lambda = n$ and also when $2g/\lambda = n$ both for $n = 1, 2, 3, \cdots$. A more accurate approximation is obtained by substituting the leading terms of $\varphi^{\mathrm{II}}(x, 0)$ (2.42) into (4.2) to get

$$\begin{aligned}\frac{\widehat{H}_y^{a\,\mathrm{II}}}{V} &= \coth(\kappa t)\left\{\sin(\kappa L)\left(\frac{1-e^{-2\kappa t}}{\kappa t}\right)\right. \\ &\left. + \frac{4\kappa t}{\pi}\int_0^\infty \frac{\sin^2(k)}{k\left[k^2+(\kappa t)^2\right]}\left[\frac{\cos(\kappa L)}{\tanh(kG/t)} - \frac{\cos(\kappa(L+G)}{\sinh(kG/t)}\right] dk\right\} .(4.42)\end{aligned}$$

This approximation requires numerical integration and therefore is less convenient to evaluate than the exact response except that no Fourier coefficients are required.

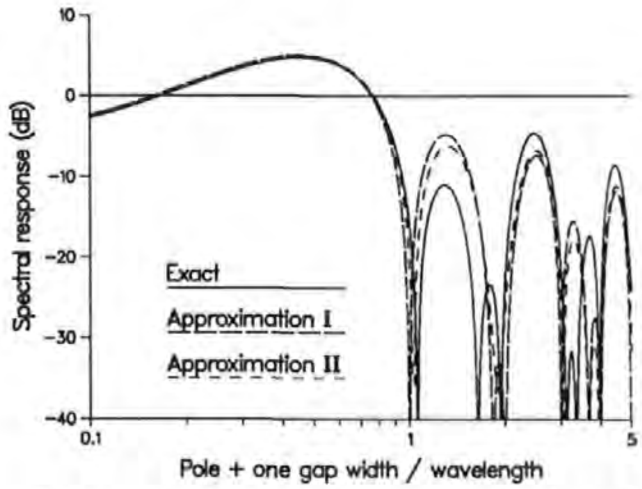

Figure 4.21: Exact and approximate spectral response functions for a symmetrically shielded pole head, $L/g = 0.833, g/t = 0.15$. $\widehat{H}_y^{a\,\mathrm{I}}/V$ and $\widehat{H}_y^{a\,\mathrm{II}}/V$ are denoted I and II respectively.

Fig. 4.21 compares both approximations and the exact spectral response function for a symmetrically shielded pole head with $L/g = 0.833$ and $g/t = 0.15$. For these head dimensions, where g/t is small, $\widehat{H}_y^{a\,\mathrm{II}}/V$ is only a little more accurate than $\widehat{H}_y^{a\,\mathrm{I}}/V$. Both approximations, in this very general case, predict only one set of the peaks and nulls reliably. As g/t increases the accuracy of $\widehat{H}_y^{a\,\mathrm{I}}/V$ declines. When $L = g$, as shown in Fig. 4.22, $\widehat{H}_y^{a\,\mathrm{II}}/V$ correctly predicts minima not nulls at $2(L+g)/\lambda \approx 2n$ for $n = 1, 2, 3, \cdots$. The positions of the mimina and the magnitudes of the peaks are also

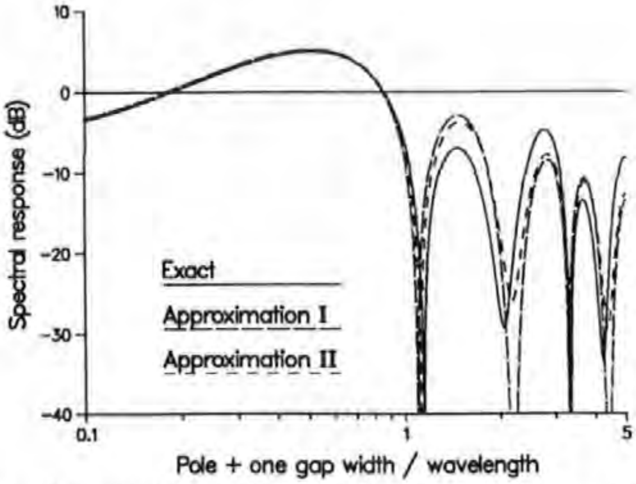

Figure 4.22: Exact and approximate spectral response functions for a symmetrically shielded pole head, $L/g = 1.0, g/t = 0.125$. $\widehat{H}_y^{a\,\mathrm{I}}/V$ and $\widehat{H}_y^{a\,\mathrm{I}}/V$ are denoted I and II respectively.

predicted slightly more accurately by $\widehat{H}_y^{a\,\mathrm{II}}/V$, even though $g/t = 0.125$ in this example. Similar results are obtained for a very thin pole. Again, $\widehat{H}_y^{a\,\mathrm{II}}/V$ predicts minima where $\widehat{H}_y^{a\,\mathrm{I}}/V$ predicts nulls. Potter [65] derived expressions for the flux entering a symmetrically shielded magnetoresistive head by assuming a Karlqvist-type linear potential drop across both gaps at $y = 0$, due to a sinusoidal magnetisation on a thick medium, without an underlayer. The zeros of his expression depend only on the two terms $\sin(\kappa g)$ and $\sin(\kappa(L + g))$ as also happens in $\widehat{H}_y^{a\,\mathrm{I}}/V$ with an underlayer present. Hence his approximation also predicts true nulls for $2(L + g)/\lambda = n$, for $n = 1, 2, 3, \cdots$.

4.1.7 Shielded Magnetoresistive Heads

For perpendicular magnetoresistive, the spectral response function is evaulated using $\widehat{\varphi}(\kappa, 0)\coth(\kappa t)$, as discussed in Section 4.1.1. The spectral response functions for shielded, infinitely thin magnetoresistive heads have been obtained numerically using:

$$\mathrm{Re}\left[\frac{\widehat{H}_y^A}{\kappa}\right] = \coth(\kappa t) \int_{-G_2}^{G_1} \varphi^A(x, 0)\cos(\kappa x)\, dx \qquad (4.43)$$

and

$$\operatorname{Im}\left[\frac{\widehat{H}_y^A}{\kappa}\right] = \coth(\kappa t)\int_{-G_2}^{G_1} \varphi^A(x,0)\sin(\kappa x)\,dx\,, \tag{4.44}$$

where $\varphi^A(x,0)$ is the real part of (3.137).

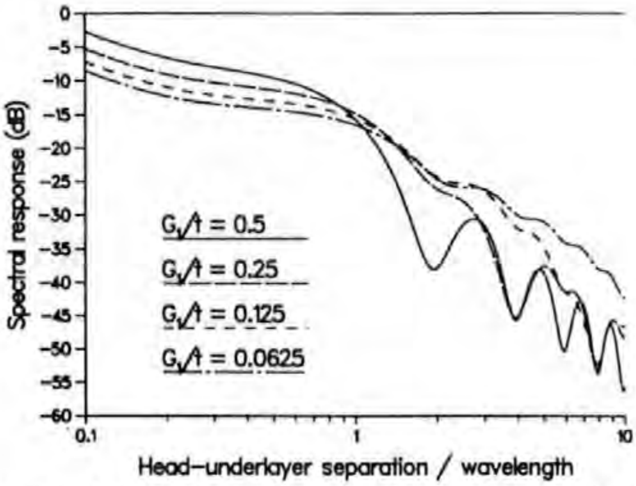

Figure 4.23: Variation in the spectral response functions of shielded, non-recessed, infinitely thin MR sensors with asymmetry, $G_2/t = 0.5$.

In Section 4.1.6 it has been shown that the spectral response of a very thin symmetrically shielded pole exhibits minima but no true nulls over a wide range of wavelengths. This model similarly predicts no true nulls over the range of usable wavelengths. Fig. 4.23 shows the variation in spectral response with asymmetry for non-recessed poles. In each case the left-hand gap remains fixed at $G_2/t = 0.5$. Clearly, the positions of the deeper minima depend on G_2/G_1 and the average gradient of the spectral response decreases as the shields are brought closer together. Lindholm [55] has used a boundary element method to compute the spectral response of a symmetrically shielded MR sensor with finite height and length. The shields are assumed to be only twice as long as the gap width and only twice as high as the sensor itself. The finite dimensions of the shields result in the spectral response tending to zero at very long wavelengths. Here, with semi-infinite shields, the spectral response appears to be unbounded as the wavelength increases. In [30], the spectral response function, for an MR sensor reading from a single layer medium, has been defined as $\kappa\widehat{\varphi}(\kappa,0)$ and hence the spectra obtained there approach zero as $\kappa \longrightarrow 0$.

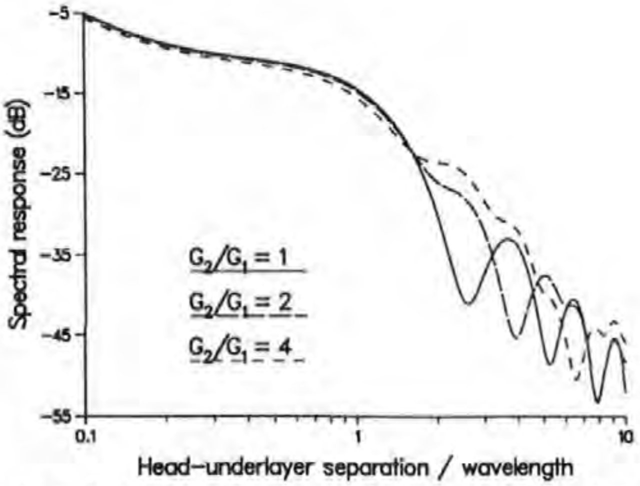

Figure 4.24: Comparison between the spectral response functions of symmetrically and asymmetrically shielded, non-recessed, infinitely thin MR sensors with the same inter-shield separation, $(G_1 + G_2)/t = 0.75$.

Fig. 4.24 shows the spectral response functions for three shielded MR sensors with the same inter-shield distance, $(G_1 + G_2)/t = 0.75$, one with a symmetrically placed pole and the other two with gap ratios $G_2/G_1 = 2$ and $G_2/G_1 = 4$, respectively. As the asymmetry of the head increases, the magnitude of the spectral response at long wavelengths marginally decreases but the main difference lies in the positions of some of the minima. Minima occur at wavelengths corresponding approximately to multiples of the gapwidths. So, in Fig. 4.24, for the symmetric case, minima occur at $G_1/\lambda t \approx 1, 2, 3, \cdots$. When $G_2/G_1 = 2$, the deeper minima occur where both $G_1/\lambda t \approx 2, 4, \cdots$ and $G_2/\lambda t \approx 1, 2, \cdots$, but only slight dips occur at $G_1/\lambda t \approx 1, 3, \cdots$ as there is a detectable signal from the left-hand side of the head. Similarly when $G_2/G_1 = 4$, the first deep minimum occurs where both $G_2/\lambda t \approx 1$ and $G_1/\lambda t \approx 4$. As a result of this, the first deep minimum for an asymmetrically shielded MR sensor occurs at a higher frequency than for a symmetrically shielded head with the same inter-shield dimension. Schwarz and Decker [66] have replayed a sinusoidal magnetisation recorded on a medium without an underlayer, through a shielded MR head and have found no nulls or minima over the range of wavelengths that they tested. Nulls were expected due to the use of the Potter [65] approximations which were derived assuming a linear potential drop across the gaps at $y = 0$, as in $\widehat{H}_y^{\mathrm{I}}$ (see Section 4.1.6), but without an underlayer. They attribute the lack of nulls to practical asymmetry in their head and give a gap ratio of 1.5 as possible within the tolerance of the head fabrication. For a symmetric head, minima but not nulls are predicted within the waveband tested, as stated above, but if the gap ratio was 1.5, the first minimum would not occur until $(G_1 + G_2)/\lambda \approx 4.9$ which is higher than the highest frequency detected by Schwarz and Decker.

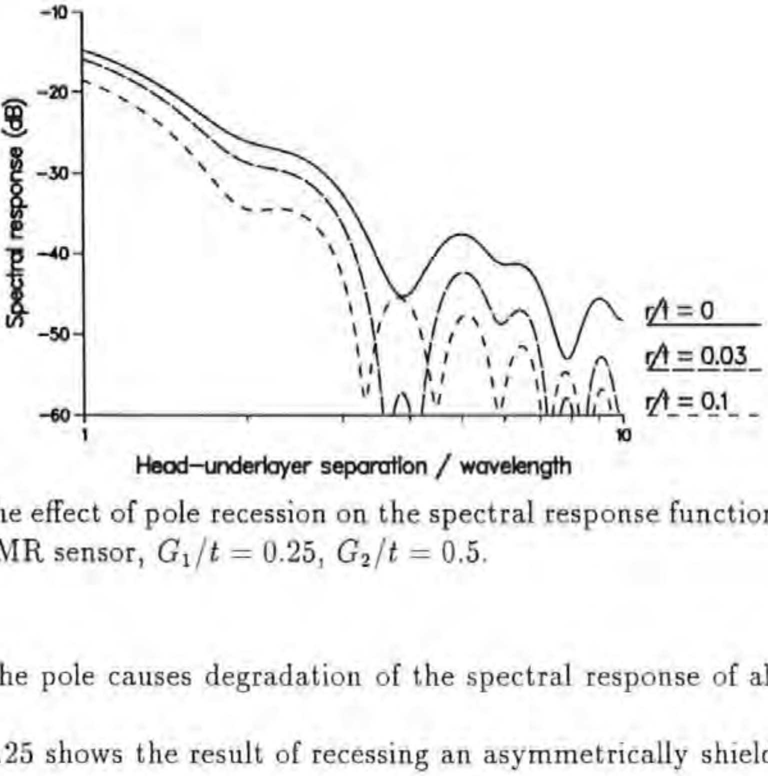

Figure 4.25: The effect of pole recession on the spectral response function of a shielded, infinitely thin MR sensor, $G_1/t = 0.25$, $G_2/t = 0.5$.

Recessing the pole causes degradation of the spectral response of all shielded MR sensors. Fig. 4.25 shows the result of recessing an asymmetrically shielded MR sensor where $G_1/t = 0.25$, and $G_2/t = 0.5$. Recession causes the minima to deepen and the rate of decline of the spectral response to increase so that if the pole is recessed sufficiently, true nulls occur within the frequency range depicted. The degree of recession necessary to cause true nulls depends only on the gap widths. For the example shown in Fig. 4.25 true nulls occur within the range of wavelengths shown for $r/t > 0.02$. For the head with a non-recessed pole, the interactions between both gap widths and the inter-shield separation distance results in minima rather than true nulls. When the pole is recessed, both 'inclined' gaps become effectively wider than the perpendicular distance from pole to shield. Therefore the sum of the two gap widths exceeds the inter-shield separation so that true nulls occur at longer wavelengths than in a non-recessed head. Symmetrically shielded poles suffer slightly worse than their equivalent asymmetric heads, due to the presence of deep minima only in the spectra of the non-recessed, symmetric heads.

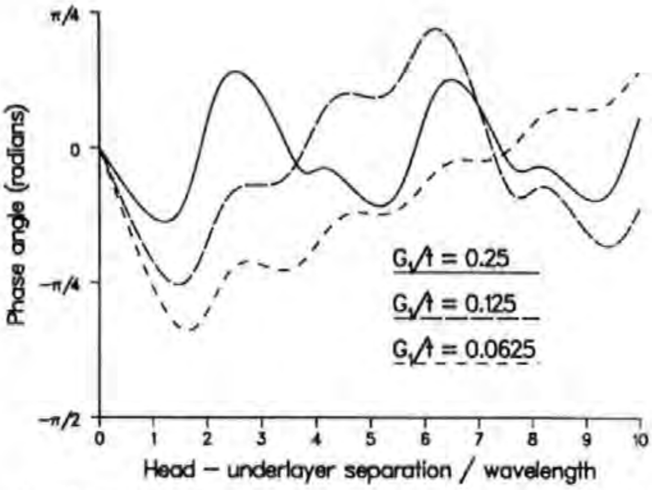

Figure 4.26: Variation in the phase of the spectral response of shielded, non-recessed, infinitely thin MR sensors with asymmetry, $G_2/t = 0.5$.

The spectral response of a symmetrically shielded MR sensor has an even component only. Therefore the phase changes abruptly by π radians, at the same frequencies which cause true nulls in the spectral response. Hence, for a non-recessed, symmetrically shielded pole no phase change would be detectable at the wavelengths used in practice.

An asymmetrically shielded MR sensor has both odd and even spectral response components and therefore the phase changes continuously over the full range of frequencies where no nulls occur in the spectral response, and there are abrupt changes in the phase where true nulls are found. Fig. 4.26 shows the variation in phase with asymmetry. The left-hand gap remains fixed at $G_2/t = 0.5$ while G_1/t varies from 0.25 to 0.0625. For $G_1/t = 0.5$ the phase is zero over the entire range of wavelengths shown. As the degree of asymmetry increases the amplitude and the period of the oscillations

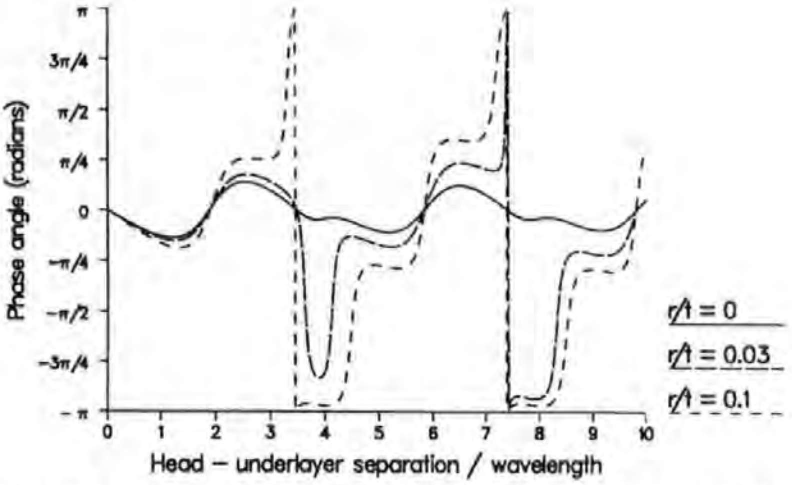

Figure 4.27: The effect of pole recession on the phase of the spectral response of a shielded, infinitely thin MR sensor, $G_1/t = 0.25$, $G_2/t = 0.5$.

increases.

Recessing the pole causes the phase to oscillate with greater amplitude and more irregularly at long magnetisation wavelengths than for the head with a non-recessed pole of the same dimensions. This effect is summarised in Fig. 4.27 where $G_1/t = 0.25$, $G_2/t = 0.5$ and the recession of the sensor varies from $r/t = 0$ to $r/t = 0.1$.

4.2 Square Wave Output

4.2.1 Linear Dibit Shift

Ideal magnetisation transitions are assumed to be recorded on perpendicular media so that

$$M_y(x') = \begin{cases} -M_r & x' < 0 \\ +M_r & x' > 0\,. \end{cases} \tag{4.45}$$

Therefore for an inductive perpendicular replay head, by reciprocity (2.70) the normalised output voltage due to a single transition is

$$\frac{e^{In}(\bar{x})}{M_r C'^{In}} = \int_{y=d}^{d+\delta} \int_{x=-\infty}^{\infty} 2\delta(x - \bar{x}) H_y(x, y)\, dx\, dy \tag{4.46}$$

which leads to

$$\frac{e^{In}(\bar{x})}{M_r C^{In}} = 2[\varphi(\bar{x}, d+\delta) - \varphi(\bar{x}, d)]\,. \tag{4.47}$$

The corresponding normalised output voltage due to a single transition read by an MR sensor is

$$\frac{e^{MR}(\bar{x})}{M_r C^{MR}} = \int_{-\infty}^{\bar{x}} [\varphi(x, d) - \varphi(x, d+\delta)]\, dx + \int_{\bar{x}}^{\infty} [\varphi(x, d+\delta) - \varphi(x, d)]\, dx\,. \tag{4.48}$$

Linear dibit shift is caused by the interference of the fields of two adjacent magnetisation transitions (a dibit) during replay. It is assumed that it is valid to superpose the ouput due to the individual transitions [91] so that for a pair of ideal transitions situated a distance b apart on the medium,

$$M_y(x) = \begin{cases} -M_r & x' < 0 \\ +M_r & 0 < x' < b \\ -M_r & x' > b \end{cases} \tag{4.49}$$

the output voltage is given by

$$e_{\text{dibit}}(\bar{x}) = e(\bar{x}) - e(\bar{x} - b) \tag{4.50}$$

Therefore for an inductive head the dibit output is

$$\frac{e^{In}_{\text{dibit}}(\bar{x})}{M_r C^{In}} = 2[\varphi(\bar{x}, d+\delta) - \varphi(\bar{x}, d) - \varphi(\bar{x} - b, d+\delta) + \varphi(\bar{x} - b, d)] \tag{4.51}$$

which produces output amplitude peaks corresponding to the transitions, while for an

MR head

$$\frac{e^{MR}_{\text{dibit}}(\bar{x})}{M_r C^{MR}} \propto \int_{\bar{x}}^{\bar{x}+b} [\varphi(x, d+\delta) - \varphi(x, d)]\, dx \tag{4.52}$$

for which zero crossings are expected at the transitions.

For all the inductive heads, analysed using the Fourier method, the dibit shift has been computed exactly. For the shielded MR heads, analysed using the conformal mapping method, it is difficult to calculate the potential for extreme values of x, where crowding in the transformation occurs. In these cases the exact potential is obtained at discrete intervals of 10^{-4} over the range $[-2G_2, 2G_2]$ (as $G_2 \geq G_1$ in all examples considered here). Linear interpolation is employed within the range and outside this interval the potential is assumed to drop off exponentially in accordance with solutions of Laplace's equation.

Linear dibit shift is a problem of pulse crowding. The superposition of the individual responses causes a shift in the position of the replayed transitions which can lead to errors in decoding as each transition is expected to occur within a cell of a particular length. This shift is measured as the difference between the bit cell length replayed and that recorded, as a percentage of the recorded bit length *ie.* $(T - b)/b$ where T is the distance between the replayed transitions. Clearly substituting from (4.2) into (4.51) allows the approximations to $\varphi(x, 0)$ to be used to provide good estimates of the dibit shift.

The simple dibit is only a representative example. Other combinations of bit patterns often cause greater shifts than the dibit. Worst case patterns depend on the coding method employed and therefore, in general, are not considered here. The numerical results are discussed in Section 4.3.2.

4.2.2 The Roll-off Curve

The spectral response function relates to output due to a sinusoidal magnetisation on the medium which allows comparison of different head configurations. In practice the magnetisation on a medium with perpendicular anisotropy is more closely approximated by a square wave. The roll-off curve is the peak output voltage due to a square wave magnetisation as a function of bit density. This type of response curve can be obtained experimentally for perpendicular heads, notably Fig. 5 of [8].

There are two ways of calculating the square wave output. Pulse superposition of ideal transitions (4.45) as described in Section 4.2.1 can be extended so that for a periodic rectangular magnetisation of wavelength λ

$$e^{SQ}(\bar{x}) = \sum_{n=-\infty}^{\infty} (-1)^n e\left(\bar{x} - \frac{n\lambda}{2}\right) . \tag{4.53}$$

Alternatively a square wave magnetisation of wavelength $\lambda = 2b$ can be represented by the Fourier sine series

$$M_y^{SQ}(x) = \frac{4M_r}{\pi} \sum_{n=1}^{\infty} \frac{1}{(2n-1)} \sin\left[(2n-1)\frac{\pi x}{b}\right] . \tag{4.54}$$

For a pure sinusoidal magnetisation with wavenumber κ, the output for a perpendicular inductive head is given in equn. (4.8) while for an MR sensor also in the presence of an underlayer it is given by (4.11). Hence, by superposing the output for $\kappa = (2n-1)\pi/b$ for $n = 1, 2, 3, \cdots$ using equn. (4.54), the square wave output may be computed in either case. Good estimate roll-off curves can be obtained by using the approximations to $\varphi(x, 0)$ in these computations in the same way as described for the approximate spectral response functions.

Interference between the adjacent bits, as the bit length decreases, affects the amplitude of the output voltage. The bit density at which the amplitude reduces to half that due to an isolated transition is termed the D_{50} density. Clearly, replay cannot be achieved if the amplitude of the signal is too small for detection. Numerical results are discussed in Section 4.3.3.

4.3 Discussion

4.3.1 Spectral Response Functions

4.3.1.1 The effects due to the geometric factors

HEAD	DOMINANT FACTOR	CONTRIBUTORY FACTORS
Ring	g	
Constant thin film	g	$g+2L$
Linear thin film	g	$g+L$, $g+2L$, L
Single pole	L	
Symmetrically shielded pole	$L+g$	g

Table 4.1: Geometric parameters responsible for spectral response nulls and minima.

Nulls in the spectral response function for a symmetric read head arise from non-zero gap and pole widths. Table 4.1 summarises the geometric parameters which cause nulls or minima in the spectral response functions of the heads considered in this thesis, which are evident from the expressions given in this chapter. The dominant factor causes the major nulls, and in particular the first null, while the contributory factor(s) cause other series of nulls or minima. It has already been shown (in Sections 4.1.6 and 4.1.7) that minima not true nulls occur over usable frequencies for very thin shielded pole heads.

The head–underlayer separation affects the spectral response in two ways. As t

increases from zero the coth(κt) term of (4.4) decreases to 1, and so influences the magnitude of the response, which increases as t decreases, for given head dimensions. The Fourier coefficients, which occur in all the exact spectral response functions given in this chapter, depend on the ratios L/t or g/t or combinations of both and the magnitudes of these coefficicients influence the positions of the nulls and minima. For example, in the case of the ring head both with and without an underlayer shown in Fig. 4.1. The presence of the underlayer causes a slight shift in null positions towards longer wavelengths and increases the magnitude of the response, especially at long wavelengths. Fig. 4.28 demonstrates the effect of head–underlayer separation on the

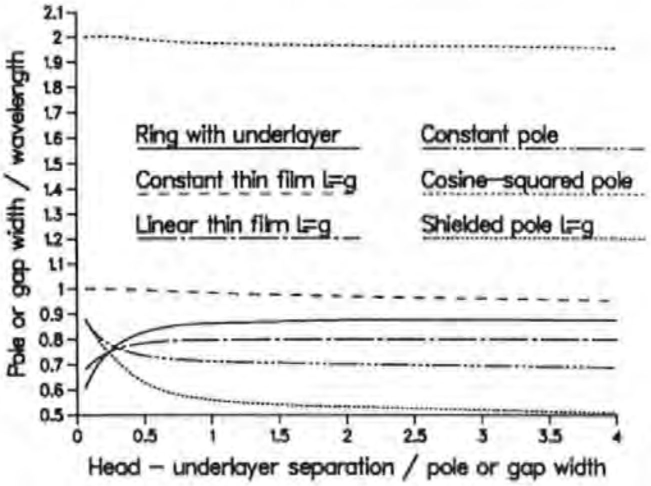

Figure 4.28: Variation in first spectral response null with head – underlayer separation.

position of the first null for various head configurations. For the shielded pole head and the thin film head the particular cases when pole and gap widths are equal have been chosen for ease of illustration.

For a ring head with an underlayer, as t decreases so the frequency at which the first null occurs decreases. Using a conformal mapping, Bertram and Lindholm [92] obtained the same change in the first null position for a ring head without an underlayer as a function of head-medium separation when the medium permeability was assumed to be infinite. A similar effect can be seen for the linear thin film head.

The cosine-squared pole and the constant potential thin film head with $L = g$ have first null positions which vary by only 4% over the range of underlayer separations shown. For the cosine-squared pole this is due to the lack of interaction between the pole edge and the underlayer, but for the constant potential thin film head, variation in t affects the potential in the gap as well as beyond the poles. When $L \neq g$ for a constant thin film head the first null position is still only slightly influenced by t.

For a relatively wide, shielded pole with L/g constant, as t decreases the pole – shield interaction diminishes so that the first null occurs at similar wavelengths to those for a corresponding conventional single pole. For $g/t \leq 0.25$ the coefficients A'_n and B'_n in (4.40) are almost independent of t [29] and $\coth(\kappa t) \to 1$ as t increases so that the position of the first null with respect to t is bounded. Similarly, head to underlayer separation has been found to have almost no influence on the spectral response function for a shielded MR sensor when $t > G_2$. This is corroborated by the results published for an MR sensor without an underlayer [30] where the null positions shown appear to be the same as those obtained here for $t > G_2$.

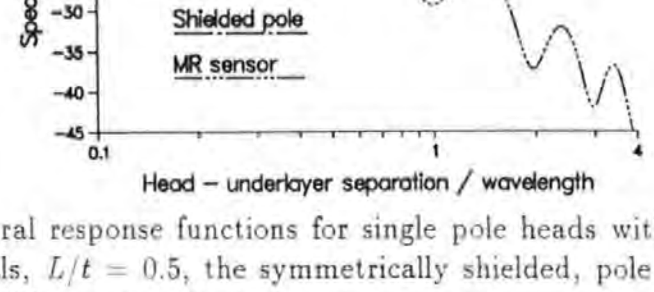

Figure 4.29: Spectral response functions for single pole heads with linear, quadratic and cubic potentials, $L/t = 0.5$, the symmetrically shielded, pole head $L/t = 0.001$ and infinitely thin MR sensor, $g/t = 0.5$.

Heads with asymmetric potentials and very thin shielded pole heads, including MR sensors, have no true nulls in their spectral response over the range of usable frequencies. Fig. 4.29 compares the spectral response of single poles with linear, quadratic and cubic pole potentials, each with $L/t = 0.5$, and of symmetrically shielded poles, both inductive and magnetoresistive with $g/t = 0.5$. The inductive shielded pole is very thin with $L/t = 0.001$, hence the positions of the minima for these shielded heads are virtually identical. The magnitude of the inductive shielded pole head remains higher than that of the MR sensor at high frequencies, but the spectral response function is independent of the efficiency of the head. The output voltage from a magnetoresistive head would be greater than that from a geometrically identical, inductive head. The spectral response function of the linear potential pole head is both flatter at long wavelengths and has its first minimum at higher frequency than either the thin symmetrically shielded pole or the symmetrically shielded MR sensor, both of whose gap widths equal the pole width of the linear potential single pole head. But the phase of the shielded pole is constant across the frequency range depicted, whereas that of the linear potential pole varies continuously. The positions of the minima for the linear and quadratic potential single poles vary less with t than do the nulls of the constant potential pole, but do still tend towards shorter wavelengths as t decreases. For example, when $L/t = 2.0$ the first minimum in the linear potential case occurs at $2L/\lambda = 1.14$, while for $L/t = 0.5$ this minimum occurs at $2L/\lambda = 1.12$, both correct to 2dp. The corresponding minima for the quadratic potential pole occur at $2L/\lambda = 1.49$ and $2L/\lambda = 1.35$ respectively. Minima in the response for the cubic potential pole are insignificant for $L/t \geq 0.5$. As $t \to \infty$ these models are inappropriate.

Fig. 4.30 compares the spectral response function of a single pole head with a cosine-squared potential with that of a conventional constant potential single pole of half the width. The first null in the case of the cosine-squared potential occurs at a frequency 41% higher than that for the thinner conventional single pole. Due to the

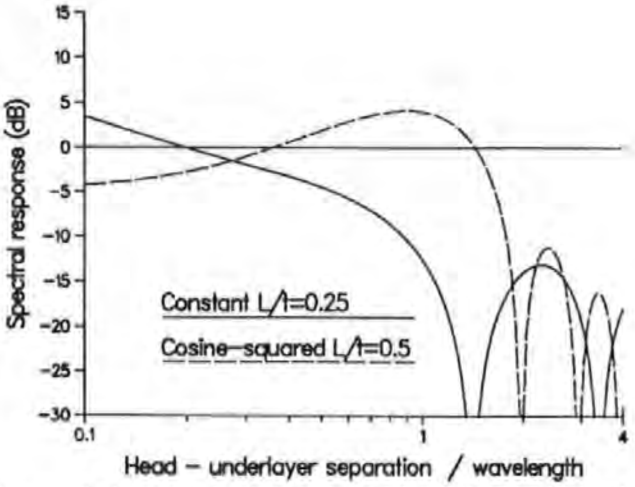

Figure 4.30: Comparison of the spectral response functions of single poles heads with constant potential, $L/t = 0.25$, and with a cosine-squared potential, $L/t = 0.5$.

similarity between the vertical field components of a cosine-squared potential single pole head when $L/t = 0.5$ and a symmetrically shielded pole head when $L/t = 0.125$ and $g/t = 0.15$, demonstrated in Fig. 3.58, the readback characteristics for these two heads are very similar also. This is confirmed by their spectral response functions shown in Fig. 4.31, where close correspondence can be seen up to the second null. But for $t/\lambda > 2$ the shielded pole experiences more nulls than the cosine-squared potential pole.

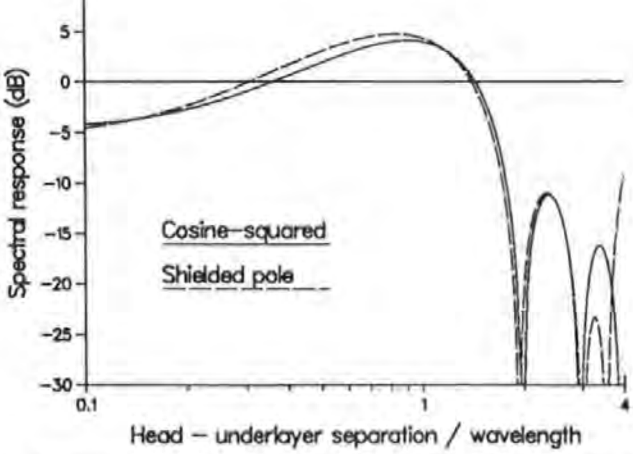

Figure 4.31: Spectral response functions for a cosine-squared potential single pole, $L/t = 0.5$, and a symmetrically shielded pole, $L/t = 0.125$, $g/t = 0.15$.

4.3.1.2 Comparison with experimental results

Experimental output results for a single pole head with a graded pole potential are given in [12]. The published result is a normalised roll-off curve which is compared with the spectral response function of a ring head without an underlayer. The gap width for the ring head is 1.2 times the width of the graded potential pole. It is claimed that this ring head result is equivalent to the spectral response for a conventional constant potential pole, of the same dimensions as the tested graded potential pole head.

The potential grading across the pole was achieved by using a sequence of laminations with varying chemical compositions. A constant maximum potential extends from the leading edge across 5/9.2 of the pole width, from where the potential decreases to zero at the trailing edge. The form of the recorded transitions is not specified, but as the medium used was of CoCr alloy with an underlayer (discussed in Section 1.2) an almost perfect square wave is likely, especially at high frequencies. The head – medium spacing has not been given explicitly, so it has been neccessary to assume this dimension. Accurate computation of the roll-off curve, under these circumstances, would provide no greater accuracy than the spectral response function. A comparison between the roll-off curve and the spectral response function, for a constant potential single pole head, is made in Section 4.3.3.1. From (4.54), it is clear that the spectral response function can be evaluated significantly faster than the roll-off curve.

The details of the laminations used in the construction of the head and the roll-off curve are reproduced here in Fig. 4.32. The total pole width is given as 9.2μm and a head – underlayer separation of 0.45μm has been assumed, based on the given medium thickness of 0.2μm. Two possible pole potential distributions have been considered for this head.

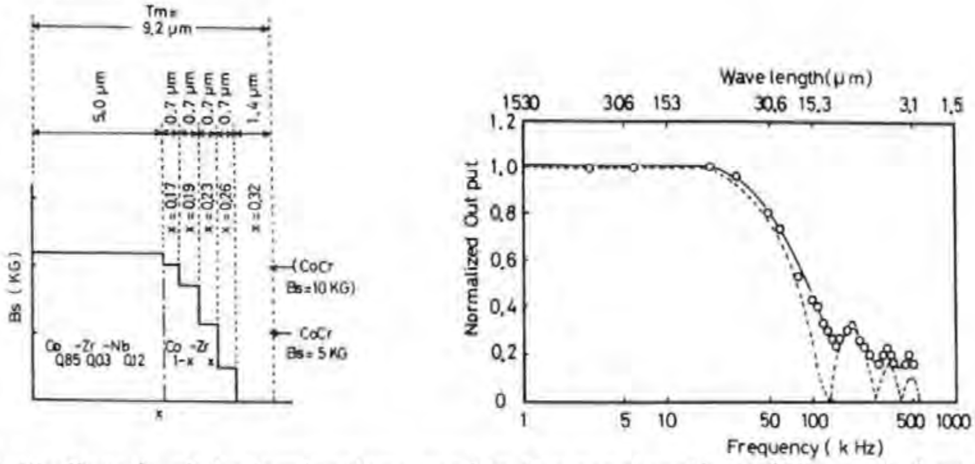

Figure 4.32: Details of the laminations used in the construction of the graded potential pole and its observed wavelength response (solid line) plotted with the theoretical spectral response of a ring head, $g = 5.5$, (dotted line). Figs. 3(a) and 4 of [12] respectively.

1. Constant-linear:

$$\frac{f(x)}{V} = \begin{cases} 1 & -L \leq x \leq 0.08L \\ (L - x)/0.92L & 0.08L \leq x \leq L \end{cases} \tag{4.55}$$

2. Contant-cosine-squared:

$$\frac{f(x)}{V} = \begin{cases} 1 & -L \leq x \leq 0 \\ \cos^2(\pi x/2L) & 0 \leq x \leq L\,. \end{cases} \tag{4.56}$$

The spectral response functions for both of these potential distributions are shown in Fig. 4.33, with the ring head result given in [12] and the exact spectral response for a constant potential single pole head. Each result has been normalised by its own magnitude at a frequency of 1. For each of the single pole-type heads, dimensions of $L = 4.6$ and $t = 0.45$ have been used and for the ring head $g = 5.5$ has been taken. There is a clear discrepancy between the responses of the constant potential pole and the ring head of these dimensions. The first null for this ring head occurs at a frequency of 123 kHz (if the dimensions are in μm and the disc drive operates at

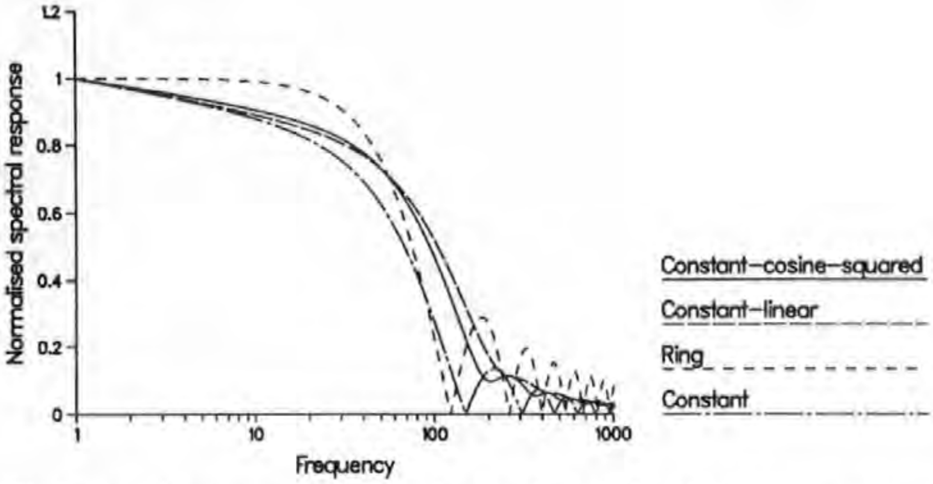

Figure 4.33: Spectral response functions for single pole heads with constant, constant-linear and constant-cosine-squared pole potentials, $L = 4.6$, $t = 0.45$, and for a ring head without an underlayer, $g = 5.5$.

300 rpm) which is 18% lower than the frequency at which the first null occurs for the constant potential single pole with $L/t = 10.2$. A ring head with a semi-gap width of 4.6 has its first null at a frequency only 3.4% lower than the conventional single pole considered here. Apart from the difference in the magnitude of the response, inherent in plotting the spectral response function instead of the roll-off curve, the results for the constant-cosine-squared potential closely match those shown in Fig. 4 of [12]. The minima in the response for this potential appear to occur at slightly higher frequencies than those obtained experimentally. The response for constant-linear potential is not such a good fit.

The first minimum in the response for the experimental head appears to occur at a similar frequency to that of a conventional single pole head with the same ratio of L/t. Unless the magnitude of the response of the graded potential head falls significantly less rapidly than that of the conventional single pole head, little advantage would be gained by using this particular potential distribution across the pole.

4.3.2 Linear Dibit Shift

4.3.2.1 Introduction

If an inductive perpendicular head reads a single ideal transition of the form given in (4.45) from a very thin medium, $\delta \to 0$, by reciprocity

$$e^{In}(\bar{x}) \propto \int_{-\infty}^{\infty} 2\delta(x-\bar{x}) H_y(x,d)\, dx = 2H_y(\bar{x},d). \tag{4.57}$$

The shape of the replay pulse is the same as that of the vertical head field. For a medium with finite thickness, the shape of the head field component is also evident in the replay pulse shape. Hence a head with a broad vertical field shape will experience greater linear dibit shift than one with a narrow single peak. Fig. 4.34 shows the normalised output voltage due to a perfect dibit of bit length $b/t = 1.25$ read from a thin medium, $\delta/t = 0.1$, by single pole heads of length $L/t = 0.5$, with both constant and linear pole potentials. This bit length corresponds to about 200,000 flux reversals per inch for a pole of width $0.1\mu m$. The figure illustrates the bimodal nature of each output peak for a conventional constant potential single pole, when the medium is close

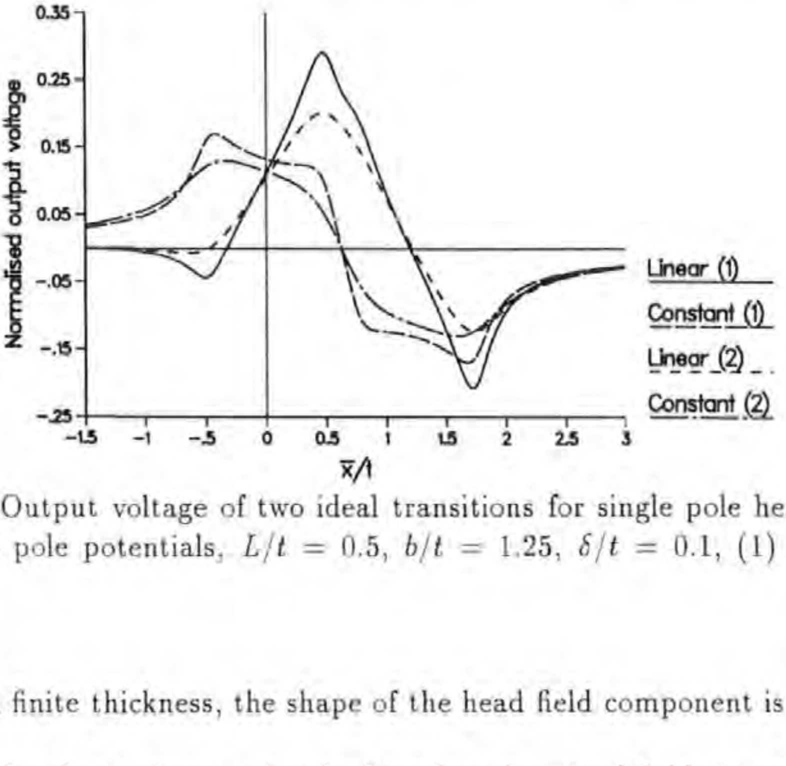

Figure 4.34: Output voltage of two ideal transitions for single pole heads with linear and constant pole potentials, $L/t = 0.5$, $b/t = 1.25$, $\delta/t = 0.1$, (1) $d/t = 0.1$, (2) $d/t = 0.25$.

to the pole face at $d/t = 0.1$. Interference between the pulses from the adjacent bits is noticeable although the bit length is relatively large. The amplitude of the output voltage is greater from the linear potential pole than from the conventional head, even when the medium is moved further from the pole face at $d/t = 0.25$.

4.3.2.2 The effects due to medium position and thickness

The spacing and thickness loss terms which occur in the output voltage expressions for inductive (4.8) and magnetoresistive (4.11) perpendicular replay heads as ratios of hyperbolic functions, both increase in magnitude as $d \to 0$ and $\delta \to t$. The highest output voltages can be achieved using thick media for in contact recording, but the linear dibit shift may be adversely affected by such media. Figs. 4.35 and 4.36 demonstrate how medium thickness and separation from the head face plane affect the linear dibit shift for single pole heads with constant and linear pole potentials respectively. The constant potential single pole head has a bimodal vertical field component, close to the pole face plane. Hence, reducing the head – medium separation from $d/t = 0.25$ to $d/t = 0.1$, for a thin medium with $\delta/t = 0.1$, causes an increase in the dibit shift. For this head, increasing the thickness of the medium from $\delta = 0.1$ to $\delta = 0.65$ while

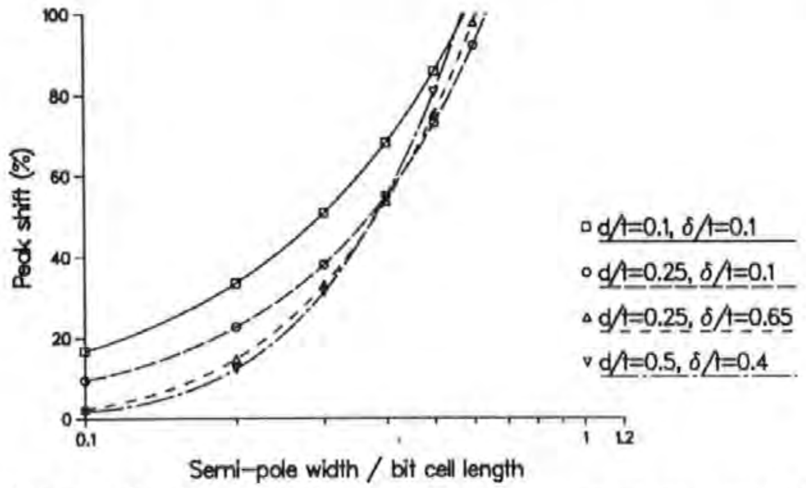

Figure 4.35: Peak shift of two ideal transitions for a constant potential single pole head, $L/t = 0.5$.

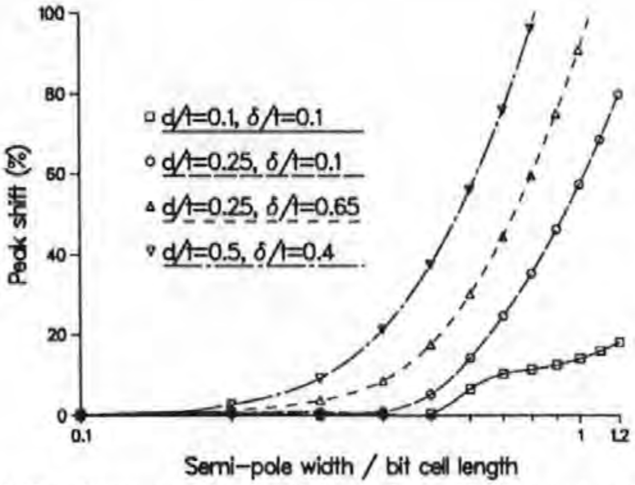

Figure 4.36: Peak shift of two ideal transitions for a linear potential single pole head, $L/t = 0.5$.

d/t remains fixed at 0.25, reduces the dibit shift for $L/b < 0.5$. Combinations of thick media fairly close to the pole face or thinner media further from the head produce similar results in this case. For each combination of d/t and δ/t, the linear potential single pole head produces less linear dibit shift than the corresponding constant potential pole. This is because its vertical field component has a single narrow peak. The worst shift shown for the linear potential pole is 92% at $L/b = 0.8$ while for each of the examples given for the constant potential pole, shifts of over 100% occur for $L/b < 0.6$. Clearly, increasing either the medium thicknes or its separation from the pole face is detrimental to the dibit shift for the linear potential single pole head. Sim-

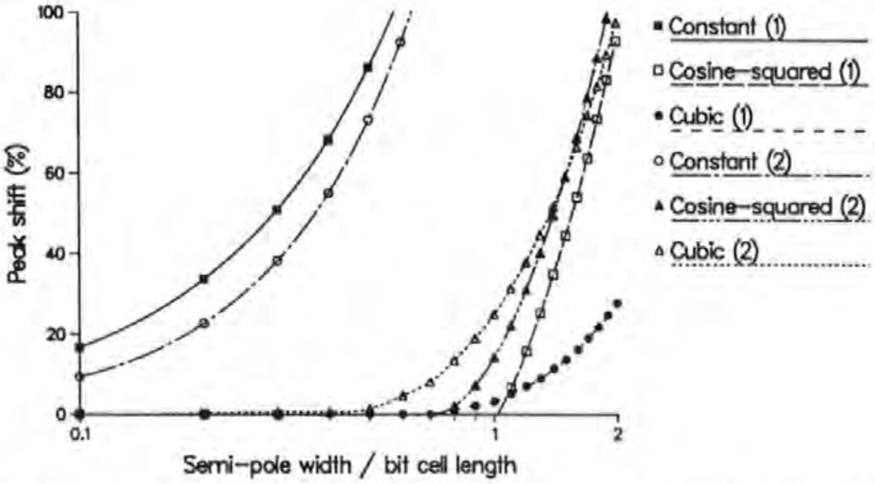

Figure 4.37: Peak shift of two ideal transitions for single pole heads with constant, cubic and cosine-squared pole potentials, $L/t = 0.5$.

ilar results are obtained for other heads whose vertical field components have localised single peaks as can be seen in Fig. 4.37. Here dibit shift results are shown for single poles with constant, cubic and cosine-squared potentials, reading from a thin medium, $\delta = 0.1$, situated at $d/t = 0.1$ and $d/t = 0.25$. The shifts for both the cubic and the cosine-squared potentials are better than those for a linear potential. The increase in head - medium separation is not as detrimental for the cosine-squared potential pole as for the poles with the asymmetric potentials analysed here.

4.3.2.3 The effects due to head geometry

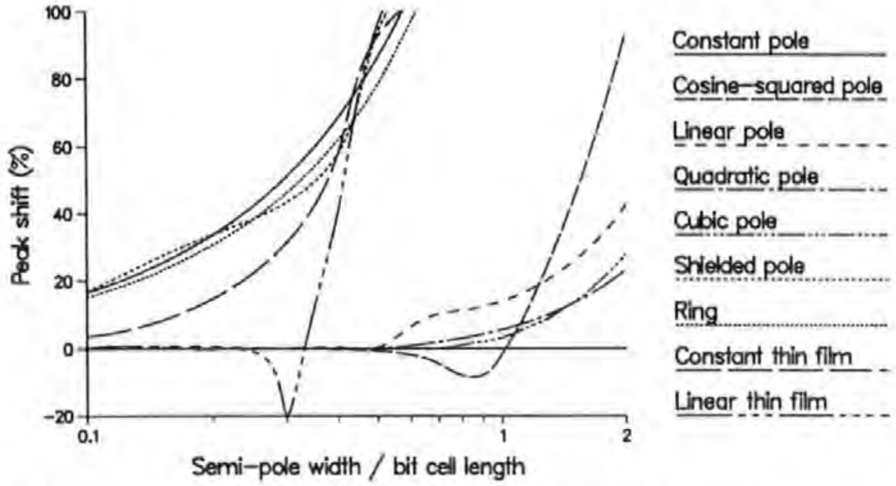

Figure 4.38: Linear dibit shift for each of the inductive heads considered here, $g/t = 0.5$ and $L/t = 0.5$.

Fig. 4.38 compares the linear shift for each of the inductive heads considered in this thesis, reading an ideal dibit from a thin medium, $\delta/t = 0.1$, situated close to the head face at $d/t = 0.1$. For ease of comparison, $L/g = 1$ for the thin film heads and the shielded pole head. The shielded pole and the thin film heads, of these dimensions, suffer similar magnitude dibit shifts to the ring head and constant potential pole. For all of these heads dibit shift is more limiting than first null position when readback is from a medium so close to the head, unless complex decoding procedures are employed. For the constant potential thin film head, the example given in Fig. 4.38 is probably the best that can be expected because the vertical component of the head field has peaks which occur close to the outer edges of the pole pieces so that interference between adjacent bits can be expected to increase if L/g increases. Bloomberg [93] also concluded that zero crossing shift is a major problem for the thin film head.

The linear, quadratic, cubic and cosine-squared potential single poles suffer less dibit shift than any of the more conventional inductive heads of comparable dimensions, particularly when used for 'in contact' replay from thin media. As the first null for a single pole with a cosine-squared pole potential occurs at $2L/\lambda = L/b = 1.98$, dibit shift is the limiting factor for this head also. Present day practical systems can accommodate shifts of about 20%. At this level, the single pole with a cosine-squared potential offers an order of magnitude improvement in replay bit density over the conventional single pole head, when reading from a thin medium situated close to the pole face.

The dependence of the linear dibit shift on the geometric parameters of shielded, infinitely thin MR sensors is demonstrated in Figs. 4.39 – 4.41. In Figs. 4.39 and 4.41 the recording medium is $0.25t$ thick, situated $0.1t$ from the shield face plane and $G_2/t = 0.5$, while in Fig. 4.40 $d = 0.2G_2$ and $\delta = 0.5G_2$. Linear dibit shift has been calculated using zero crossing detection.

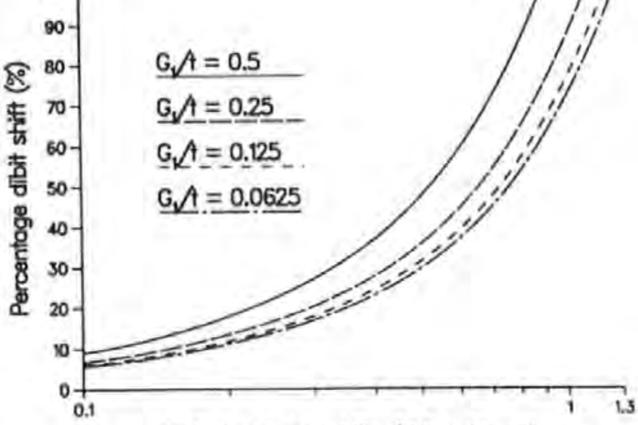

Figure 4.39: Variation in the linear dibit shift of shielded, non-recessed, infinitely thin MR sensors with asymmetry, $G_2/t = 0.5$, $d/t = 0.1$, $\delta/t = 0.25$.

Fig. 4.39 demonstrates the effect of increasing the asymmetry of the head. The ratio of the gap widths G_2/G_1 varies from 1 to 8. As the degree of asymmetry increases the dibit shift decreases for a fixed left-hand gap width : bit cell length ratio. This is due to the reduced width of the head field peak as the inter-shield spacing decreases. For a fixed inter-shield separation, placing the pole asymmetrically between the shields marginally increases the dibit shift. For two heads both with $(G_1 + G_2)/t = 0.75$, one with the pole placed centrally, and the other with $G_2/G_1 = 2$, the dibit shifts for a bit cell length of $b/t = 2.5$ are 13% and 13.5%, respectively.

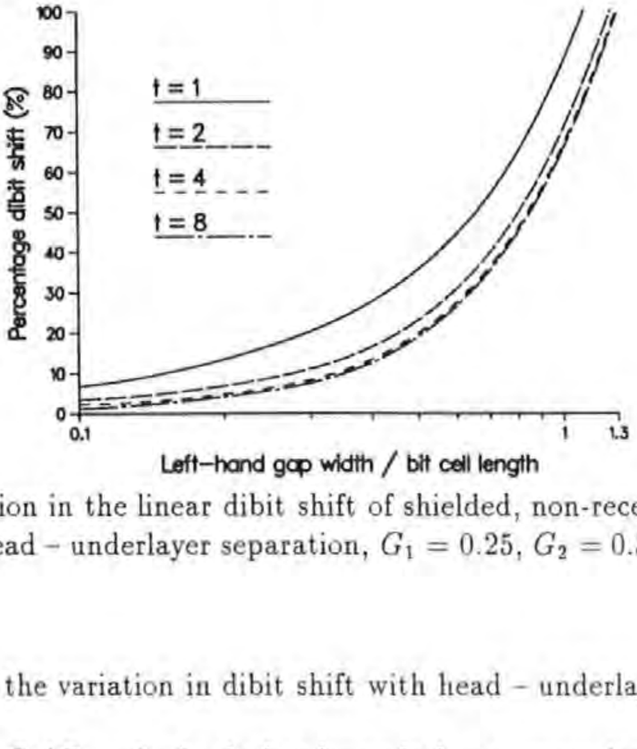

Figure 4.40: Variation in the linear dibit shift of shielded, non-recessed, infinitely thin MR sensors with head – underlayer separation, $G_1 = 0.25$, $G_2 = 0.5$, $d = 0.1$, $\delta = 0.25$.

Fig. 4.40 shows the variation in dibit shift with head – underlayer separation. The gap ratio is fixed at $G_2/G_1 = 2$. As the head – underlayer separation increases, the dibit shift decreases, clearly approaching a minimum which corresponds to the no underlayer case. That the presence of an underlayer increases dibit shift was also concluded in [69].

Recessing the MR sensor causes increased dibit shift, as shown in Fig. 4.41, where $G_2/G_1 = 2$. The percentage increase in the shift caused by recessing the sensor depends on the severity of the dibit shift that occurs when the same dibit is read by a head with a non-recessed pole. For the example shown in Fig. 4.41, where $(G_1 + G_2)/t = 0.75$,

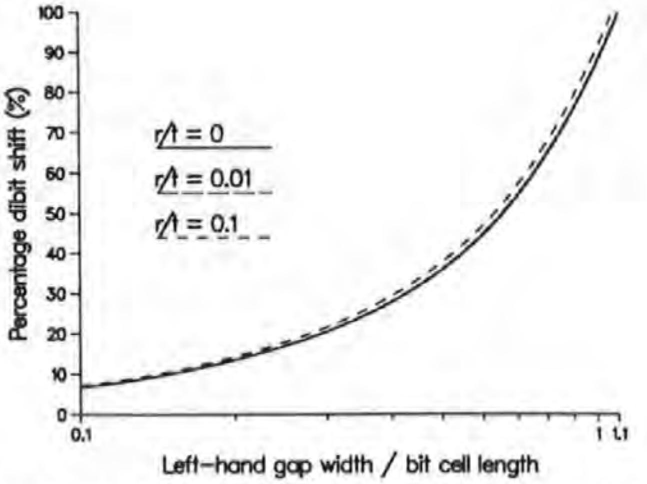

Figure 4.41: Variation in the linear dibit shift of shielded, infinitely thin MR sensors with pole recession, $G_1/t = 0.25$, $G_2/t = 0.5$, $d/t = 0.1$, $\delta/t = 0.25$.

$d/t = 0.1$ and $\delta/t = 0.25$, when a non-recessed head is used to read a dibit of bit cell length of $b/t = 2.5$, a shift of 13.5% occurs, but if the sensor is moved back into the gap so that $r/t = 0.1$, a shift of 14.3% occurs in reading the same dibit from the same medium; this is an increase of 5.9%. If a second pair of heads for which $(G_1 + G_2)/t = 1.0$, one with a non-recessed pole and the other with a pole recession of $r/t = 0.1$, both read the same dibit from the same medium as used for the first pair of heads, the shifts which occur are 18.0% and 19.2% respectively, so that here the increase in shift is 6.7%.

4.3.2.4 Comparison with experimental results

Experimental output results for a W-shaped head reading from a double-layer medium have been published in [94]. This head, which is described in [13], has a single pole extending from a W-shaped core. Exact dimensions for the core pieces are not given but it is indicated that the cores and the gaps between them are very large compared to the pole width. The relevant dimensions given in [94] are: $L = 0.15\mu$m and $\delta = 0.15\mu$m. For a ring head, used in the same series of experiments, $d = 0.1\mu$m; this head – medium separation has been assumed to apply in the case of the W-shaped head also. D_{50} is defined in practical terms in the paper, as the bit density at which the output voltage drops to half that obtained from a bit density of 1000 bits per inch.

The code read in this experiment was a continuous string of '110's in MFM code. This is the worst pattern for this code [94]. For this method, '1's are coded by either a positive or a negative magnetisation on the medium while single '0's produce no magnetisation. Clocking transitions occur between successive '0's. Bit cells of several different lengths occur in this code which makes it particularly sensititive to linear bit shift [1].

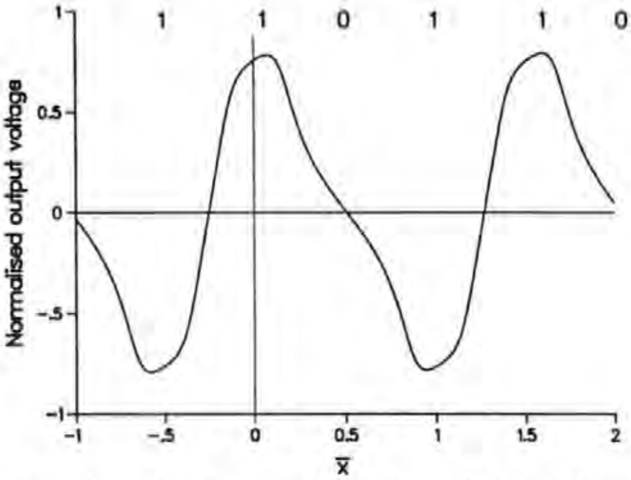

Figure 4.42: Output voltage from a constant potential single pole head, $L = 0.15$, $t = 0.25$, reading '110' pattern, MFM code, $b = 0.508$, $d = 0.1$, $\delta = 0.15$.

In estimating this output theoretically, it has been neccessary to assume that a single pole with constant pole potential, with no spacing layer between the medium and the underlayer, is a suitable model. Fig. 4.42 shows output voltage obtained when $b = 0.508\mu m$, which corresponds to the 50,000 bits per inch depicted in [94]. The theoretical output waveform is similar to that shown in Fig. 1 of [94], and reproduced here in Fig. 4.43. The theoretical peaks appear to be slightly broader than those in the published picture.

In this case, the linear bit shift has been evaluated for two consecutive '1's, by comparing the corresponding difference in peak output positions with the known bit

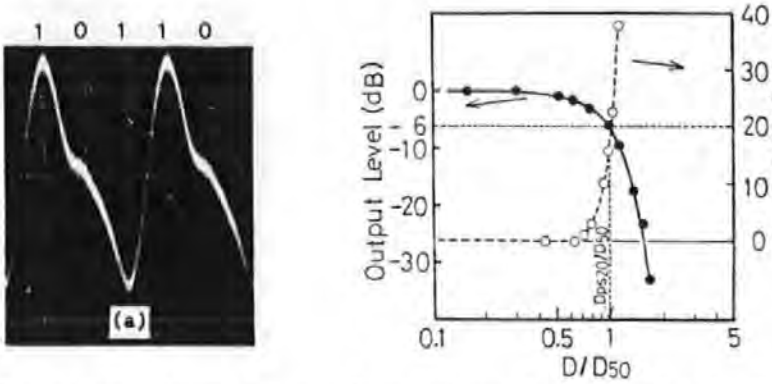

Figure 4.43: Experimental output waveform (a), peak shift and roll-off as published in Figs. 1 and 2 of [94].

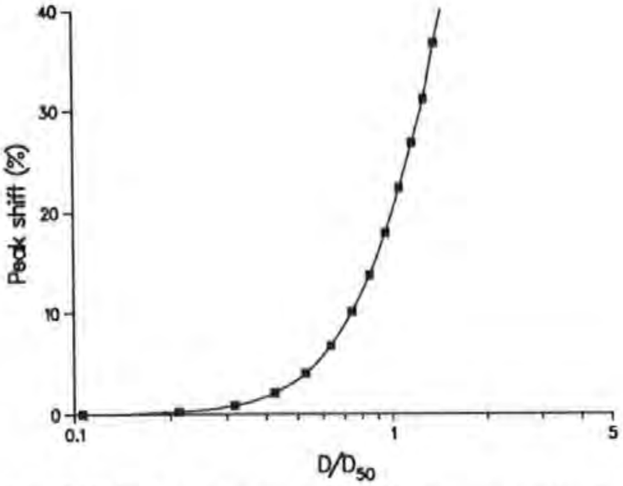

Figure 4.44: Linear bit shift in two consecutive '1's occurring in a string of '110's, MFM code, read by a constant potential single pole head, $L/t = 0.6$, $d/t = 0.1$, $\delta/t = 0.15$.

cell length. Fig. 4.44 shows the linear bit shift as a function of the ratio between the bit density, D, and D_{50}. These results are very similar to those given in Fig. 2 of [94] (Fig. 4.43 here).

The experimental shift results appear to be zero for $D/D_{50} \leq 0.6$. The linear bit shift obtained here, and shown in Fig. 4.44, is about 10% for $D/D_{50} = 0.6$. As the bit density increases further, the theoretical shift does not rise as quickly as the observed shift, so that at $D/D_{50} \approx 1.1$ both results are the same. Bit shifts for a ring head reading the same code pattern from a single layer medium are also given in [94]. The gap width of the ring head used was the same as the pole width of the pole-type head.

The shifts measured for the ring head as a function of its D_{50} are greater than those of the pole-type head. The theoretical shifts for a single pole head obtained here, are consistently lower than those shown for a ring head in [94].

4.3.3 The Roll-off Curve

4.3.3.1 Comparison with spectral response function

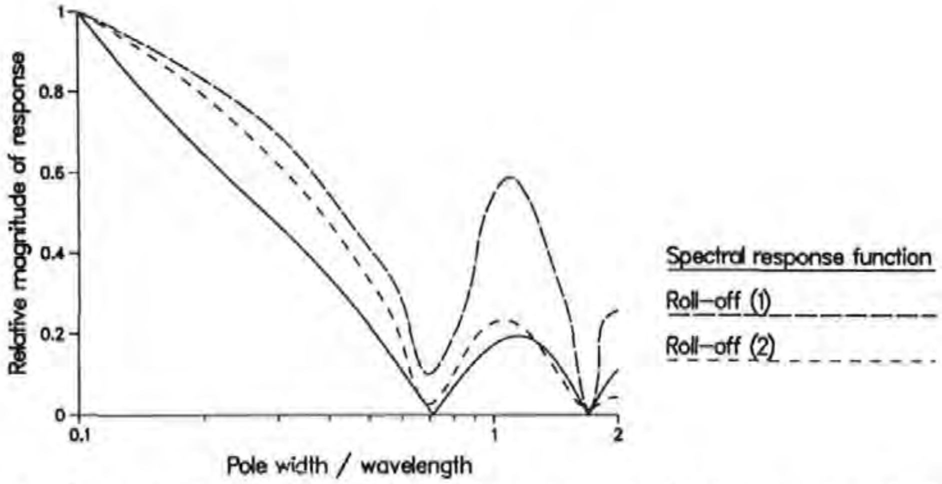

Figure 4.45: Comparison between the spectral response function and roll-off curves for a constant potential single pole head, $L/t = 0.5$, $\delta/t = 0.1$, (1) $d/t = 0.1$, (2) $d/t = 0.25$.

Fig. 4.45 shows the spectral response function for a single pole head with constant potential when $L/t = 0.5$ and the roll-off curves for the same head reading a perfect square wave from a thin medium at two different separations from the head. These roll-off curves are based on only 20 computed values each and have been plotted using an interpolation routine. Each curve has been normalised by its own magnitude at $2L/\lambda = 0.1$. The minima of both roll-off curves occur at very similar frequencies to those of the nulls in the spectral response function. Minima not nulls occur in the roll-off curve. Although the output due to the fundamental wavelength is zero, that due to the other harmonics of the square wave is not.

4.3.3.2 The effects of medium thickness and position

Throughout this section, single pole-type heads are used to demonstrate the effects that the position and the thickness of the medium have on roll-off curves in perpendicular replay.

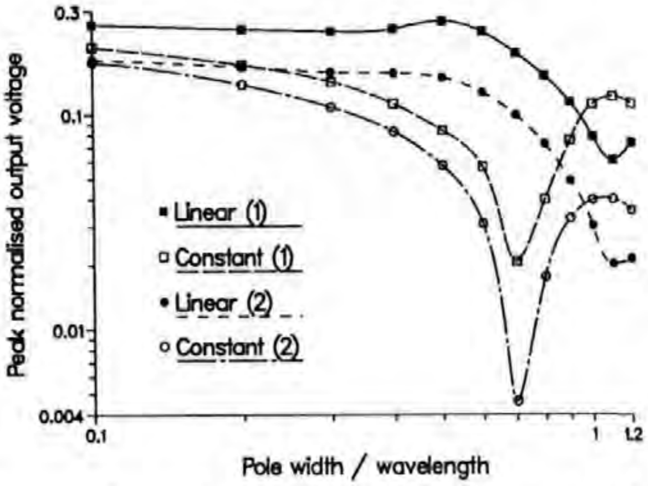

Figure 4.46: Roll-off curves for single pole heads with constant and linear pole potentials, $L/t = 0.5$, $\delta = 0.1$, (1) $d/t = 0.1$, (2) $d/t = 0.25$.

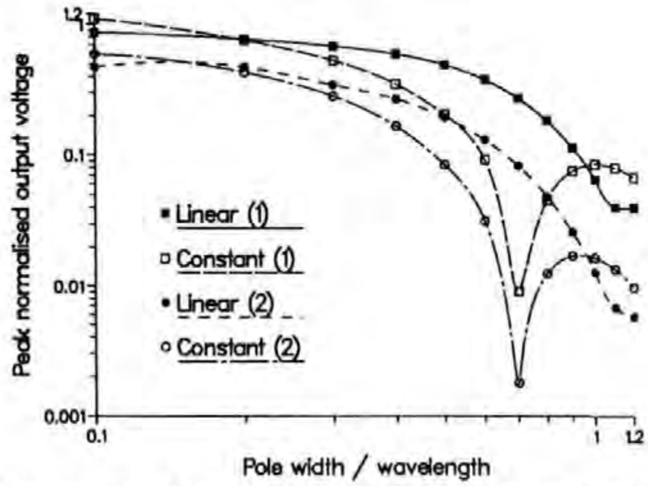

Figure 4.47: Roll-off curves for single pole heads with constant and linear pole potentials, $L/t = 0.5$, (1) $\delta = 0.65$, $d/t = 0.25$, (2) $\delta/t = 0.4$, $d/t = 0.5$.

Figs. (4.46) and (4.47) show the roll-off curves for single pole heads when $L/t = 0.5$, with constant and linear pole potentials, for various head – medium spacings and media thicknesses. Greater output voltages are obtained from thicker media. Reducing the head – medium separation also increases the magnitude the output voltage. These effects are typical for perpendicular recording heads due to the spacing and thickness loss term. The magnitude of the vertical field component at the appropriate distance from the head face plane also influences the output voltage. The vertical field of the linear potential single pole head is more localised than that of the constant potential single pole, resulting in greater output from the linear potential pole for $2L/\lambda < 0.95$, except at low frequencies in cases where either d/t or δ/t is large.

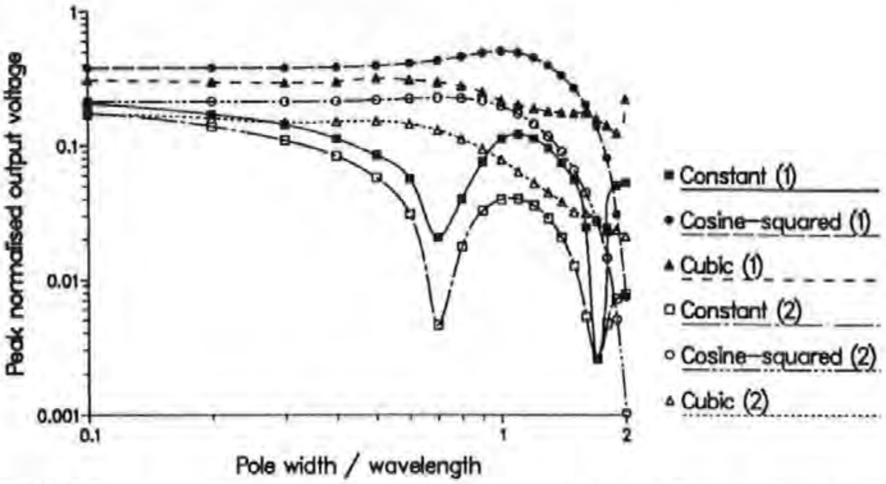

Figure 4.48: Roll-off curves for single pole heads with constant, cosine-squared and cubic pole potentials, $L/t = 0.5$, $\delta = 0.1$, (1) $d/t = 0.1$, (2) $d/t = 0.25$.

Fig. 4.48 compares the roll-off curves for single pole heads with cosine-squared and cubic pole potentials, each when $L/t = 0.5$, with the corresponding results for a constant potential single pole. Two cases are shown: the medium has the same thickness, $\delta/t = 0.1$, for both, while results for two different head – medium separations, $d/t = 0.1$ and $d/t = 0.25$, are depicted. These results are consistent with the spectral response functions for each of these heads.

Fig. 4.49 summarizes the effects of head – medium separation on the magnitude of the peak output voltage for single pole heads with constant, cosine-squared and cubic pole potentials, each when $L/t = 0.5$, reading perfect square waves from a thin medium for which $\delta/t = 0.1$. A high D_{50} value is desirable as replay systems can only operate over a limited range of output voltages. Single pole heads with either cosine-squared or cubic pole potentials have higher D_{50} values than those with constant potentials,

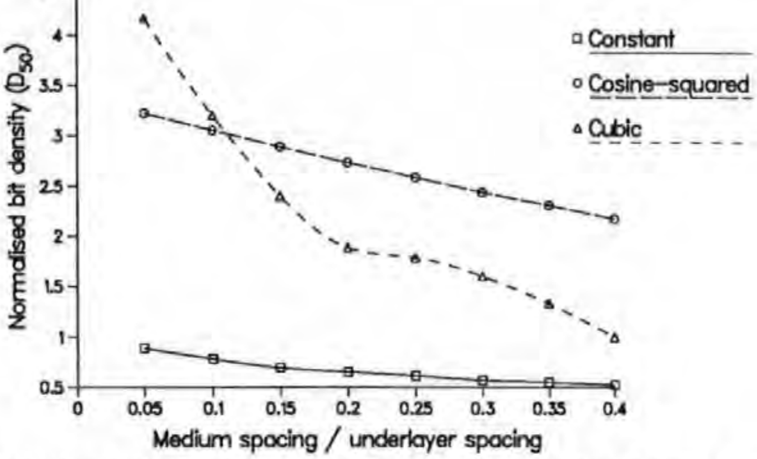

Figure 4.49: Variation in D_{50} with pole – medium separation for single pole heads with constant, cosine-squared and cubic pole potentials, $L/t = 0.5$, $\delta = 0.1$.

over the range of head – medium separations shown. Results for heads with linear and quadratic pole potentials can be expected to lie between those for the constant and the cubic potential poles.

4.3.3.3 Shielded, infinitely thin MR sensors

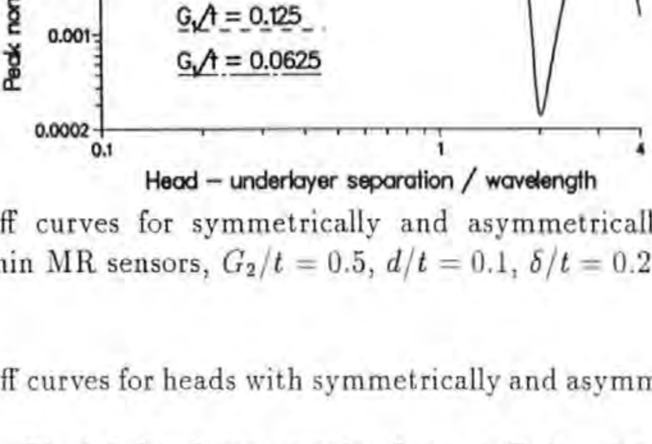

Figure 4.50: Roll-off curves for symmetrically and asymmetrically shielded, non-recessed, infinitely thin MR sensors, $G_2/t = 0.5$, $d/t = 0.1$, $\delta/t = 0.25$.

Fig. 4.50 shows roll-off curves for heads with symmetrically and asymmetrically shielded, non-recessed sensors. The left-hand gap remains fixed at $G_2/t = 0.5$ while G_1/t varies from 0.5 to 0.0625. The magnitude of the maximum output due to a square wave of long wavelength recorded on the medium falls as the head asymmetry increases, but for shorter wavelengths the converse is true. As the inter-shield separation decreases the slight peak due to pulse crowding shifts towards shorter wavelengths, and becomes less pronounced.

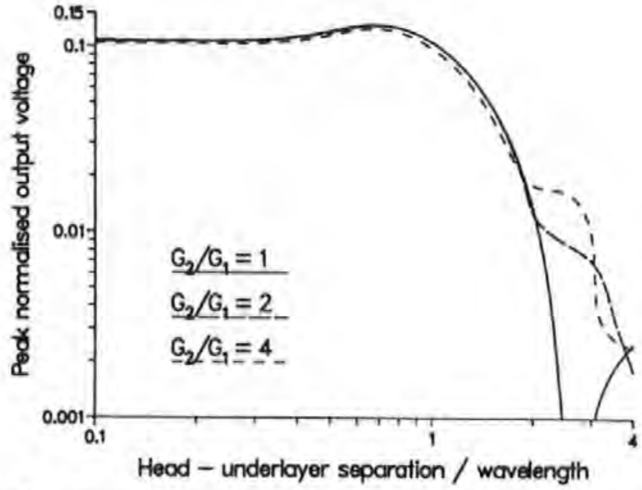

Figure 4.51: Roll-off curves for symmetrically and asymmetrically shielded, non-recessed, infinitely thin MR sensors, $(G_1 + G_2)/t = 0.75$, $d/t = 0.1$, $\delta/t = 0.25$.

In Fig. 4.51 the roll-off curves for MR sensors with the same inter-shield separation $(G_1 + G_2)/t = 0.75$ but differing gap ratios $G_2/G_1 = 1, 2, 4$ are compared. The differences are such that, in practice, the usable waveband of a head of fixed overall dimensions would be unaltered by the asymmetric placement of the MR sensor.

Head – underlayer separation has only a slight effect on the roll-off curve. When the underlayer is close to the head ($t \leq 2G_2$) the height of the roll-off curve marginally exceeds that of the no underlayer case for most wavelengths. For all head – underlayer separations greater than $4G_2$ the roll-off curves effectively do not change. In [69] greater differences between the roll-off curves of heads with and without underlayers present were obtained. In particular, it was found that the magnitude of the roll-off curve when an underlayer was present, was only greater than that for the same head without an underlayer, over a short range of long wavelengths.

Recessing the MR sensor has a strong influence on the roll-off curve. Fig. 4.52 shows how the maximum output amplitude drops with recession of the pole when

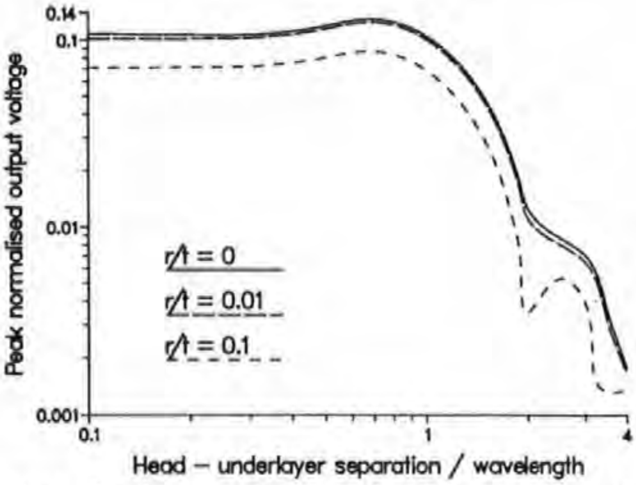

Figure 4.52: The effect of pole recession on roll-off curves for a shielded, infinitely thin MR sensor, $G_1/t = 0.25$, $G_2/t = 0.5$, $d/t = 0.1$, $\delta/t = 0.25$.

$G_1/t = 0.25$, $G_2/t = 0.5$ and $r/t = 0, 0.01, 0.1$. This loss of output amplitude is mainly due to the increase in sensor – medium separation, but it is less than the loss that would occur if the medium itself were moved away from a non-recessed head by the same distance.

4.3.4 Comparison with Experimental Results

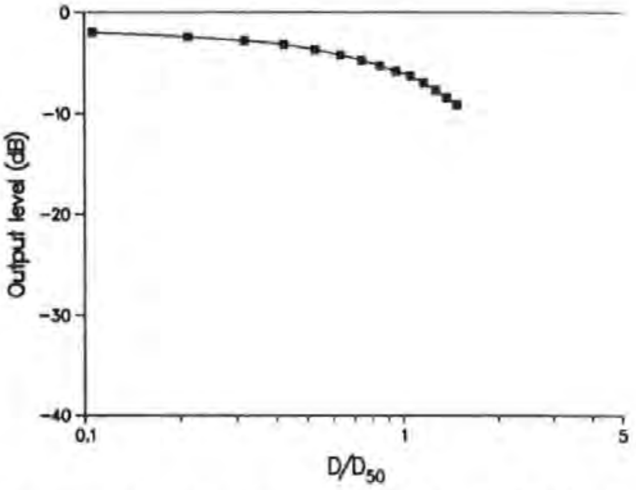

Figure 4.53: Roll-off curve for a constant potential single pole head reading a sequence of '110's, MFM code, $L = 0.15$, $t = 0.25$, $d = 0.1$, $\delta = 0.15$.

The experimental roll-off curve for the system described in Section 4.3.2.4 is also shown in Fig. 4.43. The published curve was obtained by replaying a sequence of '110's in MFM code. The same pattern of ideal transitions has been used to determine the theoretical roll-off curve shown in Fig. 4.53. As for the linear bit shift, it has been neccessary to assume the head – medium spacing, and the definition for D_{50} given in [94]. The curve is plotted on axes with the same scales as Fig. 2 of [94], where there appears to be no reduction in peak output voltage for $D/D_{50} < 0.2$. The rate of increase in the voltage reduction as the bit density increases is much greater in the experimental curve than for the theoretical one shown here. Experimentally, the putput voltage is reduced to less than −30 dB for $D/D_{50} = 1.4$. The exact cause of these discrepancies is unknown. Four possible reasons are:

1. The assumed head – medium separation may be incorrect.
2. The transitions on the medium would not have been perfectly rectangular, especially at long wavelengths.
3. The single pole head is not a suitable model for the W-shaped head used in the experiments.
4. The experimental error tolerances could be greater at high and at low output voltages than for the intermediate responses.

4.4 Summary

This chapter has discussed:

- The derivation of the exact spectral response function for:
    1. Ring heads.
    2. Thin film heads with constant or linearly varying potential poles.
    3. Single pole heads with linear or arbitrarily varying pole potentials.
    4. Symmetrically shieded single pole heads.

5. Shielded, recessed and non-recessed, infinitely thin MR sensors.

all in the presence of an underlayer.

- The derivation of approximations to the spectral response functions whose accuracy has been demonstrated.
- The definitions of linear dibit shift and the roll-off curve.
- Numerical results which have been presented.
- Comparisons with published theoretical and experimental results.

Chapter 5

Conclusions

5.1 Mathematical Methods

New mathematical analyses have been carried out for some existing magnetic recording heads and also for some novel graded potential heads. The published literature only reports one such head which has been built. The new potential distributions for single pole heads, which have been investigated here, result in improved characteristics over that experimental head. Mathematical analyses prior to head construction can reduce development time and cost. Two particular analytical approaches have been used in this thesis.

Exact two-dimensional head fields have been derived by the Fourier method for thin film heads with constant and linearly varying pole potentials, and for single pole heads with linearly and arbitrarily varying potential poles. For these solutions, as the head – underlayer separation increases, the magnitudes of the Fourier coefficients increase. Hence, the number of terms required for convergence of the solutions increases with t, especially near the boundaries between the different regions defined for a particular case. The number of sets of Fourier coefficients, for a particular solution, depends on the minimum number of rectangular regions into which it is possible to subdivide the total area exterior to the head and the underlayer. The number of terms involving these coefficients required to achieve convergence of the solution, depends on the positions of the chosen boundaries as well as the magnitudes of the coefficients.

The conformal mapping method has been used to derive exact two-dimensional head fields for symmetrically and asymmetrically shielded, recessed and non-recessed infinitely thin MR sensors. This method can be applied to more complicated geometries than the Fourier method. In general, the complexity of the solution rises with the number of vertices in the head geometry. Crowding of the indiviual points in certain areas of the transformation are inevitable, as the mapping is non-linear. In the crowded areas, very accurate initial values are needed for the successful convergence of the inversion routine. Crowding, in the transformations defined here, has been found to increase as the head – underlayer separation decreases relative to the other dimensions of the head.

Therefore, the two analytic methods are complementary. The Fourier method is best suited to simple geometries and, in most cases, when an underlayer is present, to small head – underlayer separations. The analytic results obtained can lead to single term approximations. Conformal mappings of the form used here are more easily implemented when the head – underlayer separation is large. The results are usually computationally less expensive than those from the Fourier method but are purely numerical.

5.2 The Effects of Pole Potential Grading

For conventional heads which are assumed to have constant pole potentials, the only way to increase the frequency at which the first null in the spectral response occurs, and to reduce linear dibit shift is to minimise the relevant dimensions of the head. Graded pole potentials offer the benefits of extended frequency ranges to the first output null, or even complete elimination of nulls, as well as substantially reducing linear dibit shifts. Hence it is expected that higher areal bit densities will be achieved in the future by the prudent use of potential grading.

Each of the pole potential gradings considered here have at least one zero potential edge. Heads with these potentials have been shown to have locally higher and narrower peaks in their vertical field components close to the head. Hence such heads produce less linear dibit shift than the corresponding conventional heads. Linear dibit shift has been shown to be the limiting factor for conventional heads. For replay, when the head is almost in contact with the medium, higher output voltages are also obtained from heads with graded pole potentials.

Heads with asymmetrically graded pole potentials have no nulls in their spectral response function. Deep minima indicate that the output voltage would be too low, relative to the peak, for detection. The degree of asymmetry affects the depth of the minima. For a cubic potential across a single pole head, the minima are very shallow and would be unlikely to be more limiting than the general reduction in output voltage at high bit densities for this head.

When the pole potential is asymmetric, the phase of the spectral response function varies continuously over the entire range of frequencies. For the single pole with a cubic potential, the phase is almost linear. Heads with symmetric pole potentials have spectral response functions with abrupt phase changes by π radians at the frequencies which cause nulls. Increasing the bandwidth of these heads, other than by reducing the pole or the gap widths, can be achieved by suitably grading the potential of the pole pieces. The cosine-squared potential distribution across a single pole head has been shown to offer as increase in bandwidth to the first null of over 177%, compared with the conventional, constant potential single pole head, when $L/t = 0.5$.

The cosine-squared potential distribution across a single pole head has been shown to have a head field which is very similar to that of a particular symmetrically shielded pole head. This suggests that any desired field distribution may be achieved by careful grading of the potential across a single pole head.

The accuracy with which the theoretical models predict the output characteristics of experimental heads gives further confidence in the methods used and the results obtained.

5.3 Head – Underlayer Separation

In general, reducing the head-underlayer separation increases the peak magnitudes and the gradients of the head field components, although optimum dimension ratios have been found for the constant potential single pole head and for a symmetrically shielded pole head.

Over the range of dimension ratios tested for a shielded MR sensor, the position of the underlayer has little influence. The ratios between the sensor width and the gap widths, as well as the ratio of each of these dimensions with the pole – underlayer separation, t, affect the peak magnitude of the field. Here $L/t = 0$ for all $t > 0$ but in a practical system the small sensor width results in L/t remaining small unless 'in contact' recording with very thin media is achieved. This does not mean that the underlayer is unneccessary, its original purpose, of enhancing the detectable field of the medium, still remains.

5.4 Shielded Heads

Asymmetry in shielded pole heads is almost inevitable. Very slight accidental asymmetry will have little observable effect on the response of a shielded pole head. Very thin symmetrically shielded pole heads, whether inductive or magnetoresistive, have minima not nulls in their spectral response functions, over the usable range of frequencies. Therefore no phase change occurs either. This makes shielded magnetoresistive heads particularly suitable for replay.

5.5 Future Work

Shielded MR sensors with recessed and non-recessed poles have been analysed. The same model may be used to investigate the effects when the pole protudes from the shield face plane.

Increasing the asymmetry from a linear potential to a cubic potential across a single pole head reduces the depth of the minima in the spectral response function and lessens linear dibit shift. It would be interesting to test the effects of other potential distributions applied to the poles of thin film heads and to the shields of magnetoresistive heads. It is suspected that, with the correct choice of pole potential, the complex sets of nulls in the spectral response of the thin film heads can be eliminated. Similarly, the finite length of the shields of an MR sensor have not been taken into account here. Grading the potential across the shields could enhance the vertical head field component above the sensor, while preventing undesirable peaks above the outer edges of the shields.

The possibilities for potential grading in longitudinal recording heads have not yet been explored. The models for the particular heads with graded potential poles presented here, are not applicable when the underlayer is removed. In real heads the corners of the pole pieces and the shields are not perfectly rectangular. The effects due to micro-rounded corners can be investigated using the conformal mapping method.

Other head configurations exist which have not been analysed, for example the MR sensor, shielded on one side only, and the magnetoresistive head with a soft magnetic adjacent layer. The former is a special case of the shielded MR sensor analysed here, but crowding in the transformation would limit the use of the existing model. For the latter, the biasing layer is magnetised by the field from the current in the MR sensor. In modelling such a structure the biasing layer must be taken into account since it acts as another pole and changes the overall head field. As new head geometries are introduced, there will be a need for further accurate mathematical analyses. The future development of magnetic recording heads may also be motivated by the mathematical analyses of novel head geometries. Experimental work is already planned, at the University of Plymouth, to verify the results of the new analyses, especially those for the graded potential single pole heads.

Appendix A

Analytic Integral Results

A.1 Special functions

Many of the integrals quoted in Chapters 2, 3 and 4 can be expressed in closed form. Where integrals of the same form occur in the analysis of different head geometries, general results are given. Substitutions for the specific cases are given in Section A.3.8. Some of these analytic results depend on the complex exponential integral Ei, and other functions related to it as well as on the elementary transcendental functions. These special functions are defined as [95]:

$$\mathrm{Ei}(z) = -\mathrm{E}_1(-z) \tag{A.1}$$

and

$$\mathrm{E}_1(z) = \int_z^\infty \frac{e^{-t}}{t}\,dt = -\gamma - \ln(z) - \sum_{n=1}^{\infty} \frac{(-1)^n z^n}{n n!} \tag{A.2}$$

where γ is Euler's constant.

$$\overline{\mathrm{Ei}}(z) = \mathrm{Ei}(z) - i\pi\,. \tag{A.3}$$

The sine and cosine integral are

$$\mathrm{Si}(x) = \int_0^x \frac{\sin(t)}{t}\,dt \tag{A.4}$$

and

$$\mathrm{Ci}(x) = -\int_x^\infty \frac{\cos(t)}{t}\,dt \tag{A.5}$$

respectively, which can be evaluated using library routines [33].

A.2 Integrals arising in the evaluation of the coefficients

A.2.1 I_{mn}

$$I_{mn} = \int_0^\infty \frac{k\sin^2(k)}{[k^2-(m\pi)^2][k^2-(n\pi)^2]}\,dk\,. \tag{A.6}$$

$$\text{When } n=0,\quad I_{m0} = \frac{1}{2(m\pi)^2}\left[\mathrm{Ci}(2m\pi)-\gamma-\ln(2m\pi)\right] \tag{A.7}$$

$$\text{else}\qquad I_{mn} = \begin{cases} \frac{1}{2m\pi}\mathrm{Si}(2m\pi), & m=n \\ \frac{1}{2\pi^2(n^2-m^2)}\left[\ln\left(\frac{m}{n}\right)-\mathrm{Ci}(2m\pi)+\mathrm{Ci}(2n\pi)\right], & m\neq n, \end{cases} \tag{A.8}$$

which differs in sign from the result given in [23] when $m \neq n$.

A.2.2 N_{mN}

$$\begin{aligned} N_{mN} &= \int_0^\infty \frac{k\sin^2(k)}{[k^2-(m\pi)^2][k^2+(N\pi s)^2]}\,dk\,. && \text{(A.9)} \\ &= \frac{1}{4\left[(m\pi)^2+(N\pi s)^2\right]}\left\{2\ln\left(\frac{Ns}{m}\right)+2\mathrm{Ci}(2m\pi)\right. \\ &- \left.\left(e^{-2N\pi s}\overline{\mathrm{Ei}}(2N\pi s)+e^{2N\pi s}\mathrm{Ei}(-2N\pi s)\right)\right\}. && \text{(A.10)} \end{aligned}$$

For the single pole head with arbitrary pole potential, $s = t/2L$.

A.2.3 P_{mN}

$$\begin{aligned} P_{mN} &= \int_0^\infty \frac{k\sin(k)\cos(k)}{[k^2-(m\pi)^2][k^2+(N\pi s)^2]}\,dk\,. && \text{(A.11)} \\ &= \frac{1}{4\left[(m\pi)^2+(N\pi s)^2\right]}\left\{2m\pi\mathrm{Si}(2m\pi)\right. \\ &\quad \left.+N\pi s\left(e^{-2N\pi s}\overline{\mathrm{Ei}}(2N\pi s)-e^{2N\pi s}\mathrm{Ei}(-2N\pi s)\right)\right\}. && \text{(A.12)} \end{aligned}$$

For the single pole head with arbitrary pole potential, $s = t/2L$.

A.3 Integrals arising in expressions for the potential and field components

A.3.1 I_n

$$I_n = \int_0^\infty \frac{\sin(k)\sin(kq/r)e^{-kp/r}}{k^2-(n\pi)^2}\,dk\,. \qquad \text{(A.13)}$$

$$I_0 = \frac{1}{2r}\left[\frac{p}{2}\ln\left(\frac{(r-q)^2+p^2}{(r+q)^2+p^2}\right)\right.$$
$$\left.+(r+q)\arctan\left(\frac{r+q}{p}\right)-(r-q)\arctan\left(\frac{r-q}{p}\right)\right] \quad (A.14)$$

$$I_n = \frac{1}{4n\pi}\mathrm{Re}[e^{-a}\mathrm{Ei}(a)-e^{a}\mathrm{Ei}(-a)-e^{-b}\mathrm{Ei}(b)+e^{b}\mathrm{Ei}(-b)]$$
$$+\frac{1}{2n}e^{-n\pi p/r}(-1)^n\sin\left(\frac{n\pi q}{r}\right) \quad (A.15)$$

for $0 < q/r < 1$, where

$$a = \frac{n\pi}{r}[p-(r+q)i] \quad \text{and} \quad b = \frac{n\pi}{r}[p-(r-q)i]\,. \quad (A.16)$$

This result differs in the sign of two terms from that given in [25].

A.3.2 J_n

$$J_n = \int_0^\infty \frac{k\sin(k)\sin(kq/r)}{k^2-(n\pi)^2}e^{-kp/r}\,dk\,. \quad (A.17)$$

When $n=0$, $J_0 = \frac{1}{4}\left[\ln\left(\frac{p^2+(r+q)^2}{p^2+(r-q)^2}\right)\right]$ (A.18)

else $J_n = \frac{1}{4}\mathrm{Re}\left[e^{a}\mathrm{E}_1(a)+e^{-a}\mathrm{E}_1(-a)-e^{b}\mathrm{E}_1(b)-e^{-b}\mathrm{E}_1(-b)\right]+S$ (A.19)

where a and b are given by (A.16) and

$$S = \begin{cases} \frac{\pi}{2}(-1)^n e^{-n\pi p/r}\sin\left(\frac{n\pi q}{r}\right) & 0 \le q \le r \\ 0 & q < 0 \end{cases}$$

as given in [25].

A.3.3 K_n

$$K_n = \int_0^\infty \frac{k \sin(k) \cos(kq/r)}{k^2 - (n\pi)^2} e^{-kp/r}\, dk\,. \tag{A.20}$$

$$\text{When } n = 0,\ K_0 = \frac{1}{2}\left[\arctan\left(\frac{r+q}{p}\right) + \arctan\left(\frac{r-q}{p}\right)\right] \tag{A.21}$$

$$\text{else} \qquad K_n = \frac{1}{4}\mathrm{Im}\left[e^{a}\mathrm{E}_1(a) + e^{-a}\mathrm{E}_1(-a) + e^{b}\mathrm{E}_1(b) + e^{-b}\mathrm{E}_1(-b)\right] + T \tag{A.22}$$

where a and b are given by (A.16) and

$$T = \begin{cases} \frac{\pi}{2}(-1)^n e^{-n\pi p/r} \cos\left(\frac{n\pi q}{r}\right) & 0 \le q \le r \\ 0 & q < 0. \end{cases}$$

as given in [25].

A.3.4 T_N

$$\begin{aligned} T_N &= \int_0^\infty \frac{\sin(k)\sin(k(t-y)/t)}{k^2 + (N\pi s)^2} e^{-k(|x|-L)/t}\, dk \\ &= \frac{1}{4N\pi s}\mathrm{Im}\left[e^{\mu_1}\mathrm{E}_1(\mu_1) - e^{-\mu_1}\mathrm{E}_1(-\mu_1) - e^{\mu_2}\mathrm{E}_1(\mu_2) + e^{-\mu_2}\mathrm{E}_1(-\mu_2)\right] \end{aligned} \tag{A.23}$$

where

$$\mu_1 = N\pi s\left[\left(\frac{t + (t-y)}{t} + i\frac{(|x| - L)}{t}\right)\right] \tag{A.24}$$

and

$$\mu_2 = N\pi s\left[\left(\frac{t - (t-y)}{t} + i\frac{(|x| - L)}{t}\right)\right] \tag{A.25}$$

When $N = 0$, $T_0 = I_0$ as given in Section A.3.1 with $p = |x| - L$, $q = t - y$ and $r = t$.

A.3.5 U_N

$$U_N = \int_0^\infty \frac{k\cos(k)\sin(k(t-y)/t)}{k^2+(N\pi s)^2} e^{-k(|x|-L)/t}\,dk \tag{A.26}$$

$$U_0 = \frac{1}{2}\arctan\left(\frac{2(t-y)(|x|-L)}{(|x|-L)^2+y(2t-y)}\right) \tag{A.27}$$

$$U_N = \frac{1}{4}\mathrm{Im}\left[e^{\mu_1}\mathrm{E}_1(\mu_1)+e^{-\mu_1}\mathrm{E}_1(-\mu_1)-e^{\mu_2}\mathrm{E}_1(\mu_2)-e^{-\mu_2}\mathrm{E}_1(-\mu_2)\right] \tag{A.28}$$

where μ_1 and μ_2 are given by equns. (A.24) and (A.25) respectively.

A.3.6 W_0

$$\begin{aligned} W_0 &= \int_0^\infty \cos(k)\sin(k(t-y)/t)e^{-k(|x|-L)/t}\,dk & \text{(A.29)}\\ &= \frac{t}{2}\left[\frac{2t-y}{(|x|-L)^2+(2t-y)^2}-\frac{y}{(|x|-L)^2+y^2}\right] & \text{(A.30)}\end{aligned}$$

A.3.7 Y_0

$$\begin{aligned} Y_0 &= \int_0^\infty \cos(k)\cos(k(t-y)/t)e^{-k(|x|-L)/t}\,dk & \text{(A.31)}\\ &= \frac{t(|x|-L)}{2}\left[\frac{1}{(|x|-L)^2+(2t-y)^2}+\frac{1}{(|x|-L)^2+y^2}\right] & \text{(A.32)}\end{aligned}$$

A.3.8 The specific cases

The results given in Sections A.3.1, A.3.2, A.3.3 apply in the following cases.

For all the single pole-type heads, in I_n^P, J_n^P and K_n^P,

$$p = x - L, \qquad q = t - y, \quad \text{and} \quad r = t. \tag{A.33}$$

For a ring head without an underlayer in I_n^R, J_n^R and K_n^R,

$$p = y, \qquad q = x, \quad \text{and} \quad r = g \, . \tag{A.34}$$

For the thin film heads in I_n^{TF}, J_n^{TF} and K_n^{TF}

$$p = x - L - g, \qquad q = t - y, \quad \text{and} \quad r = t \, . \tag{A.35}$$

A.4 Integrals arising in the spectral response functions

A.4.1 SM

$$\begin{aligned} SM &= \kappa t \int_0^\infty \frac{\sin^2(k)}{k^2[k^2 + (\kappa t)^2]} \, dk & \text{(A.36)} \\ &= \frac{\pi}{4} \left[\frac{2\kappa t + e^{-2\kappa t} - 1}{(\kappa t)^2} \right] . & \text{(A.37)} \end{aligned}$$

A.4.2 SN

$$\begin{aligned} SN &= \int_0^\infty \frac{\sin(k)\cos(k)}{k^2 + (\kappa t)^2} \, dk \\ &= \frac{1}{4\kappa t} \left[e^{-2\kappa t} \mathrm{Ei}(2\kappa t) - e^{2\kappa t} \mathrm{Ei}(-2\kappa t) \right] . & \text{(A.38)} \end{aligned}$$

A.4.3 SR

$$SR = \kappa t \int_0^\infty \frac{\sin(k)\cos(k)}{k[k^2 + (\kappa t)^2]} \, dk \tag{A.39}$$

$$= \frac{\pi}{4}\left[\frac{1-e^{-2\kappa t}}{\kappa t}\right]. \qquad (A.40)$$

A.4.4 ST_n^P

$$ST_n^P = \kappa t \int_0^\infty \frac{\sin^2(k)}{[k^2-(n\pi)^2][k^2+(\kappa t)^2]}\, dk \qquad (A.41)$$

$$= \frac{\pi}{4}\left[\frac{e^{-2\kappa t}-1}{(n\pi)^2+(\kappa t)^2}\right], n \neq 0. \qquad (A.42)$$

A.4.5 SU_N

$$SU_N = \int_0^\infty \frac{k\,\sin^2(k)}{[k^2+\xi_N^2][k^2+(\kappa t)^2]}\, dk \qquad (A.43)$$

$$= \frac{1}{4[(\kappa t)^2-\xi_N^2]}\left[2\ln\left(\frac{\kappa t}{\xi_N}\right) + e^{-2\xi_N}\mathrm{Ei}(2\xi_N) + e^{2\xi_N}\mathrm{Ei}(-2\xi_N)\right.$$

$$\left. -e^{-2\kappa t}\mathrm{Ei}(2\kappa t) - e^{2\kappa t}\mathrm{Ei}(-2\kappa t)\right]. \qquad (A.44)$$

A.4.6 SV_N

$$SV_N = \kappa t \int_0^\infty \frac{\sin^2(k)}{[k^2+\xi_N^2][k^2+(\kappa t)^2]}\, dk \qquad (A.45)$$

$$= \frac{\pi}{4[(\kappa t)^2-\xi_N^2]}\left[\frac{\kappa t}{\xi_N}(1-e^{-2\xi_N}) + e^{-2\kappa t} - 1\right]. \qquad (A.46)$$

A.4.7 SW_N

$$SW_N = \int_0^\infty \frac{k^2\,\sin(k)\cos(k)}{[k^2+\xi_N^2][k^2+(\kappa t)^2]}\, dk \qquad (A.47)$$

$$= \frac{1}{4[(\kappa t)^2 - \xi_N^2]}\left[\kappa t\left(e^{-2\kappa t}\mathrm{Ei}(2\kappa t) - e^{2\kappa t}\mathrm{Ei}(-2\kappa t)\right)\right.$$
$$\left. -\xi_N\left(e^{-2\xi_N}\mathrm{Ei}(2\xi_N) - e^{2\xi_N}\mathrm{Ei}(-2\xi_N)\right)\right]. \qquad (A.48)$$

A.4.8 SX_N

$$SX_N \equiv \kappa t\int_0^\infty \frac{k\sin(k)\cos(k)}{[k^2+\xi_N^2][k^2+(\kappa t)^2]}\,dk \qquad (A.49)$$
$$= \frac{\pi}{4}\kappa t\left[\frac{e^{-2\xi_N} - e^{-2\kappa t}}{(\kappa t)^2 - \xi_N^2}\right]. \qquad (A.50)$$

Appendix B

Tables of Coefficients / Constants

B.1 Thin film heads

						Scaled	Pole head	Pole head
g/t	0.125	0.5	2.0	8.0	16.0	16.0	$L/t = 0.5$	$L/t = 0.5$
							$N = 40$	Extrapolated
$B_1^{C'}$	-0.0871	-0.0866	-0.0863	-0.0863	-0.0863	-0.0900	-0.0900	-0.090097
$B_2^{C'}$	0.0296	0.0293	0.0292	0.0292	0.0292	0.0292	0.0292	0.029305
$B_3^{C'}$	-0.0155	-0.0153	-0.0153	-0.0153	-0.0153	-0.0153	-0.0153	-0.015317
$B_4^{C'}$	0.0098	0.0096	0.0096	0.0096	0.0096	0.0096	0.0096	0.009635
$B_5^{C'}$	-0.0068	-0.0067	-0.0067	-0.0067	-0.0067	-0.0067	-0.0067	-0.006711
$B_6^{C'}$	0.0050	0.0050	0.0050	0.0050	0.0050	0.0050	0.0050	0.004989
$D_1^{C'}$	-0.4417	-0.2101	-0.0997	-0.0871	-0.0865	-0.0902		
$D_2^{C'}$	0.1637	0.0625	0.0328	0.0294	0.0292	0.0293		
$D_3^{C'}$	-0.0851	-0.0309	-0.0170	-0.0154	-0.0153	-0.0153		
$D_4^{C'}$	0.0520	0.0188	0.0106	0.0097	0.0096	0.0096		
$D_5^{C'}$	-0.0351	-0.0128	-0.0073	-0.0067	-0.0067	-0.0067		
$D_6^{C'}$	0.0253	0.0094	0.0054	0.0050	0.0050	0.0050		

Table B.1: Coefficients $B_n^{C'}$ and $D_n^{C'}$ for thin film heads with poles at constant potential, $L/t = 0.5$.

L/t	0.03125	0.125	0.5	2.0	Ring head no underlayer $N = 40$	Ring head no underlayer Extrapolated	Ring head with underlayer $g/t = 2.0$, $N = 40$
$B_1^{C'}$	-0.0996	-0.0922	-0.0866	-0.0861	-0.0861	-0.086157	
$B_2^{C'}$	0.0360	0.0321	0.0293	0.0291	0.0291	0.029150	
$B_3^{C'}$	-0.0196	-0.0171	-0.0153	-0.0152	-0.0152	-0.015254	
$B_4^{C'}$	0.0126	0.0108	0.0096	0.0095	0.0095	0.009593	
$B_5^{C'}$	-0.0090	-0.0076	-0.0067	-0.0066	-0.0066	-0.006680	
$B_6^{C'}$	0.0068	0.0057	0.0050	0.0049	0.0049	0.004965	
$D_1^{C'}$	-0.2099	-0.2096	-0.2101	-0.2102			-0.2103
$D_2^{C'}$	0.0648	0.0633	0.0625	0.0625			0.0625
$D_3^{C'}$	-0.0326	-0.0315	-0.0309	-0.0309			-0.0309
$D_4^{C'}$	0.0201	0.0192	0.0188	0.0188			0.0188
$D_5^{C'}$	-0.0138	-0.0131	-0.0128	-0.0128			-0.0128
$D_6^{C'}$	0.0102	0.0096	0.0094	0.0094			0.0094

Table B.2: Coefficients $B_n^{C'}$ and $D_n^{C'}$ for thin film heads with poles at constant potential, $g/t = 0.5$.

t	0.125	1.0	4.0	16.0
$B_1^{C'}$	-0.0861	-0.0866	-0.0990	-0.1262
$B_2^{C'}$	0.0291	0.0293	0.0355	0.0503
$B_3^{C'}$	-0.0152	-0.0153	-0.0192	-0.0290
$B_4^{C'}$	0.0095	0.0096	0.0123	0.0194
$B_5^{C'}$	-0.0066	-0.0067	-0.0087	-0.0142
$B_6^{C'}$	0.0049	0.0050	0.0065	0.0109
$D_1^{C'}$	-0.0896	-0.2101	-0.4229	-0.4931
$D_2^{C'}$	0.0300	0.0625	0.1623	0.2406
$D_3^{C'}$	-0.0156	-0.0309	-0.0850	-0.1518
$D_4^{C'}$	0.0098	0.0188	0.0520	0.1067
$D_5^{C'}$	-0.0068	-0.0128	-0.0351	-0.0797
$D_6^{C'}$	0.0051	0.0094	0.0254	0.0619

Table B.3: Coefficients $B_n^{C'}$ and $D_n^{C'}$ for thin film heads with poles at constant potential, $g/L = 1.0$.

g/t	0.125	0.5	2.0	8.0	16.0
$B_1^{L'}$	0.1084	0.1089	0.1091	0.1092	0.1092
$B_2^{L'}$	-0.0291	-0.0293	-0.0294	-0.0294	-0.0294
$B_3^{L'}$	0.0137	0.0138	0.0139	0.0139	0.0139
$B_4^{L'}$	-0.0081	-0.0082	-0.0082	-0.0082	-0.0082
$B_5^{L'}$	0.0054	0.0054	0.0055	0.0055	0.0055
$B_6^{L'}$	-0.0039	-0.0039	-0.0039	-0.0039	-0.0039
$D_1^{L'}$	-0.5009	-0.3112	-0.2088	-0.1963	-0.1956
$D_2^{L'}$	0.1841	0.0962	0.0622	0.0588	0.0587
$D_3^{L'}$	-0.0956	-0.0442	-0.0308	-0.0293	-0.0292
$D_4^{L'}$	0.0584	0.0267	0.0188	0.0179	0.0178
$D_5^{L'}$	-0.0394	-0.0181	-0.0128	-0.0122	-0.0122
$D_6^{L'}$	0.0284	0.0132	0.0094	0.0089	0.0089

Table B.4: Coefficients $B_n^{L'}$ and $D_n^{L'}$ for thin film heads with linearly varying pole potentials, $L/t = 0.5$.

L/t	0.03125	0.125	0.5	2.0
$B_1^{L'}$	1.6428	0.4208	0.1089	0.0274
$B_2^{L'}$	-0.4180	-0.1098	-0.0293	-0.0074
$B_3^{L'}$	0.1890	0.0507	0.0138	0.0035
$B_4^{L'}$	-0.1080	-0.0295	-0.0082	-0.0021
$B_5^{L'}$	0.0702	0.0194	0.0054	0.0014
$B_6^{L'}$	-0.0493	-0.0139	-0.0039	-0.0010
$D_1^{L'}$	-1.8387	-0.6171	-0.3112	-0.2354
$D_2^{L'}$	0.4822	0.1718	0.0962	0.0695
$D_3^{L'}$	-0.2218	-0.0818	-0.0442	-0.0342
$D_4^{L'}$	0.1285	0.0486	0.0267	0.0208
$D_5^{L'}$	-0.0843	-0.0325	-0.0181	-0.0141
$D_6^{L'}$	0.0599	0.0235	0.0132	0.0103

Table B.5: Coefficients $B_n^{L'}$ and $D_n^{L'}$ for thin film heads with linearly varying pole potentials, $g/t = 0.5$.

t	0.125	1.0	4.0	16.0
$B_1^{L'}$	0.0137	0.1089	0.4163	1.6283
$B_2^{L'}$	-0.0037	-0.0293	-0.1076	-0.4100
$B_3^{L'}$	0.0018	0.0138	0.0493	0.1836
$B_4^{L'}$	-0.0100	-0.0082	-0.0285	-0.1041
$B_5^{L'}$	0.0007	0.0054	0.0187	0.0672
$B_6^{L'}$	-0.0005	-0.0039	-0.0133	-0.0470
$D_1^{L'}$	-0.1033	-0.3112	-0.7513	-1.9669
$D_2^{L'}$	0.0337	0.0906	0.2498	0.5821
$D_3^{L'}$	-0.0174	-0.0442	-0.1275	-0.2976
$D_4^{L'}$	0.0108	0.0267	0.0775	0.1876
$D_5^{L'}$	-0.0075	-0.0181	-0.0521	-0.1318
$D_6^{L'}$	0.0056	0.0132	0.0376	0.0988

Table B.6: Coefficients $B_n^{L'}$ and $D_n^{L'}$ for thin film heads with linearly varying pole potentials, $g/L = 1.0$.

B.2 Single pole heads

							Constant
L/t	0.125	0.25	0.5	1.0	2.0	50	50
$B_1^{LP'}$	-0.064657	-0.052681	-0.045049	-0.043163	-0.043079	-0.043079	-0.086157
$B_2^{LP'}$	0.018400	0.015477	0.014653	0.014577	0.014575	0.014575	0.029150
$B_3^{LP'}$	-0.008797	-0.007857	-0.007658	-0.007628	-0.007627	-0.007627	-0.015254
$B_4^{LP'}$	0.005299	0.004916	0.004817	0.004797	0.004796	0.004796	0.009593
$B_5^{LP'}$	-0.003621	-0.003423	-0.003356	-0.003341	-0.003340	-0.003340	-0.006680
$B_6^{LP'}$	0.002671	0.002546	0.002495	0.002483	0.002483	0.002483	0.004965
$D_1^{LP'}$	-0.254826	-0.205421	-0.145825	-0.097735	-0.070503	-0.044176	
$D_2^{LP'}$	0.100366	0.069302	0.044008	0.029416	0.021998	0.014872	
$D_3^{LP'}$	-0.054119	-0.034508	-0.021582	-0.014656	-0.011143	-0.007768	
$D_4^{LP'}$	0.033787	0.020791	0.013061	0.008964	0.006881	0.004880	
$D_5^{LP'}$	-0.023094	-0.014022	-0.008867	-0.006129	-0.004735	-0.003396	
$D_6^{LP'}$	0.016811	0.010173	0.006470	0.004496	0.003490	0.002523	

Table B.7: Coefficients $B_n^{LP'}$ and $D_n^{LP'}$ for single pole heads with linearly varying pole potentials.

$\varphi_B(x,0)$	Linear	Quadratic	Cubic	Cosine-squared	Linear $B_n^{LP'}$ N=320	Linear $B_n^{LP'}$ corr. to 6dp.
$B_1^{AP'}$	-0.04505	-0.00189	0.01969	-0.12193	-0.04505	-0.045049
$B_2^{AP'}$	0.01465	-0.00025	-0.00771	0.03445	0.01465	0.014653
$B_3^{AP'}$	-0.00766	-0.00042	0.00319	-0.01287	-0.00766	-0.007658
$B_4^{AP'}$	0.00482	0.00068	-0.00138	0.00550	0.00482	0.004817
$B_5^{AP'}$	-0.00335	-0.00074	0.00057	-0.00253	-0.00335	-0.003356
$B_6^{AP'}$	0.00249	0.00072	-0.00017	0.00118	0.00249	0.002495
$D_1^{AP'}$	0.04003	0.04003	0.04496		-0.14582	-0.145825
$D_2^{AP'}$	-0.00647	-0.00647	-0.01021		0.04400	0.044008
$D_3^{AP'}$	0.00093	0.00093	0.00332		-0.02158	-0.021582
$D_4^{AP'}$	0.00039	0.00039	-0.00119		0.01306	0.013061
$D_5^{AP'}$	-0.00076	-0.00076	0.00035		-0.00886	-0.008867
$D_6^{AP'}$	0.00084	0.00084	0.00003		0.00647	0.006470

Table B.8: Coefficients $B_n^{AP'}$ and $D_n^{AP'}$ for single pole heads with various pole potentials, $L/t = 0.5$.

B.3 Shielded, infinitely thin MR sensors

G_1	α	β	γ	δ	S^A	z_0^A
0.5	0.593636	1.894831	0.593636	1.0	-1.280774	-0.441271
0.25	0.579534	3.178338	0.920963	1.599118	-2.102338	-0.733081
0.125	0.583152	5.456887	1.490165	2.653571	-3.585123	-1.012372
0.0625	0.590413	9.262212	2.426713	4.404794	-6.072661	-1.292910

Table B.9: Schwarz-Christoffel mapping constants for shielded, infinitely thin MR sensors where $G_2 = 0.5$, $t = 1$ and $r = 0$.

t	α	β	γ	δ	S^A	z_0^A
1	0.579534	3.178338	0.920963	1.599118	-2.102338	-0.733081
2	0.569728	6.135041	0.917552	1.671889	-7.892897	-1.376321
4	0.567153	12.156259	0.916591	1.692733	-31.037872	-2.647432
8	0.566501	24.255204	0.916343	1.698136	-123.613129	-5.180072

Table B.10: Schwarz-Christoffel mapping constants for shielded, infinitely thin MR sensors where $G_1 = 0.25$, $G_2 = 0.5$ and $r = 0$.

r	α	β	γ	δ	S^A	z_0^A
0	0.579534	3.178338	0.920963	1.599118	-2.102338	-0.733081
0.01	0.560295	3.208590	0.901076	1.598002	-2.126556	-0.732808
0.1	0.392090	3.341347	0.691780	1.525901	-2.243159	-0.714890
1.0	0.007387	2.866324	0.014773	1.012951	-1.948830	-0.570381

Table B.11: Schwarz-Christoffel mapping constants for shielded, infinitely thin MR sensors where $G_1 = 0.25$, $G_2 = 0.5$ and $t = 1$.

Glossary

a	Prefix to a superscript: an approximation.
aGP	Superscript: an approximation generalised to an arbitrary potential.
A	Subscript: region A.
$\bar{A}$	Superscript: asymmetrically shielded MR sensor.
Å	Angstrom unit.
AP	Superscript: arbitrary potential single pole .
b	Bit cell length.
B	Subscript: region B.
$\underline{B}$	Magnetic flux density.
C	Subscript: region C.
C	Superscript: constant potential thin film head.
C	Real constant.
d	Head – medium separation.
D_{50}	Bit density at which output voltage is half that for isolated transition.
e	Voltage.
g	Semi-gap width.
G	Full gap width.
$\underline{H}$	Magnetic field strength.
H_x	Horizontal field component.
H_y	Vertical field component.
$\widehat{H}_y$	Fourier transform of H_y.
i	$\sqrt{-1}$.
In	Superscript: inductive.

$\underline{j}$	Current density.
L	Semi-pole thickness.
L	Superscript: linear pole potential thin film head.
L_m	Mutual inductance.
LP	Superscript: linear potential single pole head.
M_r	Remanent magnetisation.
MR	Magnetoresistive (also as superscript).
P	Superscript: constant potential single pole head.
r	Pole recession.
R	Superscript: ring head without an underlayer.
RU	Superscript: ring head with an underlayer.
S	Complex constant.
S	Superscript: derived by Szczech *et al.*
t	Head – underlayer separation, time in Section 2.1.5.
TF	Superscript: thin film head.
v	Velocity.
V	Maximum pole potential.
w	Track width.
$\bar{x}$	Position on medium relative to coordinates of the head.
z_0	Complex constant.
α	Proportion of the maximum potential at the leading pole edge.
$\alpha, \beta, \gamma, \delta$	Real constants in the complex w-plane.
β	Proportion of the maximum potential at the trailing pole edge.
ε_0	Permittivity of a vacuum.
δ	Medium thickness.

γ	Euler's constant.
κ	Wavenumber.
λ	Wavelength.
μ	Permeability of a material, relative to μ_0.
μ_0	Permeability of a vacuum.
$\bar{\phi}$	Flux.
φ	Magnetic potential.
$\widehat{\varphi}$	Fourier transform of φ.
Φ	Phase angle.
ρ	Charge density.

References

[1] F. Jorgensen. *The Complete Handbook of Magnetic Recording.* Tab Books , Blue Ridge Summit, Pa, 1980.

[2] R. Nass. Hard-disk drives pack more data into less space. *Electronic Design*, 73–83, 3rd May 1993.

[3] S. Iwasaki and Y. Nakamura. An analysis for the magnetization mode for high density magnetic recording. *IEEE Trans. Magn.*, MAG-13(5):1272–1277, Sept. 1977.

[4] S. Iwasaki, Y. Nakamura and K. Ouchi. Perpendicular magnetic recording with a composite anisotropy film. *IEEE Trans. Magn.*, MAG-15(6):1456–1458, Nov. 1979.

[5] S. Iwasaki. Magnetism and information. *J. Mag. Soc. Japan*, 15(S2):1–14, 1991.

[6] S. Yamamoto, Y. Nakamura and S. Iwasaki. Extemely high bit density recording with single-pole perpendicular head. *IEEE Trans. Magn.*, MAG-23(5):2070–2072, Sept. 1987.

[7] D.J. Mapps. Jumbo memories. The Times Higher Education Supplement 14.6.91, VIII–IX.

[8] S. Iwasaki, Y. Nakamura and H. Muraoka. Wavelength response of perpendicular magnetic recording. *IEEE Trans. Magn.*, MAG-17(6):2535–2537, Nov. 1981.

[9] K. Yamamori, R. Nishikawa, T. Asano and T. Fujiwara. Perpendicular magnetic recording performace of double-layer media. *IEEE Trans. Magn.*, MAG-17(6):2538–2540, Nov. 1981.

[10] H.N. Bertram. Fundamentals of the magnetic recording process. *Proc. IEEE*, 74(11):1494–1512, Nov. 1986.

[11] A. Ohtsubo and Y. Satoh. Thick non-parallel single pole heade for perpendicular recording from one side. *IEEE Trans. Magn.*, MAG-18(6):1173–1175, Nov. 1982.

[12] Y. Satoh, A. Ohtsubo and Y. Shimada. Design of a single-edge-sensitive thin film head core with perpendicular double layer medium. *IEEE Trans. Magn.*, MAG-21(5):1551–1553, Sept. 1985.

[13] J. Hokkyo, K. Hayakawa, I. Saito and K. Shirane. A new W-shaped single-pole head and a high density flexible disk perpendicular magnetic recording system. *IEEE Trans. Magn.*, MAG-20(1):72–74, Jan. 1984.

[14] R.E. Jones and C.D. Mee, Recording Heads, Ch.4 . *Magnetic Recording Handbook: Technology and Applications.* C.D. Mee and E.D. Daniel (eds.), McGraw-Hill, New York, 1990.

[15] M.H. Kryder, Ch.2. *Applied Magnetism.* R. Gerber, C.D.Wright and G. Asti (eds.), Kluwer Academic Publishers, The Netherlands, 1994.

[16] R.M. White, (ed.), Ch.1. *Introduction to Magnetic Recording.* IEEE Press, New York, 1985.

[17] D.T. Wilton, D.J. Mapps and H.A. Shute. Exact field calculations for conventional and graded magnetisation thin film recording heads. *IEEE Trans. Magn.*, 30(2):253–263, Mar. 1994.

[18] D.T. Wilton, D.J. Mapps and H.A. Shute. Improved replay performance of a single pole head with graded magnetisation for perpendicular recording. *J. Mag. Soc. Japan*, 18(S1):157–160, 1994.

[19] D.T. Wilton, D.J. Mapps and H.A. Shute. A graded magnetisation single pole head for perpendicular recording. *IEEE Trans. Magn.*, 31(3):2339–2350, May 1995.

[20] H.A. Shute, D.T. Wilton and D.J. Mapps. Exact spectral response functions for various perpendicular recording heads. *IEEE Trans. Magn.*, submitted Jan. 1995.

[21] H.A. Shute, D.T. Wilton and D.J. Mapps. Approximate spectral response functions for perpendicular recording heads. *JMMM*, accepted Sept. 1995.

[22] H.A. Shute, D.T. Wilton and D.J. Mapps. A theoretical analysis of shielded magnetoresistive heads by conformal mapping. *IEEE Trans. Magn.*, submitted Jul. 1995.

[23] G.J.Y. Fan. Analysis of a practical perpendicular head for digital purposes. *J. Appl. Phys.*, 31(5):402S–403S, May 1960.

[24] G.J.Y. Fan. A study of the playback process of a magnetic ring head. *IBM J. Res. Devel.*, (5):321–325, Oct. 1961.

[25] A.W. Baird. An evaluation and approximation of the Fan equations describing magnetic fields near recording heads. *IEEE Trans. Magn.*, MAG-16(5):1350–1352, Sept. 1980.

[26] H.L. Huang and H.Y. Deng. Comparison of ring head and SPT head write fields. *IEEE Trans. Magn.*, MAG-22(5):1305–1309, Sept. 1986.

[27] D.T. Wilton. Comparison of ring and pole head magnetic fields. *IEEE Trans. Magn.*, 26(3):1229–1232, May 1990.

[28] D.T. Wilton. An analysis of the magnetic field of a ring head with a highly permeable underlayer. *IEEE Trans. Magn.*, 27(4):3751–3755, Jul. 1991.

[29] D.T. Wilton and D.J. Mapps. An analysis of a shielded magnetic pole for perpendicular recording. *IEEE Trans. Magn.*, 29(6):4182–4193, Nov. 1993.

[30] E. Champion and H.N. Bertram. The effect of MR head geometry on playback pulse shape and spectra. *IEEE Trans. Magn.*, 31(4):2461–2470, Jul. 1995.

[31] J.C. Mallinson. *The Foundations of Magnetic Recording.* Academic Press, New York, 1993.

[32] K.J. Binns and P.J. Lawrenson. *Analysis and Computation of Electric and Magnetic Field Problems.* Pergamon Press, Oxford, 1973.

[33] *Numerical Algorithms Group Ltd Fortran Library Manual.* Oxford.

[34] A.D. Booth. On two problems in potential theory and their application to the design of magnetic recording heads for digital computers. *British J. App. Ph.*, 3:307–308, 1952.

[35] W.K. Westmijze. Studies on magnetic recording . II field configuration around the gap and the gap-length formula. *Philips Res. Rep.*, 8:161–183, Jun. 1953.

[36] J.S. Yang and H.L. Huang. Calculation of exact head and image fields of recording heads by conformal mapping. *IEEE Trans. Magn.*, 25(3):2761–2768, May 1989.

[37] O. Karlqvist. Calculation of the magnetic field in the ferromagnetic layer of a magnetic drum. *Trans. Roy. Inst. Technol. Stockholm*, 86:1–27, 1954.

[38] N. Curland and J.H. Judy. Calculation of exact ring head fields using conformal mapping. *IEEE Trans. Magn.*, MAG-22(6):1901–1903, Nov. 1986.

[39] O. Lopez, W.P. Wood, N.H. Yeh and M. Jursich. Interaction of a ring head and double layer media - field calculations. *IEEE Trans. Magn.*, MAG-18(6):1179–1181, Nov. 1982.

[40] I. Elabd. A study of the field around magnetic heads of finite length. *IEEE Trans. Audio*, 21–27, Jan.–Feb. 1963.

[41] I. Megory-Cohen and T.D. Howell. Exact field calculations for asymmetric finite-pole-tip ring heads. *IEEE Trans. Magn.*, 24(3):2074–2080, May 1988.

[42] M. Steinback, J.A. Gerber and T.J. Szczech. Exact solution for the field of a perpendicular head. *IEEE Trans. Magn.*, MAG-17(6):3117–3119, Nov. 1981.

[43] M.F. Beusekamp. *Simulation of the Perpendicular Magnetic Recording Process.* PhD thesis, Twente University, Netherlands, 1987.

[44] D.E. Heim. The sensitivity function for shielded magnetoresistive heads by conformal mapping. *IEEE Trans. Magn.*, MAG-19(5):1620–1622, Sept. 1983.

[45] V.B. Minuhin. Comparison of sensitivity functions for ideal probe and ring-type heads. *IEEE Trans. Magn.*, MAG-20(3):488–494, May 1984.

[46] V.B. Minuhin. Field of thin-film head of finite dimensions. *J. Appl. Phys.*, 67(9):4866–4868, May 1990.

[47] C.S. Wang and H.L. Huang. Gap-null free spectral response of asymmetric ring heads for longitudinal and perpendicular recording. *IEEE Trans. Magn.*, 26(5):2403–2405, Sept. 1990.

[48] J.S. Yang and C.R. Chang. Exact field calculations for asymmetric ring heads. *IEEE Trans. Magn.*, 28(5):2072–2076, Sept. 1992.

[49] J.S. Yang and C.R. Chang. Magnetic field of an asymmetric ring head with an underlayer. *IEEE Trans. Magn.*, 29(2):2069–2072, Mar. 1993.

[50] V.B. Minuhin. A general solution for the field of polygonal electromagnet. *IEEE Trans. Magn.*, 29(6):4121–4141, Nov. 1993.

[51] P. Henrici. *Applied and Computational Complex Analysis, Vol. 1.* John Wiley & Sons, Inc., New York, 1974.

[52] M.R. Spiegel. *Theory and Problems of Complex Variables with an Introduction to Conformal Mapping and its Applications.* Schaum Publishing Co., New York, 1964.

[53] B.K. Middleton, Recording and Reproducing Processes, Ch.2 . *Magnetic Recording Handbook: Technology and Applications.* C.D. Mee and E.D. Daniel (eds.), McGraw-Hill, New York, 1990.

[54] R.I. Potter and I.A. Beardsley. Self-consistent computer calculations for perpendicular magnetic recording. *IEEE Trans. Magn.*, MAG-16(5):967–972, Sept. 1980.

[55] D.A Lindholm. Application of higher order boundary integral equations to two-dimensional magnetic head problems. *IEEE Trans. Magn.*, MAG-17(5):2445–2452, Sept. 1981.

[56] T.J. Szczech and K.E. Palmquist. A 3-D comparison of the fields from six basic head configurations. *IERE Conf. Proc.*, (59):17–22, Apr. 1984.

[57] J.S. Yang. Magnetic field of a thin film head with an underlayer. *IEEE Trans. Magn.*, 30(4):1504–1508, Jul. 1994.

[58] R.I. Potter. Analytic expressions for the fringe fields of finite pole-tip length recording heads. *IEEE Trans. Magn.*, MAG-11(1):80–81, Jan. 1975.

[59] T.J. Szczech. Analytic expressions for field components of nonsymmetrical finite pole tip length magnetic head based on measurements on large-scale model. *IEEE Trans. Magn.*, MAG-15(5):1319–1322, Sept. 1979.

[60] T.J. Szczech and P.R. Iverson. An approach for deriving field equations for magnetic heads of different geometric configurations. *IEEE Trans. Magn.*, MAG-22(5):355–360, Sept. 1986.

[61] T.J. Szczech and P.R. Iverson. Improvement of the coefficients in field equations for thin-film recording heads. *IEEE Trans. Magn.*, MAG-23(5):3866–3867, Sept. 1987.

[62] G.A. Bertero, H.N. Bertram and D.M. Barnett. Fields and transforms for thin film heads. *IEEE Trans. Magn.*, 29(1):67–76, Jan. 1993.

[63] N.H. Yeh. Anomalous wavelength response of a thin film head from double-layer perpendicular media. *IEEE Trans. Magn.*, MAG-19(5):1611–1613, Sept. 1983.

[64] J.C. Mallinson. On recording head field theory. *IEEE Trans. Magn.*, MAG-10(5):773–775, Sept. 1974.

[65] R.I. Potter. Digital magnetic recording theory. *IEEE Trans. Magn.*, MAG-10(5):502–508, Sept. 1974.

[66] T.A. Schwarz and S.K. Decker. Comparison of calculated and actual density responses of a magnetoresistive head. *IEEE Trans. Magn.*, MAG-15(6):1622–1624, Nov. 1979.

[67] D.J. O'Connor, F.B. Shelledy and D.E. Heim. Mathematical model of a magnetoresistive read head for a magnetic tape drive. *IEEE Trans. Magn.*, MAG-21(5):1560–1562, Sept. 1985.

[68] J.S. Feng. Gap length and sensor height effects on readback signals in shielded magnetoresistive sensors. *IEEE Trans. Magn.*, 28(2):1031–1037, Mar. 1992.

[69] C. Tsang and I.A. Beardsley. A theoretical study of MR sensors in vertical recording. *JMMM*, 54-57:1595–1597, 1986.

[70] M. Huang and J.H. Judy. FEM model of a shielded and biased single-layer magnetorestitive read head. *J. Mag. Soc. Japan*, 13(S1):505–509, 1989.

[71] M.K. Bhattacharyya, G.J. Tarnopolsky and L.T. Tran. 3D analysis of MR readback on perpendicular medium. *IEEE Trans. Magn.*, 27(6):4707–4709, Nov. 1991.

[72] T.R. Koehler. Simulation of micromagnetic and magnetoresistive response in a shielded permalloy strip. *IEEE Trans. Magn.*, 30(6):3867–3869, Nov. 1994.

[73] A.V. Davies and B.K. Middleton. The resolution of vertical magneto-resistive readout heads. *IEEE Trans. Magn.*, MAG-11(6):1689–1691, Nov. 1975.

[74] B.K. Middleton, A.V. Davies and D.J. Sansom. The modelling of shielded magneto-resistive replay head performance. *Proc. IERE Conf.*, (43):353–363, 1979.

[75] D.A. Lindholm. Dependence of reproducing gap null on head geometry. *IEEE Trans. Magn.*, MAG-11(6):1692–1696, Nov. 1975.

[76] Y. Ichiyama. Reproducing characteristics of thin film heads. *IEEE Trans. Magn.*, MAG-11(5):1203–1205, Sept. 1975.

[77] D.S. Bloomberg. Spectral response from perpendicular media with gapped head and underlayer. *IEEE Trans. Magn.*, MAG-19(4):1493–1502, Jul. 1983.

[78] K. Krusch, M. Hettrich, C. Scholz, G. Schulz and G. Leyendecker. Configurational dependence of the read - write properties of thin film heads. *IEEE Trans. Magn.*, 24(6):2847–2849, Nov. 1988.

[79] D.A. Lindholm. Reproduce characteristics of rectangular magnetic heads. *IEEE Trans. Magn.*, MAG-12(6):710–712, Nov. 1976.

[80] A. Ulanovskii and N. Ulanovskii. 1993. Private communication.

[81] I.S. Gradshteyn and I.M. Ryzhik. *Table of Integrals, Series and Products.* Academic Press, New York, 1993.

[82] A. Ralston and P. Rabinowitz. *A First Course in Numerical Analysis.* McGraw-Hill, New York, 1978.

[83] T.J. Szczech, M. Steinback and M. Jodeit Jr. Equations for the field components of a perpendicular magnetic head. *IEEE Trans. Magn.*, MAG-18(1):229–232, Jan. 1982.

[84] B.K. Middleton. Modelling the digital magnetic behaviour of shielded magnetoresistive replay heads with displaced elements. *Radio Electron. Eng.*, 50(8):419–425, Aug. 1980.

[85] M.J. Vos and J.H. Judy. Sensitivity function and spectral response without gap-nulls of an inductive perpendicular head geometry. *IEEE Trans. Magn.*, 24(6):2401–2403, Nov. 1988.

[86] H. Lübeck. Magnetische Schallaufzeichnung mit Filmen und Ringköpfen. *Akust. Z.*, (2):273 - 295, Nov. 1937.

[87] J.C. Mallinson, Recording Limitations, Ch.5. in. *Magnetic Recording Handbook: Technology and Applications.* C.D. Mee and E.D. Daniel (eds.), McGraw-Hill, New York, 1990.

[88] V. Zieren, S.B. Luitjens, C.P.G. Schrauwen, R.W. de Bie and M. Piena. Properties of one-sided probe heads on double-layer perpendicular recording media. *IEEE Trans. Magn.*, MAG-22(5):370–372, Sept. 1986.

[89] M.J. Vos, S.B. Luitjens, R.W. de Bie and J.C. Lodder. Magnetization transitions obtained by deconvolution of measured replay pulses in perpendicular magnetic recording. *IEEE Trans. Magn.*, MAG-22(5):373–375, Sept. 1986.

[90] S. Iwasaki. Perpendicular magnetic recording — evolution and future —. *IEEE Trans. Magn.*, MAG-20(5):657–662, Sept. 1984.

[91] A.S. Hoagland and J.E. Monson. *Digital Magnetic Recording.* Wiley, New York, 1991.

[92] H.N. Bertram and D.A. Lindholm. Dependence of reproducing gap null on medium permeability and spacing. *IEEE Trans. Magn.*, MAG-18(3):893–897, May 1982.

[93] D.S. Bloomberg, M.H. Lean and G.V. Kelley. Readback bit shift with finite pole-length heads on perpendicular media. *IEEE Trans. Magn.*, MAG-19(5):1617–1619, Sept. 1983.

[94] I. Saito, S. Satake, K. Kawazoe and J. Hokkyo. Peakshift characteristics of perpendicular magnetic recording. *IEEE Trans. Magn.*, MAG-20(5):903–905, Sept. 1984.

[95] M. Abramowitz and I.A. Stegun. *Handbook of Mathematical Functions.* Dover Pub Inc., 1965.